Beyond the Blur

Construction and Characterization of the First Autonomous AO System and An AO Survey of Magnetar Proper Motions

A Thesis by
Shriharsh Prakash Tendulkar
Advisor
Prof. Shrinivas R. Kulkarni

In Partial Fulfillment of the Requirements
for the Degree of
Doctor of Philosophy

California Institute of Technology
Pasadena, California

2014

(Defended August 26, 2013)

Acknowledgments

As a child, I had always heard of Caltech as the Mecca of sciences, a place where giants like Feynman, Gell-Mann and Zwicky (in alphabetical order) roamed. It has been my greatest fortune to work at Caltech among such intellectual peers. My work over the past four years was advised by two incredible advisors: Shri Kulkarni and Christoph Baranec. In his inimitable flair, Shri provided the 'big-picture' advice, the sharp scientific guidance, the patient yet frank appraisal and critical feedback. He taught me to think critically and to look at the big-picture without immediately getting bogged down in minor details. Christoph, as an expert in AO, taught me all I know about optical engineering and design and practical optical work, mostly in the COO laboratory and often during long drives to and from Palomar in his station wagon (listening to the interminable trance music). From him, I learnt the importance of the minutiae, the importance of considering all possible details before committing a hardware design and the importance of maintaining documentation as a project progresses.

On the Robo-AO project, many thanks are due to Reed Riddle and Nicholas Law for all the excellent discussions and work together (while maintaining patience through my mistakes). I would like to thank our partners at IUCAA, Ramprakash, for his advice and mentorship when I was a young graduate student just beginning work, and Mahesh Burse and Hillol Das for their help on Robo-AO.

It has been enjoyable to work with Lynne Hillenbrand on pre-main-sequence stars. The vastness of her knowledge of stars and everything people know about them never ceases to amaze me. I look forward to continue the work through the future.

It has been a pleasure to spend long observing runs at Palomar because of the amazingly dedicated staff. None of this work would have been possible without their support. Special warm thanks to Dipali Crosse who makes a Palomar trip just like homecoming, pampering us with delicious food and stern warnings to eat our proteins. The observatory crew: Steve Kunzman, Mike Doyle, Greg van Idsinga, Bruce Baker, Drew Roderick helped countless times with the Robo-AO installation and removal and for many machining requests. John Henning and Kevin Rykoski were the quick and patient responders to my multitude of computer and electronics requests, often made in the middle of the night. Jean Mueller and Kajsa Peffer provided great help and guidance during my 200-inch observing runs. At COO, Richard Dekany kept his office open for anytime advice and suggestions. Ernest Croner, Jason Fucik and others helped out with my laboratory setups.

I thank Brian Cameron for his support on precision astrometry and our magnetar work through his busy schedule. The Keck support astronomers: Marc Kassis, Hien Tran, Luca Rizzi and Jim Lyke who helped through all the NIRC2 nights, some beautiful and some

marred with software bugs were of great help in the magnetar proper motion survey.

I believe one of the greatest reasons for Caltech's success is the extremely dedicated staff who would go far out of their way to accomodate our whimsy requests: Patrick, Anu and Jose ran an amazing computer setup, responding to software SOS emails in the middle of the night. The administrators Gita, Gina, Althea, Bronagh, Anna-Marie, Pam and Judith who helped out at each and every step of the way with a cheerful smile. I must specially thank Efrain Hernandez for all the wonderful discussions in the corridors and the sunny encouragement.

I've had the greatest fun discussing everything from quantum chromodynamics to travel and rock-climbing and recipes with a wonderful group of colleagues over the past five years. Swarnima, Ryan and Dmitiry, my classmates, my seniors: Elisabeth, Walter, Laura, Joey, Gwen, Drew, Matthew, Krzysztof, Thiago, Karin and my juniors: Kunal, Matt, Ke, Sebastian, Jackie, Michael, Tejaswi, Ben, John, Melodie, Mislav, Antonija, Allison and others. You guys and girls are AWESOME!

My extended family away from home has been my very close circle of friends who have always been around to support, encourage, cheer up and when necessary scold: In approximate order of decreasing senescence and uniformly high awesomeness, they are: Ashish, Anu, Vijay, Sowmya, Varun, Pinkesh, Zeeshan, Naresh, Mansi, Setu, Prabha, Krishna, Arundhati, Samir, JK, Sushree, Ravi Teja.

To my 'brothers': Varun, Pinkesh and Abhilash and 'sisters': Swarnima and Ishwari, I have no words to describe how much your support has meant to me. Thank you for bearing with my bad, bad jokes, for feeding me when I was hungry and cranky and taking me to the mountains when I was still crankier.

Through many years of our friendship, Kartiki has been a pillar of support by my side; celebrating success and consoling failure.

And most importantly, I'm immensely grateful to my parents Jyotsna and Prakash and my sister Mallika who have supported me fully in everything that I did.

To my parents and my sister,
who brought me up to be who I am.

The road to wisdom? — Well, its plain
and simple to express:
Err and err and err again
but less and less and less.
—Piet Hein

I thought I knew I knew it all,
But now I must confess,
The more I know I know I know,
I know I know the less.
—Anon

Abstract

Adaptive optics (AO) corrects distortions created by atmospheric turbulence and delivers diffraction-limited images on ground-based telescopes. The vastly improved spatial resolution and sensitivity has been utilized for studying everything from the magnetic fields of sunspots upto the internal dynamics of high-redshift galaxies. This thesis about AO science from small and large telescopes is divided into two parts: Robo-AO and magnetar kinematics.

In the first part, I discuss the construction and performance of the world's first fully autonomous visible light AO system, Robo-AO, at the Palomar 60-inch telescope. Robo-AO operates extremely efficiently with an overhead $< 50\,\mathrm{s}$, typically observing about 22 targets every hour. We have performed large AO programs observing a total of over 7,500 targets since May 2012. In the visible band, the images have a Strehl ratio of about 10% and achieve a contrast of upto 6 magnitudes at a separation of $1''$. The full-width at half maximum achieved is 110–130 milli-arcsecond. I describe how Robo-AO is used to constrain the evolutionary models of low-mass pre-main-sequence stars by measuring resolved spectral energy distributions of stellar multiples in the visible band, more than doubling the current sample. I conclude this part with a discussion of possible future improvements to the Robo-AO system.

In the second part, I describe a study of magnetar kinematics using high-resolution near-infrared (NIR) AO imaging from the 10-meter Keck II telescope. Measuring the proper motions of five magnetars with a precision of upto $0.7\,\mathrm{milli\text{-}arcsecond\,yr^{-1}}$, we have more than tripled the previously known sample of magnetar proper motions and proved that magnetar kinematics are equivalent to those of radio pulsars. We conclusively showed that SGR 1900+14 and SGR 1806−20 were ejected from the stellar clusters with which they were traditionally associated. The inferred kinematic ages of these two magnetars are $6 \pm 1.8\,\mathrm{kyr}$ and $650 \pm 300\,\mathrm{yr}$ respectively. These ages are a factor of three to four times greater than their respective characteristic ages. The calculated braking index is close to unity as compared to three for the vacuum dipole model and 2.5–2.8 as measured for young pulsars. I conclude this section by describing a search for NIR counterparts of new magnetars and a future promise of polarimetric investigation of a magnetars' NIR emission mechanism.

A full-color electronic version of this thesis may be accessed at http://resolver.caltech.edu/CaltechTHESIS:11192013-181748112.

Contents

List of Figures

List of Tables

List of Acronyms

ADC: atmospheric dispersion corrector
AGN: active galactic nuclei
AO: adaptive optics
AXP: anomalous X-ray pulsar
BH: black hole
CCD: charge-coupled device
DM: deformable mirror
EMCCD: electron multiplying CCD
FITS: flexible image transport system
FOV: field of view
FWHM: full width at half maximum
JSpOC: joint space operations center
LCH: laser clearing house
LGS: laser guide star
mas: milli-arcsecond
NS: neutron star
OAP: off-axis paraboloid
PSF: point-spread function
QE: quantum efficiency
SGR: soft gamma repeater
SNR: signal-to-noise ratio, supernova remnant[1]
ToO: target of opportunity
TTM: tip-tilt mirror
WF: wavefront
WFE: wavefront error
WFS: wavefront sensor

[1] Whenever used, the distinction is clear from the context.

Chapter 1

Introduction

1.1 The Problems of Atmospheric Turbulence

The performance of ground-based astronomical instruments (cameras, spectrographs etc) working at visible, infrared (IR) and to some extent radio wavelengths is significantly limited by the presence of the turbulent atmosphere above us. The twinkling of stars, glorified as it has been by idle poets, was never admired by astronomers because it blurred images of astronomical objects.

Astronomers, having to contend with such blurring, sought to alleviate the blurring effects by setting up observatories in locations where the atmospheric turbulence was the lowest. As early as 1704, scientists such as Issac Newton has pointed out that *"the Air through which we look upon the Stars is in a perpetual Tremor"* and that *"The only Remedy is a most serene and quiet Air, such as may perhaps be found on the tops of the highest Mountains above the grosser Clouds"*. Newton's advice was taken well and most ground-based observatories constructed since have been on mountain tops with as little turbulence as possible.

The effect of turbulence, at a given moment, is to split the image of the star into multiple speckles that jitter around as the atmosphere changes. Each speckle is about the size of the diffraction limited PSF. These speckles follow a Gaussian distribution whose full-width half-maximum (FWHM) usually measured in arcseconds is known as the 'seeing' at the telescope at the time of observation. Over a long time scale ($>\approx 5\,\mathrm{s}$), the speckles add up into the Gaussian profile (Figure 1.1) that is known as the 'seeing disk' or the seeing point spread function (PSF). An observatory with a typical (median) seeing of $0.7''$ is considered to be good by modern standards. The median seeing at the Palomar Observatory (altitude 5500 ft) is $\approx 1.2''$ whereas the median seeing at the Keck observatory (altitude 13500 ft) is $0.7''$. Seeing values can change drastically from night to night and even from hour to hour in extreme cases and are affected by non-atmospheric parameters such as the temperature difference between the telescope mirror and the air in front of it, the temperature difference between the dome air and the outside air. Modern observatories carefully consider dome airflows, mirror cooling systems and ventilation to alleviate these sources of turbulence as much as possible.

The blurring of images causes two immediate problems: 1) light from closely separated

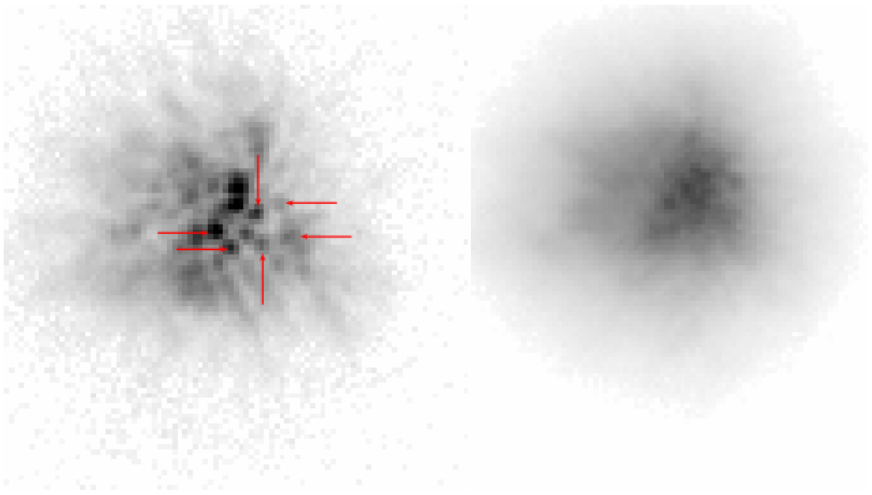

Figure 1.1. The effect of atmospheric turbulence on the image. *Left Panel:* On a short time-scale (≈0.1 s) the light from the star breaks up into small 'speckles' denoted by the red arrows. Each speckle has a size scale similar to the diffraction limited PSF. *Right Panel:* The image created by averaging about 200 frames of short timescale images. The average profile of the image is approximated by a Gaussian and the full-width at half maximum (FWHM) is stated as the 'seeing' during the observation.

objects is blended together and the objects may not be recognizable as separate; this is known is 'confusion'. 2) light from a single object is spread over a larger angular area making it harder to detect against the noisy background.

Adaptive optics (AO) systems attempt to mitigate both these issues by nearly completely nulling the effects of turbulent blurring. Briefly, an AO system operates by observing the deformation caused by the atmosphere for a bright reference source at a very high rate (≈1 kHz) and corrects for it using actuated mirrors. The reference source is chosen to be near the science target, such that the correction calculated for the reference is also valid for the science target. The bright reference source is either a nearby star for a Natural Guide Star AO (NGS-AO) system or, more often, an artificial star created with a laser beacon for a Laser Guide Star AO (LGS-AO) system. The efficacy of the corrections depends on the the brightness of the reference star, the frequency of the correction and many other parameters. We shall discuss the mathematics and the engineering of AO systems in Section 1.4 after we discuss the scientific impacts of AO systems.

1.2 Science with Adaptive Optics

As much as I would like to describe the rich history of AO and trace its developments from the initial suggestions by Babcock (1953) and others and the development of early systems (declassified at a later date) by the US Department of Defense, the lack of space and time force me to merely point the interested reader to the well written AO textbook by Hardy (1998). As a technology, AO matured to regular astronomical use in the 1990's

but has shown no signs of having reached a saturation in its capability. New electronics, new opto-mechanical technologies and faster computers have made it possible to achieve far better AO performances than once thought possible (see Hart, 2010, for a review of AO advances). An excellent recent review by Davies & Kasper (2012) describes the modern improvements in AO and the progress they have generated in astrophysics, from the Sun and the solar system to high-redshift galaxies. We shall discuss a few science cases below.

1.2.1 Solar System Science

AO imaging of the solar surface has revealed much detail about the role of magnetic fields in the mechanics of the photosphere and understanding the applicability of Kolmogorov turbulence from the size scales of tiny jet-like features to ubiquitous granules (Goode et al., 2010). Moving outward, AO surveys of binary asteroids have revealed extremely low internal densities (0.8–3.6 $\mathrm{g\,cm^{-3}}$; see Marchis et al., 2006; Descamps et al., 2011, etc.). Planetary observations have helped us understand the formation of storm systems on Jupiter (de Pater et al., 2010) and haze clouds in Titan's atmosphere.

1.2.2 Galactic Science

The fields of star formation and evolution have seen major breakthroughs through the AO surveys of stellar multiplicity (Close et al., 2003), imaging and study of disks around young stars (starting from Golimowski et al., 1993; Roddier et al., 1996; Duchêne et al., 2004, etc.) and even detections of holes in disks possibly carved by orbiting planets (Kraus & Ireland, 2012). The contrast provided by AO systems and AO supported coronographs is critical for direct detection, imaging and spectroscopy of exoplanets and low mass companions around stars. Although very few planets have been found by this method till date, its promise makes it one of the leading science goals for the future ELTs (reviewed by Oppenheimer & Hinkley, 2009). The high resolution afforded by AO systems is also important for stellar work in globular clusters and galactic bulges: resolved spectra for measuring metallicity gradients, probing the star formation rates and ages and the initial mass function. The ability to measure proper motions with precisions competing with radio VLBI (Tendulkar et al., 2012, 2013) has allowed us to infer the origins of magnetars and measure the first kinematics ages for these enigmatic objects. In crowded fields with hundreds of reference stars, such as the Galactic center, the proper motion precision has enabled extremely precise measurements of the mass of the Milky Way central black hole and the distributions of stars around it with great precision.

1.2.3 Extra-galactic Science

High redshift galaxies tend to present extremely small angular sizes on the sky. With the Keck AO system and the OSIRIS integral field spectrograph, Jones et al. (2010) were able to create velocity maps of lensed galaxies at $z \approx 2$–3 with resolutions of upto 100 pc and show that the velocity fields of these galaxies were coherent and consistent with a strong spinning component without much pressure support. AO spectroscopy has also led to the

measurement of resolved kinematics in galaxy bulges and the corresponding measurement of the mass of the central blackholes (Davies et al., 2006).

1.3 Adaptive Optics on Small Telescopes

The signal to noise ratio (SNR) achieved by a seeing-limited telescope of aperture D in a given observing time Δt, background B (in units of, say, photons $\mathrm{cm}^{-2}\,\mathrm{arcsec}^{-2}$) for a source with a flux of H photons cm^{-2} is given by $\mathrm{SNR}_{\mathrm{Seeing}} = HDr_0/(2\lambda)(\Delta t\eta/B)^{1/2}$ where $r_0 = \lambda/\mathrm{seeing}$ is the Fried parameter (see Section 1.4) and η is the efficiency of the system. The same expression for an AO-equipped telescope is $\mathrm{SNR}_{\mathrm{AO}} = H\mathcal{S}D^2/(2\lambda)(\Delta t\eta/B)^{1/2}$ where $\mathcal{S}$ is the Strehl ratio[1] achieved. The 'AO Gain', i.e. the ratio of the SNRs achieved is then $\mathcal{S}\mathcal{D}/r_0$. Given this scaling and the complexity and cost of AO systems, all AO efforts remained clustered around large (diameter $\gtrsim 5\,\mathrm{m}$) telescopes. The size of AO systems and the corresponding preference for stable Nasmyth platforms[2] were two technical reasons for reducing interest in AO systems for small telescopes.

The limited time allocated to users of large telescopes made AO observations a scarce resource, observing at best few tens of targets in a single observing program[3]. With the 'classical' scheduling of observations, the number of personnel involved in LGS-AO operation and the sensitivity of AO to seeing conditions, astronomers typically observed ten to twenty targets per night. The ubiquitous smaller (diameter $\lesssim 3\,\mathrm{m}$) telescopes (which were being sidelined and underutilized in favor of their larger cousins) offer far more observing resources opening up a new phase space in observational astronomy: very large AO surveys and high-resolution monitoring.

The capability of performing large AO surveys enables a variety of science projects such as exploration of stellar multiplicity, discovery of lensed quasars, multiplicity of asteroids and (the latest) high-resolution followup of exoplanet transit surveys. In a white paper for the Astro2010 decadal survey, Baranec et al. (2010) detail the following scientific goals for automated AO on small telescopes:

Large Population Studies: Examples include stellar binarity surveys covering different mass ranges to produce a complete picture of binary formation physics across a wide range of stellar parameters, searches for lensed quasars from ∼25,000 Sloan Digital Sky Survey candidate targets, and validation of planetary transit candidates (<1% false positive probability).

[1] Strehl ratio is a metric of AO performance. It is defined as the ratio of the peak intensity achieved by the optical system to the peak intensity from a diffraction limited image. We shall discuss this further in Chapter 3.

[2] Larger instruments are correspondingly more sensitive to flexure due to varying gravity vectors. Hence it is preferred to install them on Nasmyth (or Coudé) foci of telescopes to maintain stability.

[3] The fraction of time allocated to AO users has improved since mid-2000's. For example, the Keck Observatory now routinely offers 16% of its observing time for LGS-AO observing. However, the efficiency of observing remains low (5–35 minutes between targets; Liu, 2006)

Rapid Target Characterization: Automated AO will provide high-angular-resolution images of optical transient events (e.g. supernovae) within a few minutes of their detection when triggered by existing and future survey projects such as the Catalina Sky Survey, Palomar Transient Factory, Pan-STARRS, or the LSST. Robo-AO will enable the separation of transient events from their host galaxy or other nearby sources, as well as rapid visible and near-infrared characterization. Transients in the nuclei of host galaxies may indicate AGN activity or tidal disruption flares and it is important to distinguish them from supernovae occurring close to the nuclei.

Target Monitoring: Robotic queued operation supports recurrent, regularly spaced observations of specific targets. This will enable monitoring programs that are difficult to pursue on existing AO systems such as long-term, high-precision astrometric orbit characterization, monitoring gravitational lenses and measuring the dynamic tropospheric cloud activity on Titan.

1.3.1 Getting AO to Small Telescopes

In order to make AO systems on small telescopes worthwhile, one needs to consider the following points:

- **Resolution:** Almost all the current AO systems in the world operate in the IR bands. Between J and K band, the diffraction limited resolution of a 10-meter class telescope is 26 mas and 45 mas which is well-matched with the *Hubble Space Telescope* (HST) resolution of 34 mas to 60 mas from 400 nm to 700 nm. Compare this, to the diffraction limited image for a 1.5-meter telescope in IR: 170 mas to 300 mas (From J to K band). Thus, for a small telescope to be provide well-matched resolution, it must provide useful AO performance in the visible.

- **Laser Guide Star:** The spatial scale of wavefront errors, the Fried parameter ($r_0 \propto \lambda^{6/5}$), is smaller at visible wavelengths requiring a finer sampling of the incoming wavefront than AO systems operating at IR wavelengths. The corresponding increase in the required brightness of the reference star impels the use of a laser guide star to prevent the sky coverage from shrinking to unserviceable limits. Hence the AO system must operate its own laser beacon.

- **Automation and Efficiency:** Given the science case of conducting large scale AO surveys and high-resolution transient monitoring, the need for automation is inevitable. Current AO systems require coordination between five to seven spatially distributed personnel. The setup time for such telescopes is between five to thirty minutes.

- **Cost and Reliability:** Even without the current dire funding situation, it is difficult for observatories with small telescopes to fund an expensive instrument or to maintain dedicated staff for operating a LGS-AO system. An instrument builder is compelled to reduce the construction and operating cost by using off-the-shelf components whenever possible and creating an easy-to-maintain, reliable system.

With this motivation in mind, we constructed the Robo-AO instrument as a demonstration that new technology and dedicated software enable the miniaturization of AO and allow the construction of a low-cost, fully-automated AO system. Chapter 2 is dedicated to the design, construction and operation of Robo-AO and Chapter 4 describes the study of pre main-sequence (PMS) multiples using Robo-AO.

Before we move on the Chapter 2, it is appropriate to introduce the theory of adaptive optics: how images are formed, how turbulence affects images and how adaptive optics corrects images. A small description of a general AO system then sets the stage for describing Robo-AO.

1.4 Theory Interlude

AO theory begins with an understanding of turbulence and its structure. The theory of velocity fields of turbulence was first developed by Kolmogorov (1941) who proposed a simple scaling relation in which turbulent energy was added to the fluid at a large spatial scale (denoted as $\mathcal{L}_0$, the 'outer scale') and the energy was passed down to eddies at smaller and smaller spatial scales till it dissipated when the spatial scale was small enough for viscosity to become significant[4]. This smaller scale is known as the 'inner scale', denoted by l_0 For the energy passage through spatial scales to be stable, the velocity fluctuations V must depend only on the spatial scale l and the rate of energy input or dissipation (ϵ per unit mass) at that scale. Dimensional analysis shows that for scales between l_0 and $\mathcal{L}_0$ the following should be valid:

$$V \propto \epsilon^{1/3} l^{1/3}. \tag{1.1}$$

This equation defines the one-dimensional Kolmogorov turbulence power spectrum $\Phi(\kappa)$, where $\kappa = 2\pi/l$ is the spatial wavenumber of the turbulence. Since the energy in the increment $d\kappa$ is proportional to V^2,

$$\Phi(\kappa)d\kappa \propto V^2 \propto \kappa^{-2/3}, \Phi(\kappa) \propto \kappa^{-5/3}. \tag{1.2}$$

The three-dimensional power spectrum, required for calculating the propagation of electromagnetic radiation through the atmosphere was calculated by Tatarskii (1961) as,

$$\Phi(\kappa) \propto \kappa^{-11/3}. \tag{1.3}$$

The proportionality factor is determined by the strength of the turbulence. For measuring wavefront distortions, we measure the structure parameter of refractive index changes, denoted as C_n. The final Kolmogorov three-dimensional power spectrum of refractive index variations is given by,

$$\Phi(\kappa) = 0.033 C_n^2 \kappa^{-11/3}. \tag{1.4}$$

This equation does not account for the behavior of the power spectrum towards the end

[4]Flows are characterized by their Reynolds number, $\mathcal{R}e = Vl/\nu$ where V, l and ν are the characteristic velocity, spatial scale and kinematic viscosity respectively. Flows become non-turbulent when $\mathcal{R}e$ is less than a geometry-dependent critical value.

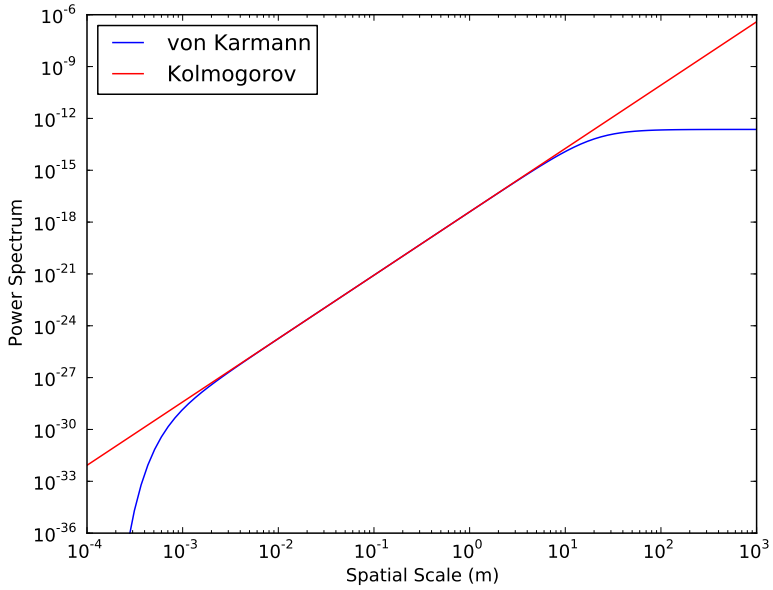

Figure 1.2. The spatial power spectra for isotropic turbulence is shown for the Kolmogorov model (red line) an the von Karmann turbulence (blue curve). The von Karmann spectrum is plotted for $\mathcal{L}_0 = 20\,\mathrm{m}$ and with an exponential drop-off at $l_0 = 1\,\mathrm{mm}$.

of its valid range, i.e. from l_0 to $\mathcal{L}_0$. The outer scale is of tremendous importance to large telescopes (diameter $\gtrsim 8\,\mathrm{m}$) where the aperture may be comparable in size to the outer scale. The von Karmann spectrum (Ishimaru, 1978) accounts for this roll off as,

$$\Phi(\kappa) = \frac{0.033 C_n^2}{(\kappa^2 + \kappa_0^2)^{-11/6}}, \tag{1.5}$$

κ_0 is the wavenumber corresponding to the outer scale $\mathcal{L}_0$.

At the lower spatial scales, the viscosity dissipates the turbulent eddies and the turbulent power drops. Tatarskii suggested an ad-hoc exponential term to account for the lowest spatial scales as,

$$\Phi(\kappa) = \frac{0.033 C_n^2}{(\kappa^2 + \kappa_0^2)^{(11/6)}} \exp(\frac{-\kappa^2}{\kappa_m^2}), \tag{1.6}$$

where κ_m is the wavenumber corresponding to the smallest scale ($\lesssim 10^{-3}\,\mathrm{m}$). The highest wavenumber of interest in AO systems is that corresponding to the WFS subaperture size ($\sim$10 cm) and $\kappa_m \gg \kappa$, hence the exponential term evaluates to unity. Figure 1.2 shows the typical roll-off of the von Karmann model.

The strength of turbulence changes as a function of height (h) in the atmosphere. This distribution profile ($C_n^2(h)$) significantly affects the correction method and the optimum AO performance that can be achieved. Usually, the two most significant layers of turbulent air

are the turbulent boundary between low altitude wind and the stationary ground, i.e. the ground layer and the boundary layer between the jet streams flowing in different directions at the top of the troposphere.

The important effects of the turbulence are usually summarized by three parameters for the purposes of AO instrumentation. Other details, such as the turbulence profiles, wind speed profiles and annual variations are useful for detailed planning before construction, but are not required for most estimates.

- **Fried Parameter r_0:**. The Fried parameter describes the spatial scale over which the RMS error in wavefront phase is one square radian. It is related to the $C_n^2(h)$ profile and zenith angle ζ as,

$$r_0 = \left[16.699\lambda^{-2}\sec(\zeta)\int_0^\infty C_n^2(h)\mathrm{d}h\right]^{-3/5}. \tag{1.7}$$

  Physically, r_0 is the aperture size that will give a diffraction limited with the same FWHM as the seeing FWHM. A seeing of $1''$ at 500 nm corresponds to an r_0 of 10 cm. r_0 is considered as the fiducial size of wavefront sensing for an AO system. If one can exactly measure and correct the wavefront for all scales equal to or larger than r_0, then we can achieve a moderate correction (Strehl ratio = 37%). As $r_0 \propto \lambda^{6/5}$, correcting at visible wavelengths requires the sampling of the wavefront to be performed at correspondingly smaller spatial scales.

- **Isoplanatic Patch θ_0:** The wavefront aberrations between two directions on the sky rapidly decorrelates as the the directions are separated. The angular scale of decorrelation (θ_0) is where the RMS error in wavefront phase is one radian and is given by,

$$\theta_0 = \left[115\lambda^{-2}(\sec\zeta)^{8/3}\int_0^\infty C_n^2(h)h^{5/3}\mathrm{d}h\right]^{-3/5} \tag{1.8}$$

  The isoplanatic patch is the radius at which the correction applied is still reasonably valid hence the wavefront measurement reference and the science target must be within this patch. It can be seen that the isoplanatic patch is significantly reduced by high altitude turbulence (due to the $h^{5/3}$ weighting). If all the turbulence is concentrated in the ground layer, a very large isoplanatic patch can be achieved, greatly enhancing the science capabilities of AO. Observing locations in Antarctica are of great interest for this reason (among a few others).

- **Coherence Time τ_0:** The timescale of wavefront changes is given approximately r_0/v where v is the averaged wind-speed. τ_0 is the timescale difference at which the RMS phase variations are one square radian. For useful AO performance, the correction bandwidth must be higher than the frequency $1/\tau_0$.

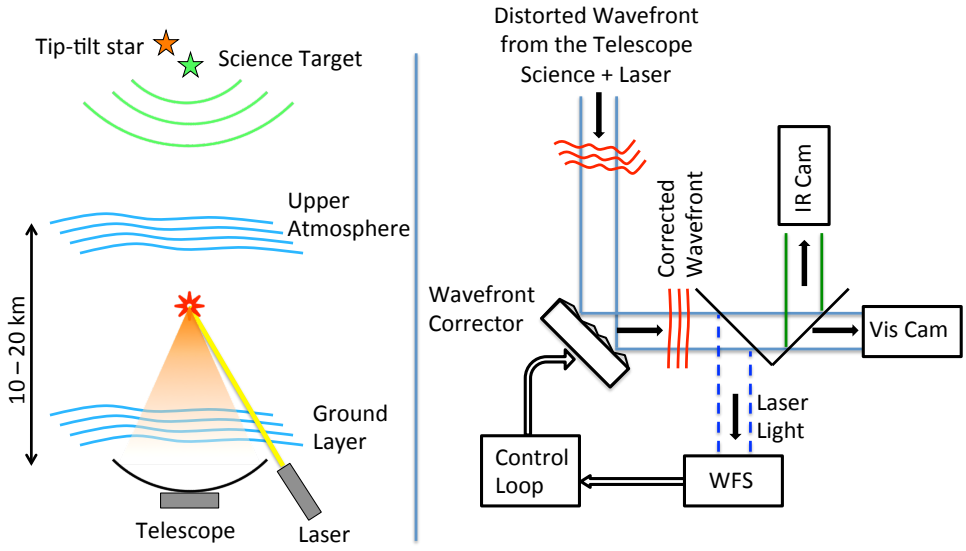

Figure 1.3. A schematic depiction of the working of an adaptive optics system. *Left Panel:* The laser light propagates through the turbulence and forms a laser 'beacon' or guide star at a certain altitude. The down scattered light from the beacon propagates through the atmosphere and measures most of the turbulence that the starlight also propagates through. *Right Panel:* Inside the instrument, a dichroic sends the laser light to the wavefront sensor (WFS) which sends appropriate commands to the deformable mirror (DM) that corrects the wavefront deformation and forms a diffraction limited image on the science camera.

1.5 Inner Workings of Adaptive Optics

In its most simplified form, an AO system performs just two major actions (at a very high rate): (A) wavefront sensing and (B) wavefront correction. Figure 1.3 is a sketch of the simplest LGS-AO system: a closed-loop, single laser, single conjugate (i.e. only one level of wavefront correction) AO system.

The left panel of the figure shows the AO system in the larger context. The telescope observes the science target through multiple layers of turbulence, summarized here as the ground layer and the jet stream turbulence. The laser projector propagates a laser beam to a certain altitude. The laser beam is scattered down to the telescope due to Rayleigh scattering (creating a Rayleigh beacon) or resonant scattering from the sodium layer at an altitude of 90 km (creating a sodium beacon). The wavefront from the beacon samples almost the same atmosphere as the wavefront arriving from the science target. An important distinction between the two wavefronts is that the laser wavefront is insensitive to the gross tip-tilt motion of the wavefront acquired by the science target. To measure the tip-tilt of the wavefront, one needs a moderately bright (15–18 magnitude depending on the telescope

aperture) within about $1'$ of the science target. This is known as the tip-tilt reference star and often may be the science target itself.

All the distorted wavefronts from the telescope (Right panel of Figure 1.3) are first incident on the wavefront corrector which corrects the estimated wavefront and of the corrected wavefronts, the laser light is directed towards the wavefront sensor and the visible and IR light is directed to the corresponding science cameras. The control loop measures the residual wavefront error after the previous wavefront estimate has been removed and calculates a new wavefront estimate for the next time step.

Wavefront Sensing: A variety of wavefront sensors (WFS) have been designed and implemented for AO systems. Robo-AO uses a Shack-Hartmann wavefront sensor which is the most commonly used design for astronomical AO. It consists of an array of lenslets placed across the telescope pupil with each lenslet size (known as the subaperture) corresponding to the spatial scale at which the wavefront is to be sampled. Each lenslet creates an image of the laser guide star using its local wavefront. The movement of the spot centroid is a measure of the local tip-tilt slope at the corresponding lenslet. The slopes measured at each lenslet can be numerically integrated to form an estimate of the wavefront.

Wavefront Correcting: Almost all astronomical AO applications use a combination of a deformable mirror (DM) and a separate tip-tilt mirror (TTM) to correct the measured wavefront[5]. A DM consists of a thin reflective surface with an array of actuators attached behind it such that the shape of the reflective surface can be changed at very short timescales. Different DM actuator technologies such a piezoelectric, magnetic voice coils, bimorph mirrors and micro-electromechanical systems (MEMS) have different advantages according to their total stroke length, actuator separation, applied force etc that make them suitable for various purposes. Till recently, the actuator spacing of DM was the driver for AO system sizes. With the advent of the MEMS technology DM (with an actuator spacing of 0.4 mm as compared to 5 mm for piezoelectric DMs) it is now possible to construct compact AO systems that can fit small telescopes. The tip-tilt of the wavefront is offloaded onto the TTM to reduce the stroke requirement on the DM. The TTM movement commands are calculated from the centroid of the tip-tilt star calculated on one of the science cameras (which is designated as the tip-tilt camera).

Having discussed the motivation of workings of a general AO system, we can now proceed to the design and construction of Robo-AO. We shall discuss the hardware components, software architecture, regular operation and the lessons learnt in the construction of the system.

[5] Although spatial light modulators (transmissive wavefront correcting optics) have been extensively used by the laser and optics communities, they are not commonplace in astronomy.

Chapter 2

Robo-AO: Design and Construction

Robo-AO is the first completely automated visible and IR adaptive optics imaging system (Baranec et al., 2013)[1]. It was built in collaboration with IUCAA (Pune, India) for demonstration on the Palomar 60-inch telescope (P-60). It operates a UV laser beacon to enable wavefront correction for faint stars. This chapter describes the hardware design, the software architecture, and the operation of Robo-AO. Below, I describe the construction of Robo-AO in general and have provided additional details in sections where I had primary contributions.

2.1 Hardware Design and Construction

Figure 2.1 shows all the components of Robo-AO setup on the P-60 telescope. It consists of the Robo-AO instrument box, which houses all the optics and electro-mechanical systems for operating the AO system, mounted at the Cassegrain focus of the telescope, a laser projector box mounted on the Southern side of the telescope, and an electronics rack mounted on the Northern side of the telescope, providing a partial counter-balance to the mass of the laser projector. The only connections coming out from the instrument are the ethernet and power cables and hoses for cooling water.

In this section, we shall discuss each hardware sub-system of Robo-AO and its relation to the other components.

2.1.1 Laser Projector

Robo-AO uses a JDSU Q-switched frequency-tripled Nd:YAG laser emitting 12 W beam at 355 nm, which emulates a star with a $\approx 10^3$ photons $\mathrm{cm}^{-2}\,\mathrm{s}^{-1}$ incident at the telescope (which if translated to V band would correspond to $\mathrm{m_v} \approx 9$) at an altitude of 10 km$\pm$250 m. The laser is operated with a Q-switching frequency of 10 kHz. Thus the instrument can receive scattered light from pulses propagating up to 15 km before a new pulse is emitted by the laser.

The laser was installed inside a projector box mounted on the side of the telescope as shown in Figure 2.2. An adapter bracket was designed to allow large-scale alignment of

[1] http://robo-ao.org

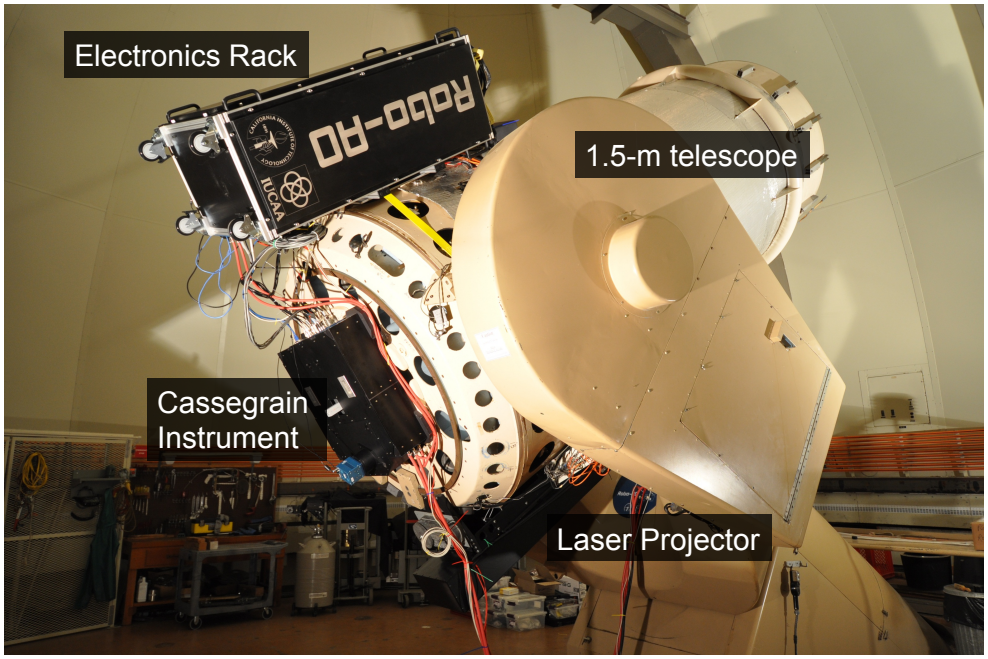

Figure 2.1. The Robo-AO components setup on the Palomar 60-inch telescope. It consists of the Robo-AO instrument box with all the optics and electro-mechanical systems for operating the AO system mounted at the Cassegrain focus of the telescope; a laser projector box mounted on the southern side of the telescope and an electronics rack mounted on the north side of the telescope, providing a partial counter-balance to the mass of the laser projector. The only connections coming out from the instrument are for ethernet, power and hoses for cooling water. Photograph by C. Baranec.

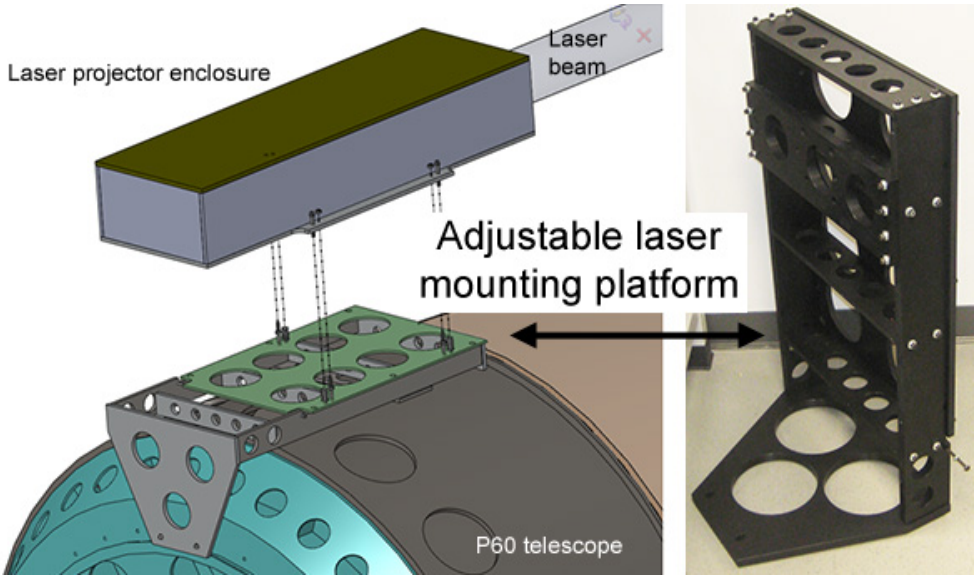

Figure 2.2. Mounting of the laser projector on the south side of the telescope using a mounting adapter. The mounting adapter is designed to allow a bi-directional adjustment in laser alignment and to minimize the redesign effort for adapting the Robo-AO design to a different telescope. Schematic by K. Bui and photograph by C. Baranec.

the laser projector with the telescope axis. The adapter also reduced the redesign effort required to adapt Robo-AO for use on another telescope.

Inside the projector, the 1 mm diameter beam from the laser is expanded using two lenses to a Gaussian beam with a width of 15 cm nominally focused at an altitude of 10 km. At the output the flux is about $19\,\mathrm{mW\,cm^{-2}}$ and it is classified as a Class I laser with respect to flying aircraft. Due to the Class I classification, the Federal Aviation Authority allows the laser beacon to be operated without requiring human spotters outside the dome at all times, thus facilitating the automated operation of Robo-AO.

The projector box also contains an external shutter (apart from the laser's internal shutter) as an independent control of laser propagation, a fast steering mirror for centering the laser beam and jitter control, and a half wave plate for rotating the linear polarization of the beam to the appropriate angle to maximize the throughput in the Pockels cell range gating system (described further in Section 2.1.2.1).

At the start of the project (September, 2010), a periscope assembly with two 10-inch diameter laser mirrors transported the beam from the side of the telescope to a location behind the secondary mirror of the telescope, and launched it into the sky. Figure 2.3 shows the laser beam propagating through the periscope and the spot formed in the sky.

It was observed that the flexure in the periscope assembly caused the laser spot to move by as much as 100″, with respect to the telescope axis, when the telescope was pointed to elevations of 45°. Figure 2.4 shows the tests of spot positions with and without the periscope assembly. The periscope flexure was significantly larger than the design goal and

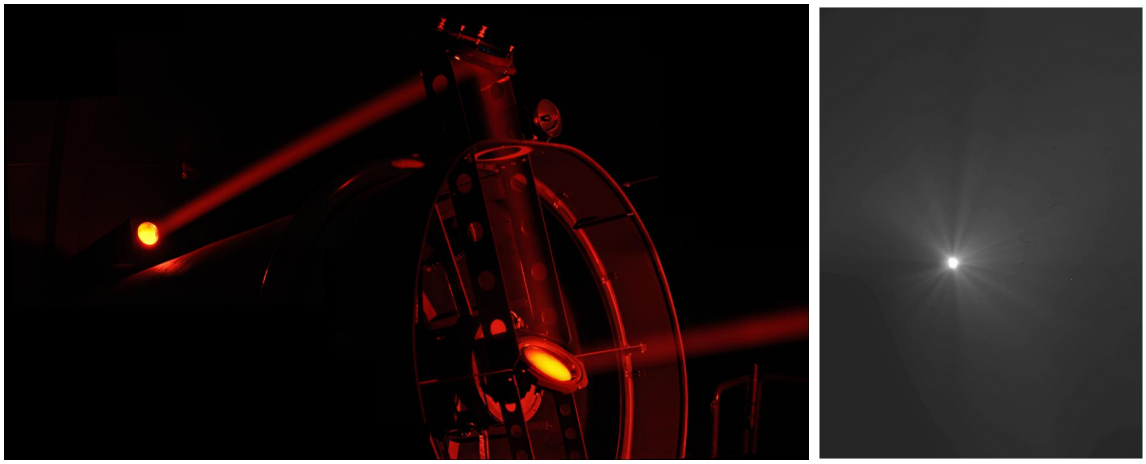

Figure 2.3. *Left Panel:* The laser periscope assembly with two 10-inch flat mirrors mounted on the top of the telescope tube. This image, taken with a UV sensitive camera shows the beam emanating from the laser projector on the left, reflecting off both the periscope mirrors and propagating into the sky. Photograph by C. Baranec. *Right Panel:* The beam launched through the periscope along the telescope axis forms a bright star of scattered light in the sky imaged by the existing GRB camera (Cenko et al., 2006) in the U filter.

was deemed unusable.

In January 2011, we attempted to reduce the laser periscope flexure by replacing the springs in the mirror mounts with significantly stiffer spring and clamping the adjustable mount points. However, the improvement in flexure was not significant, suggesting that the flexure was not dominated by the mirror mounts but the rest of the periscope structure. We decided to forego the use of the laser periscope and launch the laser from the side of the telescope.

The laser projector was assembled and commissioned during the September 2010 runs, using the existing GRB camera to take images. In order to focus the laser projector in the final side launching setup, we setup the telescope to focus the GRB camera (Cenko et al., 2006) at an altitude of 10 km. On propagating the laser, we observed the distinctive bow-tie image (Figure 2.5) of the laser beam as it passed in and out off the focal point of the telescope. The focus of the laser projector was then adjusted till the sharpest bow-tie image was achieved. With a seeing of $1.5''$ we were able to achieve a beam waist (FWHM) of $2''.2$[2]. During this commissioning run, we also tested the control of the beam position using the uplink steering mirror. The uplink mirror is used to accommodate the flexure between the laser and the telescope when the telescope is pointed to various parts of the sky. This allows the laser to be recentered in the wavefront sensor's $4.5''$field of view. We were able to achieve the desired movement range of $80''\times110''$. This was sufficient to recenter the laser to the wavefront sensor axis for all zenith angles less than $\approx50^\circ$. In January 2013, the movement range was doubled by replacing an amplifier to allow the Robo-AO laser to be

[2]The focus of the laser projector is temperature dependent and is adjusted before observing runs. This is described further in Section 2.4

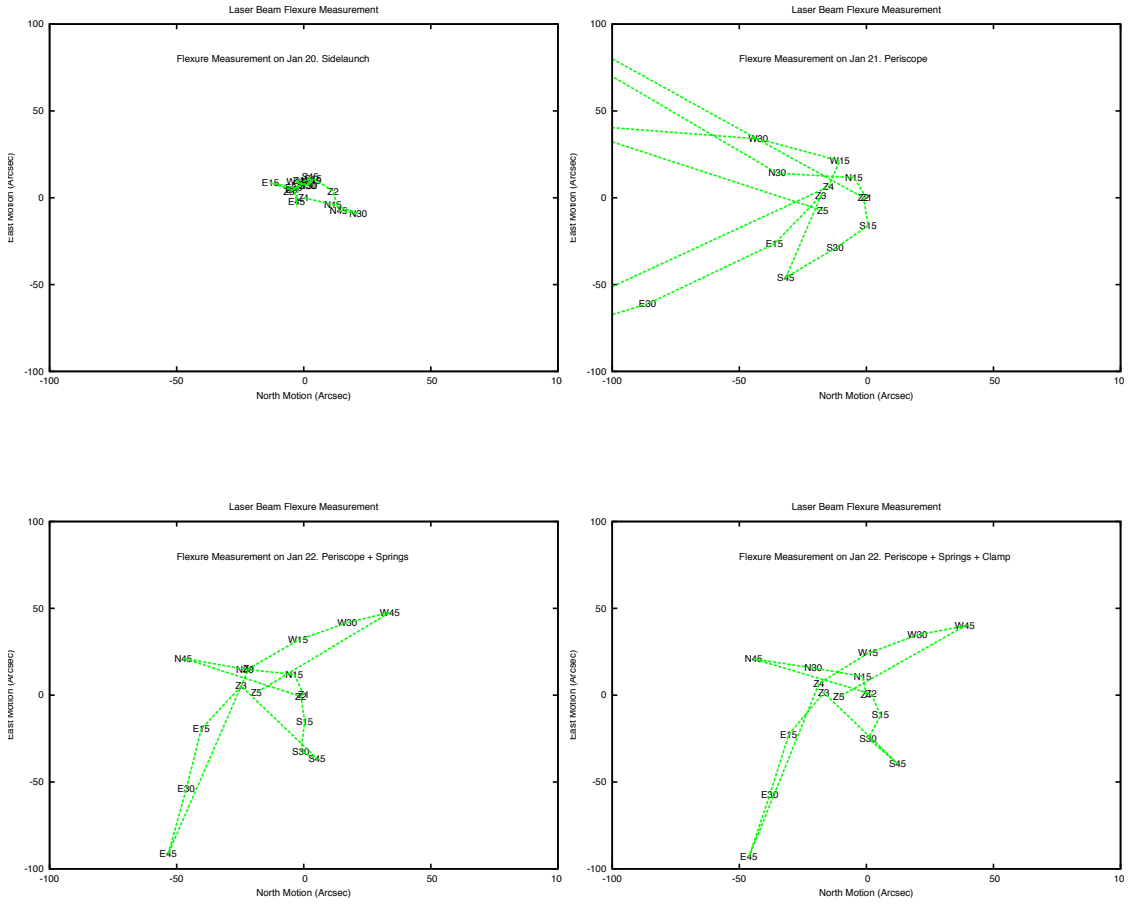

Figure 2.4. Flexure measurements of the laser spot moving with respect to the optical axis of the telescope as the telescope was pointed in different locations in the sky. With a putative zero at the zenith location (Z), we moved to three locations (zenith angles = 15°, 30° and 45°) in each of the cardinal directions (N, E, W and S). The x and the y axes are the movement of the spot towards north and east with respect to the spot location at zenith.

Figure 2.5. The Robo-AO laser launched from the side of the telescope during commissioning. The telescope was focused to an altitude of 10 km. The beam waist was measured to be 2.1″ in 1.5″ seeing conditions.

used over zenith angles of 65°to allow imaging targets in with declinations below −17°.

2.1.1.1 Laser Clearance

The Robo-AO laser operation is coordinated with the Laser Clearing House (LCH) operated by JSpOC of the US Air Force to ensure that the laser does not accidentally illuminate any space asset. All US-operated LGS-AO systems are required to provide lists of targets three days in advance for the LCH to provide lists of open and close windows for the laser shutter on each target. The presence of a few thousand targets in the Robo-AO queue prompted the handling of the laser clearances in a unique way. Instead of requesting windows on a per target basis as all other observatories do, we divided the entire sky above an elevation of 40° into fixed altitude-azimuth windows, each about 12.4 sq. deg in size supplemented by similar windows reaching an elevation of 33° toward the northern and southern directions. These fixed lists are sent to the LCH 48–72 hours in advance for clearance. During the night of operation, the queue scheduler simply chooses targets that are in an open window for the entire duration of their required observation. Due to this procedure, Robo-AO is able to obtain LGS-AO imaging for Target of Opportunity (ToO) programs almost immediately as compared to a few day wait time for other US-based LGS-AO systems.

2.1.2 Cassegrain Instrument

All the optics of Robo-AO and the electro-mechanical systems required for AO correction are assembled inside the Cassegrain instrument box. This is a 1 m×1 m×20 cm box with a 1-inch thick aluminum base-plate. The base-plate is drilled and tapped for standard 1/4-20 bolts in a 1-inch grid for anchoring optics mounts.

Figure 2.6 shows the annotated design and optical path of the Cassegrain instrument. The base-plate is mounted at the Cassegrain port of the telescope. The incoming beam from the telescope is folded perpendicular to the optical axis of the telescope by a movable fold mirror (FM1). A pupil image is formed on the deformable mirror using an off-axis paraboloid mirror (OAP; in this case OAP1). The reflected light is then split by a dichroic (cutoff $\lambda = 400\,\mathrm{nm}$). The laser light is sent through a field stop, a Pockels cell based range gating system, and a lenslet array to the CCD39 wavefront sensor camera. The visible and IR beams are reflected off an OAP relay (OAP2 and OAP3), passed through the atmospheric dispersion corrector (ADC), steered by the tip-tilt mirror (TTM) to the OAP4. The final beam is split by the visible-IR dichroic that sends visible light to the Andor EM CCD visible camera and the IR beam to the IR camera port (currently equipped with a Xenics 320×256 InGaAs array). An internal calibration source simulates a natural star (visible and IR light) at the infinity focus of the telescope and a UV laser guide star at the focus position corresponding to an altitude of 10 km. The major optical components and subsystems are described in further detail in the following sections.

2.1.2.1 AO System

The adaptive optics system consists of the deformable mirror, wavefront sensor, and the range-gating system. For Robo-AO, the AO system components were chosen for reliability and compactness.

Deformable Mirror Robo-AO uses a 12×12 actuator microelectro-mechanical system (MEMS) deformable mirror (DM) designed and fabricated by Boston Micromachines. The active area of the DM is 4.4 mm×4.4 mm with an inter-actuator spacing ('pitch') of 400 μm. The full stroke of the DM is 3.5 μm. This allows us to correct ≈80 rad of wavefront error at 500 nm. The actuator pitch of these DMs is significantly smaller than the five to seven millimeter actuator pitch of the traditional piezo-electric DMs. The reduced size of our DM allows the miniaturization of other optical components of Robo-AO and thus achieve a compact AO system.

Range Gating System Since the beam from the laser projector is continuously Rayleigh scattered from ground level to the top of the atmosphere, a range gating system is installed to isolate the light returning from the target altitude of the beacon, and also prevent unfocused stray light from contaminating the wavefront measurements. The range gating system works by opening a high-speed shutter for a specific time window such that only light returning from the desired distance is permitted to reach the detector.

The range-gating system uses a Pockels cell as an electro-optic shutter. The Pockels cell rotates the plane of linearly polarized light to an angle proportional to the voltage applied across the optical crystal. A polarizing beam splitter is used at the input to isolate the light polarized along the fast axis of the optical crystal and another polarizer (set at right angles to the input polarizer) at the output allows light to pass through only when the polarization plane has been rotated through 90° by the optical crystal. Many crystals that lack inversion symmetry, such as β barium borate, lithium niobate and potassium dihydrogen phosphate

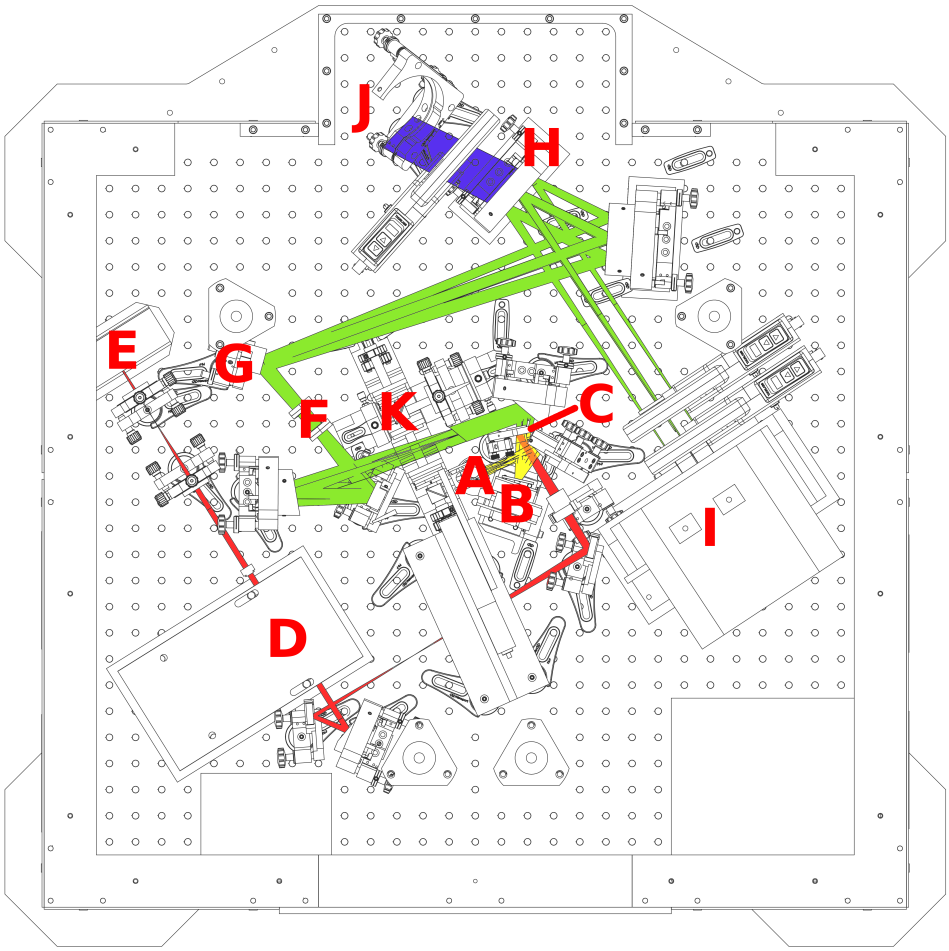

Figure 2.6. The optical paths through the Cassegrain instrument box of Robo-AO. This is the top view of the instrument (i.e. as seen on an optical bench). When mounted on the telescope, the optical axis of the telescope is perpendicular to the plane of the image. Light (UV+Vis+IR, shown as yellow) from the telescope enters through an entrance hole in the base-plate traveling outward through the plane of the image. It is reflected by a flat mirror (FM1) at A which illuminates the first off-axis parabolic mirror (OAP1, not labeled to prevent crowding) and creates an image of the telescope pupil on the deformable mirror (B). The beam reflected from B is split by the dichroic (C). The reflected UV laser light (shown as red) travels through a set of lenses, the field stop, OAP5 to the Pockels cell and range gate system (D), through the lenslet arrays to the wavefront sensor (E). The dichroic at (C) transmits the visible and IR beams (shown as green) that are reflected off an OAP relay, passed through the atmospheric dispersion corrector (F), steered by the tip-tilt mirror (G) to the OAP4. The final beam is split by the visible-IR dichroic (H) and sends visible light to the visible camera and filter wheels (I) and the IR light (shown as purple) to the IR camera (J; not shown). The fold mirror (at A) can be moved out of the way to reveal the internal calibration source (K) to the instrument.

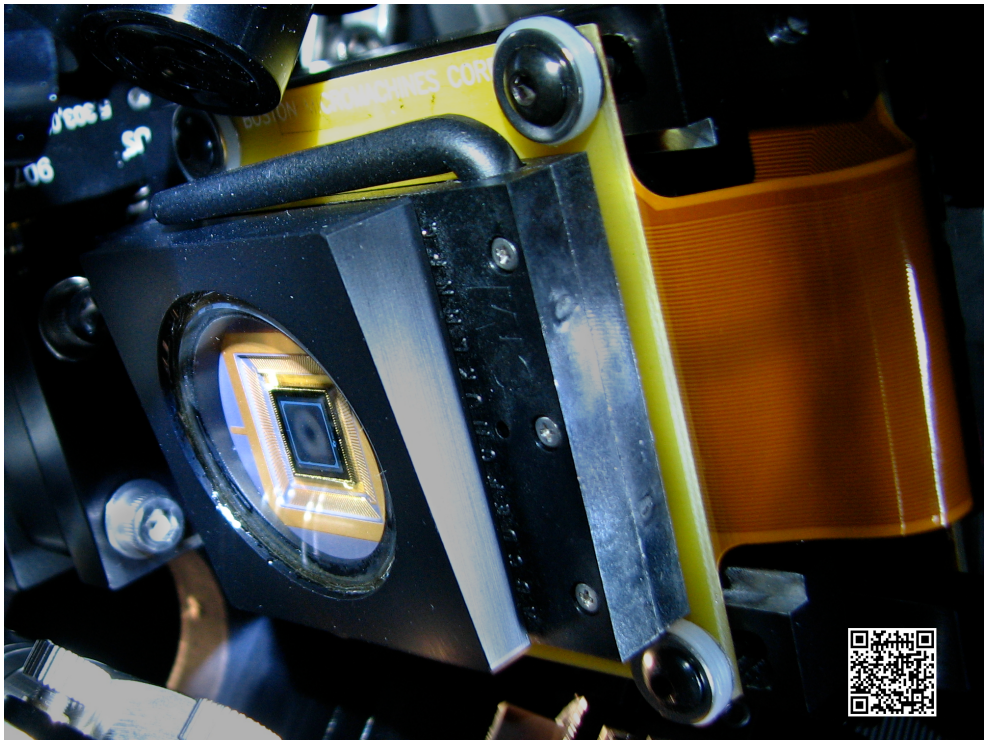

Figure 2.7. The deformable mirror mounted inside the Cassegrain box. The active area of the deformable mirror (central silver square) is 4.4 mm×4.4 mm. This MEMS based deformable mirror is significantly smaller than other wavefront correction technologies, allowing Robo-AO optics to be compact. The faint annular illumination on the active surface is an image of the telescope pupil illuminated by the light of a full moon. The central obscuration is the shadow of the secondary mirror.

(KDP), exhibit the Pockels effect. A β barium borate crystal was chosen to achieve the required extinction of stray light by a factor of 1500. One of the drawbacks encountered is that the BBO crystal is sensitive to thermal variations. The crystal needs to be prepared with beveled edges with a size as small as feasible. The holding cell is designed to hold the crystal with a spring loaded clip instead of epoxy to allow for thermal expansion.

A configurable delay generator marks the phase of the laser pulse generation from the Q-switching clock signal that is output by the laser controller. It sends to the Pockels cell a start pulse with a delay of 64.617 μs and a stop pulse with a delay of 67.617 μs with respect to the input pulse. This selects the laser light scattered between distances of 9.7 km and 10.2 km from the telescope.

Wavefront Sensor Robo-AO uses an 11×11 lenslet Shack-Hartmann wavefront sensor built around a Scimeasure low-noise camera with an E2V CCD39 detector chip. The subapertures are registered to the deformable mirror such that each actuator is located at the corner of the subaperture (Figure 2.8). The 80×80 pixel chip is binned in a 3×3 pattern to minimize the readout time and readout noise (per subaperture). A 2×2 'quad-cell' of these binned pixels is used to centroid the spots created by the lenslet array. The resulting 26×26 pixels are readout from the four corners of the detector by four independent amplifiers. To prevent drifts in the readout electronics from affecting the measured centroid positions, the spot pattern was offset from the center such that the amplifier boundaries coincided with the subaperture boundaries. The four pixels at the corners are replaced by a frame index in the CCD controller. This encoded index facilitates frame counting and checking for dropped frames.

In June 2011, Scimeasure replaced the CCD39 detector with a higher quantum efficiency detector (72% at 350 nm) that boosted the sensitivity of the wavefront sensor by a factor of almost three.

Tip-Tilt Mirror Robo-AO uses a Physik Instrumente S-330.20L piezo-electric tip-tilt actuator to correct the tip-tilt motion introduced by the atmosphere. The optical range of the actuator is 7 mrad ($\pm 12'$) in the reduced beam. This corresponds to about $\pm 4.5''$ of tip-tilt correction, which is more than sufficient to correct for the atmospheric tip-tilt error at Palomar (3-σ error = $1.3''$ in median seeing).

Because of the reversibility of light propagation, the laser beam propagates upward and downward through the same path. This renders the laser beacon insensitive to gross tip-tilt motion acquired by the science target. As discussed in Chapter 1, the tip-tilt motion is measured using a nearby tip-tilt reference star. The design ideology of Robo-AO is to have separate visible and IR beams feeding two tip-tilt capable cameras. To acquire science data in the visible bands, the IR camera would be used as a tip-tilt measurement device while the visible camera acquired a long exposure of the stabilized image. To acquire science data in the IR, the source of the tip-tilt measurement would be switched (in software) to the visible camera and the situation is reversed. The procurement of a science grade IR camera is in progress. Currently, the tip-tilt mirror is not used for correction. The tip-tilt correction is performed in software through high frame rate image acquisition by the visible camera, as explained in the next section.

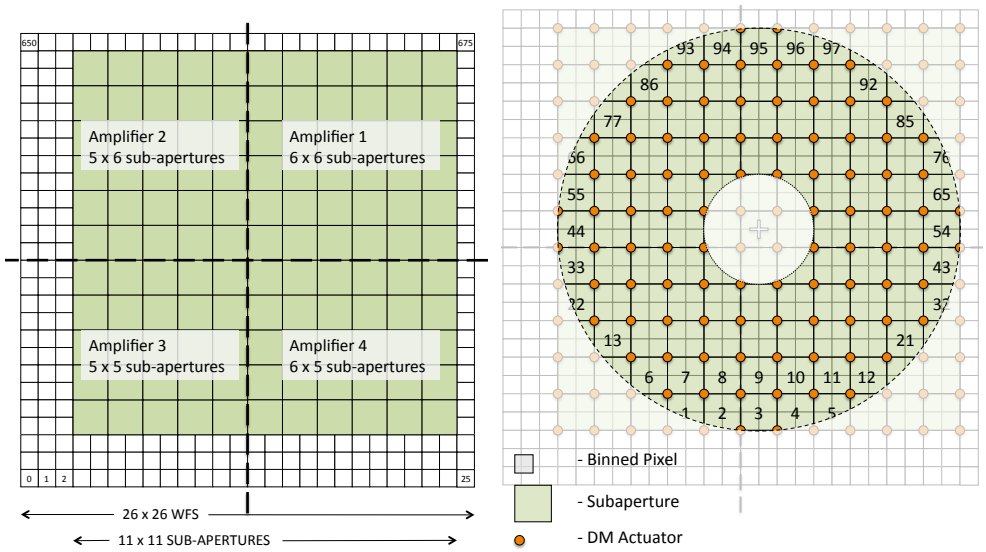

Figure 2.8. *Left Panel:* The 26×26 array of binned pixels on the CCD39 detector. Each gray box corresponds to a 3×3 binned pixels. Each quadrant of the detector is read out by an independent amplifier and electronics. The green area are the quad-cells used for measuring the positions of the Shack-Hartmann spots. The spot pattern is offset such that the boundary of the amplifiers coincides with the boundary of the quad-cells to prevent the amplifier drifts from affecting measurements. *Right Panel:* The telescope pupil pattern superimposed onto the CCD39 array. The numbering corresponds to the subapertures utilized by Robo-AO for wavefront calculations. The central 3×3 subapertures are obscured by the shadow of the secondary mirror and are not utilized for calculations. Each orange circle corresponds to a DM actuator which is registered to the corner of each subaperture.

2.1.2.2 Visible Camera and Filters

Robo-AO uses an Andor DU-888 camera for imaging in the wavelength range 0.4–0.9 μm. At the heart of this unit is a 1024×1024 pixel frame-transfer Electron Multiplying CCD (EMCCD) detector (see Mackay et al., 2004). The electron multiplication is implemented through an extra row of pixels across which the electrons are accelerated and multiplied by an avalanche process. The average multiplication factor, which can be as high as 1000, is known as the electron-multiplying gain (EM_GAIN). The voltage to be applied across the electron multiplying register (i.e. row of pixels) to achieve a specific gain is calibrated in the camera. As the chip ages, the voltages need to be recalibrated to achieve the correct gain.

Observing Modes In order to facilitate observations and calibrations, the visible camera operation is restricted to 16 preset modes that define each camera parameter. The modes and their parameter values are summarized in Table 2.1 Some variables such as the total exposure time and the region of interest are chosen by the user for each target and are defined in the target queue. Of the 16 modes, five modes from 6–10 are currently used for science data acquisition. The rest are defined for future use in the tip-tilt mode.

Data Acquisition The high-speed readout capabilities of the EMCCD enable the operation of Robo-AO even in the absence of an IR camera. We collect high frame rate images and shift and add the frames in software to correct for the tip-tilt motion. Because of the electron-multiplying capability, which can create upto a 1000 e^- for each photon on the CCD, the visible camera can be read out rapidly (10^6 pixels s^{-1}; 8.9 full frames s^{-1}) without the output being dominated by the read noise (≈47 e^- pix^{-1}).

This observing strategy is similar to LUCKY imaging (Law et al., 2006) with the exception that since the camera operates behind an AO system, the higher order wavefront errors are always corrected[3] and frame selection is unnecessary in most observations. In Chapter 3, we shall discuss how the performance changes with differing frame rates and how frame selection can be used to improve the performance at the cost of efficiency.

The data is stored in the form of FITS cubes and is processed with a shift-and-add pipeline adapted from the LUCKY Imaging pipeline (Law et al., 2009). The pipeline uses the brightest star in the frame to perform the tip-tilt correction. At the photon-noise limit of the system, we can use stars as faint as $m_{i'} = 16$ to guide the tip-tilt correction. If a broader filter (such as the 600 nm long pass filter described below) is used, the magnitude limit may be pushed to $m_{i'} = 17$ for red stars. The performance of the AO system as a function of stellar brightness is discussed further in Chapter 3.

Filters The visible arm of Robo-AO is equipped with two 6-slot filter wheels placed in series. The currently installed filters are shown in Table 2.2. The filters are placed in a slowly converging beam (≈ f/40) emerging from the final optical relay. All filters are of equal optical thickness such that the change in focal distance is same. This allows Robo-AO filters to be changed without refocusing the telescope.

[3] In short, we're always lucky!

Table 2.1. Visible Camera Observing Modes.

Mode	Name	Type[a]	Binning	Pre-amp	VSS	FT[b]	EM Gain
0	Staring_standard_min	Single	1	2	4	1	0
1	Staring_EM_min	Single	1	2	4	1	5
2	Staring_EM_low	Single	1	2	4	1	50
3	Staring_EM_med	Single	1	2	4	1	100
4	Staring_EM_hi	Single	1	2	4	1	200
5	Staring_EM_max	Single	1	2	4	1	300
6	Rapid_frame_trans_min	Rapid	1	1	2	1	5
7	Rapid_frame_trans_low	Rapid	1	1	2	1	50
8	Rapid_frame_trans_med	Rapid	1	1	2	1	100
9	Rapid_frame_trans_hi	Rapid	1	1	2	1	200
10	Rapid_frame_trans_max	Rapid	1	1	2	1	300
11	Rapid_non-frame_trans_min	Rapid	1	1	2	0	5
12	Rapid_non-frame_trans_low	Rapid	1	1	2	0	50
13	Rapid_non-frame_trans_med	Rapid	1	1	2	0	100
14	Rapid_non-frame_trans_hi	Rapid	1	1	2	0	200
15	Rapid_non-frame_trans_max	Rapid	1	1	2	0	300
16	Tip_tilt_bin_by_2_min	Tip-tilt	2	1	2	1	50
17	Tip_tilt_bin_by_2_max	Tip-tilt	2	1	2	1	300
18	Tip_tilt_bin_by_4_min	Tip-tilt	4	1	2	1	50
19	Tip_tilt_bin_by_4_max	Tip-tilt	4	1	2	1	300

[a]Single: Single frame staring mode
Rapid: Fast frame transfer mode
Tip-tilt: Binned small region readout for tip-tilt measurement

[b]FT: Frame transfer mode

Note. — Other parameters such as the analog-digital channel depth, amplifier used etc are defined in the observing mode definition but have the same values for all modes and hence are not shown in this table for brevity.

Table 2.2. Visible and IR Camera Filter Sets.

	Visible Camera		IR Camera
Slot	Wheel 1	Wheel 2	Wheel 3
1	Clear[a]	Blank	Clear[a]
2	SDSS g'	500 nm Narrow	J
3	SDSS r'	660 nm Narrow	H
4	SDSS i'	670 nm Narrow	Dark
5	SDSS z'	600 nm Longpass	Blank
6	Blank	Dark	Blank

[a]The clear filter is transparent to all wavelengths, but has the same optical thickness to maintain the focal position of the beam.

2.1.2.3 IR Camera and Filters

Robo-AO was originally designed to be equipped with an IR camera based with a 2048×2048 pixel Hawaii RG HgCdTe detector which is currently in construction. An off-the-shelf 320×256 pixel InGaAs camera was purchased from Xenics to serve as the IR camera during demonstration. This camera, although cheap and readily available, poses some challenges for scientific observations due to its high read noise ($\sim 50\,e^-$) and high dark current ($\approx 6000\,e^-\,s^{-1}\,pix^{-1}$) despite a three stage cooling. It remains an engineering grade camera that can be used to observe stars of a narrow range of brightness between the noise limit and the saturation limit of the camera.

A full 2048×2048 pixel Hawaii RG HgCdTe detector has been purchased from Teledyne Industries in the summer of 2012. IUCAA has taken the responsibility of building the dewar and the re-imaging optics for the IR camera. The IR camera will have a platescale of 86 mas pixel^{-1} (Nyquist sampling at J band) imaging the full 2′ diameter field of view passed by the Robo-AO optics. With a read noise of $< 5\,e^-$, a dark current $\sim 0.01\,e^-\,s^{-1}\,pix^{-1}$ and higher quantum efficiency, the HgCdTe detector will be 45-80 times more sensitive than the InGaAs camera (2.3).

The IR imaging arm is currently equipped with a single filter wheel with J and H band filters as described in Table 2.2.

2.1.2.4 Calibration Source

Robo-AO is designed with an internal calibration source (Figure 2.9) that can simulate the visible and IR light arriving from a natural star at infinity and a UV laser beam arriving from an altitude of 10 km. The source is revealed to the rest of the optics by translating the FM1 fold mirror out of the path. The calibration source is used for calibration of the wavefront sensor zero-points (slope offsets) and general instrument check-out at the beginning of every observing run. The calibration source was also used for the assembly and alignment of the instrument (detailed in Section 2.4).

Table 2.3. IR Camera Sensitivities.

Detector	Field of View $''$	Plate Scale $''\,\mathrm{pix}^{-1}$	Sensitivity[a] J-band	H-band	K-band
InGaAs	32×26	0.1	14.9	15.2	N/A
HgCdTe	$120''$ dia	0.086	19.7	19.4	18.2

[a]Faintest magnitude to reach a signal-to-noise ratio of 10 in 120 s of exposure. These assume a residual wavefront error of 185 nm RMS, expected under median seeing conditions.

Note. — Adapted from Baranec et al. (2012).

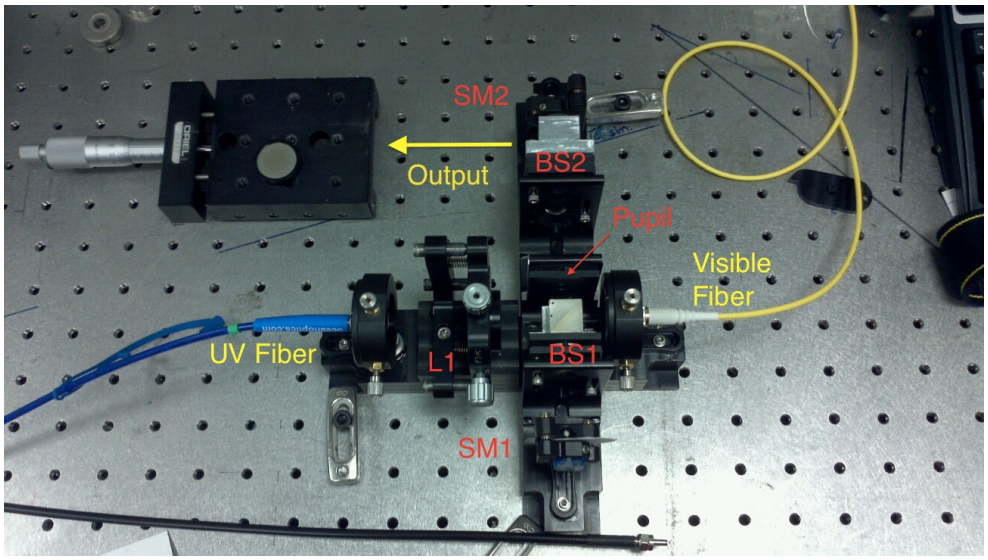

Figure 2.9. The assembled Robo-AO calibration source is shown. The entire unit is constructed on a separate base that allows it to be installed into the Cassegrain instrument after alignment on an optical bench. UV light from a UV LED source enters from the left through a 100 μm fiber (blue). The collimating lens L1 allows the divergence of the UV beam to be adjusted. Visible light from a broadband thermal source (quartz lamp) is input through the yellow fiber from the right. The beam splitter BS1 and spherical mirror SM1 allow the collimation of the visible light into a parallel beam. BS1 also combines the UV beam and the visible beam into one coaxial beam. The pupil is designed to replicate the pupil of the P60 telescope (without the secondary occultation). Both the UV and visible beams are focused by spherical mirror SM2 and sent to the input of the instrument by BS2. The multiple reflections created by the beam-splitters are attenuated by painting the appropriate surfaces black.

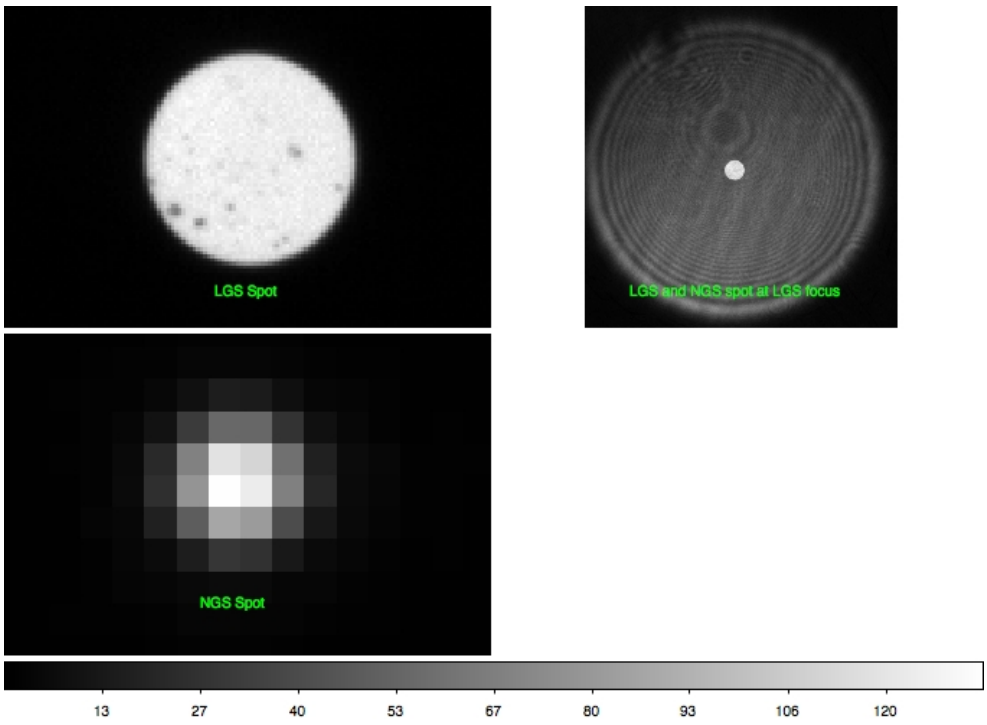

Figure 2.10. *Top Left Panel:* Image of the UV beam at the 10 km (LGS) focus. *Bottom Left Panel:* Image of the visible beam at the infinity (NGS) focus. *Top Right Panel:* Image of the UV beam (central bright spot) and the visible beam (defocused disk) at the LGS focus of the calibration source. Photographs assembled by J. Fucik.

The performance requirement for the Robo-AO calibration source were as follows:

- Provide a visible light spot that was diffraction limited at 400 nm ($\approx$ 55 milli-arcsec) at the inifinity focus of the telescope
- Provide a UV spot approximately 1.8″ in size at the 10 km focus.
- Both beams should be coaxial
- The RMS wavefront difference between the two beams, ignoring the focus difference, was to be less than 34 nm.

For one week in April 2011, Jason Fucik and I assembled and aligned the calibration source to the required specifications. The resulting wavefronts were tested with a commercial wavefront sensor from Thorlabs. Figure 2.10 shows the final results of our assembly.

The calibration source was assembled on the optical table as a unit before the instrument assembly. The completed calibration unit was finalized (by gluing all unused degrees of freedom) and installed onto the base-plate of the Cassegrain instrument. The calibration unit was positioned onto the base-plate to an accuracy of about 1 mm such that the visible light focus was co-located with the expected telescope beam focus. The UV and visible

beams from the calibration source were used as the fiducial beams for assembling the remaining optics. When the instrument was mounted on the telescope, the tip-tilt angles of the fold mirror (FM1) and the telescope focusing mechanism provided three degrees of freedom to adjust the telescope beam focus to the exact location of the calibration source focus, thus aligning the entire instrument to the telescope.

2.2 Atmospheric Dispersion Corrector

The refractive index of air has a small but non-negligible variation as a function of wavelength which, coupled with the curvature of the atmosphere, produces a dispersion of light rays along the meridian of azimuth. As shown in Figure 2.11, rays of different wavelengths are bent at different angles, and hence the image of a star in different wavelengths appears at different altitudes (defined here as the angle from the horizon measured towards the zenith). Since the refractive index for blue light is higher, as we shall see in the following discussion, the image of the blue star appears at a higher altitude. For low airmasses, the dispersion is smaller than the seeing limited PSF of a telescope, and hence is not of much concern for seeing limited imaging or spectroscopy. With an AO system, especially one operating in the visible band as we shall see in the following discussion, the dispersion can severely distort the PSF in broadband images and compromise the goal of AO correction. Roe (2002) discusses the effects of differential refraction on AO observations. However some of the effects discussed are not applicable to Robo-AO. For example, the differential position of the visible and the IR centroid can change the image rotation centers for telescopes mounted on altitude-azimuth platforms and blur the science image as it rotates with respect to the tip-tilt star.

Some AO systems such as the Keck II LGS-AO system (Wizinowich et al., 2006), the differential refraction is approximately corrected by calculating the effects from the spectral index or colors of the tip-tilt star. However, this method demands good color photometry and precise identification of the tip-tilt star making it unsuitable for automated operation. I designed the atmospheric dispersion corrector (ADC) system for Robo-AO that corrects for these effects. In this section, we shall discuss the theory, design, and calibration of the ADC.

The overall idea of an ADC is to design a prism, or a set of prisms, with a combination of glasses whose dispersion properties match and cancel the dispersion caused by the atmosphere for all relevant wavelengths and all relevant zenith angles. Before discussing the design of the ADC, we shall discuss the refractive properties of the atmosphere and the necessary physics.

2.2.1 Refractive Properties of the Atmosphere

The variation of the refractive index n of air as a function of its state has been extensively studied since the 1950s. Ciddor (1996) compiled all the previous work, and suggested an equation to calculate the refractive index based on the wavelength, air pressure, air temperature, relative humidity and composition. Equations 2.1 are the standard equations

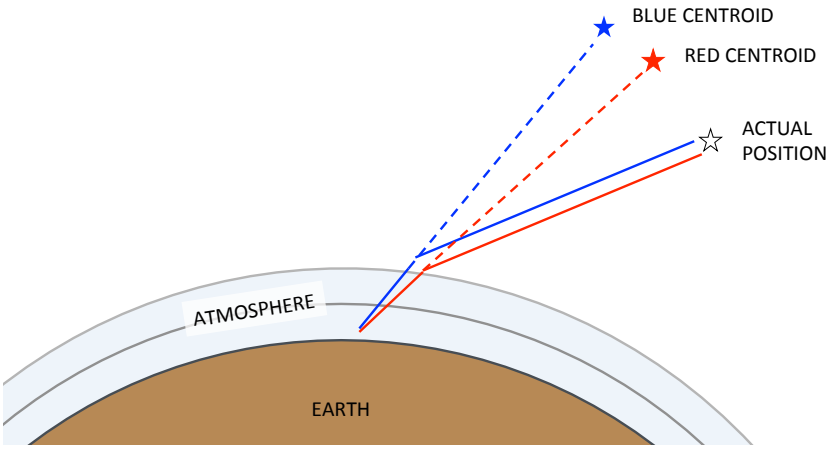

Figure 2.11. A ray diagram of starlight passing through the atmosphere. The rays of shorter wavelength (blue) light are bent more than the rays of longer wavelength (red) light. Consequently, the apparent direction of arrival of blue light is from a higher altitude than that of red light, and the position of the star in blue light (dashed blue line) is higher than the position of the star in red light (dashed red line).

for all work concerned with the atmospheric refractive index.

$$10^8(n_{as}-1) = k_1/(k_0-\sigma^2)+k_3/(k_2-\sigma^2), \tag{2.1}$$

$$(n_{axs}-1) = (n_{as}-1)[1+0.534\times10^{-6}(x_c-45)], \tag{2.2}$$

$$10^8(n_{ws}-1) = 1.022\times(w_0+w_1\sigma^2+w_2\sigma^4+w_3\sigma^6), \tag{2.3}$$

$$n_{prop}-1 = (\rho_a/\rho_{axs})(n_{axs}-1)+(\rho_w/\rho_{ws})(n_{ws}-1). \tag{2.4}$$

The parameters in the equation are as follows:

- n_{as} is the refractive index of standard air at 15°C, 101325 Pa, 0% humidity and 450 ppm of CO_2.
- $k_0 = 238.0185\,\mu\text{m}^{-2}; k_1 = 5792105\,\mu\text{m}^{-2}; k_2 = 57.362\,\mu\text{m}^{-2}; k_3 = 167917\,\mu\text{m}^{-2}$ are constants (for the Sellemeir form of the dispersion relation).
- $\sigma = \lambda^{-1}$ is the wavenumber of the light.
- n_{axs} is the refractive index of standard air with x_c ppm of CO_2.
- n_ws is the refractive index of water vapor at 20°C, 1335 Pa.
- $w_0 = 295.235\,\mu\text{m}^{-2}; w_1 = 2.6422\,\mu\text{m}^{-2}; w_2 = -0.032380\,\mu\text{m}^{-4}; w_3 = 0.004028\,\mu\text{m}^{-6}$ are constants.
- n_{prop} is the final equation for refractive index combining n_{axs} and n_{ws} for a given relative humidity.

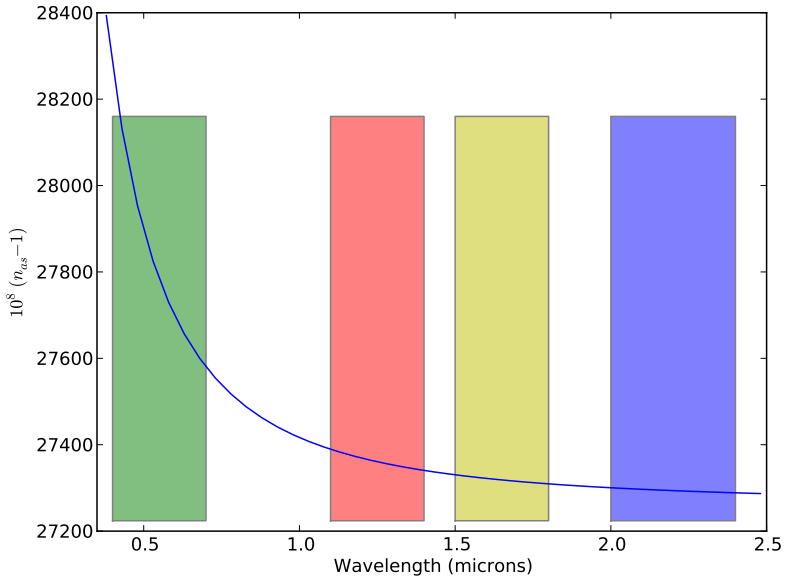

Figure 2.12. The refractive index of dry air at 15°C, 101325 Pa, 0% humidity, and 450 ppm of CO_2. The variation in refractive index as a function of wavelength is shown by the blue line. The y-axis is scaled by 10^8. The rectangles indicate different astronomical bands: green corresponds to the visible band, red corresponds to IR J band, yellow corresponds to the IR H band, and blue to the IR K band. The refractive index changes very rapidly at the visible wavelengths as compared to the variation in the entire IR band.

- ρ_a, ρ_{axs}, ρ_w and $\rho_w s$ are densities of the dry component of air, dry air at standard temperature and pressure as given above, the wet component of air and water vapor at standard temperature and pressure given above. ρ_a and ρ_w are calculated from the BIPM 1981/91 density equation from Davis (1992) that accounts for the pressure, temperature and, compressibility of the gas.

The mathematical expression for the refraction of light as a function of zenith angle has been worked on by a number of workers since early 1900's. The efforts are summarized in Stone (2002, 1996). The refraction as a function of wavelength and zenith angle are approximated as,

$$R(\lambda, z) = \kappa(n(\lambda) - 1)(1 - \beta)\tan(z) - \kappa(n(\lambda) - 1)(\beta - (n(\lambda) - 1)/2)\tan^3(z), \qquad (2.5)$$

where z is the zenith angle of observation and the parameters κ, β are described below. This formula is valid for a zenith angle of 75°. The parameter κ accounts for the deviation from a spherical atmosphere atmosphere assumption and is equal to unity for all practical purposes. The parameter β accounts for the "effective" height of the observatory above the

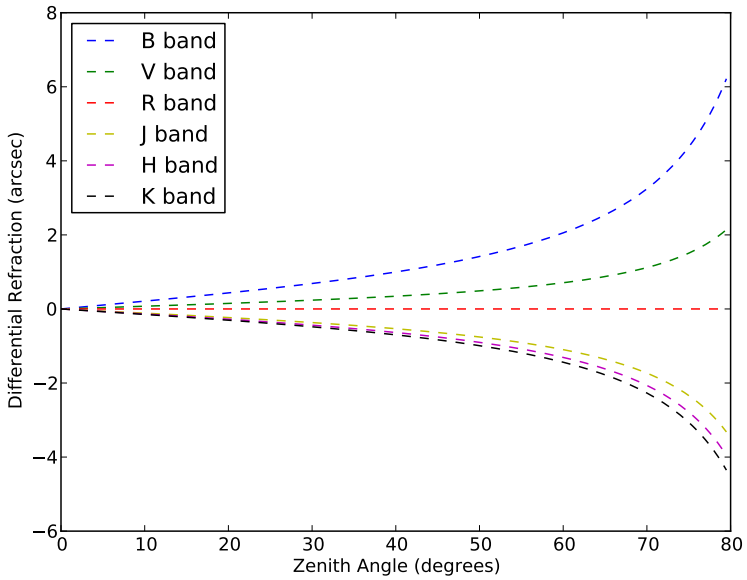

Figure 2.13. The differential refraction of light in different wavelengths as a function of zenith angle. The refraction of red light ($0.6\,\mu$m) has been subtracted. For small zenith angles and narrow wavelength ranges, seeing limited observations are not drastically affected by the differential refraction. However, differential refraction can severely affect the operation of an AO system, especially in the visible wavelengths.

surface of the earth and is calculated from the local temperature $T\,$K as,

$$\beta = 0.001254 \left(\frac{T(\mathrm{K})}{273.15\,\mathrm{K}} \right). \tag{2.6}$$

Figure 2.13 shows the differential refraction of light in different wavelengths as a function of zenith angle. The refraction of red light ($0.6\,\mu$m) has been subtracted as the fiducial refraction.

The cubic term of Equation 2.5 can be reasonably neglected for zenith angles $<65°$, allowing us to factor the equation into the wavelength dependent and zenith angle dependent terms. We use this approximation for our design of the ADC. If we design a prism that can match and correct the atmospheric dispersion for all relevant wavelengths for a maximum correction at a zenith angle of z_0, we only need to change the magnitude of the refraction to correct for any zenith angle $z < z_0$. There are different mechanisms to achieve variable dispersion, all of which involve multiple prisms that move with respect to each other, and the orientation between them allows the effective dispersion to be changed. In Section 2.2.3, we shall discuss the rotating prism design chosen for Robo-AO and the mathematics for its operation.

2.2.2 Robo-AO ADC Design Goals

The design of Robo-AO ADC was dictated by four requirements described in the Robo-AO Instrument Requirements Document.

Robo-AO shall transmit light from the telescope output to the science instruments detector planes (not including detector Q.E.) with the following quantum efficiencies:

- **RAO-IRD-0025**: 390−550 nm: QE > 25%
- **RAO-IRD-0026**: 550−900 nm: QE > 50%
- **RAO-IRD-0027**: 900−2300 nm: QE > 50%
- **RAO-IRD-0034**: Robo-AO shall compensate for atmospheric dispersion over the operating wavelengths of the science and tilt sensor wavelengths simultaneously. The allowable amount of dispersion is <20% diffraction limited PSF FWHM size at any given wavelength.

The diffraction limited FWHM of the Robo-AO PSF is 70 mas at 500 nm and 300 mas at 2.2 μm. This means that we needed an ADC that would correct the wavefront from 390 nm 2300 nm with an accuracy of 15 mas upto a zenith angle of 65°.

The total transmission of the ADC was required to be more than 88%. We expected we could achieve a coating with reflectivity < 2%. This meant that, including internal reflections on wedge interfaces and transmissivity of the glasses, the transmission should be more than 92%. The reflectivity of R of at each interface is given by,

$$R = \left(\frac{n_1 - n_2}{n_1 + n_2}\right)^2 . \tag{2.7}$$

Most previous ADCs designed for AO systems were designed to operate in the IR bands where the dispersion is low and the correction requirements for seeing limited ADCs are significantly looser than those for AO instruments; these ADC requirements are very stringent. Similar efforts have been made for the Subaru Telescope AO system by Egner et al. (2010) and for the Magellan Telescope AO system by Kopon et al. (2008), however, they had smaller wavelength coverage (0.45 − 2.2 μm for Subaru and 0.5 − 1 μm for Magellan).

The location of the ADC in the optical path was decided from design constraints to be between OAP3 and TTM that was almost conjugate to the telescope pupil. Hence the ADC was designed for nearly collimated beams, which drastically simplified the prism design.

2.2.3 Rotating Double Amici Prism ADC

Among the many designs for ADCs, the rotating double Amici prism design, studied thoroughly by (Wynne, 1997, and references therein), is the simplest and the most commonly used design. As shown in Figure 2.14, it consists of two identical compound prisms that can be independently rotated around the optical axis. Each compound prism consists of cemented wedges of glasses of similar refractive index but different dispersions. The glasses and wedge angles are chosen such that light of a particular fiducial wavelength (usually

chosen close to the middle of the range of interest) passes undeviated through it. The other wavelengths of light pass through with appropriate deviations as designed. When the prisms are aligned (Case 'a' of Figure 2.14), the dispersions of the prisms add up, doubling the total dispersion. When the prisms are counter-aligned (Case 'c'), the dispersions of the prisms cancel each other, leading to zero correction. For intermediate angles (Case 'b'), the dispersion is between the two extremes.

2.2.4 Movement Calculations

The rotation angles of the prisms can be easily calculated by considering the total dispersion as a vector sum of the individual dispersions of the prisms as shown in Figure 2.15. The length of dispersions of each prism represents half the dispersion at the maximum zenith angle z_0 the prisms were designed to correct. The angle between the two prisms 2ψ is chosen such that the sum total of the dispersion is equal to $\tan(z)/\tan(z_0)$, assuming the cubic term of Equation 2.5 is negligible. Simple trigonometry shows that

$$\cos(\psi) = \tan(z)/\tan(z_0). \tag{2.8}$$

The vector sum of the dispersions must point towards the zenith. Since Robo-AO is mounted on an equatorial telescope, the prisms must be co-rotated during the observation to account for the changing direction of zenith in relation to the instrument (i.e. the parallactic direction).

Zenith Hole The rate of change of parallactic angle increases to a very large value when the star passes very close to the zenith. The rotation stages used to control the angular positions of the prisms are designed to achieve a certain maximum angular velocity. When the zenith angle of a star is less than a certain threshold value, the required rotation speed will exceed the maximum and hence the ADC will not be able to track the zenith direction. However, at the same time, when the star is close to the zenith, the dispersion correction required is minimal and often negligible. Hence, the ADC is designed such that when the star is inside the zenith hole, the prisms are counter-aligned for zero dispersion correction and the parallactic angle tracking is disabled. This threshold zenith angle forms the radius of the 'zenith hole'.

To determine the maximum zenith angle at which Robo-AO can safely operate without an ADC, we use Equation 2.5 and find the zenith angle at which the differential refraction between light at $0.5\,\mu m$ and $2.5\,\mu m$ is much less than the PSF FWHM. We chose a zenith hole of 3° based on this requirement.

For the Newport PR50-CC rotation stages used for the Robo-AO ADC, the maximum design speed is $20^\circ\,s^{-1}$. However, the error in tracking a specified trajectory (angle as a function of time) is higher when operating close to the maximum speed and hence it is recommended to operate the rotation stages at a lower velocity. For the latitude of Palomar observatory, stars passing 3° away from the zenith require a maximum rotation speed of $0.07^\circ\,s^{-1}$, much less than the maximum speed of the rotation stages, which makes it a suitable value for the zenith hole.

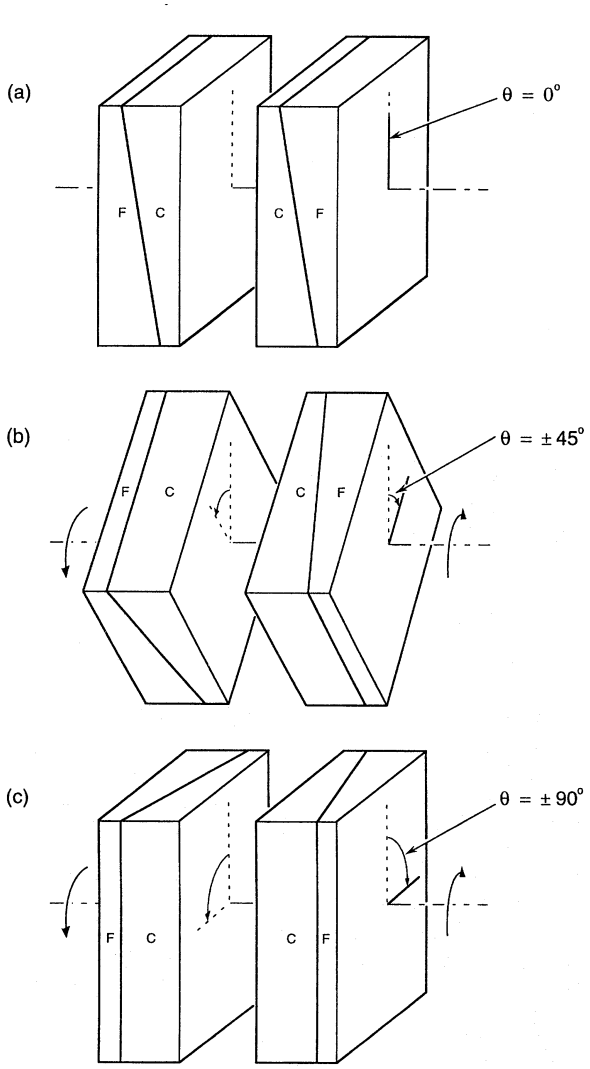

Figure 2.14. The rotating Amici prism design. Two identical compound prisms are installed serially in the optical path and can be rotated around the optical axis to vary the total dispersion of light. When the prisms are aligned (Case 'a'), the dispersions of the prisms add up, doubling the total dispersion. When the prisms are counter-aligned (Case 'c'), the dispersions of the prisms cancel each other, leading to zero correction. For intermediate angles (Case 'b'), the dispersion is between the two extremes. Figure adapted from Figure 1 of Wynne (1996).

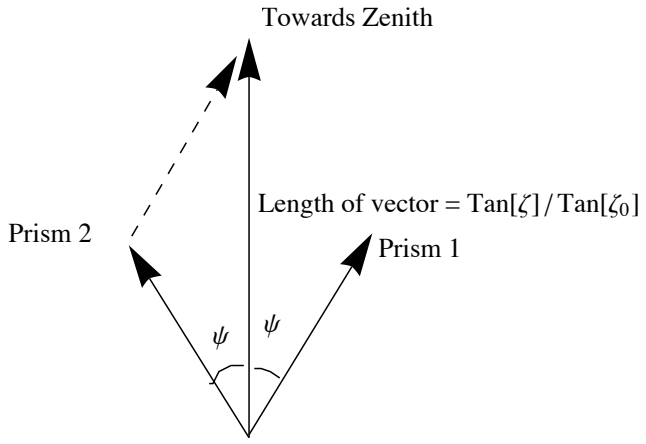

ζ_0 is the maximum zenith angle the ADC is designed for.
ζ is the actual zenith angle of observation.
Prism vectors are of unit length in this scaling.

Figure 2.15. Vector representation of the dispersion created by each prism. The length of dispersions of each prism represents half the dispersion at the maximum zenith angle z_0 the prisms were designed to correct. The angle between the two prisms 2ψ is chosen such that the sum total of the dispersion is equal to $\tan(z)/tan(z_0)$. The total dispersion of the two prisms must always point towards the zenith.

The detailed calculations of the movement and plots of maximum rotation speed are given in Appendix B.

2.2.5 Robo-AO ADC Design

For the Robo-AO ADC design, I started off with calculating the atmospheric dispersion as a function of wavelength at Palomar. The `Starlink` code library `SLALIB` procedure `SLA_REFRO` was used to calculate the dispersion. The height of Palomar observatory above sea-level (1712 m), the latitude (∼33.3°), average temperature (∼5°C; January to March), average relative humidity (40%) were input to the model. Error analysis showed that varying the temperature over the range required by Robo-AO (−5 to 20°C) and relative humidity over all operational range ($\lesssim$ 88%[4]) changed the dispersion within acceptable limits, and that the correction model used (Equation 2.5) could be operated at a specific $n(\lambda)$ defined at a fiducial temperature and relative humidity.

The next step was to find a combination of glass wedges that would accurately correct half the dispersion. I collected catalogs of glasses from glass manufacturers Schott and Ohara and collected the details of Sellmeier coefficients[5], transmissivity, thermal expansion coefficients, and cost. I wrote `MATLAB` code to simulate the dispersion of three models of compound prisms shown in Figure 2.16: (a) a two glass wedge prism that is traditionally used for all ADCs, (b) a three glass wedge prism, and (c) a two glass, three wedge prism that added an extra degree of freedom to the model (a) but would be less expensive than (b).

To find the optimum combination of glass wedges, a cost function was formed as,

$$\text{Cost}(\text{prism parameters}, \theta) = \sum_{\lambda_i} (R_{\text{prism}}(\lambda_i; \text{prism parameters}) - R_{\text{atm}}(\lambda_i) - \theta)^2, \quad (2.9)$$

where summation is over all values of wavelengths over which the dispersion is calculated and θ is a free parameter that incorporates the bulk refraction of the starlight corresponding to the refraction at some floating fiducial wavelength. For each combination of glasses in the catalog, the `MATLAB` function `fmincon` was used to reduce the cost function by varying the prism angles. To ensure that the designs were amenable to fabrication, the wedge angles of the prisms were constrained to 30°. The best performance of each combination of glasses was recorded along with the total transmissivity of the combination.

The reason for considering and preferring design (c) was two-fold. Firstly, the extra degree of freedom allowed by design (c) over design (a) allowed better control of the lateral shifting of the beam, which was useful for ensuring that the beam would stay inside both the

[4] The actual limit is specified in terms of the dewpoint depression; i.e. the difference in the air temperature and the dewpoint should be more than 3°C. For normal temperatures, this translates to an relative humidity of ∼88%.

[5] The Sellmeier equation is an empirical equation to represent the refractive index of light. The usual form for glasses is

$$n^2(\lambda) = 1 + \frac{B_1\lambda^2}{\lambda^2 - C_1} + \frac{B_2\lambda^2}{\lambda^2 - C_2} + \frac{B_3\lambda^2}{\lambda^2 - C_3}.$$

B_i and C_i are conventionally quoted for λ in microns.

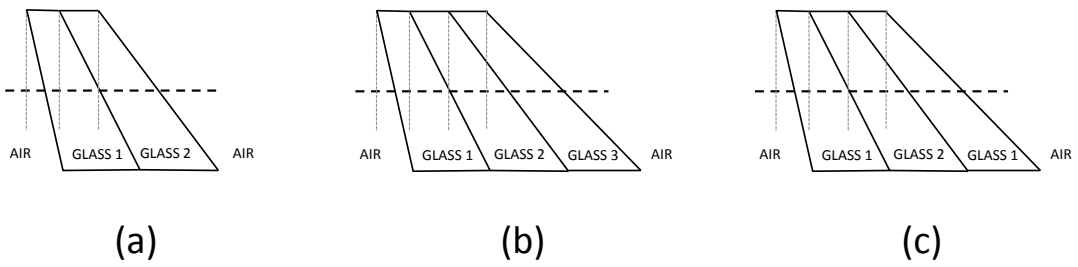

Figure 2.16. Three designs of prisms for the ADC studied in the design phase. The dashed black line is the optical axis of the prisms. Design (a) uses two wedges of two different glasses and has three surfaces. Design (b) uses three wedges of three different glasses. Design (c) has three wedges of which the first and third wedge are made from the same glass. This design is cheaper than design (b) but has more degrees of freedom than design (a) and facilitates the anti-reflection coating.

prisms of the ADC at all rotation angles. Secondly and more importantly, design (c) allowed us to have the same glass surface at both ends of the prisms, where the multi-layer anti-reflection coatings were to be applied. The thickness and composition of the anti-reflection coatings are specific to the properties of the glass-air interface for which they are intended. The Robo-AO requirement of transmissivity required a broadband anti-reflection coating, whose cost was exacerbated by the high refractive index of the glasses used. Having the same glass-air interface for all the prism surfaces allowed them to be coated in a single batch, drastically reducing the fabrication cost. We also used the lower refractive index glass on the outer wedges in the design to reduce the cost and effort required for the anti-reflection coating.

While the `MATLAB` code yielded satisfactory results and provided an excellent understanding, it performed a one dimensional calculation with a limited catalog of glasses. It was decided to confirm the results and perform optical tolerancing using the standard optical design software `ZEMAX`, which was also used to create the optical design of the rest of Robo-AO. The ADC prisms were simulated in the `ZEMAX` files along with a simulated incoming beam from the Robo-AO instrument. `ZEMAX` has an inbuilt atmospheric refraction model based on `SLA_REFRO` that was used to simulate the atmospheric refraction. A global substitution optimization algorithm was used to find the best combination of glasses. The first surface of the prism was constrained to be normal to the optical axis, allowing for easy alignments during setup. This could be achieved without sacrificing the overall performance of the ADC.

Few designs with good correction performance were chosen for further checking and tolerancing. One of the major concerns was the differential thermal expansion of the two glasses that were bonded together. If the thermal stress exceeded the breaking stress of the material, the wedges could be debonded or worse, cracked. The alignment tolerances were also checked by simulating misalignments of the prisms. The alignment tolerances for individual wedges were $1'$. However, the alignment tolerances for the bonded prisms were

up to a degree in rotation and up to a millimeter in translation.

2.2.6 Final Design

Among the many ADC designs that were created, we shall discuss three with the best performance and criteria used for choosing the final design.

2.2.6.1 N-FK51A and YAG

The optical design with the best performance was based on N-FK51A glass and YAG crystal. The design specifications are as shown in Figure 2.17. The spot diagram for the final positions of stellar images at a zenith angle of 70° for wavelengths from 0.4 μm to 2.2 μm is shown in Figure 2.18. The RMS spread of the spot diagram was 2.252 μm. The design showed excellent performance to a zenith angle of 70°, between a temperature range of $-10\,^{\circ}$C to $25\,^{\circ}$C and the entire range of relative humidity. Due to the high refractive index of YAG ($n_d = 1.8245$) as compared to the refractive index of N-FK51A ($n_d = 1.48656$), the internal reflection (1% at each interface) was slightly higher than other designs.

The thermal expansion rates of the two materials were reasonably matched with $\alpha_{\mathrm{YAG}} \approx 8 \times 10^{-6}\,\mathrm{K}$[6] for the YAG crystal and $\alpha_{\mathrm{N-FK51A}} = 12.74 \times 10^{-6}\,\mathrm{K}$ for the N-FK51A glass. The difference was considering the Young's modulus of 300 GPa and 73 GPa, respectively.

However, when requests for quotations were sent to manufacturers, it was realized that YAG crystals are extremely difficult to acquire and polish to the required surface finish. Among the eight manufacturers contacted, seven responded that they would not be able to fabricate YAG wedges. The rough estimate from one manufacturer was that it would cost between ten to twenty thousand USD to fabricate the wedges, not including the anti-reflection coating. It was decided to shelve this design and consider the other choices.

2.2.6.2 N-FK51A and S-LAH58

The second best ADC design that was considered was of N-FK51A and S-LAH58 glasses. S-LAH58 is a glass similar to YAG crystal, with a refractive index of $n_d = 1.882997$ and similar dispersion characteristics. The performance (as shown in Figure 2.20) was close to that of N-FK51A and YAG prisms. However, the design was rejected for two reasons: first, the thermal expansion coefficients of the two glasses ($\alpha_{\mathrm{S-LAH58}} = 6.6 \times 10^{-6}\,\mathrm{K}$ compared to $\alpha_{\mathrm{N-FK51A}} = 12.74 \times 10^{-6}\,\mathrm{K}$) were too divergent to be considered safe for the thermal range sought by Robo-AO, and second, the S-LAH58 glass (manufactured by Ohara) was expensive to procure and would not have been feasible with our budget.

2.2.6.3 N-SK4 and N-KZFS5

The final design selected for fabrication was a set of N-SK4 and N-KZFS5 prisms with specifications as shown in Figure 2.21. This was designed to correct up to a zenith angle of 65°. The RMS spot radius at the image plane was 5.36 μm. The correction was within

[6] The exact value depends on the orientation of the crystal. It can vary from 7.7 to $8.2\times10^{-6}\,\mathrm{K}$.

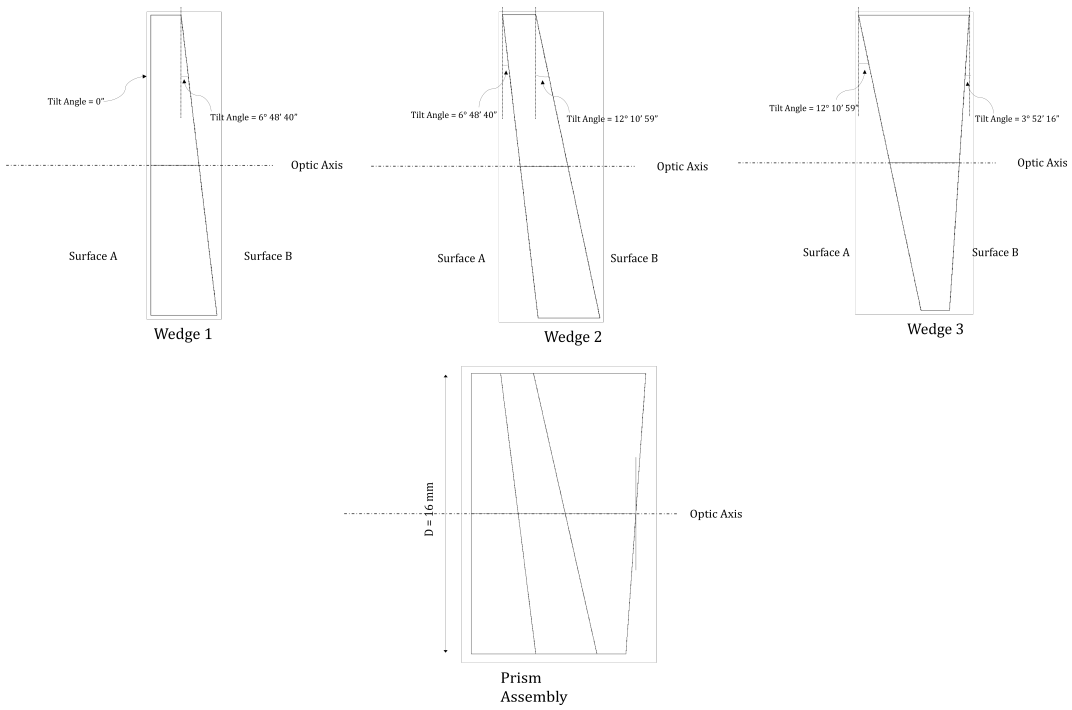

Figure 2.17. Design specifications for the N-FK51A and YAG prisms. Wedges 1 and 3 are fabricated from N-FK51A glass. Wedge 2 is fabricated from YAG crystal. The wedges are bonded to form the compound prism as shown.

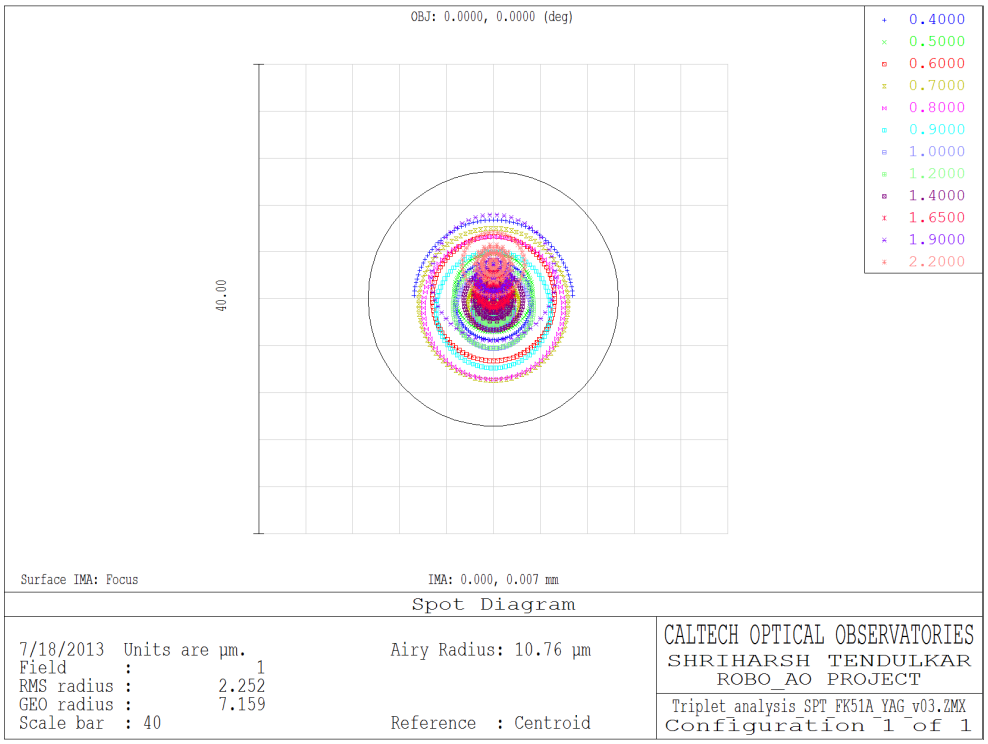

Figure 2.18. Spot diagram for dispersion corrected stellar images at a zenith angle of 70° using the N-FK51A and YAG prisms. The RMS radius of the spot is the smallest of all designs, but the design is significantly harder for fabrication.

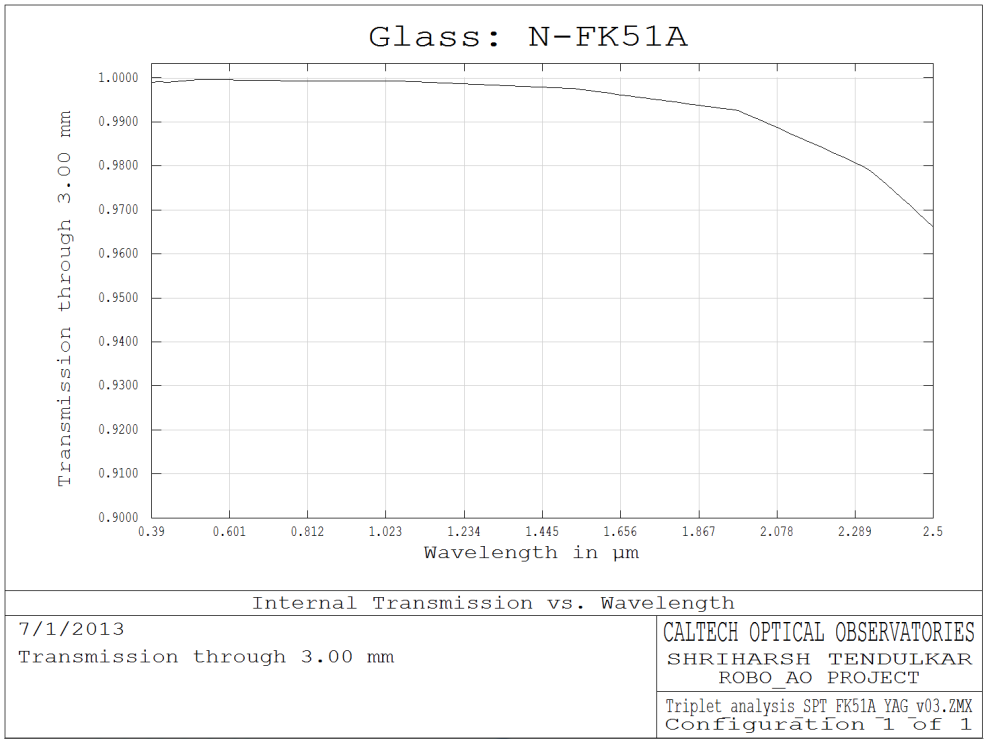

Figure 2.19. The transmission curve for 3 mm thick N-FK51A glass from 0.4 μm to 2.2 μm.

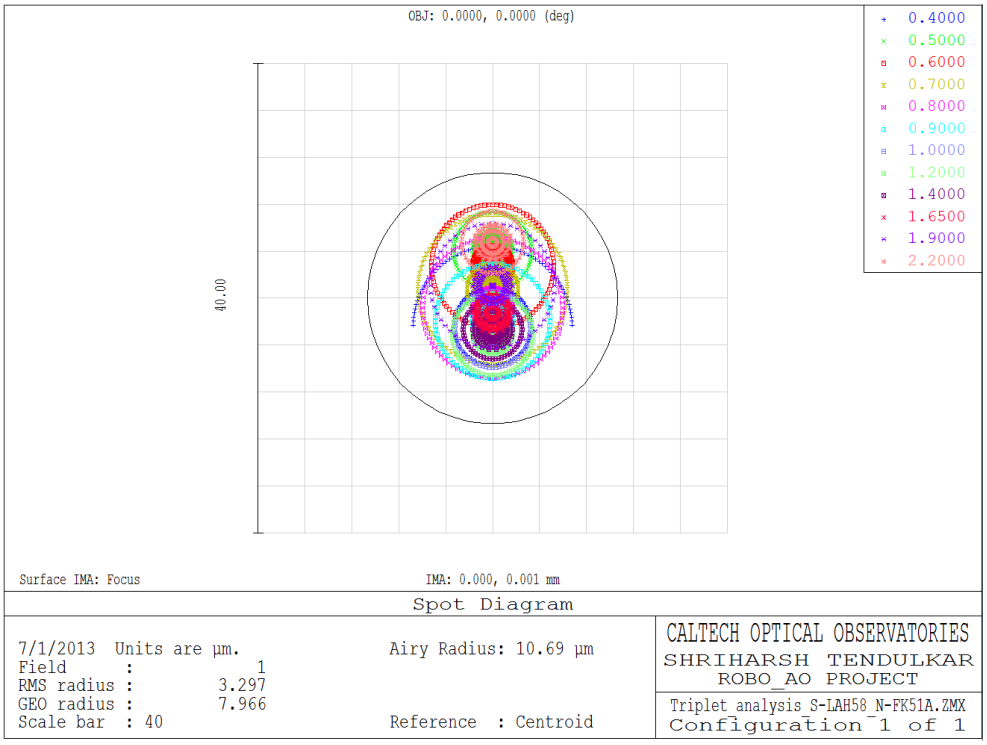

Figure 2.20. Spot diagram for the best correction achieved at a zenith angle of 65° by an N-FK51A and S-LAH58 ADC.

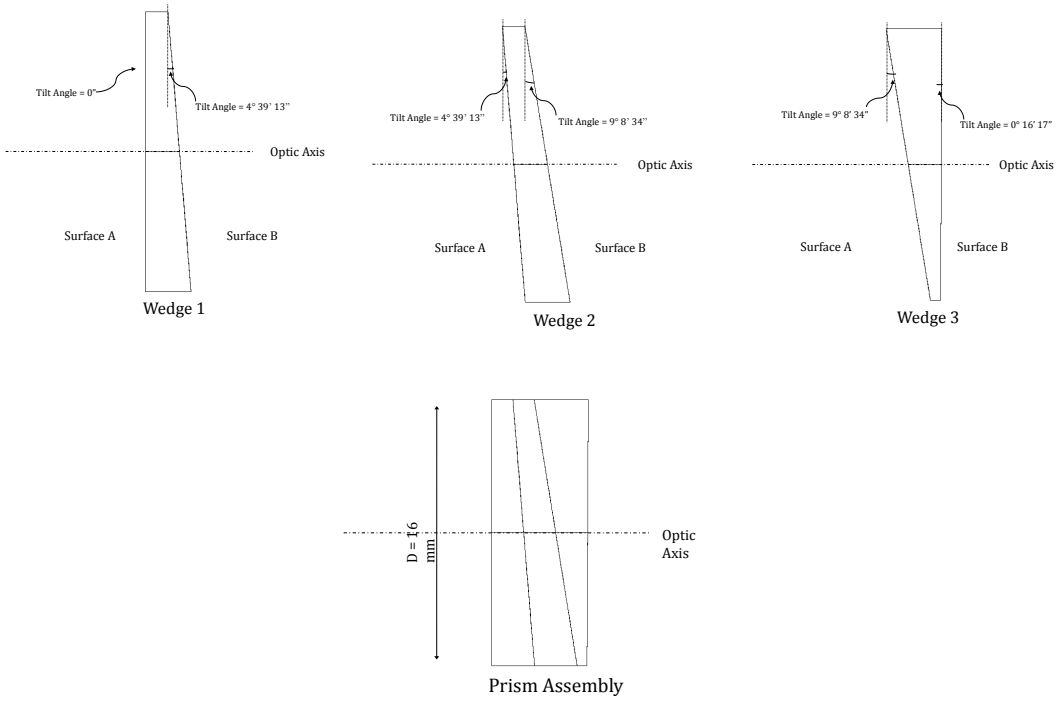

Figure 2.21. Design specifications for the N-SK4 and N-KZFS5 prisms. Wedges 1 and 3 are fabricated from N-SK4 glass. Wedge 2 is fabricated from N-KZFS5 glass. The wedges are bonded to form the compound prism as shown.

the design requirements, as shown in Figure 2.22. The transmissivity (Figure 2.23 and Figure 2.24) was within required limits but showed a slight drop-off towards 2.2 μm.

The refractive indices of N-SK4 and N-KZFS5 are $n_d = 1.61272$ and $n_d = 1.65412$. Because of the small relative difference in refractive indices, the reflection of light at each internal interface was limited to 0.016%.

The thermal expansion rates of the two glasses were also well matched with $\alpha_{\mathrm{N-SK4}} = 6.46\times10^{-6}\,\mathrm{K}$ and $\alpha_{\mathrm{N-KZFS5}} = 6.38\times10^{-6}\,\mathrm{K}$. The Young's moduli of the two glasses (84 GPa and 89 GPa respectively), although smaller than those of YAG or S-LAH58, were sufficient sustain the minor thermal expansions.

2.2.7 Testing and Calibration

The prisms were first tested in the laboratory to ensure that the wedges were at correct angles by reflecting a laser beam through the prism and calculating the expected positions of the reflections from the interfaces between the wedges. During this testing it was noticed that one of the prisms had an excessive, non-parallel thickness of epoxy that added an extra wedge to the optical path and caused excessive deviation of the light. This prism was

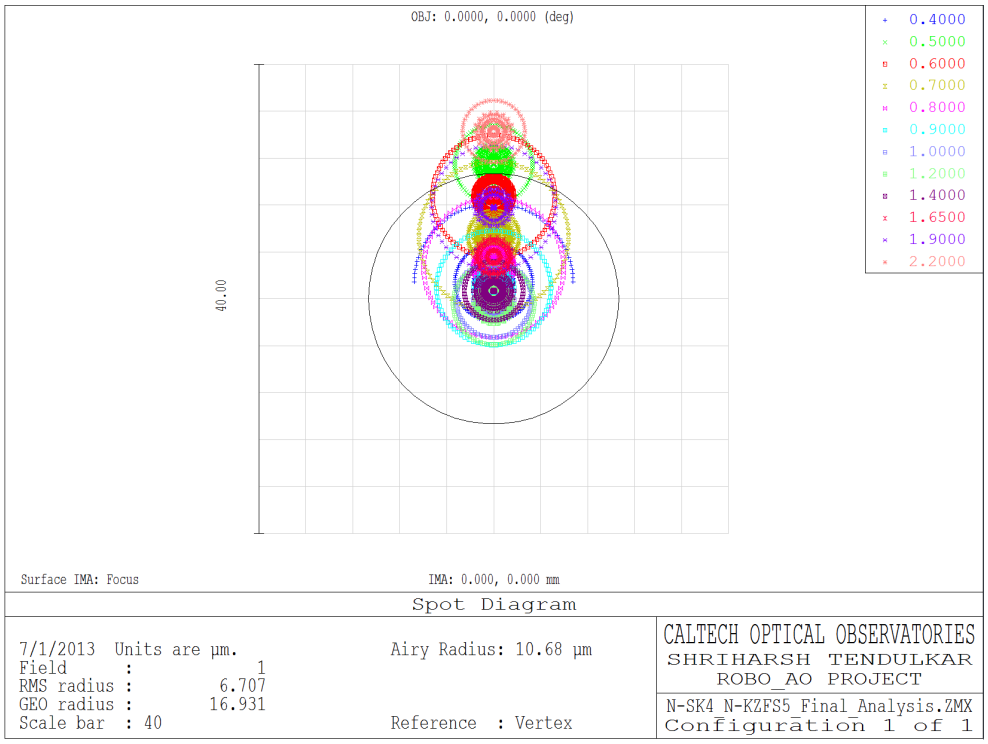

Figure 2.22. Spot diagram for dispersion corrected stellar images at a zenith angle of 65° using the N-SK4 and N-KZFS5 glass prisms. The RMS radius of the spot is slightly larger than other designs, but the design is significantly easier for fabrication.

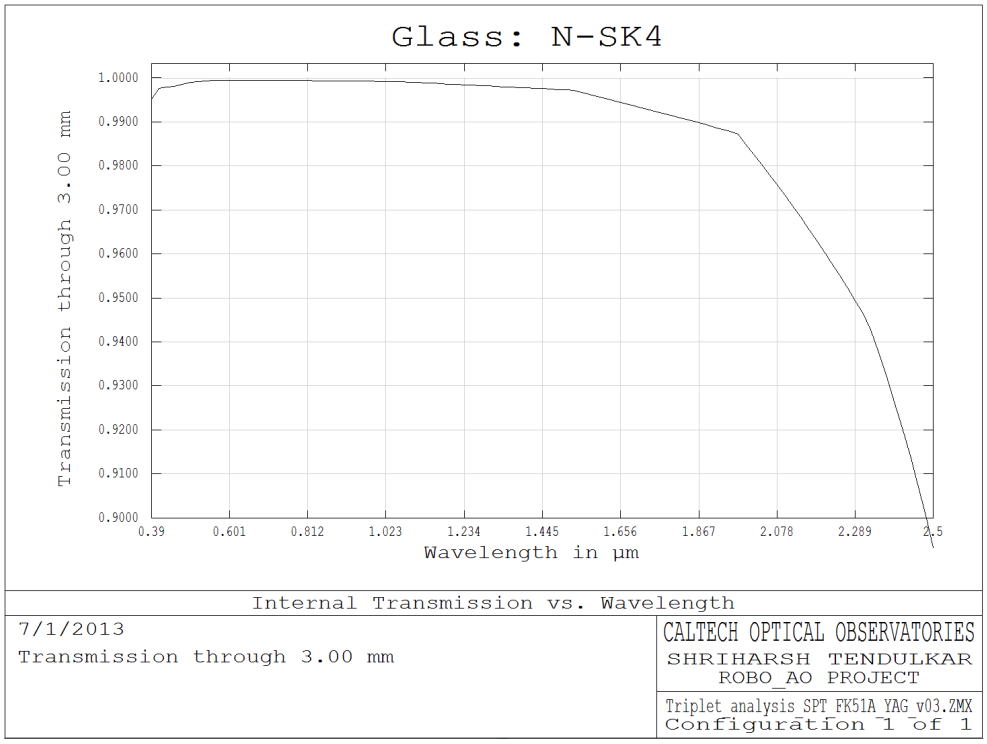

Figure 2.23. The transmission curve for 3 mm thick N-SK4 glass from 0.4 μm to 2.2 μm.

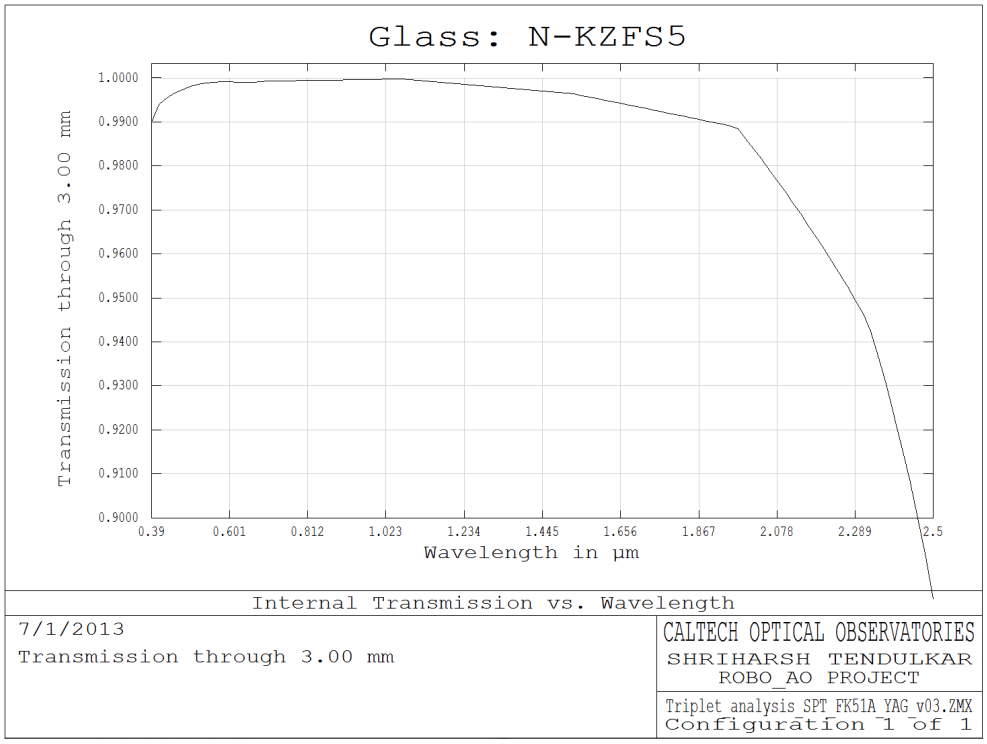

Figure 2.24. The transmission curve for 3 mm thick N-KZFS5 glass from 0.4 μm to 2.2 μm.

returned to the manufacturer, debonded, and rebonded with the proper alignment. The same testing after the prism was rebonded showed correct performance.

The prisms were then mounted into the prism holders and set into the rotation stages. Within the rotation stages, the optical axis of the prisms needed to be aligned to the rotation axis of the stages. This was done by reflecting a laser beam off the front surface of the prism (which was normal to the optic axis by design) as it was installed. The prism position and alignment were adjusted with three set screws in the prism holders till the reflected laser spot showed no movement. Simultaneous with the angular alignment, the prism was also shimmed with small pieces of shim stock until it was centered in the holders.

The other aspect of the calibration was to calculate the 'zero-point' of the orientations of the prism dispersions with respect to the parallactic angle. This was performed by manually setting the prisms to an angle of maximum dispersion, and aligning the dispersion along the vertical axis of the visible camera CCD. The angle between the North direction and the vertical axis of the visible camera of the CCD was determined to be 23.9°, from astrometric measurements of the globular cluster M15 by Sergi Hildebrandt. Combining the two measurements, I calculated the zero-point of the prism positions such that the ADC always correctly tracked the parallactic angle.

2.3 Software Architecture

The software architecture and automation of Robo-AO was designed and led by Reed Riddle (Riddle et al., 2012). It currently consists of more than 120,000 lines of documented code. The entire software is written in C++ over a Linux Fedora 13 operating system (non-real time) for easy portability. Some of the housekeeping tasks (compressing and archiving data, telemetry) are performed with custom `bash` scripts.

The overarching goal behind the Robo-AO software was to ensure easy portability to different operating setups or hardware (if another group decides to, say, use a different deformable mirror or a different camera) and easy reconfiguration for retuning and observing in different modes. To achieve this goal, the Robo-AO software consists of many different daemons (modules), each of which performs an independent task. The daemons interact through TCP/IP sockets which allow for the daemons to be run on different machines, although the entire computational load of Robo-AO is easily borne by a single quad-CPU processor machine. Each daemon uses a `bash` style configuration file that allows the user to change almost every possible variable for the daemon.

The overall architecture of the system is shown in Figure 2.25. The `robod` daemon is the main supervisor module that orchestrates the observing program throughout the night. It commands the sub-system daemons (`tcsd`; telescope control, `aosysd`; AO system, `lgsd`; laser guide star etc) to obtain targets, point the telescope, setup cameras, lock AO control loops, and to gather science data. The subsystem daemons are responsible for the minutiae of the operation and only require higher level commands (e.g. `START_AO_LOOP`) to perform all the steps required to fulfill the command. The subsystem daemons then return a status or an error message to inform the supervisor daemon of the result.

Hardware interaction is achieved through a wrapper layer between the device drivers and the daemons. This allows the daemons to maintain a standard interface while the

wrapper isolates the hardware specific commands. Thus, in order to use a different camera or actuator unit, the only section of the code that needs to be replaced is the wrapper layer.

Each daemon has multiple threads running in parallel, including error, status, and logging threads. The error thread is responsible for detecting and attempting to correct error conditions. Setting up the error conditions and the error handling functions is the biggest task for the automation of the system.

The status thread monitors the status of the daemon (`initialized, running, stopped` etc) and reports to the supervising daemons whenever the status is requested. The logging thread logs the command, warning, and error messages that were sent to or sent from each daemon into a log file.

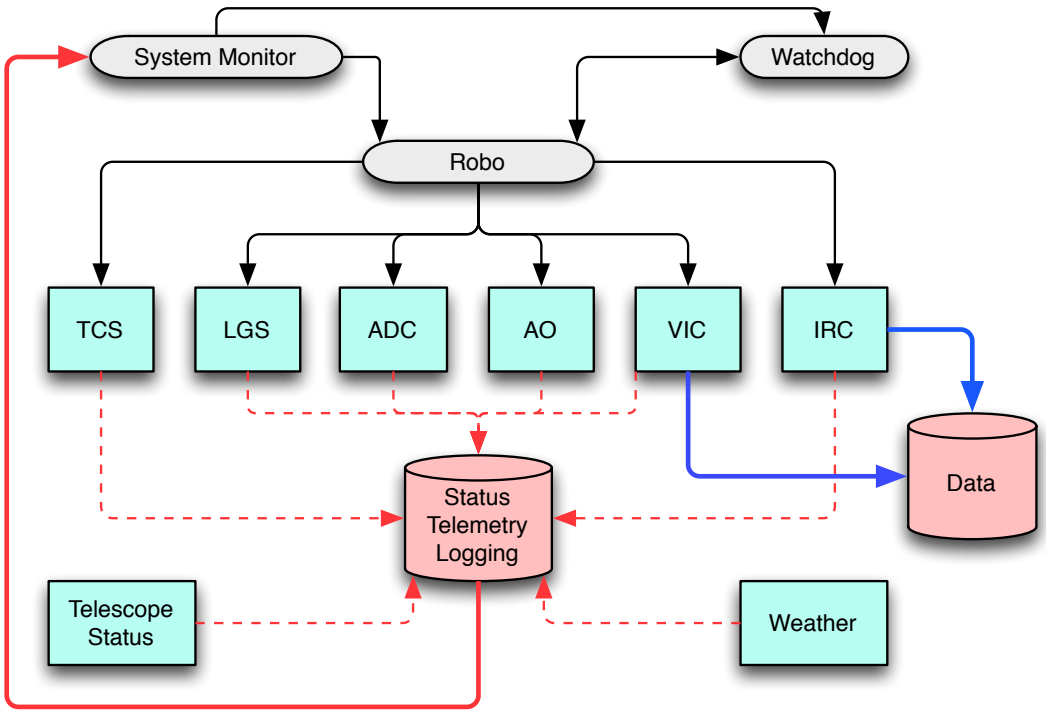

Figure 2.25. The software architecture of Robo-AO. Each hardware device is controlled by a subsystem daemon. Figure 2 from Riddle et al. (2012)

2.3.1 AO Control System

My first assignment on joining the Robo-AO project was to complete a literature survey on AO control systems and create the AO correction algorithm to be implemented in Robo-AO. Appendix C (adapted from an internal report written in April 2010) includes all the details of the implementation of the AO control system.

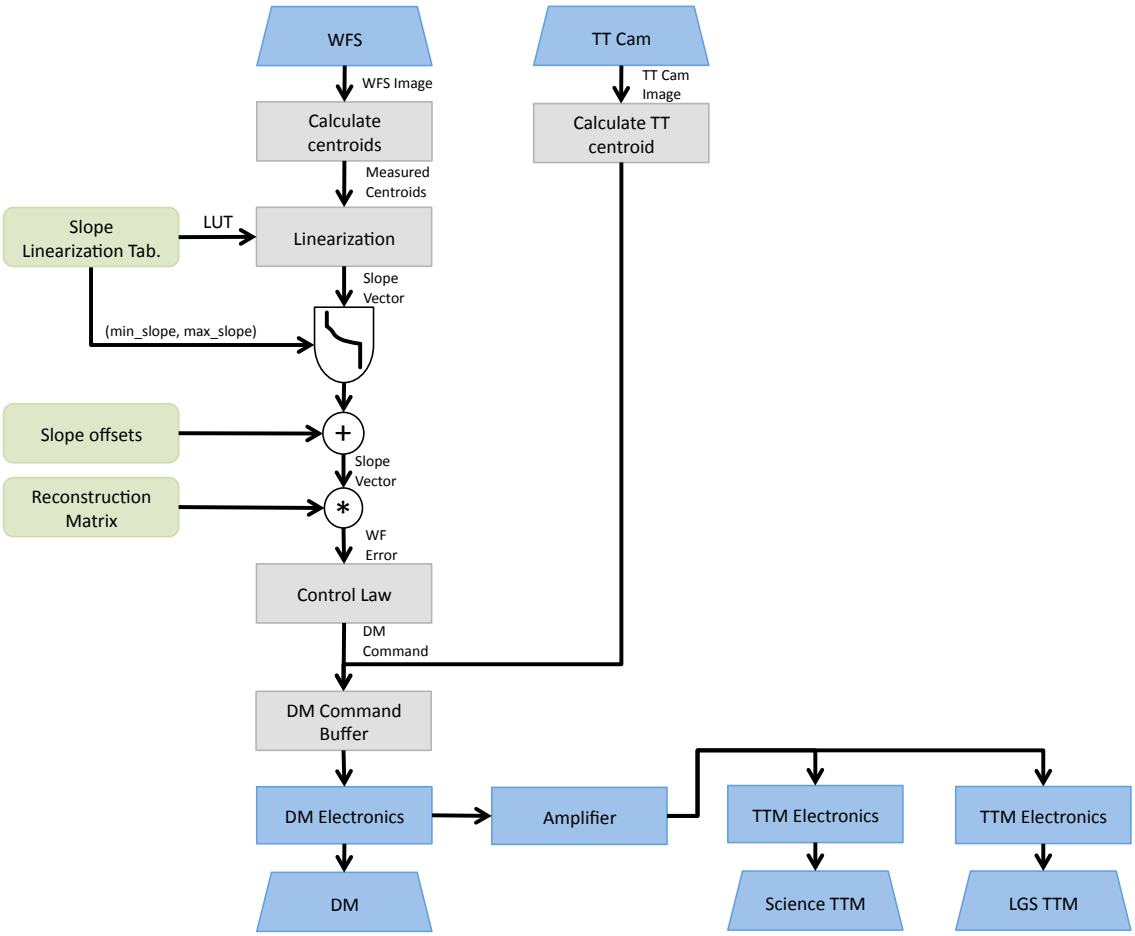

Figure 2.26. The algorithm used for processing input from the WFS sensor in LGS mode operation.

Here, we shall briefly discuss the AO control loop, as shown in Figure 2.26. The AO control loop begins with a single wavefront sensor image. For each of the 97 subapertures in each image, the total intensity of the laser spot is calculated. If the intensity is above a certain threshold, the centroid of the Shack-Hartmann spot within the subaperture (i.e. x and y slope of the local wavefront) is calculated, else the subaperture is flagged as having low light and the centroid position is not calculated. The measured slopes are linearized through a look-up table which accounts for the response of the quad-cell. The fiducial centroid positions (or slope offsets) are subtracted from the measured values, and the final values are arranged into a slope vector with $97 \times 2 = 194$ values. The measured slopes are multiplied with a reconstructor matrix, which creates a least-squares estimate of the wavefront shape as projected on the 120 deformable mirror actuators and the laser uplink tip-tilt estimate. The estimate of the wavefront error is applied to the deformable mirror through an integral control law with a small leak term that allows the deformable mirror to gracefully tend to a flat position if no slopes can be measured (in low light conditions).

The AO control loop has been demonstrated to run as fast as 1.5 kHz. However, the best operating rate to balance our error sources is 1.2 kHz, which is now the standard rate. At 1.2 kHz, the wavefront sensor integrates $8 - 9$ pulses from the laser beacon (operating at 10 kHz) before the frame is read out and processed. As we will discuss in Chapter 3, this bandwidth is sufficient to account for most of the higher order wavefront errors.

2.4 Robo-AO Operations

At present, Robo-AO is not a facility instrument. The default instrument on the P60 is the GRB camera setup by Cenko et al. (2006), which is used as a queue scheduled robotic telescope. To minimize instrument changes (and the requisite telescope balancing), Robo-AO is installed on the telescope for long observing runs, usually seven to ten nights. The installation and removal of Robo-AO (Cassegrain instrument and electronics rack) is now conducted almost entirely by the Palomar observatory staff (three members) with one Robo-AO team member available for help and for cabling the instrument. The setup/removal procedure is now in the process of being completely documented, such that the observatory staff can take charge of the setup.

Although Robo-AO science observations are now completely automated, some maintenance and pre-run calibrations are required before operating Robo-AO on sky. Most of the AO system calibration and tuning is performed once at the beginning of each observing run, unless a drastic temperature change occurs during the run. A pre-run checklist has been included in the Robo-AO instrument alignment guide in order to guide users through the procedure.

2.4.1 Setup and Calibration

The pre-run setup and calibrations required are:

- **Laser Clearance:**

- **Priming of Cooling Lines:** The laser chiller and the heat exchanger are placed in the P60 data room (about 20 to 25 feet below the laser head) and the hoses connecting the laser to the chiller and the electronics rack to the heat exchanger are disconnected at each run. When reconnected, any residual air bubbles occurring in the system must be flushed using a priming pump on each segment of the plumbing. Without this precaution, the bubbles migrate upward and settle at the laser head, preventing cooling of the laser diodes.

- **Checking Internal Alignment:** At the beginning of each run, the internal alignment (registration) of the deformable mirror, the field stop, and the wavefront sensor are checked. This ensures that the reconstruction from measured slopes to deformable mirror commands is accurate.

  With the deformable mirror at a flat position and using the internal UV source with a large (1 mm diameter) fiber, the alignment of the field stop is checked. The edges of the fiber spots should not overflow the corresponding subaperture boundaries into the neighboring subapertures. The size and position of the field stop is adjusted till the image spot size and position is satisfactory. Then the 1 mm diameter fiber is replaced with a 0.1 mm fiber and again UV fiber source is finely adjusted till the tip-tilt measurements on the wavefront sensor are zeroed (with live feedback from custom `LabView` software).

  To check the registration of the deformable mirror with the wavefront sensor, a pattern is applied to the deformable mirror that pulls in the four central and four corner actuators on the deformable mirror over an overall flat shape. These create small slope changes on the wavefront sensor that are checked for symmetry. The symmetrical locations imply that the actuators are registered at the corners of the subapertures. The wavefront sensor lens L1 and L2 are adjusted till the pattern is correctly aligned on the wavefront sensor.

- **Renewing Slope Offset Files:** After checking the alignment, the wavefront sensor slope fiducial ('zero') measurements are recorded as the slope offset files. These are subtracted from the measured slope values to estimate the actual slope variations.

  The slope linearization file[7] is set to use the linearization table for a flat-topped circular spot expected from the fiber instead of the Gaussian profile expected from an on-sky source. Using the flat shape on the deformable mirror, with the scalar gain of the AO system set to zero and the leak constant of the control law set to unity (such that no correction is applied to the deformable mirror), the AO system is run and slope telemetry is recorded. A `MATLAB` script converts the average slopes measured in the telemetry to appropriately formatted slope offset files that are used during the observing run.

[7] The relation of the spot centroid measured in the subaperture to the actual movement of the spot is non-linear and dependent on the spot shape, pixel size etc. We use pre-calculated look-up tables to linearize the centroid measurement. Two separate tables are used for the different profiles expected from the fiber source and the on-sky laser spot.

- **Adjusting Laser Focus:** Since the laser projector is continuously mounted on the telescope, it is subject to much larger temperature fluctuations and gravity flexing than the Robo-AO Cassegrain optics that are stored in the data room when not mounted on the telescope. Hence, it is important to refocus the laser projector to create a sharp focus at the beacon altitude of 10 km. This procedure should also be repeated if drastic temperature fluctuations ($\gtrsim$5°C) occur during an observing run.

  After ensuring that the telescope and the outside air have similar temperatures, the telescope is first focused on a natural star using an automated focusing loop. One may attempt to run the AO system if the laser projector focus is sufficiently close to the optimum value. If the AO system works, a finer estimate of focus can be obtained. After the telescope is suitably focused, the laser return images are observed on the wavefront sensor camera (read out in the full 80×80 pixel mode). The focus of the laser projector is adjusted using an internal translation stage till the spots are sharpest and their intensity is maximized. If the natural seeing is high ($\gtrsim$1.5″), it is extremely difficult to optimize the focus since the laser spots can almost fill up the field of view of the wavefront sensor subapertures.

- **Telescope Focusing:** At the beginning of each observing night, the telescope is focused with an automated focusing routine (written by Kristina Hogstrom). A reasonably bright star near the zenith is selected and the telescope focus distance is stepped through, and images are acquired at each focus value. A interpolated focus value that would provide the smallest FWHM is selected.

  Through the night, as the AO system is operated, a running average of the focus mode measured by the wavefront sensor is calculated and displayed in the telemetry. In July 2013, an automated offload of the wavefront sensor focus measurements to the telescope focusing has been implemented.

- **Flats and Biases:** The Andor EMCCD camera has negligible dark current, but the bias values are not flat over the entire chip. The bias values also vary over different values of the electron-multiplying gains. Biases frames are acquired in each observing mode in the evening before observations.

  Flat frames are also acquired in each filter in the evening before the observations. In order to collect sufficient photons on the 0.043″square pixels[8] in a reasonable amount of time, Robo-AO uses an industrial halogen floor lamp to illuminate the dome screen over which flats are acquired.

2.4.2 Monitoring

Once the setup and calibration is completed and the target lists are uploaded to the queue scheduler, Robo-AO can operate without human intervention unless a rare unrecoverable error occurs. Robo-AO is intended to be remotely monitored over the internet through a status website.

[8] As compared to the 0.378″pixels of the GRB camera, the pixels are 70 times smaller in area.

In regular operation, the Robo-AO control software writes a status file for each subsystem every second with information about internal workings of the daemons. `python` and `php` scripts continuously convert these status files to images and data tables that are served over the Robo-AO website.

Figure 2.27 shows the complete three window setup for monitoring Robo-AO. The left-most panel shows the shape of the deformable mirror (orange circle; left top in the panel), the wavefront sensor image (gray annulus; right top in the panel), and the visible camera image (bottom image in the panel). The deformable mirror image is coded to alert the user with bright colors if the deformable mirror actuators are hitting or are close to hitting the maximum or minimum allowed values. The central panel is an `SSH` window with color-coded logs of the Robo-AO software. The terminal alerts the user with red text and sounds if errors are encountered. The right-most panel is the Robo-AO status webpage. It serves status data from all daemons as data tables. Each value is color-coded to allow the user to check the status at a glance. Green boxes are the normal operating range, yellow is a warning color, and red shows values that are outside operational ranges.

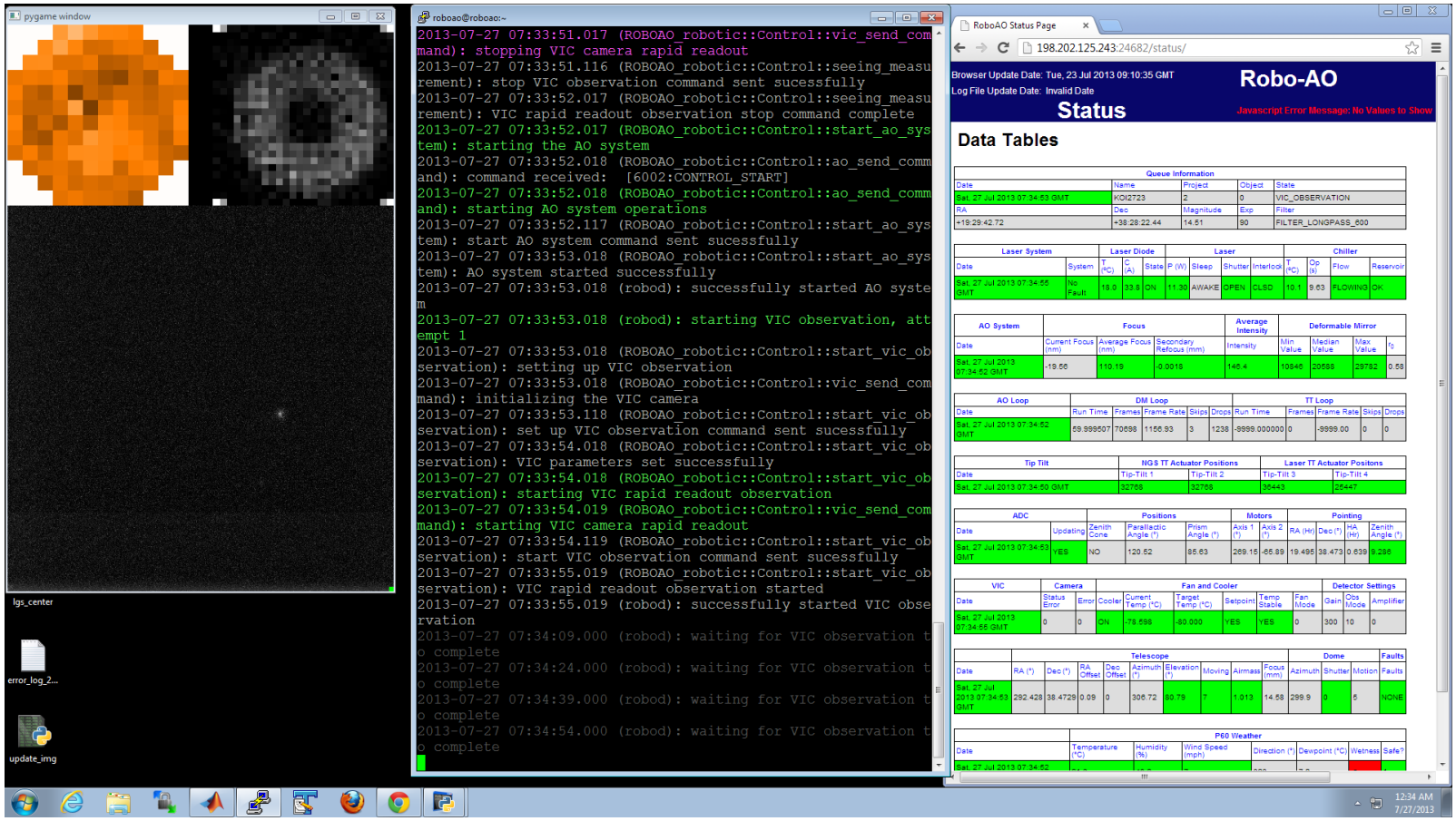

Figure 2.27. Robo-AO is monitored via telemetry and logging data created by the daemons. The left-most panel shows the shape of the deformable mirror (orange circle; left top in the panel), the wavefront sensor image (gray annulus; right top in the panel), and the visible camera image (bottom image in the panel). The deformable mirror image is coded to alert the user with bright colors if the deformable mirror actuators are hitting or are close to hitting the maximum or minimum allowed values. The central panel is an `SSH` window with color-coded logs of the Robo-AO software. The terminal alerts the user with red text and sounds if errors are encountered. The right-most panel is the Robo-AO status webpage. It serves status data from all daemons as data tables. Each value is color-coded to allow the user to check the status at a glance. Green boxes are the normal operating range, yellow is a warning color, and red shows values that are outside operational ranges.

Chapter 3

Characterization of Robo-AO Performance

3.1 Introduction

Since the beginning of Robo-AO science operations at Palomar in June 2012, we have continued to tweak the instrument to perform better and faster. During the observations, we collected telemetry and performance data that allows us to understand the capabilities of Robo-AO and the behavior of the atmosphere at Palomar.

In this chapter, we shall discuss how well Robo-AO performs under different observing conditions. First, we will briefly discuss primary instrument characteristics such as throughput, platescale, and distortion. Next, we shall discuss AO performance and an year-long characterization of the atmospheric conditions at the Palomar 60-inch telescope.

3.2 Basic Characterization

When any instrument is installed on a telescope, one worries about two main things: how much of the infalling light goes through to the detector (the 'throughput'), and how accurately does the light arrive at the destination it was intended to reach (the 'distortion').

3.2.1 Throughput and Zero-points

Because an AO system has far more components than the non-AO instrument, the throughput of the system is lowered by the sheer number of reflections light goes through before hitting the detector[1]. When Robo-AO was being assembled, I measured the reflectivities and throughputs of individual optics components to ensure that the throughput was within the error budget.

To measure the on-sky throughput and zero-points of Robo-AO, I used images of bright ($V \approx 12-13$) single targets from April 22, 2013 (except for the g' filter images, which were acquired on April 20). The nights were chosen because the sky was very clear and near-photometric quality. I gathered BVR_cI_c magnitudes of the targets from the `SIMBAD`

[1] Of course an AO system compensates for the loss by concentrating the light, thus improving the detection limit for background limited objects.

Table 3.1. Robo-AO zero-points in SDSS g',r',i' and z' filters.

Filter	ZP (mag)	E	Scatter (mag)	Date YYYY-MM-DD
SDSS g'	19.2	-0.0343	0.2	2013-01-20
SDSS r'	19.2	-0.4462	0.05	2013-04-22
SDSS i'	18.8	-0.0983	0.04	2013-04-22
SDSS z'	19.5	-1.4958	0.11	2013-04-22

database and converted them to SDSS g', r', i' and z' magnitudes through the transformations defined for all stars with $R_c - I_c < 1.15$ in Table 1 of Jester et al. (2005):

$$\begin{aligned} & \text{Transformation} && \text{Residual(mag)} \\ u - g &= 1.28 * (U - B) + 1.13 && 0.06 \\ g - r &= 1.02 * (B - V) - 0.22 && 0.04 \\ r - i &= 0.91 * (R_c - I_c) - 0.20 && 0.03 \\ r - z &= 1.72 * (R_c - I_c) - 0.41 && 0.03 \\ g &= V + 0.60 * (B - V) - 0.12 && 0.02 \\ r &= V - 0.42 * (B - V) + 0.11 && 0.03 \\ \\ \Longrightarrow i &= r - 0.91 * (R_c - I_c) + 0.20 \\ \Longrightarrow z &= r - 1.72 * (R_c - I_c) + 0.41 \end{aligned} \tag{3.1}$$

I used the Aperture Photometry tool (Laher et al., 2012) on reduced images to extract the flux from an extraction radius of $2''$ (90 pixels). The inner and outer radii for the background annulus were 110 and 130 pixels respectively. The Robo-AO pipeline averages the flux in each frame of the image (acquired at 8.9 Hz), hence these were the counts gathered in 0.112 s. I calculated the zero-point (ZP) and the extinction (E) by fitting the known magnitudes of the stars, the flux F, the electron-multiplication gain (G), and the airmass ζ with Equation 3.2. Table 3.1 lists the results of the data fitting.

$$\text{mag} = -2.5 \times \log_{10}\left(\frac{F}{G}\right) + \text{ZP} + E * \zeta \tag{3.2}$$

One caveat that must be mentioned is that the electronic gain value I used is pre-calibrated value setup in software. While this is sufficient for our purposes, the gain of the detector chip degrades with time and must be recalibrated through an internal procedure. The recalibration was last performed in July 2013, after these measurements were made.

Table 3.2. Distortion solution for Robo-AO.

Variable	α	β
1	0.4000(8)	0.3880(7)
2	−0.1719(0)	0.1771(4)
3	4.9(9)E−6	−1.0(9)E−5
4	−(5)E−8	1.0(0)E−7
5	4.9(4)E−6	−1.0(4)E−5

3.2.2 Distortion

Sergi Hildebrandt compared Robo-AO i' band images of the globular cluster M15 acquired by Robo-AO in May 2012 and reduced by myself to Hubble Space Telescope (HST) images of the same field. The HST images had been de-distorted through the HST data reduction and drizzling pipeline. 207 stars cross-matched between the Robo-AO image and the HST image were used to calculate the distortion of the Robo-AO image.

After careful centroiding of matched star positions, a quadratic distortion model was fit to the two sets of data. The HST coordinates $(\Delta X, \Delta Y)$ were written in terms of the Robo-AO coordinates $(\Delta x, \Delta y)$ as

$$\Delta X = \alpha_1 \Delta x + \alpha_2 \Delta y + \alpha_3 \Delta x^2 + 2\alpha_4 \Delta x \Delta y + \alpha_5 \Delta y^2 \quad (3.3)$$

$$\Delta Y = \beta_1 \Delta y + \beta_2 \Delta x + \beta_3 \Delta x^2 + 2\beta_4 \Delta x \Delta y + \beta_5 \Delta y^2 \quad (3.4)$$

$$(3.5)$$

The best fit values calculated by fitting the data with a Levenberg-Marquardt procedure are shown in Table 3.2. Figure 3.1 shows the star positions from Robo-AO(green plus) overlayed on the HST measurements (blue diamonds) after the distortion solution has been applied. From these, we get the platescale to be 43.102 ± 0.005 milli-arcsecond pix^{-1}. There is a small ($\approx$1 %) but statistically significant asymmetry in the x and y axis. The effect of the second-order terms is about 0.01 milli-arcsecond pix^{-1} at the edges of the images. The orientation of the Robo-AO camera is shown in Figure 3.2.

3.3 AO Performance

Before we discuss how well Robo-AO corrects the atmospheric turbulence, it would be wise to discuss the metrics used to characterize the performance of an optical system.

3.3.1 Metrics of AO Performance

There are metrics of the performance of an optical system which encompass different characteristics of the image. The wavefront error (WFE) and Strehl ratio ($\mathcal{S}$) are used most by optical engineers, while astronomers prefer to discuss the full-width at half maxima

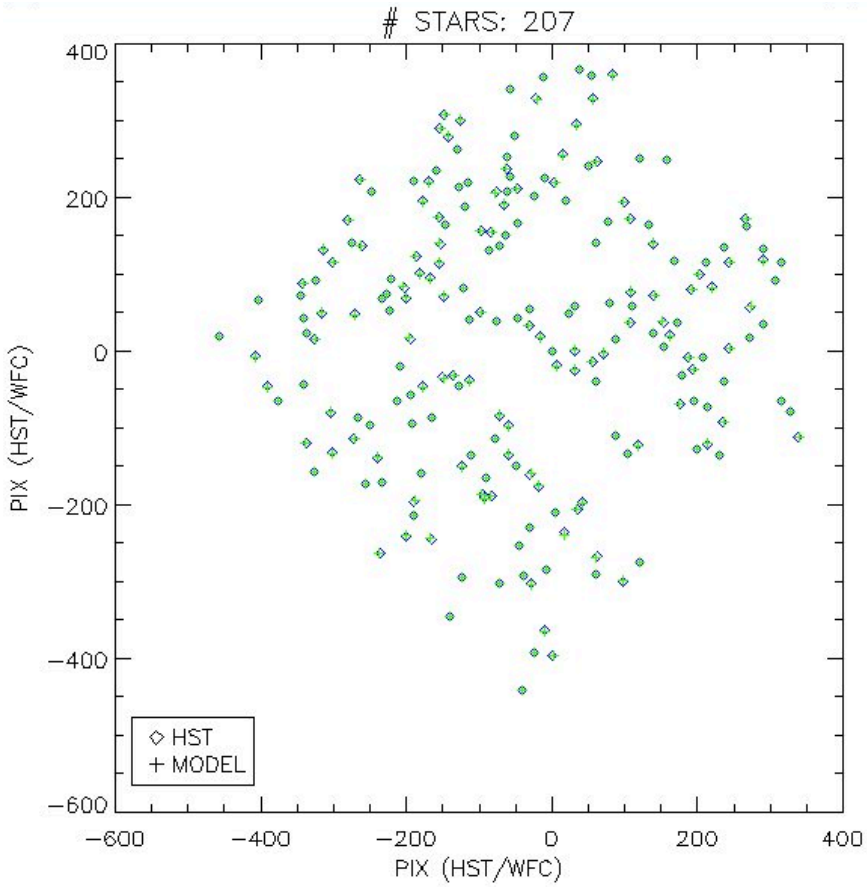

Figure 3.1. The Robo-AO star positions, corrected for distortion according to the model given in Table 3.2, is plotted in green + markers. The HST positions for all the stars are overlaid with blue diamonds. Figure created by S. Hildebrandt.

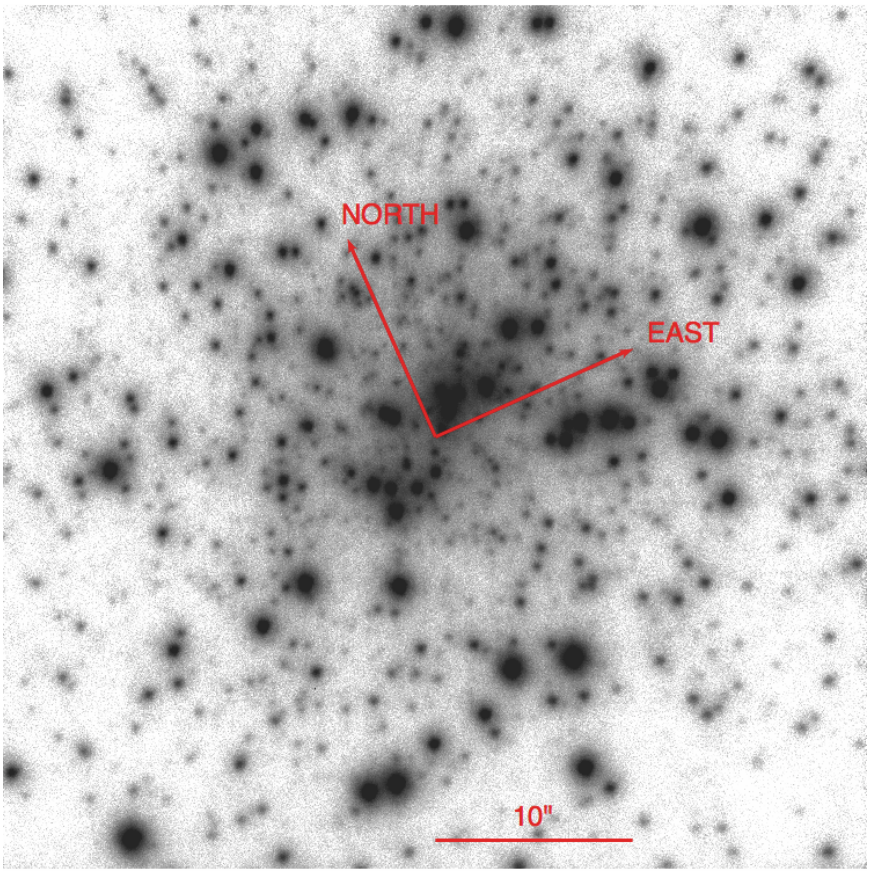

Figure 3.2. Orientation of the Robo-AO image. As compared to the usual right-handed rule of astronomical images, Robo-AO images are flipped in the East-West direction and the North vector is aligned 23.9° counterclockwise from the y axis of the detector. The platescale, as shown by the scale bar, is 43.1002 milli-arcsecond pix^{-1}. This corresponds to a field of view of $44.14'' \times 44.14''$.

(FWHM) and the contrast curve achieved.

Wavefront Error Wavefront Error (WFE) is the most fundamental measure of the performance of an optical system. It is a measure of the deviation of the wavefront at the aperture from an idealized flat wavefront. The root-mean-square (RMS) deviation averaged over the entire aperture is the metric quoted. WFE is usually quoted in units of length, conventionally nm or Å, since it is usually achromatic. Its effects on image formation are, however, wavelength dependent and are usually proportional to the phase, i.e. $2\pi\sigma_{\mathrm{WFE}}/\lambda$ where σ_{WFE} is the RMS WFE.

Strehl Ratio The Strehl ratio (or just Strehl) is analogue to WFE in the image plane. It is defined as the ratio of the peak intensity in the image plane to the peak intensity that could be achieved by a diffraction limited system (i.e. when $\sigma_{\mathrm{WFE}} = 0$). For wavefronts that are reasonably close to flat, the Strehl ratio is related to WFE by

$$\mathcal{S} = \exp(-\sigma^2), \tag{3.6}$$

where $\sigma = 2\pi\sigma_{\mathrm{WFE}}/\lambda$ is the WFE in units of phase (Mahajan, 1983). It is obvious that the Strehl ratio is extremely sensitive to wavelength, and to achieve the same Strehl value at smaller wavelengths requires far better wavefront correction. Hence it is significantly easier to perform adaptive optics corrections at IR wavelengths than at visible wavelengths.

The Strehl ratio is a useful metric for performance when either the image is close to the diffraction limit, or the distribution of WFE is Gaussian (as proved by Ross, 2009). In the cases where the errors are large (seeing-limited observations) and/or dominated by specific Zernike modes (e.g. static errors), the Strehl ratio is of limited utility for understanding the system. When the Strehl ratio is below 10 %, the estimate of σ can have as much as 10 % systematic errors. If many different abberations contribute to WFE in a balanced manner, the systematic error is reduced. However, if the wavefront error is dominated by a single mode, especially spherical abberation for annular pupils, the systematic error can be as much as 30 % (Mahajan, 1983). Since Robo-AO operates in a low Strehl regime ($\mathcal{S} < 15\,\%$) for most of the visible bands, these errors become extremely relevant. However, the definition of Strehl reduces the measured wavefront error since:

$$\Delta\mathrm{WFE} = \frac{\Delta\mathcal{S}}{2\,\mathcal{S}\,\mathrm{WFE}}. \tag{3.7}$$

FWHM The full-width at half-maximum (FWHM) is a standard measure of the width of any distribution or the size of an object in an image. As the name suggests, it is the width of the image at half the peak intensity (after the background is subtracted). The FWHM achieved by an AO system cannot be exactly related to the WFE, or the Strehl ratio since it depends on the spatial distribution of the WFE.

Contrast Curve The contrast curve achieved by an AO system defines the brightness of an star that can be detected beside a brighter neighbor at a certain separation. A one-dimensional contrast curve is calculated by calculating the variance of the intensities in

pixels at a given radius from the primary star. This assumes that a circularly symmetric PSF is expected from the optical system, which is reasonably true for Robo-AO[2], but not valid for hexagonal mirrors (Keck) and optimized apodizing coronographs, which achieve high contrast in one quadrant at the expense of contrast in another.

3.4 Robo-AO Performance

3.4.1 How Faint Can Robo-AO Operate?

Because an LGS-AO system depends on a nearby tip-tilt reference star to perform the tip-tilt correction, a crucial question to ask is how faint the star needs to be. The fainter the star, the larger the fraction of the sky that can be covered. The flux of the tip-tilt star needs to allow for accurate centering of the image. Since most AO systems are run at $\sim$1 kHz frame rates, the fluxes are pushed to photon noise limits.

To calculate the tip-tilt correction from the shifting position of the tip-tilt star, one can use either the center-of-light, calculated as a weighted average of the pixel fluxes, or one can convolve the image with the expected PSF and use the peak of the convolution as the position of the tip-tilt star. While the centroid is a robust estimator of the position, it has been shown (See Law et al., 2006, and references therein) that the convolution method is optimal. However, when Robo-AO acquires data on faint stars, the CCD often detects individual photons in frames. Thus for faint stars, the automated Robo-AO data reduction pipeline locks on to photon noise and creates a sharp artificial noise peak in the center of the image as shown in Figure 3.3.

In the course of the performance analysis, I created a pipeline to analyze images and gather together all the relevant parameters in one large database. The parameters created by the pipeline are shown in Table 3.3. All of the images gathered during 2012 and early 2013 in regular observing modes (Modes 6 to 10 of Table 2.1) with a frame rate of 8.9 Hz were analyzed in this pipeline. Separately, another database of seeing measurements was created that analyzed the FWHM of seeing-limited images gathered on target while the AO system was being setup. This database was used in part for the analysis below but majorly for the discussion in Section 3.5.

[2]For the contrast reached by Robo-AO, the diffraction spikes caused by the secondary spider and the scattered light are negligible except for extremely bright stars.

Table 3.3. Robo-AO Image Analysis Database Parameters.

Parameter	Unit	Comment
FILENAME		
OBJECT		
RA	HH:MM:SS.ss	
DEC	DD:MM:SS.ss	
HOURANG	deg	
AZIMUTH	deg	
ELVATION	deg	
AIRMASS		
MAGNITUD	mag	Magnitude (as per targetlist)
UTC	YYYMMDD HH:MM:SS	
UTSHUT	YYYMMDD HH:MM:SS	
END_TIME	YYYMMDD HH:MM:SS	
FOCUSPOS	mm	Telescope focus position
ADC_POS0	deg	Rotation angle of ADC prism 0
ADC_POS1	deg	Rotation angle of ADC prism 1
FILTER		
EXPOSURE	sec	Total exposure time
MODE_NUM		
AMPLIFIR		
EM_GAIN		Electron multiplying gain
OUT_TEMP	°C	
WINDSPD	mph	Wind speed
WINDDIR	deg	
DEWPOINT	°C	
HUMIDITY		
PRESSURE		
LAZRMEAN	counts	Mean intensity of LGS on the WFS
LAZRRMS	counts	RMS of LGS intensity
LAZRMEDN	counts	Mean intensity of LGS
LAZRMAD	counts	Median absolute deviation of LGS intensity
SLPXRMS		RMS of WFS X slopes
SLPXMAD		MAD of WFS X slopes
SLPYRMS		RMS of WFS Y slopes
SLPYMAD		MAD of WFS Y slopes
DIMMMEAN	arcsec	Mean of DIMM seeing[a]
DIMMRMS	arcsec	RMS of DIMM seeing
DIMMMEDN	arcsec	Median of DIMM seeing
DIMMMAD	arcsec	MAD of DIMM seeing
STAR		# star in the given image
NSTARS		Total stars detected
CATFLUX	counts	Flux measured by SExtractor
CATFLAGS		SExtractor detection flags[b]
CENTFLAG		Centroiding flag
XSTAR	pix	
YSTAR	pix	
XCEN	pix	

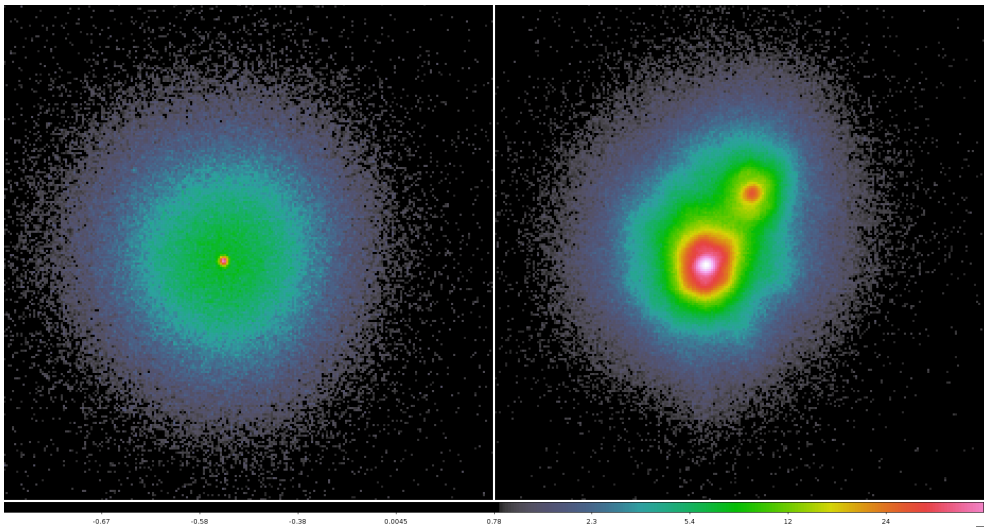

Figure 3.3. *Left Panel*: Robo-AO image of a faint star ($r' \sim 16$ mag) with a sharp noise peak in the center. *Right Panel*: A bright binary star ($r' \sim 12$ mag) observed at almost the same time, and airmass in exactly the same seeing conditions as the left panel image. The image profile has no artificial peak.

Table 3.3

Parameter	Unit	Comment
YCEN	pix	
TOTFLUX	counts	Total flux
FLUXERR	counts	
SNR		
BKGD	counts/pix	
PEAKFLUX	counts	
STREHL		
STREHLERR		
G_FLAG		Gauss profile fitting result (flag)
G_AMP	counts	Gauss profile amplitude
G_XCEN	pix	Gauss profile x center
G_YCEN	pix	Gauss profile y center
G_SMAJ	pix	Gauss profile semi-major axis
G_SMIN	pix	Gauss profile semi-minor axis
G_ELLIP		Gauss profile ellipticity
G_THETA		Gauss profile orientation
M_FLAG		Moffat profile fitting result (flag)
M_AMP	count	Moffat profile amplitude
M_XCEN	pix	Moffat profile x center
M_YCEN	pix	Moffat profile y center
M_SMAJ	pix	Moffat profile semi-major axis
M_SMIN	pix	Moffat profile semi-minor axis
M_ELLIP		Moffat profile ellipticity
M_THETA		Moffat profile orientation
M_BETA		Moffat profile beta

[a]DIMM is the differential image motion monitor. The measurement is described in Section 3.5.3.

[b]All data fields before this one are from either the FITS HEADER keywords or from external programs. The rest are calculated in the fitting pipeline.

To understand the behavior over different stars, I filtered the database using the following cuts to ensure uniformity:

- FILTER = SDSS i'
- $0 <$ TOTFLUX $< 10^7$
- $0 <$ PEAKFLUX < 8000
- $0.09 <$ SLPXRMS < 0.11
- $0.09 <$ SLPYRMS < 0.11
- LAZRMEDN>200

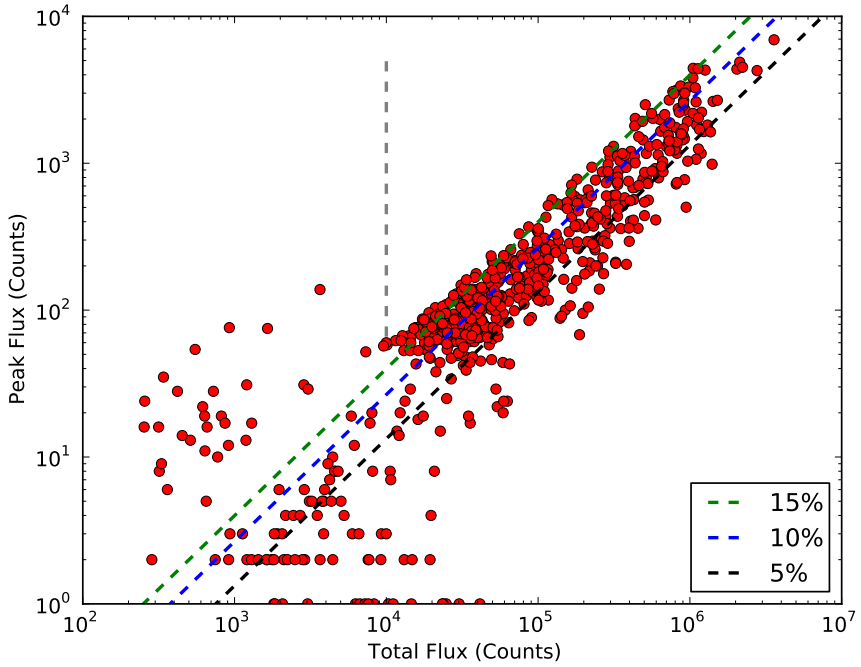

Figure 3.4. The AO performance of Robo-AO as a function of stellar flux is shown. The peak flux (counts) is plotted as a function of the total flux of the star (counts). The green, blue, and black lines are lines of 15 %, 10 %, and 5 % Strehl ratios respectively. The dashed gray line shows the limit below which the shift-and-add pipeline latches onto noise pixels. The data (all Robo-AO observations in 2012) have been filtered for suitable laser flux values, suitable wavefront sensor residuals, and crowding.

Figure 3.4 shows the peak flux (counts) is plotted as a function of the total flux of the star (counts) for over 2000 stars observed in 5 different observing modes. The green, blue, and black lines are lines of 15 %, 10 %, and 5 % Strehl ratios respectively. The dashed gray line shows the flux limit below which the shift-and-add pipeline latches onto noise. The vertical scatter in the data to the right hand side of the plot is due to varying seeing conditions and anisoplanatic errors (as discussed below). Below a limit of about 10^4 counts, the sudden rise in the peak flux is due to the emergence of the noise peak. Using Equation 3.2 and values in Table 3.1, with an `EM_GAIN` of 300 (Mode 10, for the faintest stars), we get a limit of $r' \approx 15.4$ mag on a clear night. To push below this limit, Robo-AO uses a 600 nm longpass filter that effectively combines the r', i', and z' filters. This allows us to push the magnitude limit by 1.2−1.5 magnitudes (especially for very red stars). Apart from this magnitude limit, the Strehl ratio achieved by Robo-AO seems to be independent of the magnitude of the tip-tilt star and influenced more by other environmental factors.

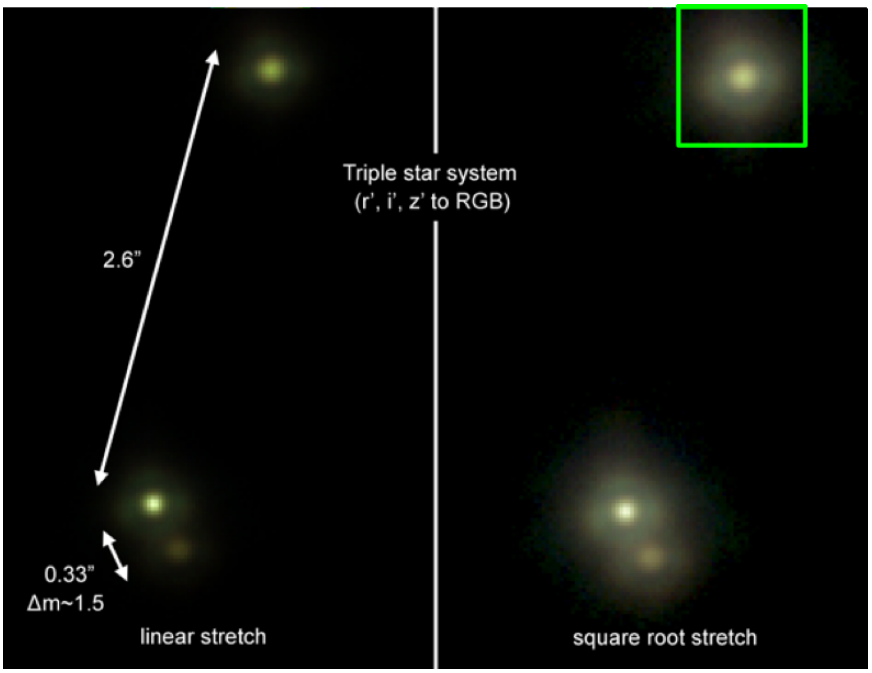

Figure 3.5. A combined multi-filter image of Haro 6-37. The left and right panel images are identical except for scaling. Each image is a combination of the r', i' and z' band images taken in succession. The bright star in the binary pair was used as a tip-tilt guide star. The measurements shown in Figure 3.6 and Figure 3.7 are calculated on the star on the upper right marked by the green square. Combined image created by C. Baranec.

3.4.2 Strehl Ratio and FWHM: Bright Targets

As one can gather from Figure 3.4, Robo-AO regularly delivers images with 15 % Strehl ratios in SDSS i' band. To study a detailed example of Robo-AO performance on a bright star, I present the analysis of Haro 6-37 with a V magnitude of 13.42. Figure 3.5 shows the image of Haro 6-37 acquired on a night with a $1''$ seeing conditions.

Figure 3.6 shows the WFE as a function of wavelength. The colored bands show approximate SDSS g', r', i', and z'band passes. The black contours show Strehl ratios achieved at each wavelength. Figure 3.7 shows the FWHM for Haro 6-37 as a function of wavelength. The lower black line denotes the diffraction limited FWHM expected from a 60-inch telescope.

3.4.2.1 Effect of Airmass

As the telescope observes at higher airmass, the effect of turbulence increases. As we discussed in Section 1.4, the Fried parameter $r_0 \propto \sec\zeta^{-3/5}$ reduces with increasing airmass ($\sec\zeta$) and the wavefront error increases. Figure 3.8 plots all the Strehl ratio achieved in all successful Robo-AO observations as a function of airmass. The datapoints are collated from my analysis pipeline and filtered in a manner similar to Figure 3.4 to reject unsuccessful

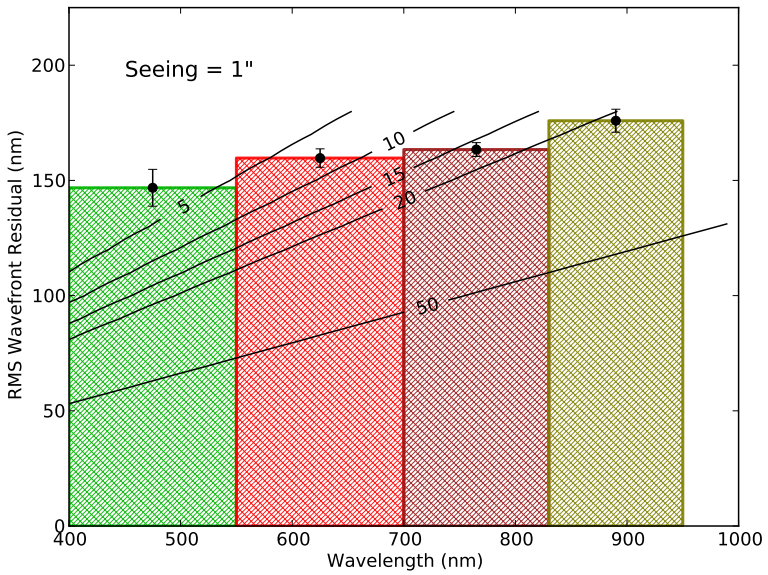

Figure 3.6. Measurement of WFE and Strehl Ratio for Haro 6-37 in different filters. The colored bands show approximate SDSS g', r', i', and z'band passes. The black contours show Strehl ratios achieved at each wavelength.

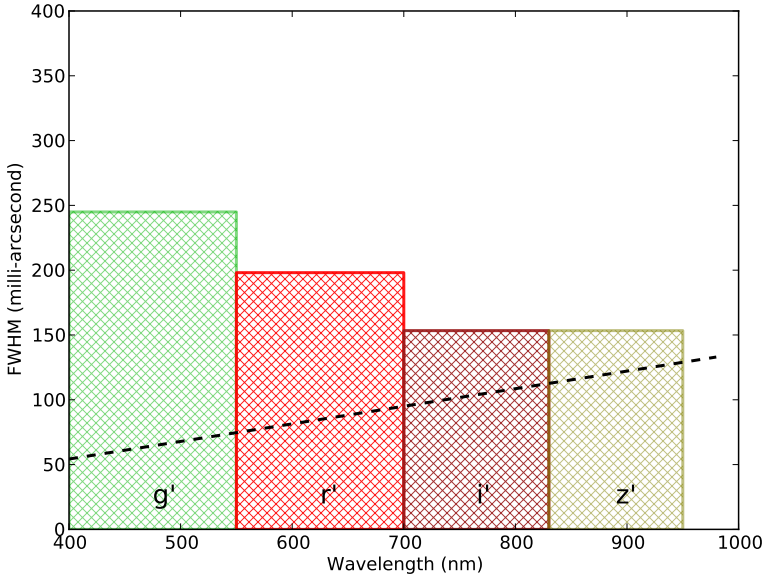

Figure 3.7. Measurement of FWHM for Haro 6-37 in different filters. The lower black line denotes the diffraction limited FWHM expected from a 60-inch telescope.

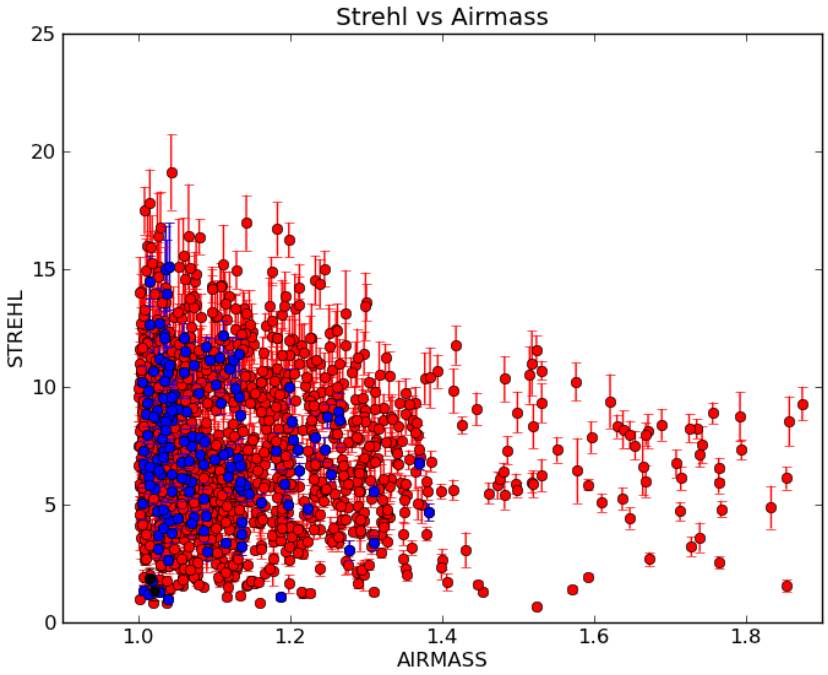

Figure 3.8. The Strehl ratio achieved in z' band (red points), i' (blue points), and r' (black points) is shown as a function of airmass. The data is for successful Robo-AO observations filtered as per Figure 3.4.

observations and analyses.

3.4.3 Contrast Curves

Since Robo-AO's major project is the ultimate binarity survey which aims to detect sub-stellar and low-mass companions around stars, the contrast achieved by the system is of utmost importance. Just as the image profile changes from faint to bright stars, the contrast curve too is significantly different. In Figure 3.9, we show the $5-\sigma$ contrast (i.e. the difference in magnitudes between the primary and a hypothetical companion that could be detected at a $5-\sigma$ significance) as a function of radius from the primary star for two stars observed in SDSS g', r', i', and z' filters. The images were acquired during the same night, with almost the same airmass and seeing conditions as described in the caption. The top panel are the contrast curves for a bright star, T Tau, that does not show a core in any filter but the contrast performance is best at longer wavelengths (z' and i' filters). The plot in the bottom panel shows a significant noise core in the g' and r' bands. It can be seen that a bright tip-tilt star significantly improves the detection contrast.

Figure 3.10 shows the contrast curves achieved for T Tau in different filters and for different frame selection percentages in the Robo-AO data reduction pipeline. The fractions

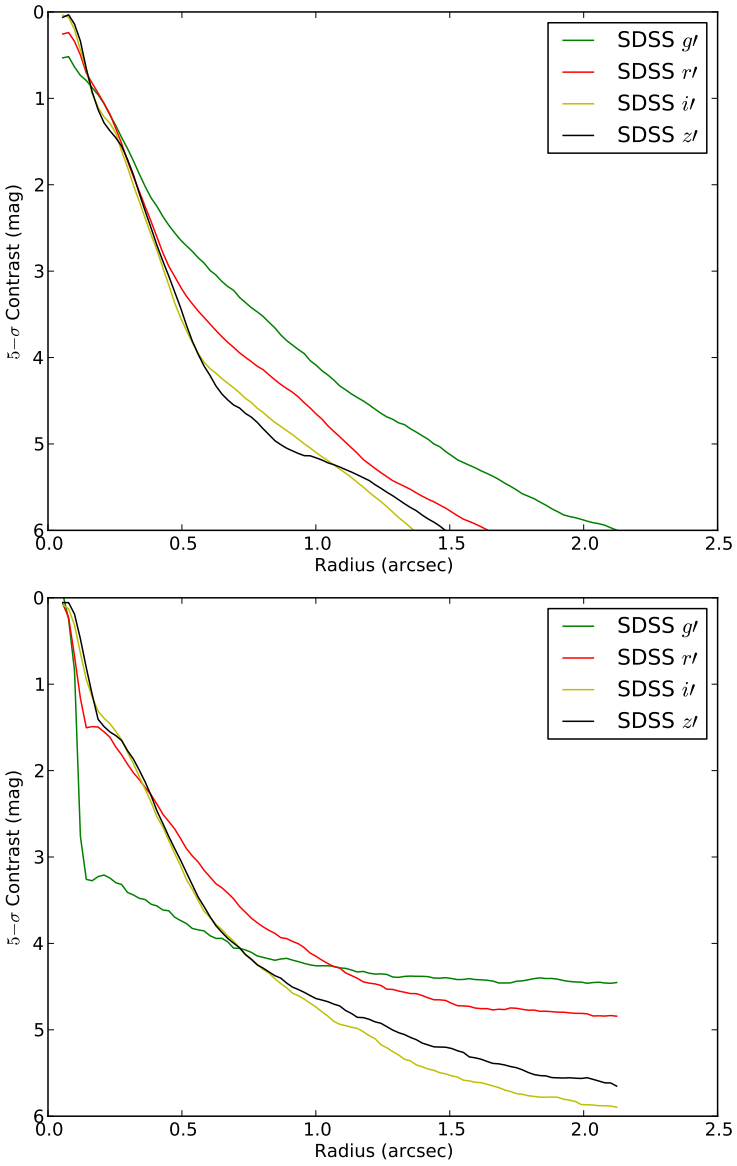

Figure 3.9. *Top Panel*: The contrast curves achieved for the bright star, T Tau, in SDSS g', r', i', and z' filters are plotted. The color coding is as described in the plot legend. *Bottom Panel*: The same contrast curves are plotted for a fainter target, XZ Tau. The target shows a clear noise peak in g' and r' bands. The surprising 'improvement' in contrast inside a radius of 150 mas is due to the noise peak and should be ignored.

refer to the percentage of frames with the best per-frame Strehl used to create the final image. We observe that using up to 50 % of frame selection can slightly improve the contrast. However, any further reduction in the selection fraction drastically increases the photon noise away from the star. The exact cutoff depends on the star and should be determined on an individual basis. For bright stars observed in the i' and z' filters, where the Strehl ratio is high enough that the first Airy ring becomes apparent, frame selection can improve the definition of the Airy ring. However, one must be careful in distinguishing real companions from lobes and speckles caused by static abberations in the AO system that are prevalent in this regime.

3.4.4 Anisoplanatism

Because the atmosphere varies as a function of position and the light from different objects travels via different paths through the atmosphere, the correction applied by the adaptive optics system decorrelates as a function of angular separation between the measurement position and the target position. This is known as the anisoplanatic error, and the angular scale at which this error occurs is known as the 'isoplanatic angle'.

Since the laser corrects the higher order wavefront and the tip-tilt reference star corrects the tip-tilt error, we define two separate sources of anisoplanatic error, the higher order (HO) anisoplanatism and the tip-tilt (TT) anisokinetism. In terms of wavefront error, the errors, to be added in quadrature, are given by

$$\sigma_{\mathrm{HO}} = \left(\frac{\theta_{\mathrm{HO}}}{\theta_{\mathrm{HO},0}}\right)^{5/3}, \tag{3.8}$$

$$\sigma_{\mathrm{TT}} = \left(\frac{\theta_{\mathrm{TT}}}{\theta_{\mathrm{TT},0}}\right)^{2}, \tag{3.9}$$

where $\theta_{\mathrm{HO}}, \theta_{\mathrm{TT}}$ are the angular separations between the target star and the laser position and the target star and the tip-tilt reference as shown in Figure 3.11 and $\theta_{\mathrm{HO},0}, \theta_{\mathrm{TT},0}$ are the isoplanatic angles for the two wavefront errors. If the basic wavefront error is σ_0, then the total wavefront error for the ith star in Figure 3.11 can be described as,

$$\sigma_i^2 = \sigma_0^2 + \left(\frac{\theta_{\mathrm{HO,i}}}{\theta_{\mathrm{HO},0}}\right)^{5/3} + \left(\frac{\theta_{\mathrm{TT,i}}}{\theta_{\mathrm{TT},0}}\right)^{2}. \tag{3.10}$$

If we have more than three stars in the field, we can calculate the three free parameters, σ_0, $\theta_{\mathrm{HO},0}$ and $\theta_{\mathrm{TT},0}$.

It is not possible to measure the Strehl ratio for stars in crowded fields because it is impossible to accurately separate the flux contributions of the target star and the neighboring stars. At the same time, one needs atleast five stars to reasonably estimate the three parameters. I chose fields with a reasonable number of stars, calculated the Strehl ratios and error estimates, and performed a least-squares fit to find the isoplanatic angles. Figure 3.12 shows the contribution of the three error sources for different stars in two images. Table 3.4 shows the anisoplanatic angles for different images and their corresponding environmental

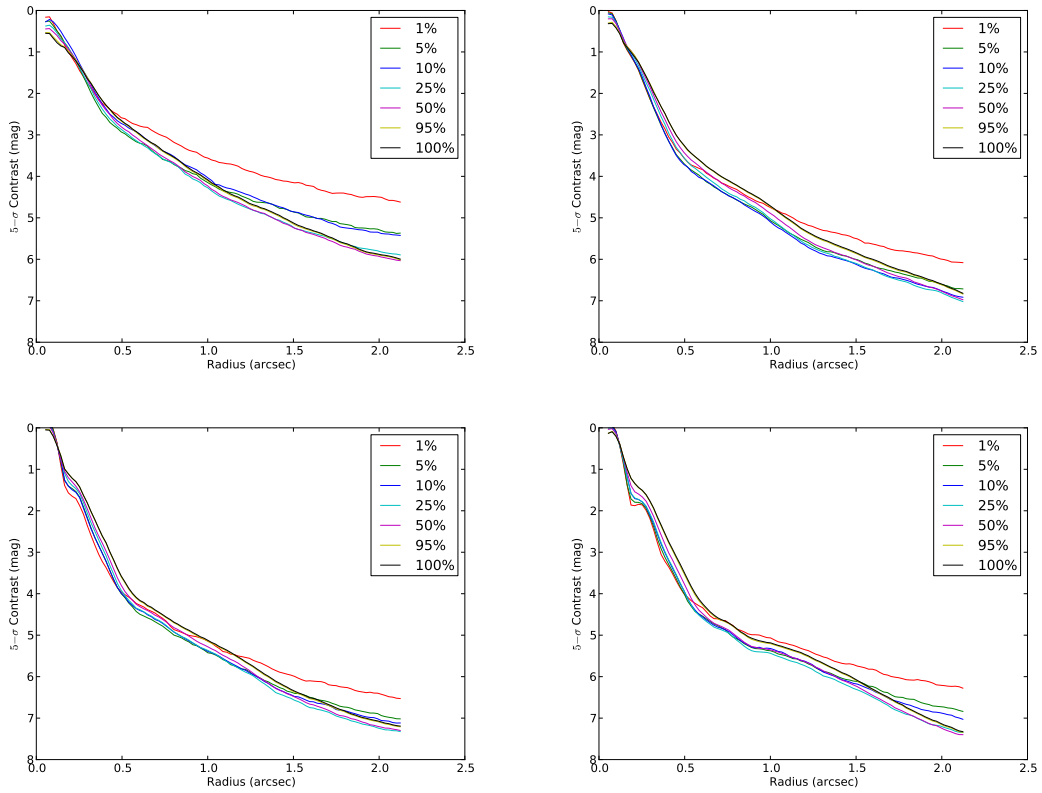

Figure 3.10. The effect of frame selection on the contrast curve of a bright target (T Tau; $V \sim 6$ mag). At the time of acquisition, the target airmass was 1.035 and the seeing was 1.32″. From top left, clockwise, the plots depict the $5-\sigma$ detection contrasts for SDSS g', r', i', and z' filters. In each plot, different color lines are the contrast curve for images constructed with a certain percentage of the best frames from the data cube as shown in the plot legend. We can see that the 1 % frame selection is significantly limited by the background noise outside the core of the image for all filters, with the effect being most severe on the g' band image. The 100 % frame selection leads to a slight reduction in FWHM very close to the core of the image. In all, we can achieve detection contrasts of 4.2, 4.9, 5.2, and 5.4 magnitudes at a separation of 1″ from the primary in the SDSS g', r', i', and z' filters.

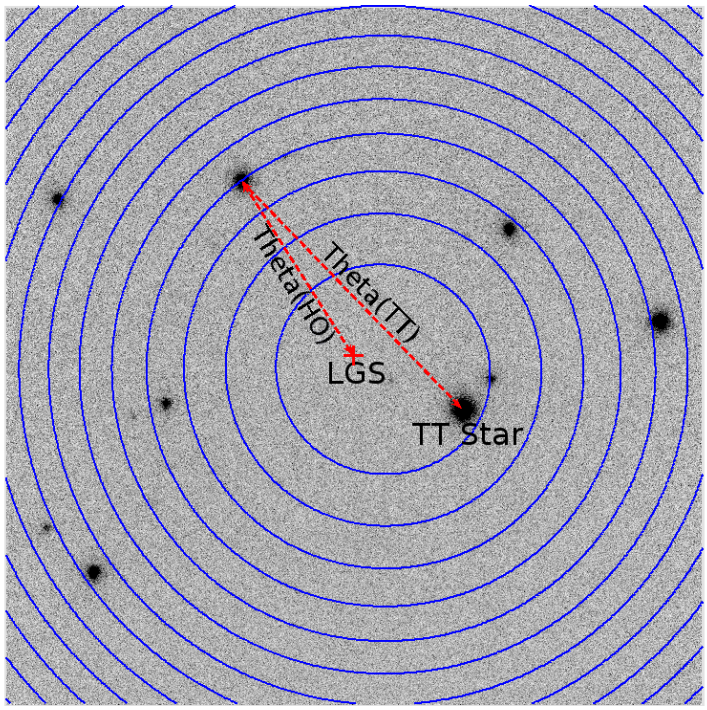

Figure 3.11. Measuring anisoplanatism in the wavefront correction. The laser beacon is internally aligned to the center of the visible camera. The tip-tilt reference, usually the brightest star in the field, may not be at the center. The anisoplanatic error at the target star is a function of the angular separations θ_{HO}; Theta(HO) and θ_{TT}; Theta(TT). The blue contours show lines of constant wavefront error using Equations 3.8 and 3.9.

Table 3.4. Isoplanatic patch measurements with Robo-AO.

	Num Stars	Filter	Airmass	σ_0 (rad)	$\theta_{HO,0}$ (arcsec)	$\theta_{TT,0}$ (arcsec)
1	8	LP600	1.009	1.59	40	62
2	6	LP600	1.075	1.47	37	79
3	8	LP600	1.015	1.50	38	81
4	6	LP600	1.111	1.36	30	78
4	5	LP600	1.119	1.45	63	66

parameters, including the two images analyzed in Figure 3.12.

Although it was not possible to measure the Strehl ratios of stars in globular clusters, I measured the FWHM of stellar images to understand the effect of using a single tip-tilt guide star as opposed to using multiple tip-tilt guide stars. The imaging data of globular cluster M3, shown in the top right panel of Figure 3.13, was reduced using the Robo-AO pipeline with (a) a single tip-tilt guide star (as marked by the red box in the figure) and (b) four well separated tip-tilt guide stars (as marked by the four blue boxes in the figure). The lower panel of Figure 3.13 shows the FWHM of stars as a function of either the distance from the tip-tilt star (red points) or the distance from the centroid of all the tip-tilt stars (blue points). By using multiple tip-tilt stars, one can tradeoff resolution in the center to achieve a more uniform PSF across the image. This is useful for imaging large distributions of stars or for accurate imaging of nebulosity distributed in the entire image.

3.4.5 Tradeoff between Frame-rate and Performance

Robo-AO's visible camera can read out its full 1024 × 1024 CCD at a maximum rate of ∼8 Hz. This is not adequate for sampling and reconstructing the tip-tilt movement of the reference star, leading to some wavefront losses. At the expense of using a smaller FoV, the frame rate can be increased and the performance improved.

In order to test the tradeoff, I experimented with a high frame-rate dataset (50 Hz) acquired on a very bright star (HR 8799; m_V ≈6 mag) such that we were not limited by photon noise in the individual frames. I simulated the measurements at different frame rates by creating image cubes, where each frame consisted of an unshifted addition of certain number of the original image frames obtained at 50 Hz. The new data cubes were then passed through the Robo-AO image reconstruction pipeline and reconstructed in an identical manner. The reconstructed images were analyzed with the Strehl and FWHM analysis code. This star was observed in SDSS i' band during 2.2″ seeing conditions. Science observations were paused because we did not get scientifically useful data.

Figure 3.14 shows the WFE and the FWHM of HR 8799 as recreated from the dataset. As shown in the upper panel, we can reduce the WFE (with 100 % frame usage) by 20 nm by increasing the frame-rate from the full-frame frame-rate of ∼8 Hz to 50 Hz. Alternatively, we can achieve the same gains at the cost of observing efficiency by selecting 50 % of the best

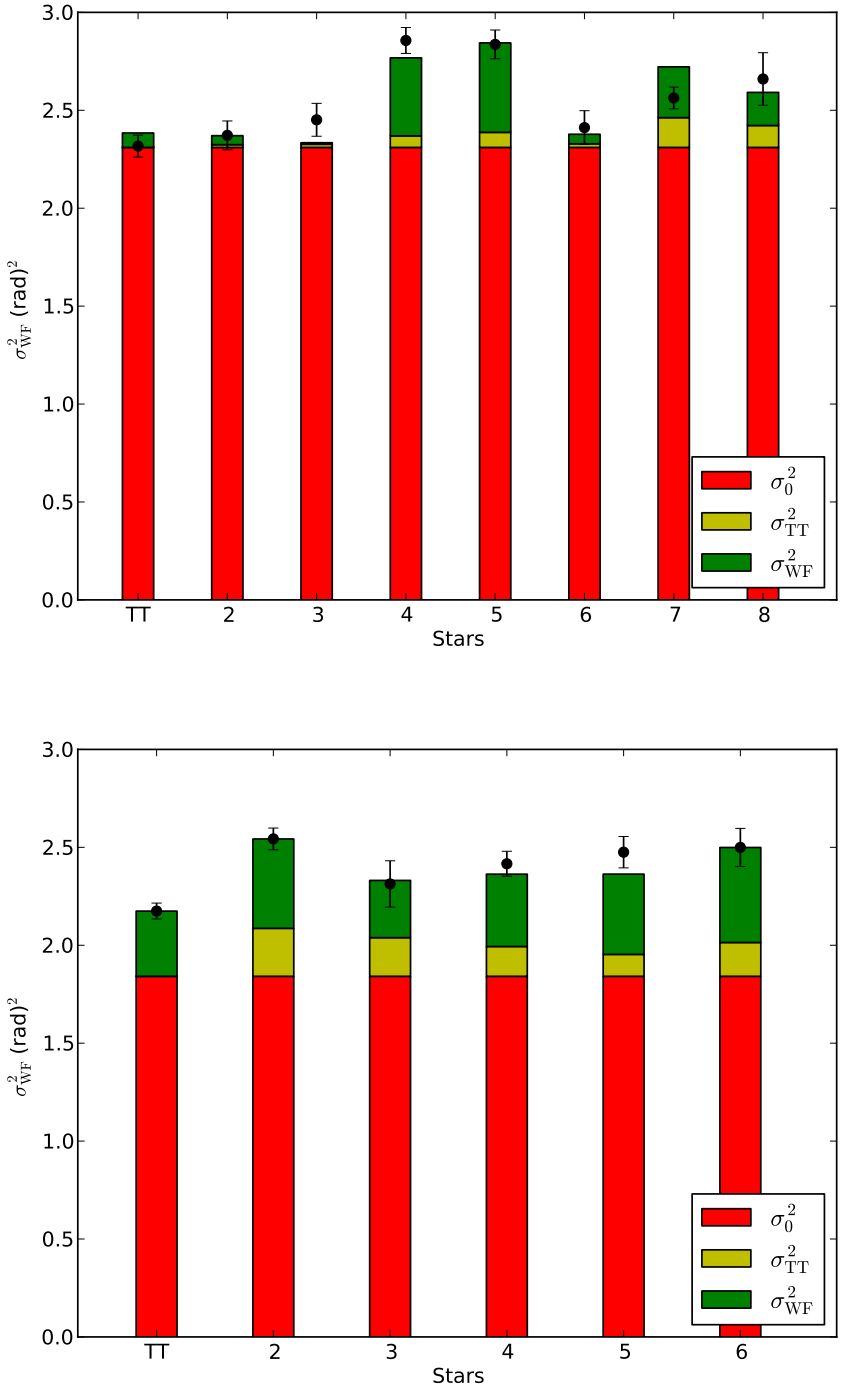

Figure 3.12. Wavefront error contributions for two different observations. Black dots are actual measurements from stars in the field. The star marked TT is the tip-tilt reference. Red bars are intrinsic wavefront error at the center of the field. Yellow bars are the contribution from the tip-tilt anisoplanatism, and green bars are the contribution from the higher order anisoplanatism.

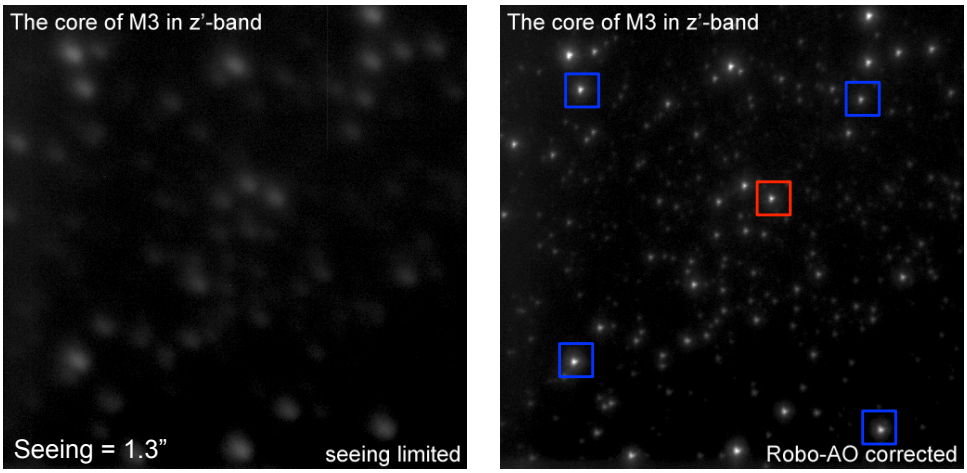

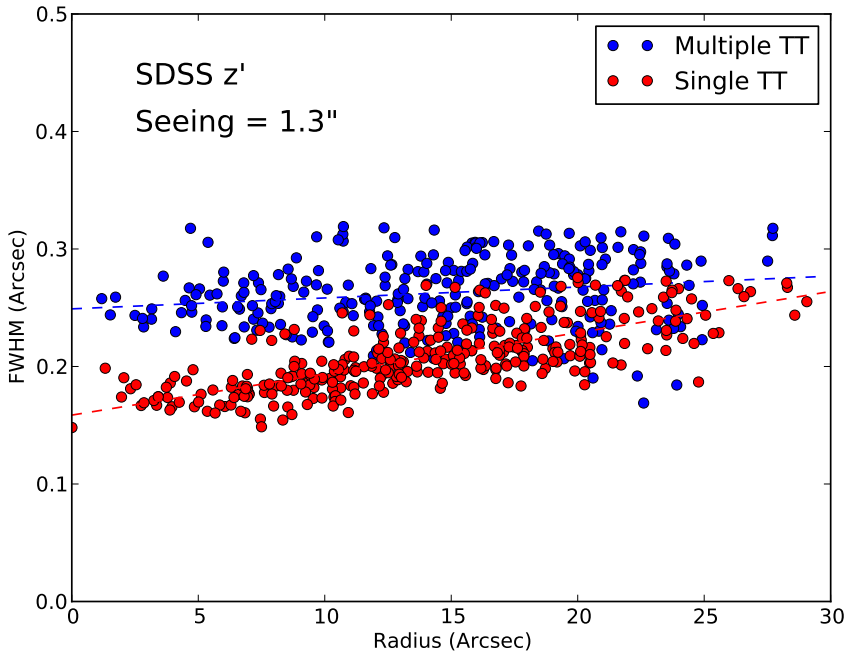

Figure 3.13. Demonstration of the anisoplanatism in Robo-AO images. The FWHM of stars in globular cluster M3 is shown as a function of radial distance from the tip-tilt star (for the single TT case; red dots) and from the mean position of the multiple reference stars (for the multiple TT case; blue dots).

frames. The bottom panel shows the FWHM as a function of frame-rate for 100 %, 50 %, and 10 % frame selection for the same dataset. At the full-frame frame-rate, we achieve an FWHM of $0''.2$ in $2.2''$ seeing conditions and a near diffraction limited FWHM at frame selections below 50 %.

3.4.6 Seeing-Improvement Observing

Another aspect of Robo-AO demonstrated by Figure 3.14 is at the slow imaging regime. We demonstrate that even in $2.2''$ seeing, we can achieve an FWHM of $0''.6$ while performing integrations over 10 s with effectively no tip-tilt correction. This 'seeing-improvement' observing mode, with only the higher order WFE being corrected, is useful for observing faint targets with no nearby star for tip-tilt correction. Along with Robo-AO's handling of laser clearance windows, this gives Robo-AO nearly 100 % sky coverage at any given time.

3.4.7 Time-scales of Turbulence

In order to estimate the timescale of turbulence variations, I calculated the temporal structure function of the wavefront using the high-speed telemetry data. Assuming time stationarity, the structure function is defined as,

$$D_\phi(\tau) = \langle (W(\mathbf{x}, t) - W(\mathbf{x}, t+\tau))^2 \rangle, \tag{3.11}$$

where $W(\mathbf{x}, t)$ is the wavefront as a function of position in the aperture plane and time and the average is over both $\mathbf{x}$ and t. Figure 3.15 shows the structure function calculated for two data sets captured on the night of April 21, 2013 separated by about one hour. We can see that the structure function saturates to its maximum value at about 0.7 s. Therefore, on this particular night, there was no correlation in the turbulence over timescales of a second or more.

In order to check stationarity, I calculated the structure function using cyclic boundary conditions where the arrays were rotated with an offset of τ, and using strict boundary conditions where the arrays were offset by τ, but only the overlapping regions were used to calculate the structure function. The results from both the methods were same within measurement error.

3.4.8 Correction Bandwidth

Although the Robo-AO correction loop runs at a frequency of 1.2 kHz, as with any control system, the actual bandwidth of the correction is lower due to latency in signal processing and inaccuracy in measurement and correction. The frequency at which the control system can still correct effectively is known as the control bandwidth. Control engineers use the 3 dB bandwidth, which is defined as the frequency at which the gain transfer function (i.e. absolute value) of the control system reduces by 3 db. In frequency space, the transfer function $H(f)$ is given as,

$$S_o(f) = ||H(f)||^2 \times S_i(f), \tag{3.12}$$

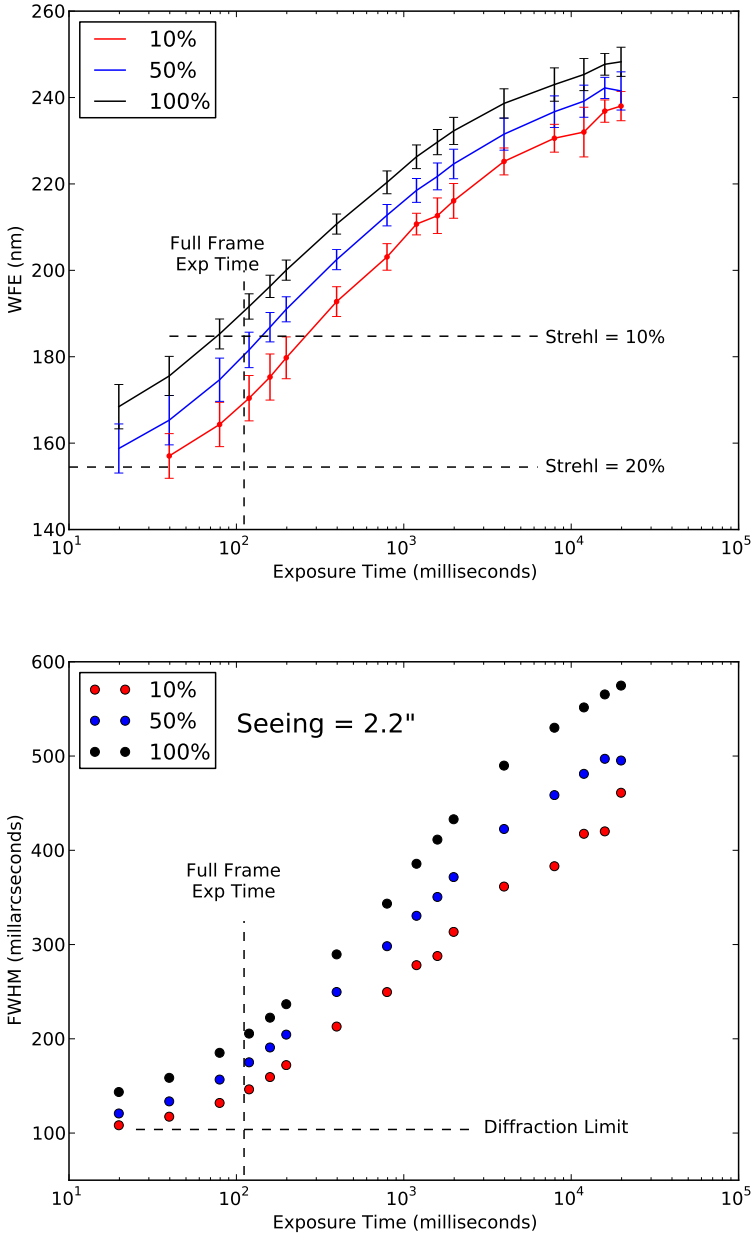

Figure 3.14. The WFE and FWHM as a function of frame-rate for HR 8799.

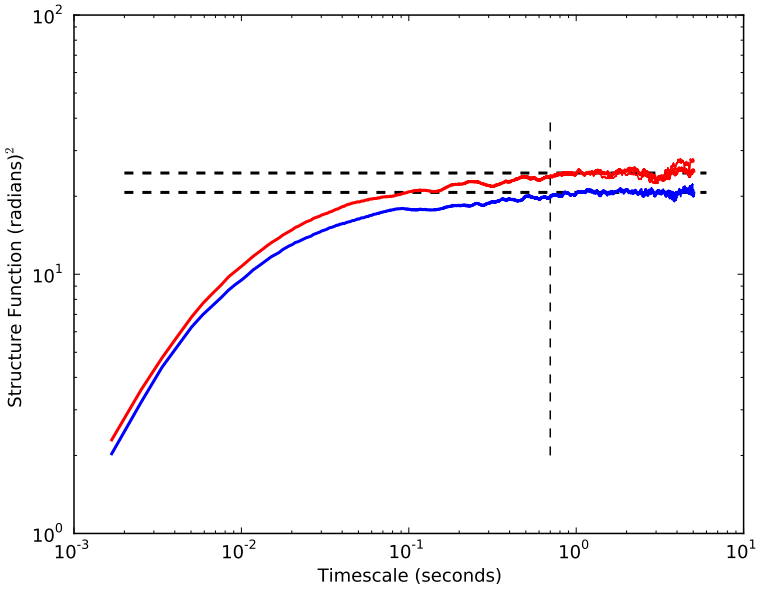

Figure 3.15. The temporal structure function for the wavefront calculated for two datasets captured on the night of April 21, 2013 are shown in red and blue. The dashed horizontal lines mark the average saturation value, calculated by averaging the structure function values between timescales from two to three seconds. The structure function seems to merge into the saturation value at 0.7 s.

where $S_o(f)$ and $S_i(f)$ are the power spectra of the output and input signals, respectively. The input signal, i.e. wavefront error created by the turbulence, has to be reconstructed from the the telemetry as the sum of the deformable mirror shape and the wavefront residual measured by the wavefront sensor. Except for fitting errors in the wavefront sensor and correction errors in the deformable mirror, this provides us with the best estimate of the distorted wavefront as a function of time.

To reduce the effect of the noise, I decomposed the 120 element wavefront measurements into their component Zernike coefficients. Since Robo-AO is constructed with 11 subapertures across the pupil, the reconstructor matrix uses Zernike modes uptil radial order 11. As the Zernike coefficients were calculated by averaging over the entire pupil, the effect of noise in individual elements is very small, especially for the lower order modes.

Figure 3.16 shows the power spectra of Zernike coefficients from $j = 3$ to $j = 26$. The blue lines show the power spectrum of the Zernike coefficients of the wavefront corrected by the deformable mirror while green lines are the power spectrum of the Zernike coefficients of the residual wavefronts measured by the wavefront sensor. Figure 3.17 shows the modulus of the gain function ($|H(f)|$) averaged over several Zernike modes to reduce noise. The 3 dB bandwidth is denoted by the blue dashed vertical line at 203 Hz. The scalar feedback gain of the AO system has been adjusted to achieve a slightly overdamped system and prevent run-away corrections.

3.5 Seeing and Turbulence Profiles at Palomar

The design and operation of an AO system critically depends on the strength and height distribution of turbulence above the telescope. The characterization and monitoring of the seeing and turbulence at an observatory is thus an important activity that supports future instrument development. With 59 nights of seeing limited observations and telemetry from the Robo-AO system, augmented with few nights of turbulence profiling with a Multi-Aperture Scintillation Sensor and Differential Image Motion Monitor (MASS-DIMM; Kornilov et al., 2007), we have a unique dataset to characterize the seeing statistics at Palomar. Here we describe independent measurements of the seeing calculated from the Robo-AO dataset.

3.5.1 Robo-AO Seeing Observations

In a regular observing sequence, Robo-AO commands the telescope to slew to the target and commences a short ($\sim$10$-$20 s) seeing-limited observation with the visible camera while the AO system runs through the steps for aligning the laser beacon to the WFS, measuring the WFS background and starting the AO correction loop. These seeing-limited observations are the most accurate direct estimate of the total turbulence at the time of the AO observation.

The seeing-limited observations are collected with the same high-frame-rate mode that is used for the AO observations. In order to calculate the seeing, all frames of the observation data cube are averaged using the `IRAF` (Tody, 1986, 1993) `imcombine` task without any shifting. The image analysis tool `SExtractor` (Bertin & Arnouts, 1996) is used to detect and estimate the FWHM of sources in the images. Metadata from the image header: the

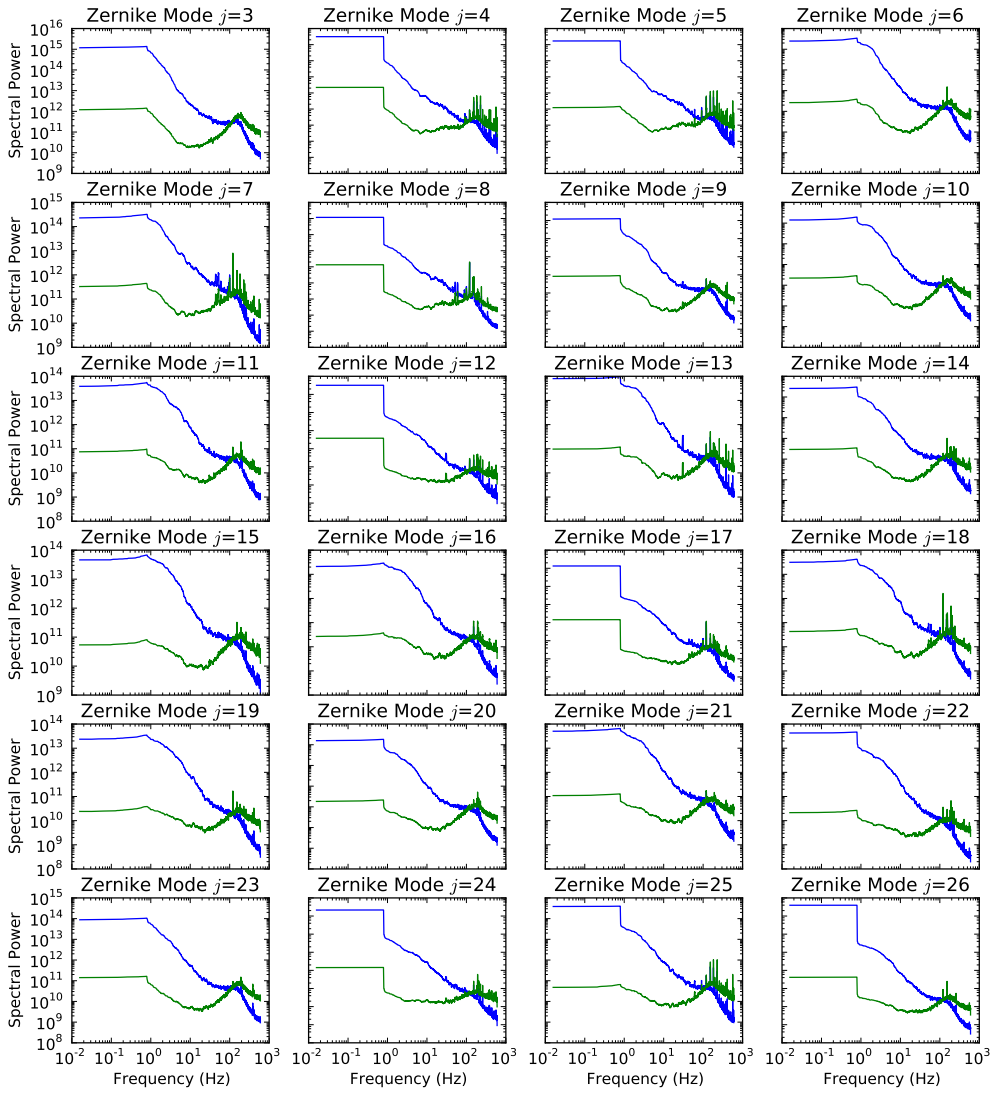

Figure 3.16. The power spectra of the Zernike coefficients corrected by the deformable mirror (in blue) and in the residuals measured by the wavefront sensor (in green) are plotted. Each sub-plot corresponds to one Zernike mode, starting from astigmatism ($j = 3$) to $j = 26$. The crossing over of the residuals with the corrected spectra at ≈ 100 Hz shows the approximate limit of useful wavefront correction.

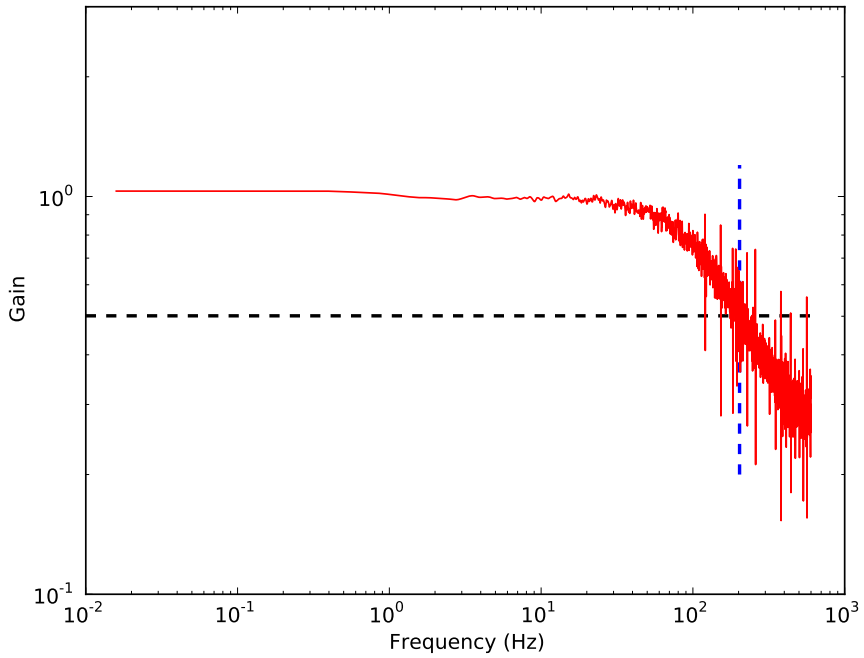

Figure 3.17. The frequency gain ($|H(f)|$) averaged over several Zernike modes is plotted as a function of frequency. 3 dB bandwidth of the control system is 203 Hz.

UTC timestamp, airmass etc. are written down to a database along with the position and FWHM of each source detected in the image. Sources are filtered for (a) elongation < 1.4, (b) flux > 500 DN and (c) position more than 25 pixels away from the edge of the image.

Table 3.5 shows the mean, median, and RMS seeing values for each night when Robo-AO was used from the Palomar 60-inch. Figure 3.18 shows the same data as a histogram of seeing values measured over observing semester B of 2012 and observing semester A of 2013. The median, 90^{th}, and 95^{th} percentile seeing values were $1.28''$, $2.07''$, and $2.33''$ respectively. Robo-AO is able to operate effectively in seeing values lower than about $2''$, i.e. in 90 % of the seeing conditions at Palomar.

Table 3.5. Seeing values as measured from the seeing data observed by Robo-AO.

Date (PST)	Seeing (arcsec) Mean	Median	RMS	Num. Stars	Comment
2012-06-15	–	–	0.00	0	AT
2012-06-16	–	–	0.00	0	AT
2012-06-17	–	–	0.00	0	AT
2012-06-18	–	–	0.00	0	AT
2012-07-11	–	–	0.00	0	CC
2012-07-12	–	–	0.00	0	CC
2012-07-13	1.24	1.05	0.47	124	CC
2012-07-14	1.24	1.08	0.43	135	CC
2012-07-15	1.36	1.37	0.43	141	
2012-07-16	1.69	1.59	0.45	124	
2012-07-17	1.48	1.42	0.44	207	
2012-07-27	1.29	1.25	0.30	582	
2012-07-28	–	–	0.00	0	LF
2012-07-29	–	–	0.00	0	LF
2012-07-30	–	–	0.00	0	LF
2012-07-31	1.98	1.94	0.28	40	CC
2012-08-01	1.11	1.05	0.27	146	
2012-08-02	1.14	1.04	0.33	111	
2012-08-03	0.96	0.94	0.21	193	
2012-08-04	1.12	1.11	0.23	137	
2012-08-05	1.00	0.95	0.24	177	
2012-08-06	0.87	0.83	0.22	154	
2012-08-27	1.06	1.03	0.25	162	
2012-08-28	1.23	1.17	0.30	161	
2012-08-29	0.86	0.84	0.16	201	
2012-08-30	1.31	1.30	0.30	201	
2012-08-31	1.72	1.72	0.24	153	
2012-09-01	1.45	1.39	0.32	108	
2012-09-02	0.96	0.89	0.31	457	
2012-09-03	0.84	0.80	0.24	221	
2012-09-10	–	–	0.00	0	CC,HH
2012-09-11	1.02	1.00	0.17	9	HH
2012-09-12	1.13	1.05	0.56	282	
2012-09-13	1.40	1.33	0.35	232	
2012-10-02	1.40	1.41	0.28	183	
2012-10-03	1.84	1.81	0.46	132	CC
2012-10-04	1.79	1.73	0.36	243	
2012-10-05	1.36	1.29	0.32	255	
2012-10-06	1.78	1.71	0.38	92	
2012-10-07	1.08	1.08	0.18	136	
2012-10-08	1.30	1.25	0.29	176	
2012-10-09	1.20	1.15	0.28	172	
2012-10-10	–	–	0.00	0	CC,HH

Table 3.5

Date (PST)	Seeing (arcsec) Mean	Median	RMS	Num. Stars	Comment
2012-10-11	–	–	0.00	0	CC,HH
2013-01-12	2.38	2.60	0.68	81	LT
2013-01-13	2.91	2.77	0.87	103	LT
2013-01-14	–	–	0.00	0	LT
2013-01-15	–	–	0.00	0	LT
2013-01-16	–	–	0.00	0	LT[a]
2013-01-17	1.90	1.82	0.43	130	
2013-01-18	1.64	1.62	0.39	157	
2013-01-19	1.19	1.15	0.32	212	
2013-01-20	1.57	1.52	0.41	108	
2013-01-21	1.78	1.72	0.34	168	
2013-04-15	–	–	0.00	0	CC
2013-04-18	1.92	1.95	0.51	150	CC
2013-04-19	1.58	1.54	0.38	123	
2013-04-20	1.07	1.02	0.30	169	
2013-04-21	1.02	0.97	0.27	167	

Note. — AT: Automation Testing
CC: Cloud Cover
HH: High Humidity
LF: Laser Failure
LT: Low Temperature

[a]The atmosphere demonstrated its turbulent magnificence on January 16, 2013 in no uncertain terms. FWHMs as high as 8″ were measured!

3.5.2 Seeing Values from DM Telemetry

Another source of data for calculating the seeing values is the telemetry stored by the Robo-AO system. Using the deformable mirror positions stored in the telemetry, we can recreate how 'hard' the AO system needed to work to correct the wavefront errors caused by the atmospheric turbulence. Specifically, we reconstruct the wavefront shape and its Zernike coefficients at each moment in time. The variances of the Zernike coefficients is related to the Fried parameter, r_0 as,

$$\sigma_j^2 = C_j \left(\frac{D}{r_0}\right)^{(5/3)}, \tag{3.13}$$

where σ_j^2 is the variance of the j^{th} Zernike coefficient (based on the Noll indexing (Noll, 1976), which is commonly used in optics fields), D is the diameter of the aperture over which the Zernike coefficients are calculated and C_j are coefficients dependent on the spatial

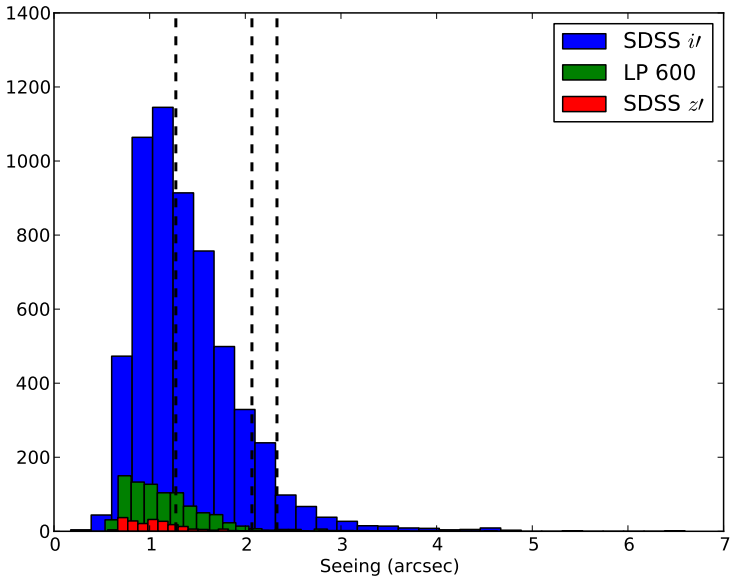

Figure 3.18. A histogram of seeing values measured from the Palomar 60-inch telescope dome is shown. The median, 90^{th}, and 95^{th} percentile seeing values were $1.28''$, $2.07''$, and $2.33''$ respectively.

spectral energy distribution of the turbulence. For the Kolmogorov spectrum of turbulence discussed in Section 1.4, the values of these coefficients were calculated by Noll (1976). The equivalent relations for calculating r_0 and $\mathcal{L}_0$ for the von Karmann model (which empirically accounts for the outer scale) were calculated by Chassat (1992) as,

$$\begin{aligned}\sigma_n^2 =& 1.168 \times (n+1)\left(\frac{D}{r_0}\right)^{(5/3)} \times \\ & \sum_{p=0}^{\infty} \frac{(-1)^p}{p!}\left(\frac{2\pi D}{\mathcal{L}_0}\right)^{2p}\Bigg(\left(\frac{2\pi D}{\mathcal{L}_0}\right)^{2n-\frac{5}{3}} \frac{\Gamma(p+n+3/2)\Gamma(-p-n+5/6)\Gamma(p+n+1)}{\Gamma(p+2n+3)\Gamma(p+n+2)} \\ & + \frac{\Gamma(-p+n-5/6)\Gamma(p+7/3)\Gamma(p+11/6)}{\Gamma(p+n+23/6)\Gamma(p+17/6)}\Bigg)\end{aligned} \tag{3.14}$$

For $\mathcal{L}_0 > D$, the summation quickly converges as higher order terms of $D/\mathcal{L}_0$ rapidly become very small. For D =1.5 m and $\mathcal{L}_0 \gtrsim 10$ m, we find that summing 8 terms estimates the summation to 0.1 %.

I wrote a pipeline to estimate r_0 and $\mathcal{L}_0$ that took all the telemetry data saved by Robo-AO and reconstructed the wavefront at each epoch. I used a minimum of 60 data points (corresponding to 60 seconds in the slow telemetry) to estimate the variances of the Zernike coefficients. For the high speed telemetry, I used 30 seconds worth of data, corresponding to $\sim$ 3600 data points, because the turbulence pattern changes very slightly at timescales of 1 ms and we would underestimate the power in the turbulence. The calculated variances for each minute were scaled to convert them from DN representation of the DM to radians of phase at a wavelength of 500 nm. I performed a least-squares fit on the variances using Equation 3.14 for all Zernike modes from $j = 4$ to 25. I ignored the tip-tilt modes because they are not physically measured by the WFS and the higher order modes that have significant contribution from the noise in the WFS.

Figure 3.19 shows the summary of $L0$ and $r0$ measurements over a typical night of observing (January 19, 2013). In Figure 3.20, we show the distribution of $\mathcal{L}_0$ in the atmosphere at Palomar. I measured the median value of $\mathcal{L}_0$ to be 980 cm over the almost year-long measurement. This value is slightly smaller than the median $\mathcal{L}_0 = 17.5$ m measurement (Ziad et al., 2004) gathered over 10 days in September 2001 from the generalized seeing monitors at Palomar. We attribute this to differing test conditions: long-term measurements from inside the 60-inch telescope dome vs short-term open-air measurements which encounters no dome-seeing. $\mathcal{L}_0$ measurements made simultaneously with the generalized seeing monitor measurements showed upto 54 % differences. Linfield et al. (2001) used four nights of Palomar Testbed Inteferometer data to show that the outerscale varied between 6–54 m and that most of the values were between 10–25 m.

3.5.3 MASS-DIMM Measurements

The Multi-Aperture Scintillation Sensor (MASS) and Differential Image Motion Monitor (DIMM) are two instruments ubiquitously used for turbulence characterization of observing sites. The combined MASS-DIMM instrument developed and described by Kornilov

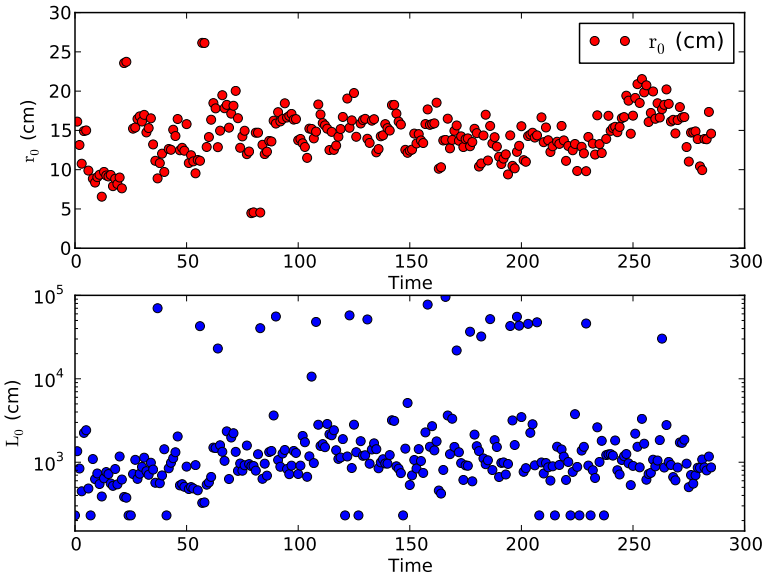

Figure 3.19. A typical nightly variation of $\mathcal{L}_0$ and r_0 from our telemetry data. The x-axis shows sequential data points through the ∼12 hour long night.

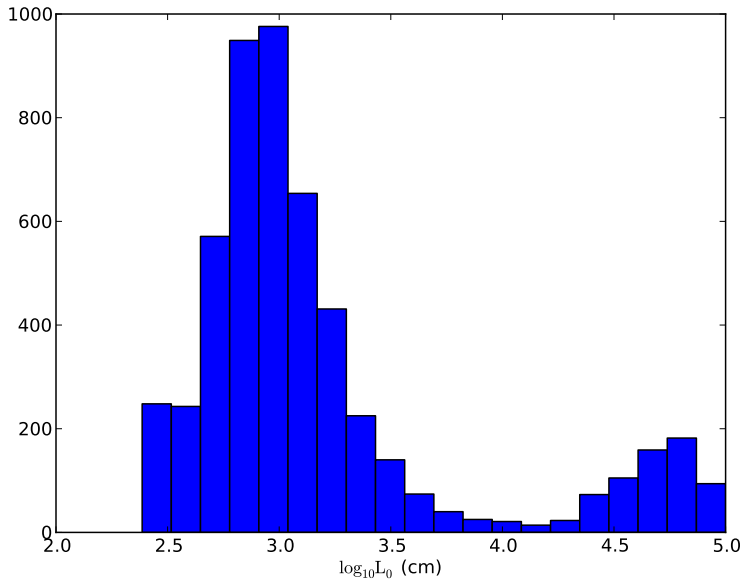

Figure 3.20. The histogram of $\log_{10}\mathcal{L}_0$ values gathered from fitting telemetry of all the Robo-AO observations in 2012 and early 2013. The median $\mathcal{L}_0$ value is 980 cm.

et al. (2007) is a compact unit that fits on commercially available telescopes between 10 to 14 inches in diameter. Here we briefly describe the instruments before describing the measurements.

MASS The MASS unit performs high-speed intensity measurements of starlight passing through different apertures and calculates the correlations between them. Given the geometry of the apertures, the correlations can then be fit to a model of the turbulence profile above the observing site. In the combined MASS-DIMM design, four concentric apertures, one circular and three annular, are used to collect light from the star and focus it onto four independent avalanche photodiodes. From the four measurements, six correlations and four intrinsic scintillation values are calculated and a 6-parameter model of the turbulence profile is fit to the data. The four intrinsic scintillation measures are used for checking for drifts in the APD measurements.

The apertures of the MASS unit are designed to fit the size scales of Fresnel fringes (size $\sim \sqrt{\lambda h}$) caused by atmospheric turbulence at altitudes $h > 500\,\mathrm{m}$. Hence, it measures the 'free-air' seeing and is not sensitive to the turbulence inside the dome or to the ground-layer turbulence caused by the boundary layer between the wind and the ground.

DIMM The Differential Image Motion Monitor (first developed by Sarazin & Roddier, 1990) uses two apertures separated by a significant distance to create two images of the same star on a CCD detector. The CCD reads out the images at a very high frame rate and the separation between the centroids of the two star images is measured. The variance in the longitudinal and transverse motions is related to r_0 as,

$$\sigma_l^2 = 2\lambda^2 r_0^{-5/3}[0.179D^{-1/3} - 0.0968d^{-1/3}], \sigma_t^2 = 2\lambda^2 r_0^{-5/3}[0.179D^{-1/3} - 0.145d^{-1/3}], \quad (3.15)$$

where D is the separation of the apertures and d is the diameter of the apertures.

The DIMM provides a measure of the integrated seeing (free-air+ground-layer+dome-seeing) that is quite robust to telescope jitter, tracking error, defocus, and cloud cover in the sky.

3.5.3.1 MASS-DIMM at Palomar

In 2006, a MASS-DIMM unit was setup at Palomar by Thomsen et al. (2007) that operated for about an year. It was mounted on an alt-azimuth mounted 12-inch RCX-400 telescope manufactured by the Meade Corporation in the (old) 18-inch telescope dome along with the seeing-monitor. However, mechanical issues in the telescope mounting caused the telescope to be disabled, and the system was decommissioned.

Over the summer of 2012, I got the RCX-400 telescope down from Palomar to the COO labs with the help of Paul Gardner. We cleaned and refurbished the optical tube assembly. The control system of the telescope showed repeated errors due to a sensor fault. During slews, the telescope control system would freeze and the slew would continue unabated till the power was switched off. As can be imagined, this is not suitable for robotic operations with multiple cables connected to the telescope. The mount and OTA were shipped to

Meade's facility in San Diego for sensor replacement and electronics checkout. After they were returned, the telescope was checked out for long term operation at COO labs and then driven back to Palomar.

The MASS-DIMM unit was calibrated according to the procedures specified in the MASS-DIMM user guide. This involved:

1. Measurement of the non-linearity of the MASS photodiodes.
2. Measurement of the gain of MASS photodiodes.
3. Measurement of MASS background levels and cutoff thresholds.
4. Measurement of the DIMM CCD platescale using known binaries.
5. Measurement of the physical size and separation of the DIMM apertures.

The new numbers were recorded to the configuration files of the control and data analysis softwares for the MASS and DIMM units.

During the 2006 setup, the MASS-DIMM supervisor and observation planning software was setup to only observe Polaris throughout the night. This was convenient for robotic operation, but the measurement was performed at an airmass of 2. I modified the software to cycle through multiple stars that transit near the zenith, such that the measurements were always made at a zenith angle $< 30°$.

Due to some problems with the object searching and centering routine, the roboticization was never completed. However, I operated the MASS-DIMM in a semi-autonomous mode during the October 2012 observing run. I acquired simultaneous MASS-DIMM measurements from the Palomar 18-inch dome and seeing measurements from the Palomar 60-inch telescope.

Figure 3.21 shows the free air seeing (above an altitude of 0.5 km) measured by the MASS (red dots) and the integrated seeing measured by the DIMM unit (blue line) during the first week of observations. Figure 3.22 shows the corresponding turbulence profiles as a function of altitude. The interruptions in the data are due to high clouds moving through the sky. We observed that the free air seeing at Palomar can be as low as 0.3 to 0.4″when most of the turbulence is concentrated at the lower altitudes. This provides an extremely large isoplanatic angle and excellent corrections from the AO system. Occasionally, when the turbulence is concentrated at high altitudes, the free air seeing becomes the dominant contributor to the integrated seeing.

Although we have very little data from the turbulence monitor, continuous turbulence data is useful for the optimum scientific scheduling of Robo-AO observations. Depending on turbulence conditions, the queue scheduler can prioritize targets with large isoplanatism requirements over narrow field images and targets with high performance requirements over targets with moderate AO requirements.

3.6 Possible Improvements to Robo-AO

While Robo-AO continues to gloriously beaver away at large chunks of targets, we can take a moment to step back and consider the future. What changes can we make to improve

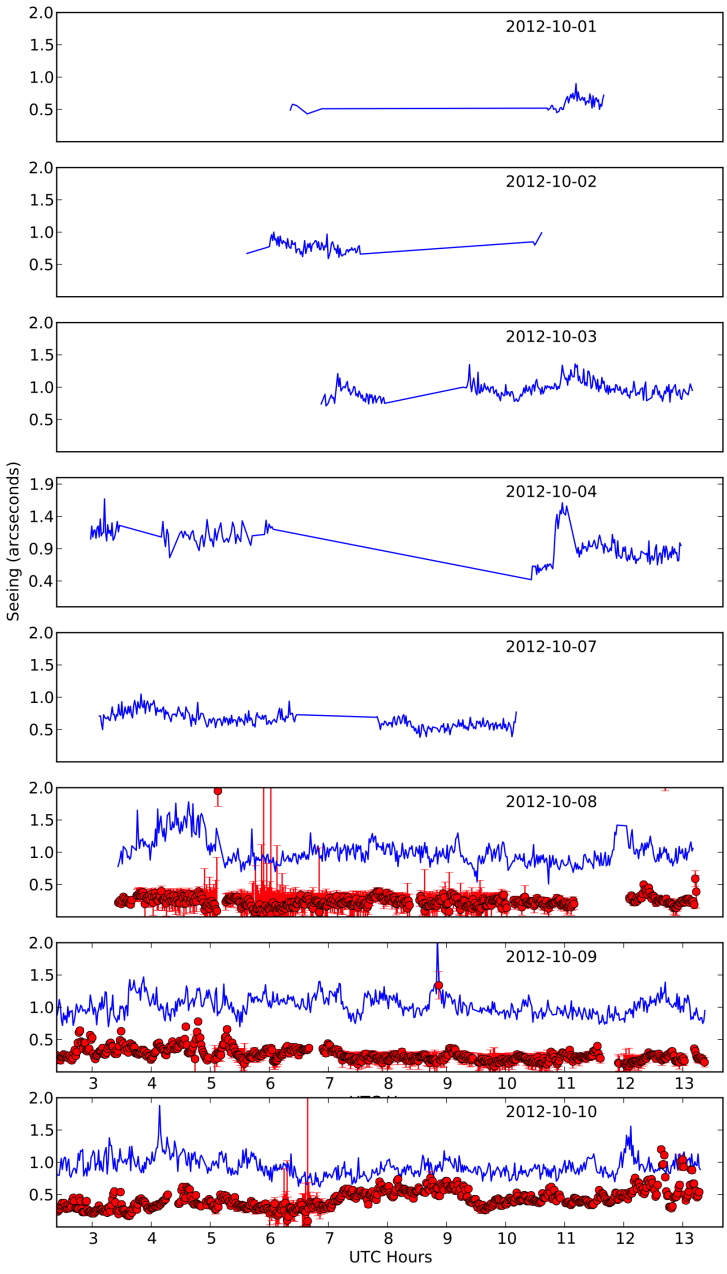

Figure 3.21. Integrated seeing measurements from the DIMM (blue line) and free-atmosphere (above 0.5 km) seeing (red dots) from the MASS during the first week of October. The UTC dates are indicated on each sub-plot.

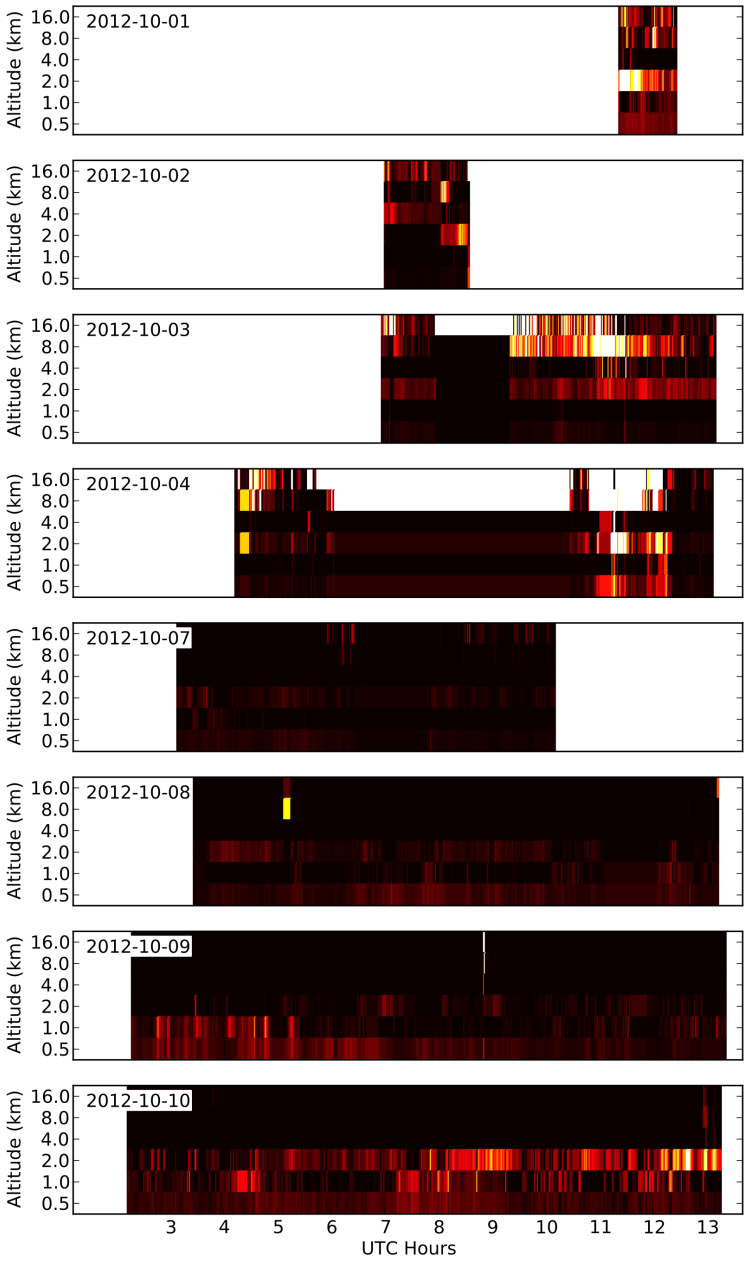

Figure 3.22. Turbulence profile measured over Palomar during the first week of October. The colorbar indicates turbulence strength (C_n^2) in units of meter$^{-2/3}$. The turbulence reconstructed with six fixed layers at 0.5, 1, 2, 4, 8, and 16 km altitudes using scintillation data from the MASS. The 8 sub-plots are data collected on individual nights with the dates indicated in the upper-left corners. The interruptions in early nights are due to commissioning troubles and high clouds.

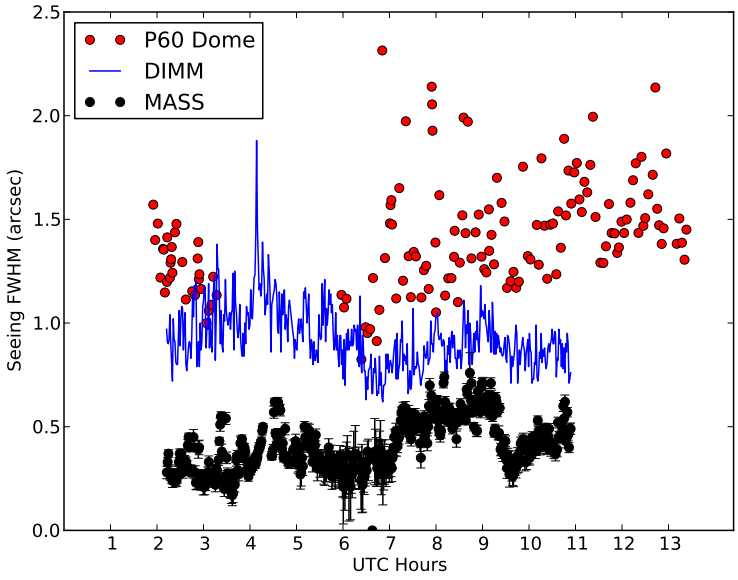

Figure 3.23. Comparison of different seeing measurements for the night of October 10, 2012. The red points are seeing measurements from the Palomar 60-inch dome taken as observed by the Robo-AO camera. The blue line is the integrated seeing from the Palomar 18-inch dome measured by the DIMM unit, and the black points are free-air seeing measurements from the MASS unit also from the Palomar 18-inch dome.

the performance in terms of two criteria: AO performance and observing efficiency? Let us consider the cases one by one.

3.6.1 AO Performance

One of the key sources of residual wavefronts are slowly changing wavefront errors that are either not detected or detected but not appropriately corrected by the AO system. These quasi-static errors materialize from a variety of sources:

1. **Non-common path inside the instrument:** After the first dichroic, the UV laser beam and the visible-IR light reach their destinations through different optical relays, acquiring different optical aberrations.

2. **Quasi-static errors added by telescope optics:** When the wavefront sensor slope offsets are calibrated with the internal calibration source, they do not account for the aberrations added by the telescope optics. Without this, the WFS continuously attempts to control to the AO system to reach a flat state as defined by the internal source. Also, the wavefront errors change as the telescope mirror temperature changes through the night, creating a variable PSF.

3. **Long time scale ($\sim$1 min) atmospheric modes not measured by LGS:** Since laser beacon does not sample the entire volume of air traversed by the stellar wavefront, there are residual errors that need to be corrected. Some of the modes are long lived allowing us to correct them with non-AO wavefront sensing.

3.6.1.1 Gerchberg-Saxton Algorithm

One method to measure the wavefront error of a system in the focal plane is to iteratively model the pupil amplitude image and the focal plane amplitude image using EM propagation theory to calculate the wavefront phase distortion (Gerchberg & Saxton, 1972). It poses some challenges to implement as imaging the pupil requires a field lens to be introduced in front of the camera. Alternatively one can model the pupil shape including all the shadows of the secondary and its mounting. An improvement to this algorithm is to use two focal plane images symmetrically separated around the focal point of the system (Basinger et al., 2000). The focus diversity is sufficient to retrieve the pupil phase and the symmetry minimized most systematic errors. The wavefront measurements are used to reconfigure the WFS slope offsets to change the goal of the control system. The implementation of this algorithm necessitate the camera to be mounted on a focus stage. This method does not provide real-time static error information.

3.6.1.2 Low Bandwidth WFS

Another idea to reduce static errors during observations is to install a low bandwidth wavefront sensor (LBWFS) as implemented by Wizinowich et al. (2006) on Keck II[3]. This idea

[3]At Keck II, the main purpose of the LBWFS is to account for the up-down movement of the layer of sodium that scatters the laser. The WFS perceives the vertical motion of the laser beacon as a focus change

is currently being tested by C. Baranec. The low bandwidth WFS observes the wavefront of one of the natural stars in the field at a very low frame rate (integration time ∼1–90 sec, depending on brightness) to correct for any long-term static error acquired by the natural star wavefront. The advantage of the LBWFS is that it provides real-time feedback to the AO control system. However, it uses light from the same field which can possibly increase errors in tip-tilt registration and also increase the required integration time in the current system. It is beneficial if the LBWFS is implemented in a separate waveband that is not used for science and/or tip-tilt measurements.

Visible Laser Beacon One of the suggestions to the idea of LBWFS is to launch a visible laser coaxially with the UV laser such that the returning light will pass through the visible light path. At a beam location before the visible camera, a laser mirror (reflecting only the wavelength of the laser) redirects the visible laser beam to the LBWFS. The advantage of this that a the brightness of the star is guaranteed, allowing the LBWFS to run at a fast rate. In order for the LBWFS to calculate the wavefront at a rate of say, 0.1 Hz, with a spatial resolution same as the UV WFS, we'll need a visible guide star of about 0.2 magnitude brighter than the current tip-tilt star magnitude limit: i.e. about 15 magnitude. To estimate the leakage of the light into the visible camera, we find that commercially available laser mirrors (say at 532 nm, from Edmund Optics or Thorlabs) have reflectivities of 98 % – 99 %. Specialized coatings (Precision Photonics and others) can provide reflectivities upto 99.9 %. This implies that the leakage light will be 5 magnitudes fainter, i.e. about 20 magnitude glow for Robo-AO.

I feel the challenges outweigh the advantage: (1) The visible laser beacon will sample the same atmosphere as the UV laser beacon, so the residual atmospheric error is not corrected, (2) A visible laser with output power similar to the current UV beacon will be subject to the FAA human-spotter requirement, hampering automated AO operations and (3) the leakage may hamper long science integrations intended to study faint objects.

3.6.2 Observing Efficiency

Observing efficiency for Robo-AO does not simply mean reducing the time spent between observations or maximizing the observations per hour. The aim is to maximize the science output of the system: for example, minimizing the number of observations that were repeated because the science requirements of the observer were not met.

3.6.2.1 Reducing Overheads

At <50 s LGS-AO setup time between targets, Robo-AO's overheads for setting up the AO loops is already far lower than that of any other AO system (5–35 minutes; (Liu, 2006)). A 15–20 second reduction can be achieved by replacing the networked power switch software to switch faster. The limitation occurs because the laser projector needs to be shuttered

and commands the DM to correct for it. The LBWFS prevents this by adjusting the position of the WFS to be conjugate to the sodium laser. This reason is not applicable to Robo-AO since the beacon height is controlled by the timing delay of the range gating system.

twice to acquire two background images for the wavefront sensor. This switching time can be reduced to a negligible (< 1 s) value with appropriate software interface changes. On an average, the telescope slewing and dome slewing time are greater than the AO setup time. We attempt to minimize these by selecting appropriate weights in the queue scheduler cost function. The optimization of the weights is in progress.

3.6.2.2 Cloud and Turbulence Monitoring

AO system performance is extremely sensitive to atmospheric conditions. The Strehl ratio achieved in high seeing is far lower than optimal. Similarly, the presence of clouds can either completely disrupt observations (in thick clouds) or change the throughput (for thin clouds) sufficiently to make photometry challenging. As seen from Column 6 of Table 3.5, Robo-AO lost about 18 % of its nights to cloud cover.

One can increase the observing efficiency of Robo-AO by incorporating cloud and extinction information from the existing Palomar all-sky camera into the queue scheduling system and prioritize observations in areas without extinction or observations of targets where photometry is not critical (say, astrometric monitoring). Infact, the work of distortion removal and astrometric detection has already been performed for the Facilities Summary (`FACSUM`) display at the Palomar 200-inch telescope[4] by Jennifer Milburn, reducing the implementation effort.

As we have seen in Figure 3.22, the turbulence profile at Palomar can rapidly change from ground-layer dominated turbulence to high-altitude dominated turbulence within few tens of minutes (as seen on the night of October 3rd). Since different programs on Robo-AO may have different AO performance priorities, the queue scheduler can optimize the observations, based on inputs of the turbulence profile, isoplanatic angle and free air seeing from a MASS-DIMM unit. In periods with large isoplanatic patches and low free-air seeing values, targets demanding wide field corrections or targets with high-airmass (southern declinations) may be prioritized.

3.6.3 Automating Laser Projector Focus

As discussed in Chapter 2, the laser projector focus can drift significantly if the observatory temperature changes drastically. Currently, the projector focus is adjusted manually when required, usually once at the beginning of each run. The process can be automated in the current setup by adding a motor controller and minor software modifications.

The centroiding sensitivity of the laser spot in the WFS subaperture is proportional to the peak intensity (or correspondingly the Strehl) of the spots in the image. The effect of the focus drift is to blur the spots, reducing the sensitivity of the WFS to wavefront deformations. The wavefront measurement error (median seeing, 20° zenith angle) is about 57 nm RMS (out of a total 156 nm higher order error budget, see Table 1 of Baranec et al. (2012)). Although it is not the most significant contributor to the error budget, it can

[4] See http://www.astro.caltech.edu/palomar/software/facsum/FACSUMUserManual%20V300_02_nofront.pdf by Jennifer Milburn.

become dominant if the spots enlarge to a size comparable to the WFS pixels (2.3″). Empirically, we have found that the laser must be refocused when the ambient temperature has changed by more than about 5°C, which can occur within a single night. Automating this procedure and performing a quick (≈10 s) optimization every few hours would ensure that the WFS system operates at its optimum.

3.6.3.1 Separate Tip-Tilt Sensor

Another idea to improve the scientific throughput of Robo-AO would be to utilize an avalanche photo diode (APD) quadrant cell to perform the TT correction with scientifically unused light. Since most observations are performed in specific filters, the large waveband of the unused light would allow a fainter tip-tilt star limit. More importantly, this allows the visible and IR cameras to operate simultaneously, doubling the observing efficiency by allowing simultaneous observations in visible and IR.

The alternative to this is to perform high-speed readout of a small strip from the HgCdTe camera while integrating the rest of the image for a longer time. This mode is to be implemented on IUCAA's Sidecar Drive Electronics Card (ISDEC) which controls HgCdTe detectors. However, this has two main disadvantages: (1) the light from the tip-tilt star is restricted to be within the IR filter used for science observation and (2) the tip-tilt reference star must be separate from the science target, else the long integration advantage is lost. Robo-AO's science cases overwhelmingly use the science target as the tip-tilt reference star, thus nulling the advantage of this method.

Chapter 4

Constraining Pre-Main Sequence Evolution of Low Mass Stars

4.1 Introduction

The theory of stellar structure is well understood to the point, that given a mass of a star that is on the MS (and for many post-MS cases), we can predict its luminosity, temperature, surface gravity and spectrum to a few percent accuracy. The knowledge of metallicity and rotation further improve the accuracy of these predictions. Because the star spends a large fraction of its lifetime on the MS, its state is in quasi-equilibrium and hence amenable to calculation. During star formation, all parameters and observables of the star are functions of time and the calculations of their relationships are significantly more difficult and consequently our understanding of such systems is limited.

There is a large scatter in current models of stellar evolution in the pre-main sequence (PMS) lives of stars, especially at the low-mass ($\lesssim 1\,M_\odot$) range (Hillenbrand & White, 2004). As shown in Figure 4.1, different models of stellar evolution predict temperatures with discrepancies of 500 to 1000 K and correspondingly different luminosities and evolutionary tracks for stars of the same mass. Conversely, a large range of masses is predicted for specific values of temperature, luminosity and metallicity which are the observables of astronomical studies. These differences arise due to different assumptions of initial conditions, prescriptions for convection and opacities. Similarly, there are large discrepancies between the various models in the locations of PMS isochrones. Measurements of fundamental stellar parameters such as mass, spectral energy distribution (providing luminosity and temperature) and surface gravity are required to better anchor evolutionary models at young ages.

Young stellar binaries and multiple systems provide the most stringent constraints on models of stellar evolution since they form from the same fragment withing a molecular gas cloud at around the same epoch. The only major difference between their properties is this due to their mass difference. Hence, measuring the luminosities, temperatures and, if possible, the masses of these objects facilitates comparison with theory by allowing us to marginalize the dataset over the ages and metallicities. By placing the members of the clusters on the Hertzsprung-Russell diagram and fitting theoretical isochrones to the locations, one can constrain the evolutionary models. This method has a long history of

use by Kraus & Hillenbrand (2009); Luhman (2004); White et al. (1999).

Conveniently, a majority of the young stars in sparse star-forming regions such as Taurus are binaries (Ghez et al., 1993; Simon et al., 1995)[1]. Kraus et al. (2011) found that 2/3 to 3/4 of all stars in the Taurus star-forming region were multiples with a log-flat separation distribution between 3 and 5000 AU. At a distance of 145 pc, this implies that about half of the binaries are unresolvable from seeing-limited observing (seeing = 1″).

The technical challenge in the study of PMS star binaries is that most of them are unresolved in seeing-limited observations and require the use of adaptive optics or space-based telescopes. There have been several high-resolution ground-based studies of these binaries using lunar occultations, speckle imaging, adaptive optics and using the Hubble Space Telescope (HST). Table 4.1 is a compilation of all the high resolution surveys of pre-main sequence stars performed. As ground based systems have previously been capable of resolving these binaries only in the infrared and the high resolution optical imaging from the HST is a scarce resource, almost all the targets observed in high resolution photometric

[1]As to why the same results are not found in field stars or in denser clusters such as IC 348 and the ONC (Duchêne et al., 1999; Köhler et al., 2006; Reipurth et al., 2007) is another compelling question. Kraus et al. (2011) suggest that this may be due to dynamical disruptions of multiple star systems in dense young clusters and sparse old clusters.

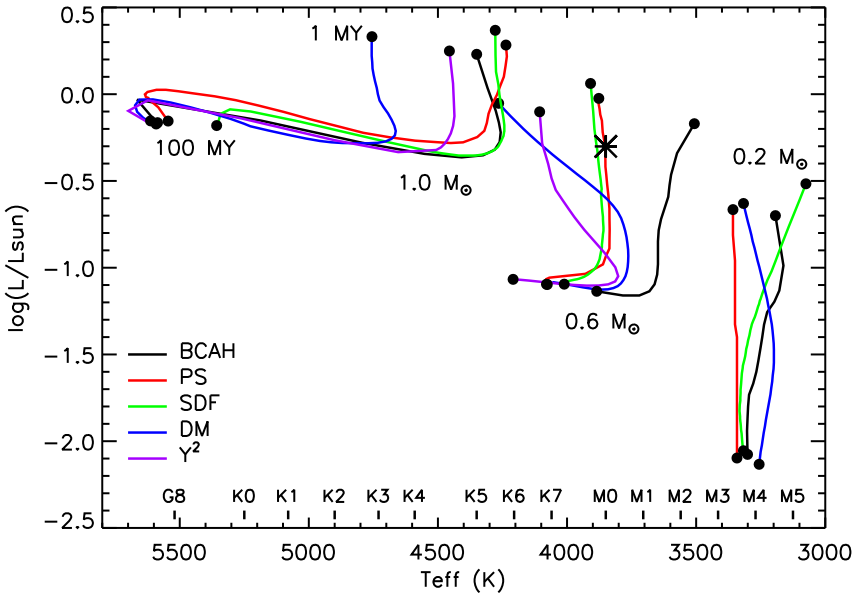

Figure 4.1. Pre-main sequence evolutionary tracks from 1 Myr to 100 Myr computed by various authors for stellar masses of 0.2, 0.6 and 1.0 $M_\odot$ are compared. Black lines (BCAH) are from Baraffe et al. (1998), red lines (PS) are from Palla & Stahler (1999), green lines (SDF) are from Siess et al. (2000), blue lines (DM) are from D'Antona & Mazzitelli (1997) and the purple lines (Y^2) are from Yi et al. (2003). The asterisk shows the position of a young PMS M0 star with a luminosity of 0.5 $L_\odot$. Figure adapted from Schaefer (2011).

Table 4.1. Previous high-resolution photometric studies of close pre-main-sequence multiples.

Reference	Method	Targets (Region)	Waveband
Leinert et al. (1993)	Speckle Interferometry	140 (Tau)	NIR
Ghez et al. (1993)	Speckle Interferometry	69 (Oph + Tau)	NIR
Richichi et al. (1994)	Lunar Occultations	26 (Tau)	NIR
Simon et al. (1995)	Lunar Occultations	35 (Oph) + 47 (Tau)	NIR
Aspin et al. (1997)	High Speed Imaging	12 (Oph)	NIR
Leinert et al. (1997)	Speckle Interferometry	31 (Mixed)	NIR
Patience et al. (1998)	Speckle Interferometry	167 (Hya)	NIR
Duchêne et al. (1999)	Adaptive Optics	66 (IC 348)	NIR
Simon et al. (1999a)	Lunar Occultations	6 (Tau)	NIR
Simon et al. (1999b)	Adaptive Optics	292 (Ori)	NIR
Köhler et al. (2000)	Speckle Interferometry	118 (Sco-Cent)	NIR
White & Ghez (2001)	Hubble Space Telescope	44 (Tau)	Opt
Kraus et al. (2005)	Hubble Space Telescope	12 (Sco)	Opt
Kraus et al. (2006)	Hubble Space Telescope	22 (Tau)	Opt
Correia et al. (2006)	Adaptive Optics	58 (Mixed)	NIR
Köhler et al. (2006)	Adaptive Optics	228 (Ori)	NIR
Konopacky et al. (2007)	Adaptive Optics	13 (Tau)	NIR
Ahmic et al. (2007)	Adaptive Optics	31 (Cha)	NIR
Kraus et al. (2008)	Aperture Masking	82 (Sco)	NIR
Kraus et al. (2011)	Adaptive Optics	82 (Tau)	NIR
Kraus & Hillenbrand (2012)	Adaptive Optics	78 (Tau)	NIR

Note. — Arranged in a chronological order.

Note. — Star forming regions: Tau (Taurus-Auriga), Sco (Scorpius-Ophiuchus), Cha (Chameleon), Ori (Orion), Hya (Hyades), Sco-Cent (Scorpius-Centaurus), Mixed (Various regions).

and spatially resolved spectroscopic studies have been measured in the NIR wavebands. Only a small subset of these binaries was studied in the optical: 44 targets by White & Ghez (2001) for which photometry was performed in the F336W, F439W, F555W, F675W, F814W and F656N filters (equivalent to the Johnson-Cousins U, B, V, $R_{\rm C}$ and $I_{\rm C}$ and $\rm H_{\alpha}$) and 12 + 22 targets by Kraus et al. (2005, 2006) for which photometry was performed in the F555W (V), F775W (i'), and F850LP (approximately z') filters.

Young PMS stars and their neighborhoods are abuzz with activity which needs to be accounted for in the study of PMS evolution. The presence of dusty disks and accretion around these young objects implies that the spectro-photometric measurements in the NIR are corrupted by excess flux (also known as veiling) from the dusty disk and are not accurate indicators of the photospheric flux. Folha & Emerson (1999) and Johns-Krull & Valenti (2001) reported from spectroscopic studies that the excess flux in the NIR K band can be a factor of 1.5 higher than the photospheric flux of the star itself. The emission from the disks is reduced towards shorter wavelengths ($T_{\rm dust} \sim 2000\,{\rm K}$) hence the photometric measurements in the optical bands would improve our anchoring of stellar photosphere models.

Robo-AO is the world first AO system to routinely observe in the visible wavelengths. This unique capability along with the high efficiency of observations ($\gtrsim$180 observations per night) make Robo-AO well suited for a large SDSS g', r', i' and z' band high-resolution survey of PMS multiples.

From the previous AO and speckle imaging surveys of the Taurus-Auriga region (age $\leq 1-3\,{\rm Myr}$) and of the Upper Scorpius-Ophiuchus region (age $\leq 3-5\,{\rm Myr}$), we selected PMS multiple systems on the basis of their primary magnitudes ($m_i < 15.5$), separations ($0.15'' < {\rm sep} < 30''$) and declination $> -27°$. Originally, a sample of 100 systems in the Taurus-Auriga region and 150 systems in the Upper Scorpius-Ophiuchus region was proposed for observing in semester 2013A. However, due to time allocation constraints, we acquired 148 observations of 37 systems in the Taurus-Auriga region and 117 observations of 30 systems in the Upper Scorpius-Ophiuchus region.

For a handful of PMS binaries, dynamical masses have been measured through careful astrometric and radial velocity followup (for example, see Boden et al., 2012; Schaefer et al., 2012; Torres et al., 2012, and references therein). The latest thorough compilation of these measurements is an excellent review by Luhman (2012). This subset will serve as an excellent comparison between masses calculated from photometric data and dynamical masses.

4.2 Observations and Data Analysis

We undertook Robo-AO observations of the sample in January and April 2013. The details of the observations are specified in Tables 4.2 and 4.3. The classification of the observations as 'high_flux', 'faint' and 'zero_flux' is explained in the next section. Figures 4.2, 4.3, 4.4, 4.5 show combined images with SDSS r', i' and z' bands mapped to RGB colors. All images are square-root scaled from zero to the peak value in any one filter. Thus, the blue color shows objects brighter in z' filter while the red and yellow colors indicate objects brighter in the r' and i' filters.

Table 4.2. Robo-AO observations of PMS multiple systems in the Taurus-Auriga region.

Target	RA	Dec	Filter	Date	Time	Airmass	Quality
2MASS	+04h55m47.57s	+30d28m7.7s	r'	14	09 06 21	1.569	zero flux
J04554757+3028			z'	14	05 25 54	1.004	faint
CFHT-Tau-17	+04h40m1.75s	+25d56m29.2s	g'	22	04 35 41	1.01	zero flux
			i'	22	04 37 54	1.011	zero flux
			r'	22	04 40 06	1.011	zero flux
			z'	22	04 42 19	1.012	zero flux
CIDA-9	+05h05m22.86s	+25d31m31.2s	g'	22	03 15 50	1.071	zero flux
			i'	22	03 18 03	1.067	faint
			r'	22	03 20 15	1.064	faint
			z'	22	03 22 28	1.062	zero flux
CoKuTau1	+04h18m51.48s	+28d20m26.5s	i'	21	03 03 12	1.03	zero flux
			r'	21	02 54 04	1.039	zero flux
			z'	21	02 51 51	1.041	zero flux
CoKuTau3	+04h35m40.94s	+24d11m8.8s	g'	20	05 48 53	1.071	zero flux
			i'	20	05 51 06	1.074	bright
			r'	21	03 42 33	1.024	faint
			z'	21	03 44 46	1.022	faint
DF Tau	+04h27m2.8s	+25d42m22.3s	g'	22	03 25 53	1.021	faint
			i'	22	03 28 06	1.02	bright
			r'	22	03 30 18	1.019	bright
			z'	22	03 32 31	1.017	bright
FU Tau	+04h23m35.39s	+25d03m3.1s	g'	22	02 05 01	1.121	zero flux
			i'	22	02 12 17	1.111	faint
			r'	22	02 14 29	1.106	zero flux
			z'	22	02 16 42	1.1	faint

Table 4.2

Target	RA	Dec	Filter	Date	Time	Airmass	Quality
FX Tau	+04h30m29.61s	+24d26m45s	g'	21	04 15 47	1.012	faint
			i'	21	04 18 00	1.012	bright
			r'	21	04 20 12	1.012	bright
			z'	21	04 22 25	1.012	bright
GH Tau	+04h33m6.22s	+24d09m34s	g'	20	03 44 10	1.023	bright
			i'	20	03 46 23	1.022	bright
			r'	20	03 48 35	1.021	bright
			z'	20	03 50 48	1.019	bright
GN Tau	+04h39m20.91s	+25d45m2.1s	g'	22	03 35 50	1.022	zero flux
			i'	22	03 38 03	1.021	faint
			r'	22	03 40 15	1.02	faint
			z'	22	03 42 28	1.018	faint
GV Tau	+04h29m23.73s	+24d33m0.3s	g'	21	04 47 42	1.02	zero flux
			i'	21	04 49 55	1.021	faint
			r'	21	04 52 07	1.023	zero flux
			z'	21	04 40 52	1.017	faint
HBC 351	+03h52m2.24s	+24d39m47.9s	g'	21	04 10 10	1.02	bright
			i'	21	04 12 23	1.021	bright
			r'	21	04 44 19	1.046	bright
			z'	21	04 55 34	1.059	bright
HBC 352	+03h54m29.51s	+32d03m1.4s	g'	14	04 45 52	1.011	bright
			i'	14	04 39 14	1.008	bright
			r'	14	04 37 02	1.007	bright
			z'	14	04 27 32	1.003	bright
HBC 356	+04h03m13.96s	+25d52m59.8s	g'	22	04 20 08	1.019	faint

Table 4.2

Target	RA	Dec	Filter	Date	Time	Airmass	Quality
			i'	22	04 22 21	1.02	bright
			r'	22	04 24 33	1.021	bright
			z'	22	04 26 46	1.022	faint
HBC 407	+04h34m18.04s	+18d30m6.7s	g'	20	02 51 32	1.105	bright
			i'	20	02 53 45	1.101	bright
			r'	20	02 55 57	1.097	bright
			z'	20	02 58 10	1.095	bright
HK Tau	+04h31m50.57s	+24d24m18.1s	g'	21	03 57 58	1.015	faint
			i'	21	04 00 11	1.014	bright
			r'	21	04 02 23	1.014	bright
			z'	21	04 04 36	1.013	bright
HP Tau-G2	+04h35m54.15s	+22d54m13.5s	g'	20	03 24 28	1.044	bright
			i'	20	03 26 41	1.042	bright
			r'	20	03 28 53	1.04	bright
			z'	20	03 31 06	1.039	bright
Haro 6-28	+04h35m56.84s	+22d54m36s	g'	20	03 34 17	1.035	zero flux
			i'	20	03 36 30	1.034	bright
			r'	20	03 38 42	1.032	faint
			z'	20	03 40 55	1.03	bright
I 04361+2547	+04h39m13.89s	+25d53m20.9s	g'	22	04 14 31	1.009	zero flux
			i'	22	04 16 44	1.008	zero flux
			r'	22	04 30 09	1.009	zero flux
			z'	22	04 32 22	1.01	zero flux
IRAS	+04h26m56.3s	+24d43m35.3s	g'	21	05 14 59	1.042	zero flux
04239+2436			i'	21	05 17 12	1.044	zero flux

Table 4.2

Target	RA	Dec	Filter	Date	Time	Airmass	Quality
			r'	21	05 19 24	1.046	zero flux
			z'	21	05 21 37	1.048	zero flux
IW Tau	+04h41m4.71s	+24d51m6.2s	g'	21	05 09 26	1.025	faint
			i'	21	05 11 39	1.027	bright
			r'	21	05 44 26	1.058	bright
			z'	21	05 46 39	1.061	bright
J2 2041	+04h33m55.47s	+18d38m39.1s	g'	20	03 01 27	1.087	faint
			i'	20	03 03 40	1.083	bright
			r'	20	03 05 52	1.082	bright
			z'	20	03 08 05	1.078	bright
JH 112	+04h32m49.11s	+22d53m2.8s	g'	19	05 18 21	1.039	faint
			i'	19	05 38 35	1.06	bright
			r'	20	03 18 59	1.046	bright
			z'	20	03 21 12	1.045	bright
JH 223	+04h40m49.51s	+25d51m19.2s	g'	22	03 45 45	1.018	zero flux
			i'	22	03 47 58	1.016	bright
			r'	22	03 50 10	1.015	faint
			z'	22	04 00 03	1.012	bright
LkHa 332-G1	+04h42m5.49s	+25d22m56.3s	g'	21	06 01 42	1.079	faint
			i'	21	06 03 55	1.083	bright
			r'	22	02 22 40	1.123	faint
			z'	22	02 24 53	1.12	bright
LkHa 332-G2	+04h42m7.33s	+25d23m3.2s	g'	22	02 56 00	1.067	zero flux
			i'	22	02 58 13	1.063	bright
			r'	22	03 00 25	1.06	bright

Table 4.2

Target	RA	Dec	Filter	Date	Time	Airmass	Quality
			z’	22	03 02 38	1.059	bright
T Tau	+04h21m59.43s	+19d32m6.4s	g’	19	04 35 08	1.033	bright
			i’	19	04 37 21	1.034	bright
			r’	19	04 39 33	1.035	bright
			z’	19	04 46 04	1.038	bright
UY Aur	+04h51m47.38s	+30d47m13.5s	g’	14	05 13 24	1.002	faint
			i’	14	05 34 35	1.008	bright
			r’	14	04 57 53	1.001	bright
			z’	14	05 00 06	1.001	bright
UZ Tau	+04h32m43.04s	+25d52m31.1s	g’	22	04 03 21	1.009	faint
			i’	22	04 05 34	1.009	bright
			r’	22	04 07 46	1.009	bright
			z’	22	04 09 59	1.009	bright
V410 Tau	+04h18m31.1s	+28d27m16.2s	g’	21	02 44 04	1.048	bright
V710 Tau	+04h31m57.79s	+18d21m38.1s	g’	19	04 29 01	1.035	zero flux
			i’	20	02 38 59	1.124	bright
			r’	20	02 46 03	1.109	bright
			z’	20	02 48 16	1.106	bright
V807 Tau	+04h33m6.64s	+24d09m55s	g’	20	03 53 56	1.018	bright
			i’	20	03 56 09	1.018	bright
			r’	20	03 58 21	1.017	bright
			z’	20	04 00 34	1.016	bright
V927 Tau	+04h31m23.82s	+24d10m52.9s	g’	20	05 38 55	1.061	faint
			i’	20	05 41 08	1.065	bright
			r’	20	05 43 20	1.067	bright

Table 4.2

Target	RA	Dec	Filter	Date	Time	Airmass	Quality
			z’	20	05 45 33	1.072	bright
V928 Tau	+04h32m18.86s	+24d22m27.1s	g’	21	03 48 04	1.019	faint
			i’	21	03 50 17	1.018	bright
			r’	21	03 52 29	1.017	bright
			z’	21	03 54 42	1.016	bright
V955 Tau	+04h42m7.77s	+25d23m11.8s	g’	22	03 05 49	1.054	zero flux
			i’	22	03 08 02	1.051	bright
			r’	22	03 10 14	1.05	faint
			z’	22	03 12 27	1.046	bright
VY Tau	+04h39m17.41s	+22d47m53.4s	g’	19	04 56 12	1.022	bright
			i’	19	04 58 25	1.023	bright
			r’	19	05 00 37	1.023	bright
			z’	19	05 02 50	1.024	bright
XZ Tau	+04h31m40.07s	+18d13m57.2s	g’	19	04 10 15	1.037	faint
			i’	19	04 12 28	1.037	bright
			r’	19	04 14 40	1.036	bright
			z’	19	04 16 53	1.036	bright

Table 4.3. Robo-AO observations of PMS multiple systems in the Upper Scorpius-Ophiochus region.

Target	RA	Dec	Filter	Date	Time	Airmass	Quality
2MASS J15492100-2600062	+15h49m21s	-26d00m6.2s	g'	2013 04 19	10 41 45	2.042	bright
			g'	2013 04 20	08 58 02	2.01	bright
			i'	2013 04 20	09 02 26	2.003	bright
			r'	2013 04 20	09 00 14	2.005	bright
			z'	2013 04 20	09 04 38	1.996	bright
2MASS J15545986-2347181	+15h54m59.86s	-23d47m18.1s	g'	2013 04 21	09 06 14	1.874	bright
			i'	2013 04 21	09 10 38	1.868	bright
			r'	2013 04 21	09 08 26	1.871	bright
			z'	2013 04 21	09 12 50	1.865	bright
2MASS J15570234-1950419	+15h57m2.34s	-19d50m41.9s	g'	2013 04 20	10 38 36	1.718	faint
			i'	2013 04 20	10 43 00	1.726	bright
			r'	2013 04 20	10 40 48	1.723	bright
			z'	2013 04 20	10 45 12	1.735	bright
2MASS J15572575-2354220	+15h57m25.75s	-23d54m22s	g'	2013 04 21	09 46 19	1.845	faint
			i'	2013 04 21	09 50 43	1.846	bright
			r'	2013 04 21	09 48 31	1.845	bright
			z'	2013 04 21	09 52 55	1.846	bright
2MASS J15580815-2405529	+15h58m8.15s	-24d05m52.9s	g'	2013 04 20	09 58 19	1.857	faint
			i'	2013 04 20	10 02 43	1.858	bright
			r'	2013 04 20	10 00 31	1.857	bright
			z'	2013 04 20	10 04 55	1.86	bright
2MASS J15590208-1844142	+15h59m2.08s	-18d44m14.2s	g'	2013 04 21	09 16 15	1.647	bright
			i'	2013 04 21	09 20 39	1.64	bright
			r'	2013 04 21	09 18 27	1.642	bright
			z'	2013 04 21	09 22 51	1.638	bright

Table 4.3

Target	RA	Dec	Filter	Date	Time	Airmass	Quality
2MASS J16003134-2027050	+16h00m31.34s	-20d27m05s	g'	2013 04 20	09 08 06	1.736	faint
			i'	2013 04 20	09 12 30	1.729	bright
			r'	2013 04 20	09 10 18	1.729	faint
			z'	2013 04 20	09 14 42	1.724	faint
2MASS J16010519-2227311	+16h01m5.19s	-22d27m31.1s	g'	2013 04 20	09 28 07	1.792	faint
			i'	2013 04 20	09 32 31	1.786	bright
			r'	2013 04 20	09 30 19	1.788	faint
			z'	2013 04 20	09 34 43	1.785	bright
2MASS J16014743-2049457	+16h01m47.43s	-20d49m45.7s	g'	2013 04 20	09 38 10	1.713	faint
			i'	2013 04 20	09 42 34	1.709	bright
			r'	2013 04 20	09 40 22	1.71	bright
			z'	2013 04 20	09 44 46	1.708	bright
2MASS J16021045-2241280	+16h02m10.45s	-22d41m28s	g'	2013 04 20	10 18 30	1.799	bright
			i'	2013 04 20	10 22 54	1.806	bright
			r'	2013 04 20	10 20 42	1.804	bright
			z'	2013 04 20	10 25 06	1.81	bright
2MASS J16025123-2401574	+16h02m51.23s	-24d01m57.4s	g'	2013 04 22	10 00 13	1.855	bright
			i'	2013 04 22	09 54 19	1.853	bright
			r'	2013 04 22	10 02 25	1.857	bright
			z'	2013 04 22	09 56 31	1.854	bright
2MASS J16025396-2022480	+16h02m53.96s	-20d22m48s	g'	2013 04 20	10 28 34	1.713	faint
			i'	2013 04 20	10 32 58	1.718	bright
			r'	2013 04 20	10 30 46	1.714	bright
			z'	2013 04 20	10 35 10	1.724	faint
2MASS J16032367-1751422	+16h03m23.67s	-17d51m42.2s	g'	2013 04 21	10 46 38	1.655	faint

Table 4.3

Target	RA	Dec	Filter	Date	Time	Airmass	Quality
			i'	2013 04 21	10 51 02	1.664	bright
			r'	2013 04 21	10 48 50	1.659	bright
			z'	2013 04 21	10 53 14	1.671	bright
2MASS J16042839-1904413	+16h04m28.39s	-19d04m41.3s	g'	2013 04 21	09 26 16	1.653	bright
			i'	2013 04 21	09 30 40	1.648	bright
			r'	2013 04 21	09 28 28	1.651	bright
			z'	2013 04 21	09 32 52	1.647	bright
2MASS J16054266-2004150	+16h05m42.66s	-20d04m15s	g'	2013 04 21	08 46 14	1.775	faint
			i'	2013 04 21	08 50 38	1.767	bright
			r'	2013 04 21	08 48 26	1.772	bright
			z'	2013 04 21	08 52 50	1.757	bright
2MASS J16062196-1928445	+16h06m21.96s	-19d28m44.5s	g'	2013 04 20	10 48 39	1.706	faint
			i'	2013 04 20	10 53 03	1.716	bright
			r'	2013 04 20	10 50 51	1.711	faint
			z'	2013 04 20	10 55 15	1.721	faint
2MASS J16063741-2108404	+16h06m37.41s	-21d08m40.4s	g'	2013 04 21	09 36 16	1.727	faint
			i'	2013 04 21	09 40 40	1.723	bright
			r'	2013 04 21	09 38 28	1.726	bright
			z'	2013 04 21	09 42 52	1.722	bright
2MASS J16065436-2416107	+16h06m54.36s	-24d16m10.7s	g'	2013 04 21	10 06 25	1.866	bright
			i'	2013 04 21	10 10 49	1.869	bright
			r'	2013 04 21	10 08 37	1.868	bright
			z'	2013 04 21	10 13 01	1.871	bright
2MASS J16070356-2036264	+16h07m3.56s	-20d36m26.4s	g'	2013 04 20	09 18 06	1.736	faint
			i'	2013 04 20	09 22 30	1.727	bright

Table 4.3

Target	RA	Dec	Filter	Date	Time	Airmass	Quality
			r'	2013 04 20	09 20 18	1.73	bright
			z'	2013 04 20	09 24 42	1.724	bright
2MASS J16070393-1911338	+16h07m3.93s	-19d11m33.8s	g'	2013 04 20	10 58 42	1.714	zero flux
			i'	2013 04 20	11 03 06	1.725	bright
			r'	2013 04 20	11 00 54	1.723	faint
			z'	2013 04 20	11 05 18	1.734	bright
2MASS J16082387-1935518	+16h08m23.87s	-19d35m51.8s	g'	2013 04 21	08 56 12	1.736	faint
			i'	2013 04 21	09 00 36	1.727	bright
			r'	2013 04 21	08 58 24	1.732	bright
			z'	2013 04 21	09 02 48	1.72	bright
2MASS J16090844-2009277	+16h09m8.44s	-20d09m27.7s	g'	2013 04 21	10 26 29	1.695	faint
			i'	2013 04 21	10 30 53	1.701	bright
			r'	2013 04 21	10 28 41	1.7	faint
			z'	2013 04 21	10 33 05	1.706	bright
2MASS J16102857-1904469	+16h10m28.57s	-19d04m46.9s	g'	2013 04 20	10 08 26	1.639	faint
			i'	2013 04 20	10 12 50	1.64	faint
			r'	2013 04 20	10 10 38	1.639	faint
			z'	2013 04 20	10 15 02	1.641	faint
2MASS J16103196-1913062	+16h10m31.96s	-19d13m6.2s	g'	2013 04 22	09 43 54	1.646	faint
			i'	2013 04 22	09 48 18	1.644	bright
			r'	2013 04 22	09 46 06	1.645	bright
			z'	2013 04 22	09 50 30	1.644	bright
2MASS J16104202-2101319	+16h10m42.02s	-21d01m31.9s	g'	2013 04 21	10 56 41	1.79	bright
			i'	2013 04 21	11 01 05	1.799	bright
			r'	2013 04 21	10 58 53	1.792	bright

Table 4.3

Target	RA	Dec	Filter	Date	Time	Airmass	Quality
			z'	2013 04 21	11 03 17	1.807	bright
2MASS J16115633-2304051	+16h11m56.33s	-23d04m5.1s	g'	2013 04 21	10 16 27	1.811	faint
			i'	2013 04 21	10 20 51	1.814	bright
			r'	2013 04 21	10 18 39	1.811	bright
			z'	2013 04 21	10 23 03	1.816	bright
2MASS J16132929-2311075	+16h13m29.29s	-23d11m7.5s	g'	2013 04 21	09 56 23	1.811	bright
			i'	2013 04 21	10 00 47	1.81	bright
			r'	2013 04 21	09 58 35	1.81	bright
			z'	2013 04 21	10 02 59	1.81	bright
2MASS J16141107-2305362	+16h14m11.07s	-23d05m36.2s	g'	2013 04 20	09 48 14	1.813	bright
			i'	2013 04 20	09 52 38	1.81	bright
			r'	2013 04 20	09 50 26	1.812	bright
			z'	2013 04 20	09 54 50	1.809	bright
2MASS J16215466-2043091	+16h21m54.66s	-20d43m9.1s	g'	2013 04 21	10 36 33	1.717	bright
			i'	2013 04 21	10 40 57	1.721	bright
			r'	2013 04 21	10 38 45	1.719	bright
			z'	2013 04 21	10 43 09	1.723	bright

4.3 Data Reduction and Analysis

As described in Chapter 3, data from the Robo-AO camera is processed through a customized pipeline based on the LUCKY imaging pipeline (Law et al., 2009). Depending on the photon flux from the brightest star in each image, the images were classified as 'high_flux', 'faint' or 'zero_flux' during an initial automated reduction. In Section 3.4.1, we showed that the flux cutoff between the 'high_flux' and the 'faint' classes was about 10^4 counts per frame in the regular imaging modes of Robo-AO. For binaries with small separations and nearly equal fluxes the shift-and-add pipeline can lock on different companions in different frames, leading to a image showing a linear 'triple' system. Examples of tripling can be seen in images of J2-2041, V297 Tau and V298 Tau in Figure 4.3. Before data analysis, the images were visually inspected and reprocessed manually if necessary to remove any tripling effects and to ensure that the same star was used as the tip-tilt star for all four filters for a given target. The images classified as 'zero_flux' are not used.

4.3.1 PSF Clean-up

As shown in Section 3.4.1 and Figure 3.3, the tip-tilt reference stars in the images classified as 'faint' have a noise peak caused by the data reduction pipeline locking on to photon noise and calculating image shifts based on the positions of these noise spikes. This artifact must be removed before attempting photometry.

The radius of the noise peak is determined by the radius of the convolution kernel chosen during the data reduction. We choose a Gaussian with the same FWHM as the Airy disk for the given wavelength and camera configuration. For a wavelength of 0.79 μm, this corresponds to 0.11″ or 5 pixels in the reduced data. We masked a 10 pixel diameter circular region around the peak for PSF shape estimation and centroiding. For flux estimation, we replaced the masked pixels with values interpolated from neighboring data.

4.3.2 PSF Fitting

The temporally and spatially variable PSF delivered by AO systems has always been an roadblock for accurate photometry of barely resolved stars. If each image has a sufficient number of stars, it is possible to use iterative methods to estimate a PSF shape and measure positions and fluxes of stars simultaneously. Software packages such as `IRAF daophot` (Tody, 1993, 1986) and `StarFinder` (Diolaiti et al., 2000) use this approach. We have described the use of these packages in detail in Chapter 5.

For the Robo-AO images obtained for this project, our efforts were complicated by the sparseness of the fields. Each field image had atmost one other star apart from the main target, which, by virtue of our sample choice, were binaries or multiples. Since the data were obtained over a few nights and in different filters, it was not possible to create a simple PSF estimate.

The problem of PSF estimation for companion detection has been the focus of a large number of exo-planet researchers. Techniques such as Angular Differential Imaging (Marois et al., 2006) and Spectral Deconvolution (Sparks & Ford, 2002; Thatte et al., 2007) and analysis methods such as Locally Optimized Combination of Images (`LOCI`; Lafrenière et al.,

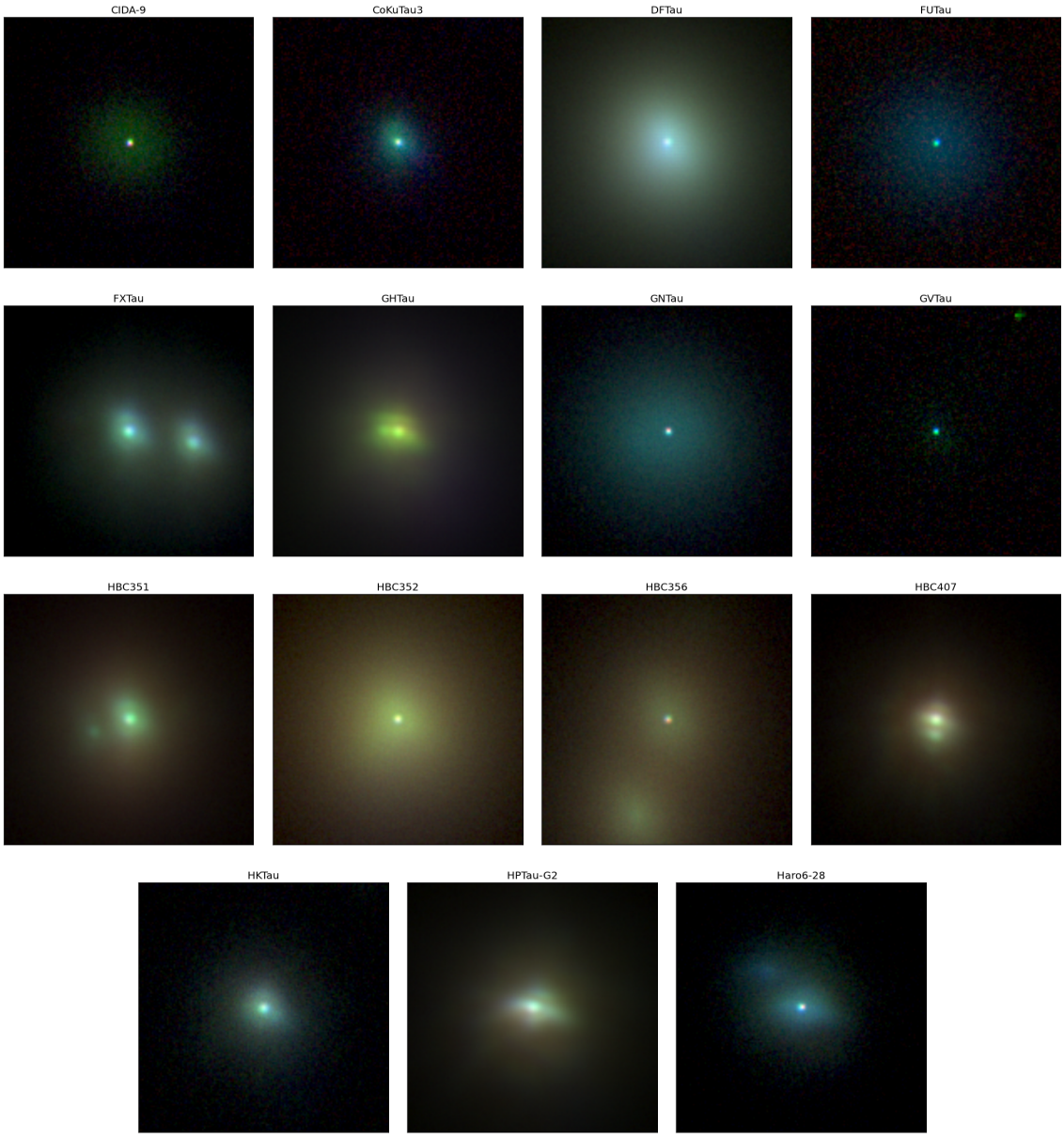

Figure 4.2. Images of targets in the Taurus-Auriga regions with r', i' and z' bands mapped to RGB channels. Each image is $3.3'' \times 3.3''$square. The r', i' and z' band images have been square-root scaled from zero to the maximum intensity in the three images. The colors are approximately representative of the spectral energy distribution. Bluer stars are brighter in z' filter. Redder and yellower stars are brighter in r' and i' filters. The images with a prominent central peak are labeled as 'faint' in Table 4.2 (and correspondingly Table 4.3 for the Scorpius targets).

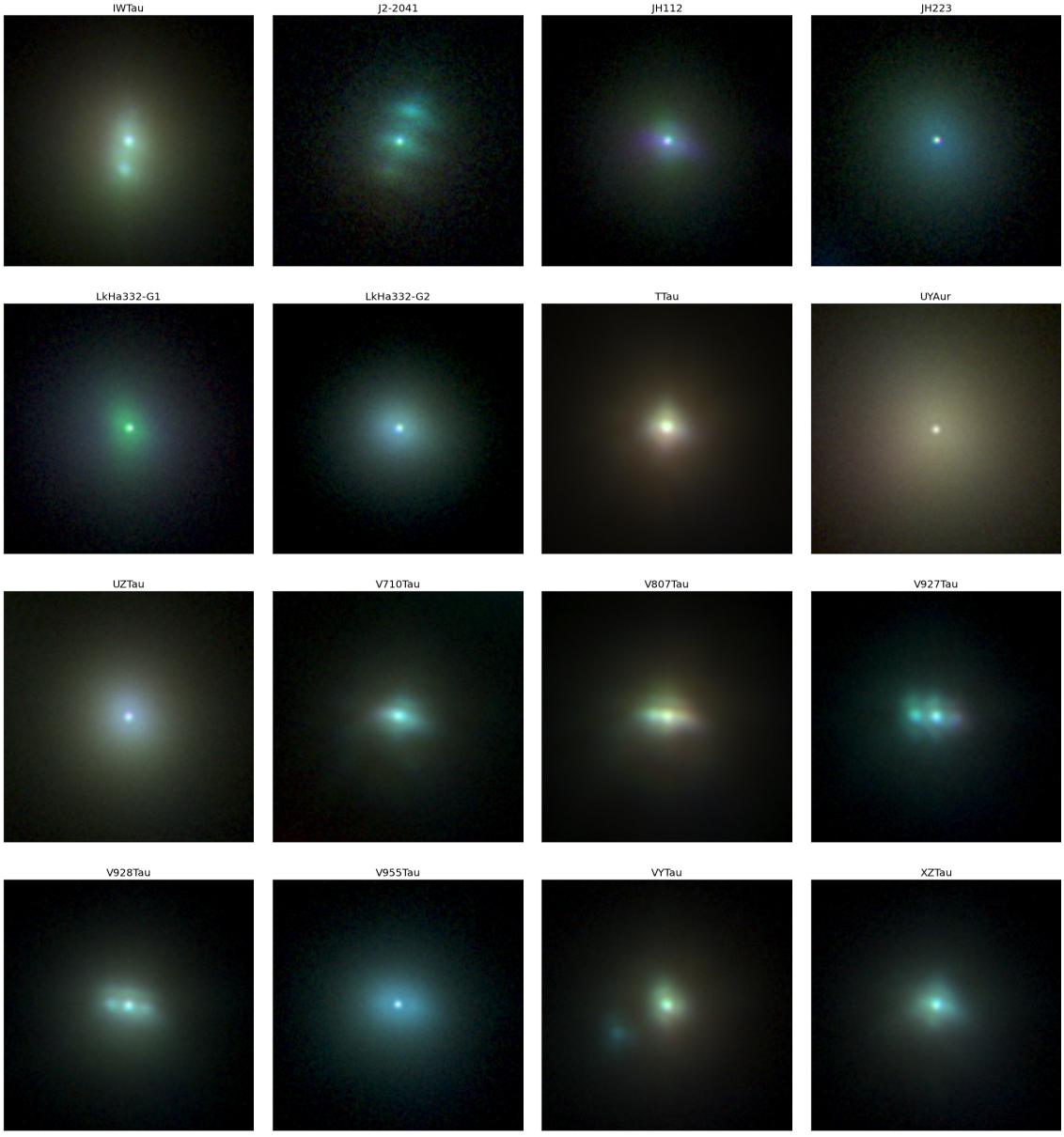

Figure 4.3. Images of targets in the Taurus-Auriga regions with r', i' and z' bands mapped to RGB channels. The image size and scaling is same as that of Figure 4.2.

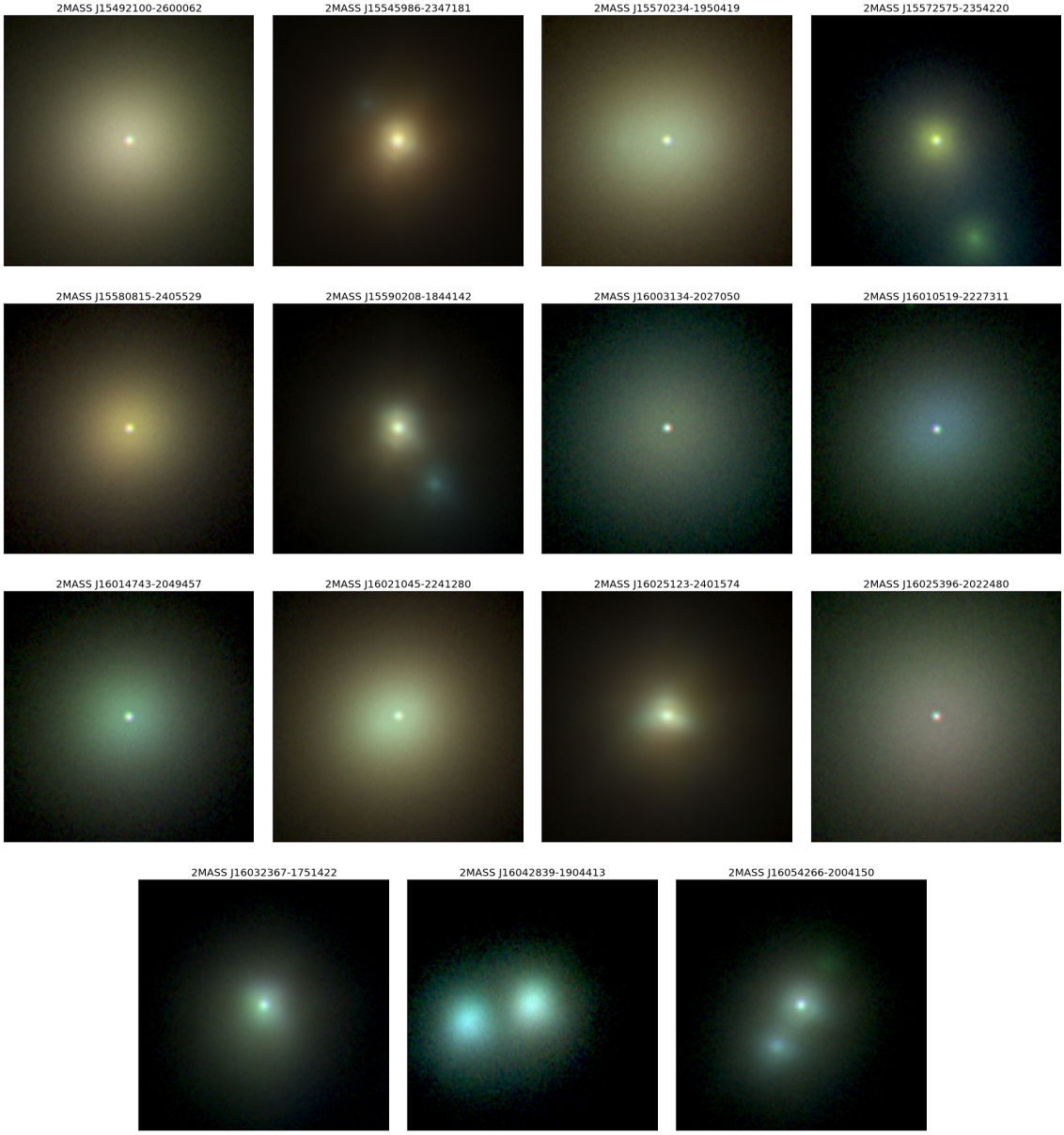

Figure 4.4. Images of targets in the Upper Scorpius-Ophiuchus regions with r', i' and z' bands mapped to RGB channels. The image size and scaling is same as that of Figure 4.2.

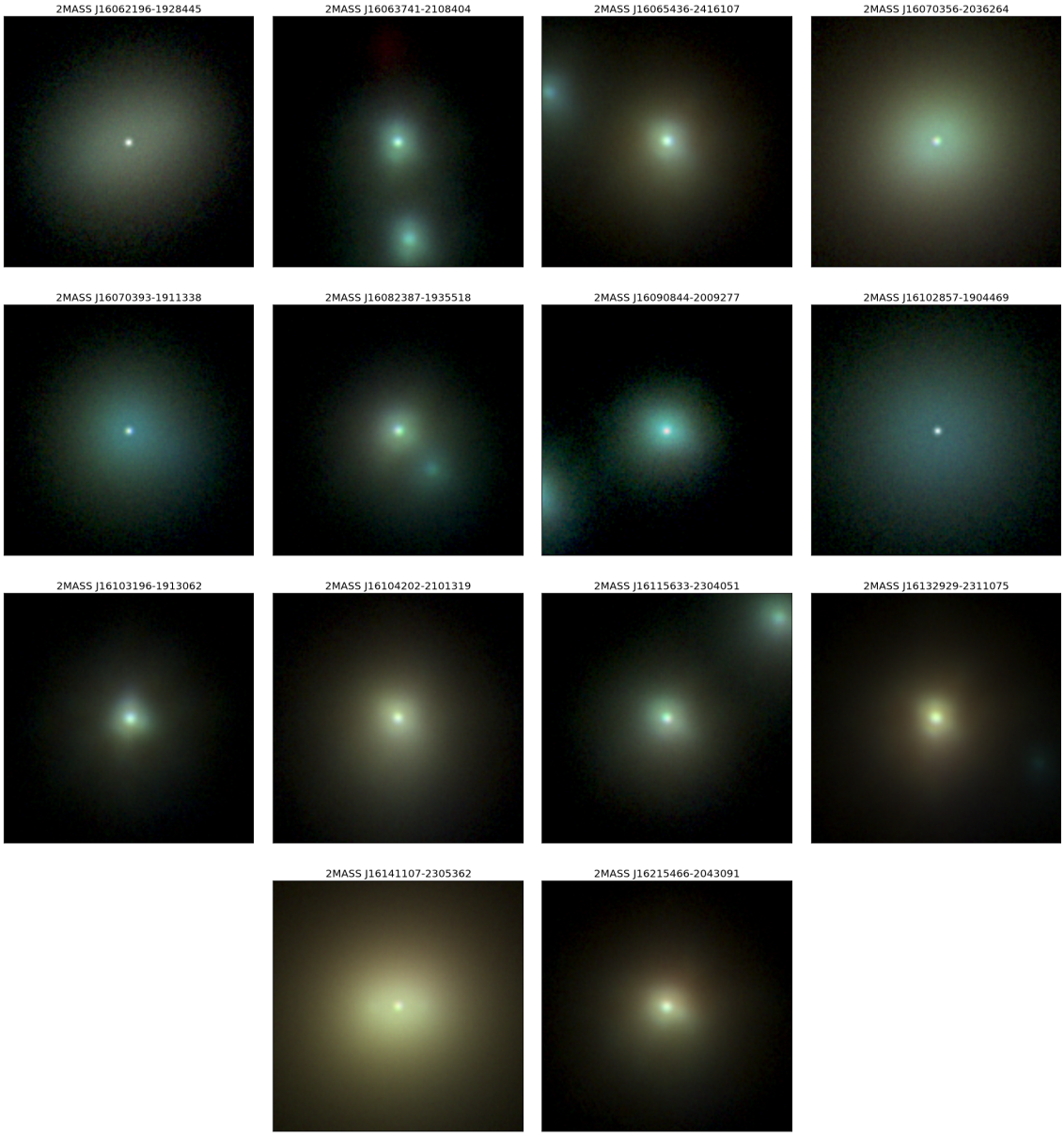

Figure 4.5. Images of targets in the Upper Scorpius-Ophiuchus regions with r', i' and z' bands mapped to RGB channels (continued from Figure 4.4).

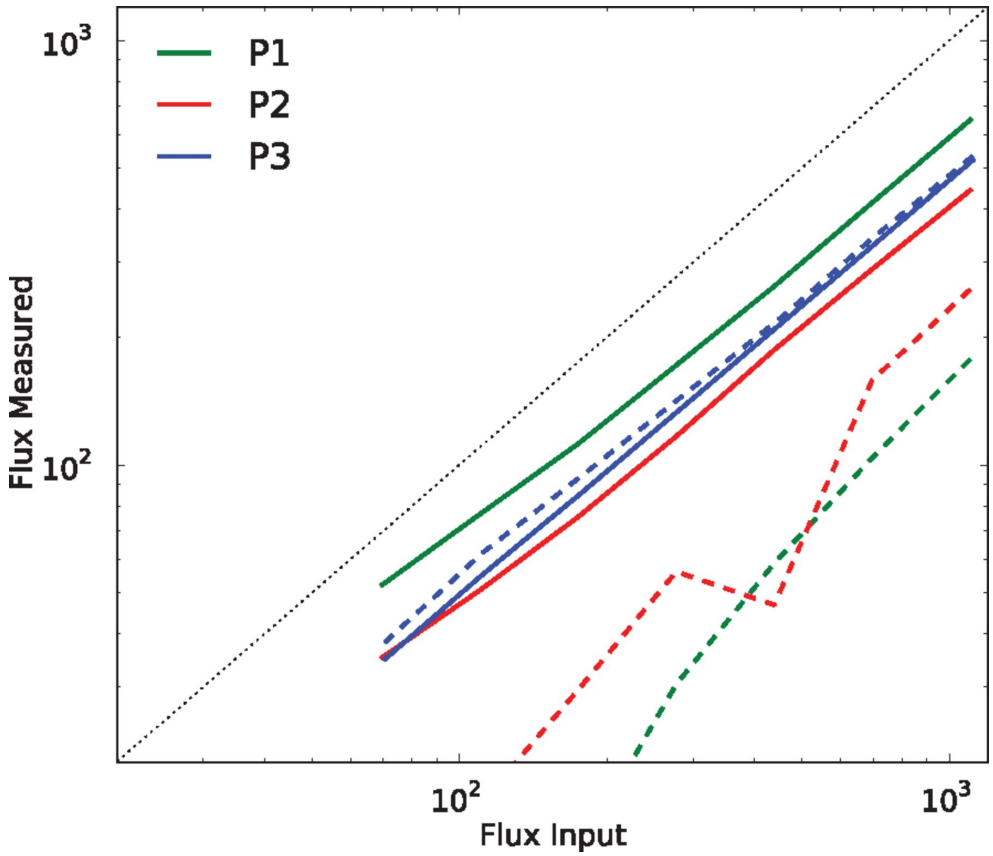

Figure 4.6. The accuracy of PYNPOINT as compared to LOCI for measuring fluxes of simulated planets injected at various distances from the central star in ADI data from the NACO instrument at VLT. The three solid lines correspond to measurements recovered by PYNPOINT and the three dashed lines correspond to the same measurements using the LOCI algorithm. It is seen that the PYNPOINT algorithm, while outperforming the LOCI algorithm, consistently underestimates the flux by as much as a factor of two. Figure adapted from Figure 5 of Amara & Quanz (2012).

2007) and PYNPOINT (Amara & Quanz, 2012) were developed specifically for accurate PSF subtraction.

Based on literature, we chose to use the PYNPOINT method for our data analysis because of its performance in flux measurement compared to LOCI (Figure 4.6). Although developed for analysis of ADI data, we were able to adapt the software[2] for use with the Robo-AO. We briefly describe the algorithm used for the PSF fitting.

Overview: The PYNPOINT algorithm uses a large number of images of targets observed with the same filter closest in time to our sample to create a basis set of PSF shapes. Then

[2]A preliminary version of the PYNPOINT code was graciously sent to us by the developers Dr. A. Amara and Dr. S. Quanz for beta testing.

for each image, the secondary target was masked and a PSF estimate was created using a finite number of basis elements. The residuals created by subtracting the PSF estimate from the image was used to estimate the flux of the secondary.

4.3.2.1 Basis Set of PSFs

For each filter (SDSS g', r', i' and z'), I collected a set of about hundred images. I created 300 pixel (6.6″) square cutouts centered on the primary star of each target. The central 8 pixel diameter circle was masked to block the central noise peak that might be present in faint images. The data were then read by the `PYNPOINT` code, normalized and subjected to a principal component analysis (PCA)[3]. The resulting independent vectors were used as the basis set for PSF estimation.

For the i' band images, I used a data set of 102 images. The first sixteen basis functions are shown in Figure 4.7.

4.3.2.2 PSF Fitting

In the images where the secondary companion was visually prominent, it was masked with a circular mask to prevent the PSF estimate from fitting the secondary peak. The diameter of the circular mask was chosen to be 0.5″, sufficient to block the companion peak and its surrounding halo, if any. However, it is small enough to allow a reasonable estimate of the local PSF shape.

Through trial and error, it was realized that the first 10 basis vectors are sufficient to recreate most of the PSF shape. This constitutes about 10% of the entire set of basis vectors showing that the chosen basis set is quite compact.

Figure 4.8 shows the original image for 2MASS 15590208-1844142 (left panel), the PSF estimate (center panel) and the residuals after subtraction (right panel). The color scale in the left and center panels are matched. The color scale for the residuals has been reduced by a factor of ten to increase contrast and show the details of the residual speckles.

We plan measure the aperture flux of the primary star on the PSF estimate and of the secondary in the residual image. In cases where the companion is not visible, we can only calculate the detection limit from the residual. Unfortunately, at the time of writing, this remains a work in progress.

As shown in Figure 4.6, Amara & Quanz (2012) calculated the systematic errors in flux estimation by injecting simulated planets in to ADI data from the NACO instrument at the 8-m VLT and comparing the measured fluxes to the original values. They observed that the measured fluxes were consistently lower than the original fluxes of the planets. However, we cannot directly use their estimates of the systematic offset for two reasons: (a) their dataset used ADI for suppressing speckles whereas the Robo-AO dataset does not and (b) the planet-star contrasts tested in their simulations were between 8 to 11 magnitudes which are a much higher contrast than those of the sub-stellar companions we are attempting to study. It is planned to redo the simulations for a sample of Robo-AO PSFs to estimate the systematic errors in our measurements.

[3]PCA was developed by Karl Pearson in 1901.

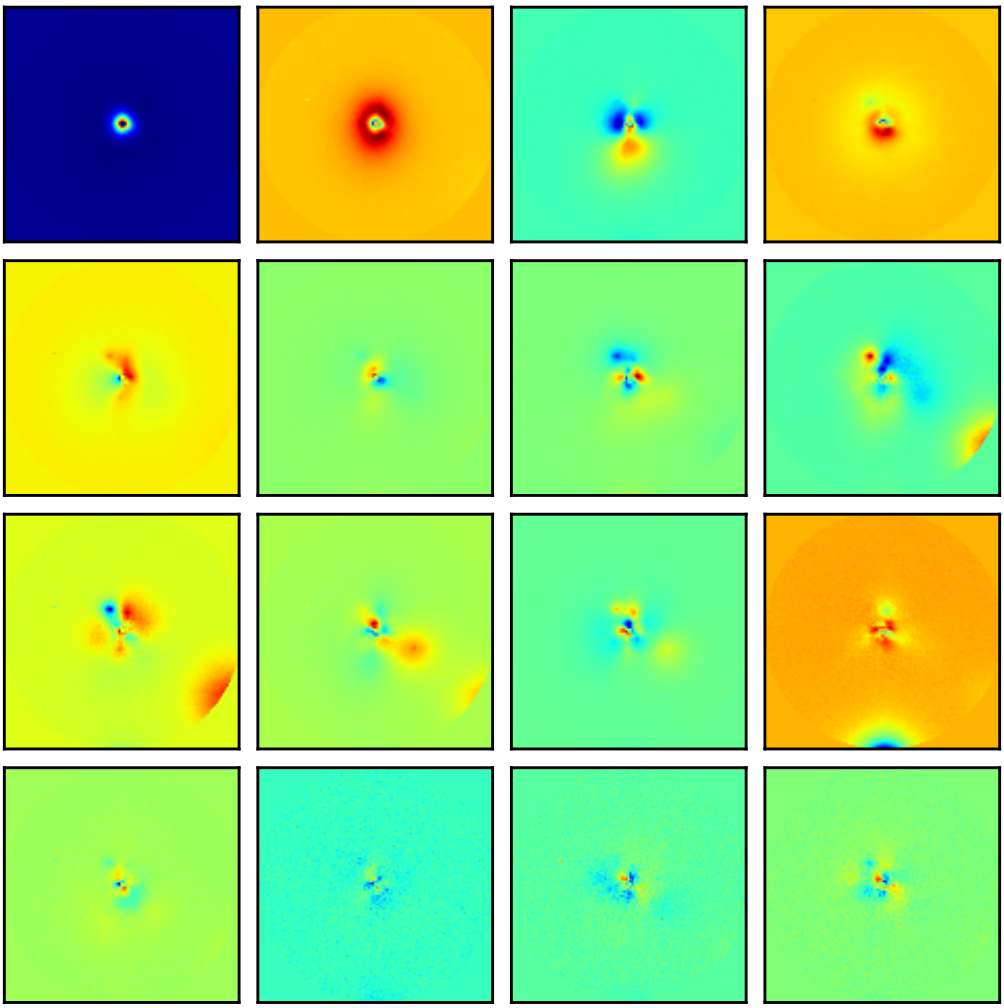

Figure 4.7. The basis functions generated from the Robo-AO SDSS i' band images are shown. The plots correspond to the first sixteen modes seen from left to right and top to bottom. Each image is 300 pixels (6.6″) in size.

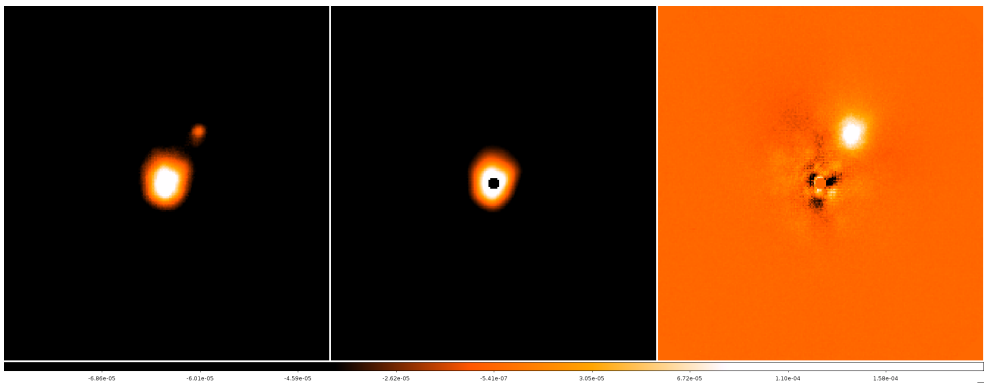

Figure 4.8. The original image of 2MASS 15590208-1844142 is shown in the left panel. The center panel is the PSF estimate formed by masking the obvious companion in the left panel. The color scales of the left and center panels have been matched. The right panel shows the residuals left after subtracting the PSF estimate from the original image. The color scale has been reduced by a factor of 10 to show the residual speckles in higher contrast.

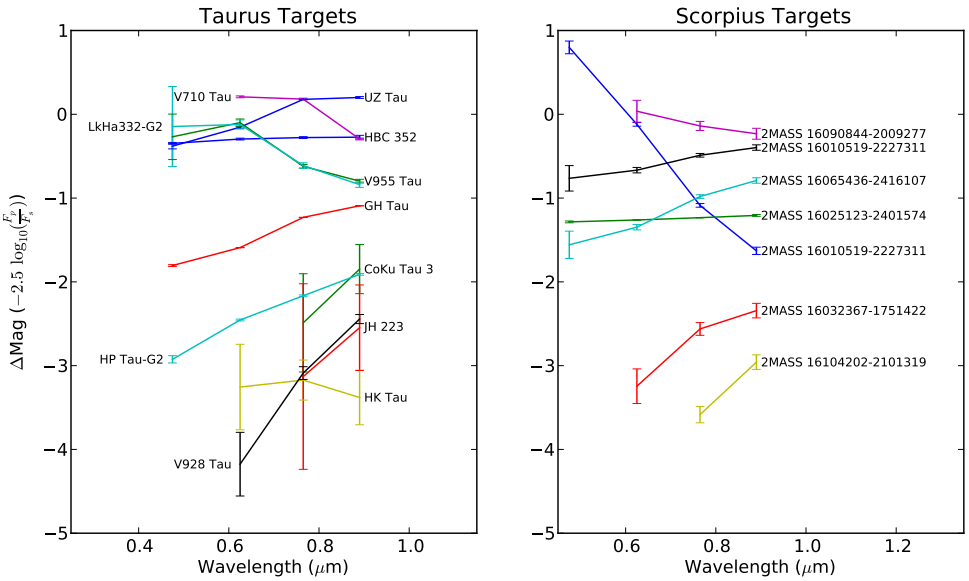

Figure 4.9. The flux ratios of widely separated ($> 1''$) stars measured using aperture photometry are plotted as a function of wavelength. The y axis is in units of the magnitude difference in each filter.

4.3.3 Aperture Photometry of Widely Separated Systems

While the PSF fitting work was in progress, performed aperture photometry on the targets where the images were widely separated (sep $> 1''$). The flux ratios and errors were calcu-

lated in each filter where the companion was visible. Figure 4.9 shows the relative fluxes plotted in magnitude differences as a function of wavelengths.

4.4 Future Work

At the time of writing, work on this project is ongoing. In the upcoming months, we shall add the PSF fitted flux ratios of the closely separated binaries and estimate stellar model parameters by fitting isochrones to the data and publish our conclusions from the resulting analysis.

This work will benefit greatly from the new HgCdTe detector based IR camera (Section 2.1.2.3) that will be installed on Robo-AO in early 2014A. This will allow Robo-AO to measure quasi-simultaneous SEDs from r' to K band and continue to monitor these variable objects.

Chapter 5

Survey of Magnetar Proper Motions

5.1 Introduction

Magnetars were proposed (Thompson & Duncan, 1995, 1996) as a unified model to explain the phenomena of soft gamma repeaters (SGRs) and anomalous X-ray pulsars (AXPs). Magnetars, unlike canonical radio pulsars, would have a very high magnetic field strength B ($\sim 10^{14}$ G) such that their internal energy was dominated by their magnetic energy rather than their rotational energy. The SGR flares were explained as resulting from violent magnetic reconnections and crustal quakes and the quiescent X-ray emission of AXPs (which is much larger than their spin-down luminosity) was attributed to the decay of intense magnetic fields. The discovery of large period derivatives ($\dot{P} \sim 10^{-10}\,\mathrm{s\,s^{-1}}$; Kouveliotou et al., 1998) confirmed the basic expectation of the magnetar model. For recent reviews of observational and theoretical progress in the field we refer the readers to Mereghetti (2008) and Hurley (2011).

Despite the successes of the magnetar model, we have little understanding of why only some neutron stars are born as magnetars. Originally, Thompson & Duncan (1993) invoked a rapidly spinning ($\sim$ one to three millisecond) proto-neutron star as essential for strong amplification of a seed magnetic field. The rapidly spinning neutron stars would result in a supernova more energetic than a canonical core-collapse supernova.

The observational support for the formation mechanism of magnetars appears to be lacking. Vink & Kuiper (2006) showed that the three supernova remnants (SNRs) to which three magnetars are best paired, (Kes 73, CTB 109 and N49), are completely consistent with the standard supernova explosion energies.

The offset between SGR 0525−66 (previously known as "5 March 1979") and its surrounding supernova remnant N49 and the notion that some halo SGRs might explain a fraction of GRBs led to the expectation of SGRs having high space motion (see Rothschild & Lingenfelter, 1996). This spawned a number of efforts to measure the space motions of magnetars.

Here, we present astrometric observations of six magnetars: two of the youngest magnetars: SGR 1806−20 and SGR 1900+14, two old AXPs: AXP 1E 2259+586 and AXP 4U 0142+61 and two other magnetars: SGR 1E 1841-045 and SGR 0501+4516. The resulting measurements of proper motion allow us to trace back SGR 1806−20 and SGR 1900+14 to their

Table 5.1. Characteristics of SGR 1806−20 and SGR 1900+14.

	SGR 1806−20	SGR 1900+14
Period P (sec)	7.6022(7)	5.19987(7)
$\dot{P}$ (10^{-11} s s^{-1}) [a]	49	17
$P/\dot{P}$ (kyr)	0.32	1.8
$B_{\rm Surf}$ (10^{14} G)	24	7.0
R.A (J2000)	$18^{\rm h}\,08^{\rm m}\,39.337^{\rm s}$	$19^{\rm h}\,07^{\rm m}\,14.31^{\rm s}$
Dec (J2000)	$20^{\circ}\,24'\,39.85''$	$9^{\circ}\,19'\,19.74''$

[a]Average period derivative calculated from X-ray period measurements from literature. See Section 5.5.2

Note. — Refer to http://www.physics.mcgill.ca/$\sim$pulsar/magnetar/main.html. Positions are from *Chandra* X-ray observations.

potential birth sites and additionally measure the space motions as well. We have measured the kinematic ages of these two magnetars. We also discuss the search for the birth-sites of AXP 4U 0142+61 and SGR 0501+4516. This chapter is composed from two journal papers, a conference proceedings and an yet unpublished result (SGR 0501+4516).

This chapter is organized as follows[1]. In Section 5.2, we summarize our knowledge of these two magnetars. In Section 5.3, we describe our observations, data reduction methodology and analysis techniques for point spread function (PSF) fitting, relative astrometry and photometry. We present the results in Sections 5.4 and in Section 5.5 we discuss the significance of our proper motion measurements.

5.2 Targets

Tables 5.1and 5.2 summarizes the essential characteristics of our targets; SGR 1806−20, SGR 1900+14, AXP 1E 2259+586 and AXP 4U 0142+61.. We discuss each target in further detail in the following sections.

5.2.1 SGR 1806−20

SGR 1806−20 (previously known as GB790107) was identified as a repeating gamma-ray burst with a soft spectrum by Laros et al. (1986). SGR 1806−20 is best known for its giant burst of December 27, 2004 (Hurley et al., 2005; Palmer et al., 2005) which was one

[1]This section composes of scientific material first published in two journal papers (Tendulkar et al., 2012, 2013) and a conference proceeding (Tendulkar, 2013) that has been reprinted with permission from the publishers: American Astronomical Society and the Cambridge University Press respectively.

Table 5.2. Characteristics of AXP 1E 2259+586 and AXP 4U 0142+61.

	AXP 1E 2259+586	AXP 4U 0142+61
Period P (sec)	6.9789484460(39)	8.68832877(2)
$\dot{P}$ (10^{-11} s s^{-1})	0.048430(8)	0.20332(7)
$P/\dot{P}$ (kyr)	460	136
$B_{\rm Surf}$ (10^{14} G)	0.59	1.3
R.A (J2000)	$23^{\rm h}\,01^{\rm m}\,08.295^{\rm s}$	$01^{\rm h}\,46^{\rm m}\,22.407^{\rm s}$
Dec (J2000)	$+58^\circ\,52'\,44.45''$	$+61^\circ\,45'\,03.19''$

Note. — Refer to http://www.physics.mcgill.ca/$\sim$pulsar/magnetar/main.html. Positions are from *Chandra* X-ray observations.

of the brightest cosmic flares ever detected. The burst was followed by a long lived radio afterglow (Cameron et al., 2005; Gaensler et al., 2005; Spreeuw et al., 2010) which allowed the precise localization of the source.

5.2.1.1 Association with Star Cluster

SGR 1806−20 lies in a radio nebula G10.0-0.3 (Kulkarni et al., 1995) which is a part of the W31 HII complex. It was earlier suggested that the massive star LBV 1806−20 and its surrounding radio nebula were associated with SGR 1806−20 (van Kerkwijk et al., 1995) but precise *Chandra* localization (Kaplan et al., 2002) proved that SGR 1806−20 was 14″ away from the center of G10.0-0.3 and 12″ away from LBV 1806−20. A cluster of massive stars, coincident with a mid-IR nebulosity, was discovered by Fuchs et al. (1999) about 7″ to the north of the magnetar.

Table 5.3 lists all the distance measurements reported to date. We place a higher premium for distance estimates related to the X-ray counterpart of SGR 1806−20 or the associated cluster of massive stars over the estimates to LBV 1806−20, since it is unclear whether LBV 1806−20 is physically near the magnetar. In Table 5.3, measurements 1–4 are distances to SGR 1806−20 or the cluster of massive stars and measurements 5 and 6 are distances to LBV 1806−20. We adopt a nominal distance of 9 ± 2 kpc which is consistent with all the measurements.

5.2.1.2 IR Counterpart

Figure 5.1 shows a 2×2 arcsec cutout near SGR 1806−20 from our laser guide star adaptive optics (LGS-AO) supported observations in the K_s band using the NIRC2 instrument (See Section 5.3 for details). Star A was suggested as the NIR counterpart for SGR 1806−20 by Kosugi et al. (2005) and independently by Israel et al. (2005) based on NIR variability over the 2004 active period. Using the NAOS-CONICA instrument on the 8.1-m Very Large

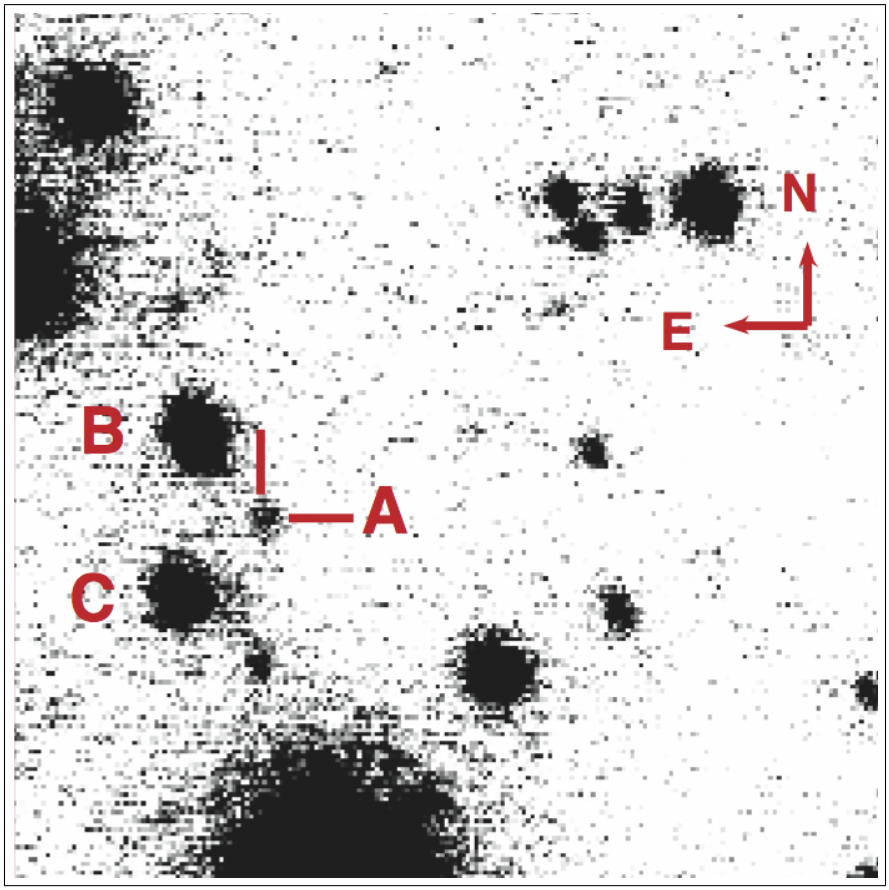

Figure 5.1. A 2×2 arcsec cutout near SGR 1806−20 from a K_s band LGS-AO supported observation from the NIRC2 camera. The IR counterpart, as identified by (Kosugi et al., 2005; Israel et al., 2005) is marked with cross hairs and labeled A as per (Israel et al., 2005) as are stars B and C.

Table 5.3. Distance to SGR 1806−20 measured by various authors.

	Reference	Distance (kpc)	Comments
1	Cameron et al. (2005)	$6.5 - 9.8$	HI absorption from Dec 2004 flare
2	McClure-Griffiths & Gaensler (2005)	> 6.5	HI absorption from Dec 2004 flare
3	Svirski et al. (2011)	$9.4 - 18.6$	X-ray scattering echos
4	Bibby et al. (2008)	$8.7^{+1.8}_{-1.5}$	Spectral classification, IR photometry and cluster isochrones
5	Figer et al. (2004)	11.8 ± 0.5	Radial Velocity (RV) of LBV 1806
6	Eikenberry et al. (2004)	$15^{+1.8}_{-1.3}$	RV of LBV 1806 and surrounding nebula and Galactic rotation curve
		strictly > 9.5	Luminosity of cluster stars
		strictly > 5.7	Ammonia absorption to LBV 1806

Telescope, Israel et al. (2005) monitored SGR 1806−20 on 11 epochs between March and October 2004. They measured a factor of two increase in the flux of the star A with a $>$ 9-σ confidence. The IR flux increase corresponded well with X-ray flux that also increased by a factor of two in the 2–10 keV and 20–100 keV bands (*XMM-Newton, INTEGRAL*; Mereghetti et al., 2005b,a). Our photometric measurements show a factor of three variability in the brightness of the same object (Section 5.4.1). The identification of the IR counterpart of SGR 1806−20 appears to be secure.

5.2.2 SGR 1900+14

The first bursts from SGR 1900+14 (originally known as B1900+14) were identified by Mazets et al. (1979). A very bright flare was detected on August 27 1998 with a γ-ray peak followed by a 300-s long tail (Hurley et al., 1999; Kouveliotou et al., 1999). Following the burst, a fading radio (Frail et al., 1999) and X-ray source (Hurley et al., 1999) was discovered. These observations led to a precise localization to within $0.15''$.

5.2.2.1 Association with Star Cluster

SGR 1900+14 is located near two objects from which it could have originated. A cluster of massive stars (Vrba et al., 2000), hidden behind two bright M5 super-giants, lies $12''$ to the east of SGR 1900+14 and a 10^4 yr old, $12'$ diameter SNR G042.8+00.6 lies $17'$ to the south-east (Mazets et al., 1979; Kouveliotou et al., 1993; Vasisht et al., 1994). If SGR 1900+14 was associated with the cluster of massive stars then it implies a young age and a space velocity close to the canonical value for pulsars. However, if it is associated with the supernova remnant then it would have a very high proper motion. An upper limit to the proper motion (based on *Chandra* X-ray observatory imaging observations) of ≤ 100 milli-arcsecond yr^{-1} is nominally inconsistent with the association of SGR 1900+14 with the SNR (Kaplan et al., 2009; de Luca et al., 2009).

Wachter et al. (2008) reported the discovery of an infrared elliptical ring or shell surrounding SGR 1900+14 which was interpreted as a dust-free cavity created by the giant flare of August 1998. The authors concluded that SGR 1900+14 is unambiguously associated with the afore mentioned star cluster.

With adaptive-optics assisted Keck/NIRC2 imaging and Keck/NIRSPEC spectroscopy of the cluster near SGR 1900, Davies et al. (2009) estimated the progenitor mass to be 17 ± 2 $M_\odot$ which is much lower than the progenitor masses estimated for other magnetars (~ 40 to $50\,M_\odot$).

5.2.2.2 Distance

Vrba et al. (1996) showed that the bright IR sources noted by Hartmann et al. (1996) at the *ROSAT* localization of SGR 1900+14 were M5 super-giant stars at a distance of 12 to 15 kpc with an extinction of $A_V \approx 19.2$ mag. Davies et al. (2009) measured a radial velocity of $-15.5 \pm 4\,\mathrm{km\,s^{-1}}$ for the cluster of stars implying a distance of 12.5 ± 1.7 kpc using the measured model of Galactic rotation. We adopt the measurement of Davies et al. (2009) for the distance to SGR 1900+14.

5.2.2.3 IR counterpart

Figure 5.2 shows a 4×4 arcsec K_s band image from our LGS-AO observations with the NIRC2 camera around the X-ray position of SGR 1900+14. The stars are labelled as per Testa et al. (2008). They obtained two K_S band AO observations of the same field around SGR 1900+14 with VLT NACO instrument in March and July 2006. Star 7 was the only source inside the radio-position error circle (dashed circle in Figure 5.2) that showed a photometric variability. They detected a 3-σ increase in the flux of star 7 and proposed it as the IR counterpart of SGR 1900+14. We accept the counterpart proposed by Testa et al. (2008).

In an attempt to gather additional evidence for the identification of the IR counterpart, we have measured K_p band photometric variability and $H - K_p$ colour for the stars in the field. These measurements are reported in Section 5.4.2. However, during this period, the X-ray counterpart did not show significant variability. Hence the absence of NIR variation of the proposed counterpart does not provide any new insights.

We report (in Section 5.4) that the proper motion of star 6 lies along the Galactic rotation curve, whereas the proper motion of star 7 is significantly different from those of galactic stars. This evidence strengthens the identification of star 7 as the IR counterpart of SGR 1900+14.

5.2.3 AXP 1E 2259+586

AXP 1E 2259+586 was discovered by Gregory & Fahlman (1980) as a bright point source (then designated GF 2259+586) at the center of curvature of a 36′ diameter semi-circular arc (then designated G109.1−1.0, now CTB 109). Fahlman & Gregory (1981) reported that the central source was an X-ray pulsar with a period of 3.4890 ± 0.0002 s. Later observations

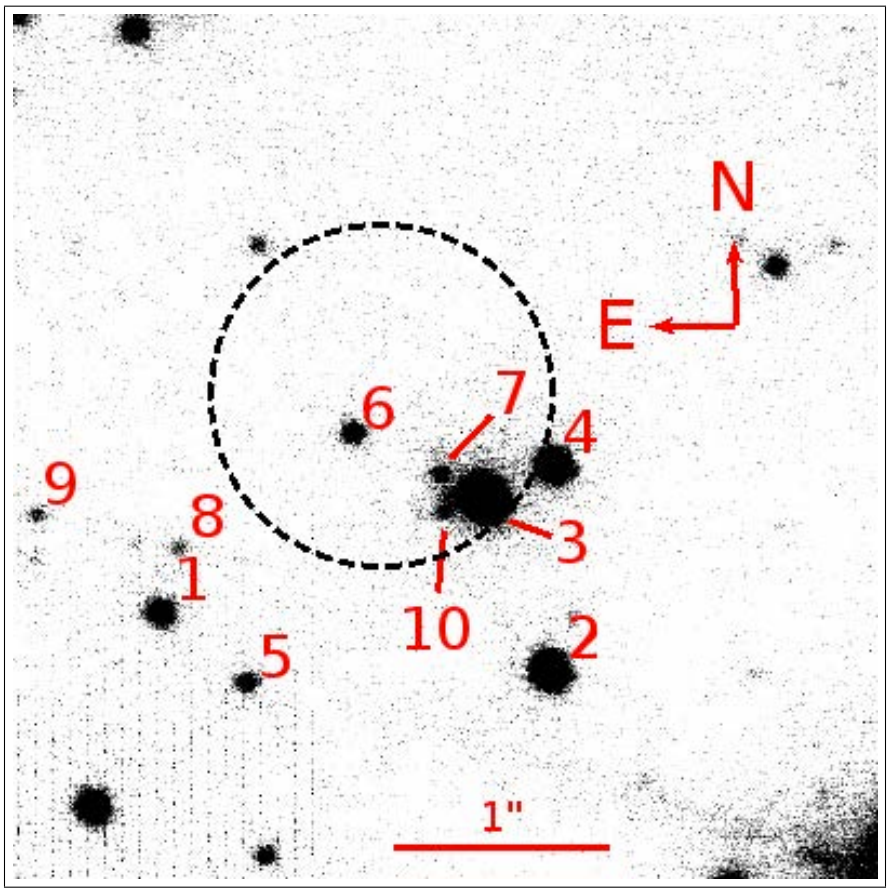

Figure 5.2. A 4×4 arcsec cutout near SGR 1900+14 from a K_s band LGS-AO supported observation from the NIRC2 camera. Stars are labelled as per Testa et al. (2008). The black circle is centered on the radio position of SGR 1900+14 from Frail et al. (1999) and encircles the $0.8''$ radius, 99%-confidence circle from Testa et al. (2008) the positions from which are used for our absolute astrometry. Star 7 is the proposed counterpart of SGR 1900+14 based on its variability.

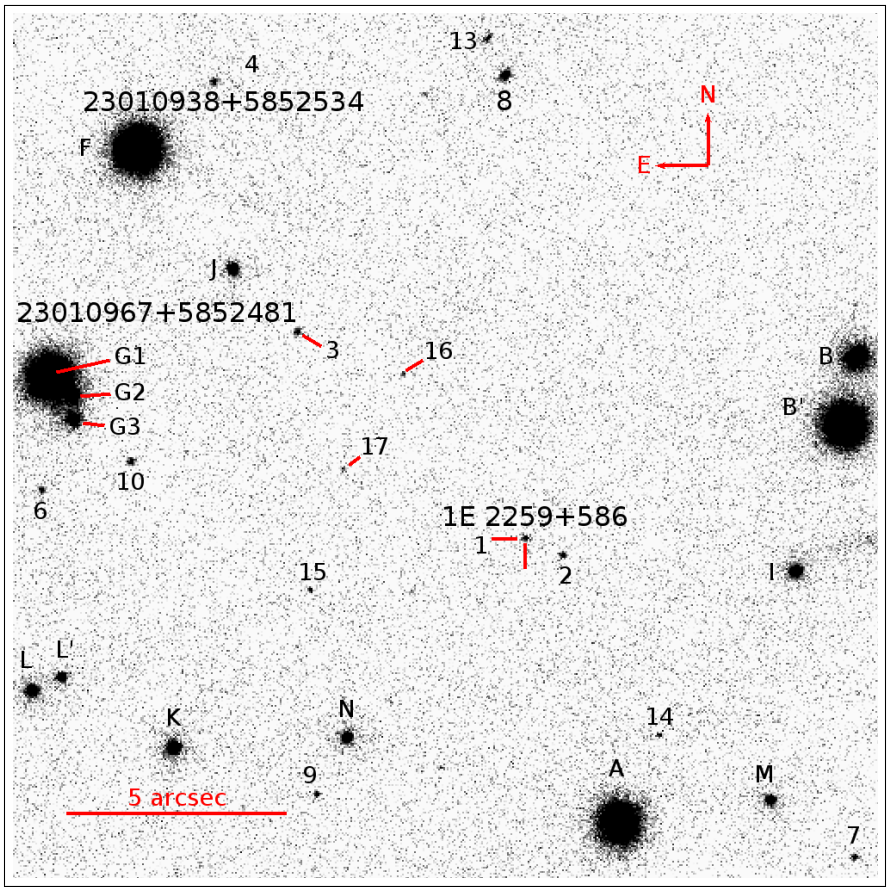

Figure 5.3. A 20″× 20″ K_p band image around AXP 1E 2259+586 acquired with the NIRC2 camera and the Keck LGS-AO system. Stars are labelled as per Hulleman et al. (2001). Star G of Hulleman et al. (2001) was resolved into 3 separate stars which we labelled as G1, G2 and G3. Stars 14, 15, 16 and 17 are new to Hulleman et al. (2001) and are labelled afresh. The counterpart to AXP 1E 2259+586 labelled 1 is marked by cross-hairs (colored red in the online version of this paper). The 2MASS stars 2MASS 23010938+5852534 and 2MASS 23010967+5852481 correspond to stars F and the G complex respectively.

showed that the fundamental period of the pulsar was 6.978725 s (Morini et al., 1988) and a spin-down rate of 6.2×10^{-13} s s^{-1} (Koyama et al., 1989).

5.2.3.1 Optical/IR Counterpart

Hulleman et al. (2001) detected a faint IR source (K_s = 21.7) at the refined position from the *Chandra X-ray Observatory*. SGR-like X-ray bursts (Kaspi et al., 2002a, 2003) on June 18, 2002 and a resultant NIR brightening confirmed the source (Kaspi et al., 2002b) identified by Hulleman et al. (2001). Figure 5.3 is a 20″ × 20″ K_p band image from our data showing the neighborhood of AXP 1E 2259+586. The stars are labelled as per the labeling scheme of Hulleman et al. (2001) with new detections marked with new labels as described

in the figure caption.

5.2.3.2 Characteristics of CTB 109

The location of AXP 1E 2259+586 within 4′ of the geometric center of CTB 109 (Fahlman & Gregory, 1981) and the very small number of X-ray sources in the neighborhood were significant evidence for the association of AXP 1E 2259+586 with CTB 109 with a false coincidence probability of $\approx 10^{-4}$ (Gaensler et al., 2001). The center of the SNR is located at RA (J2000)= $23^{\rm h}\,01^{\rm m}\,39^{\rm s}$, Dec (J2000)= $+58^\circ\,53'\,00''$) (Kothes et al., 2006). AXP 1E 2259+586 lies at $\Delta{\rm RA}\cos\delta = 3'58''$ due west and $\Delta\delta = 16''$ due south of the center of CTB 109.

5.2.3.3 Distance:

There have been multiple recent estimates of the distance to CTB 109 and AXP 1E 2259+586. Kothes & Foster (2012) gathered all observational limits of the distance (from Kothes et al., 2002; Durant & van Kerkwijk, 2006; Tian et al., 2010) and estimated a consensus distance of 3.2 ± 0.2 kpc to CTB 109 placing it inside the Perseus spiral arm of the Milky Way.

5.2.4 AXP 4U 0142+61

AXP 4U 0142+61 was discovered as a soft spectrum X-ray source in the *UHURU* survey (Giacconi et al., 1972). It remained an unexceptional source till 8.7 s X-ray pulsations were discovered through *ASCA* observations by Israel et al. (1993, 1994), including it in the AXP-binarity debate.

5.2.4.1 Optical/IR Counterpart

Hulleman et al. (2000a) located an optical counterpart (R= 24.98 and I= 23.84) coincident with the *EINSTEIN HRI* and *ROSAT* position. The presence of optical pulsations at a period of 8.7 s (Kern & Martin, 2002) confirmed the source identified by Hulleman et al. (2000a) as the counterpart of AXP 4U 0142+61. Later observations by Hulleman et al. (2004) showed that the counterpart was much brighter in IR with ($K_s = 19.8$) and showed a variability of 0.5 mag over a period of a year. Figure 5.4 is a $20'' \times 20''$ K_p band image from our data showing the neighborhood of AXP 4U 0142+61. We used the labelled catalog stars as photometric references to calculate the photometric zeropoints for each epoch.

5.2.4.2 Distance and Neighborhood

Using the red-clump method, Durant & van Kerkwijk (2006) estimated the distance to AXP 4U 0142+61 to be 3.6 ± 0.4 kpc. Radio searches for SNRs in the neighborhood of AXP 4U 0142+61 (Gaensler et al., 2001) failed to detect any emission to a limit of 0.2 mJy beam^{-1} (corresponding to an SNR surface brightness of 3.5×10^{-23} W m^{-2} Hz^{-1} sr^{-1}. AXP 4U 0142+61 is not currently associated with an SNR or a cluster of young stars. With our proper motion measurement, we can narrow down the search to a cone with an opening angle of 24°. We discuss this further in Section 5.4.

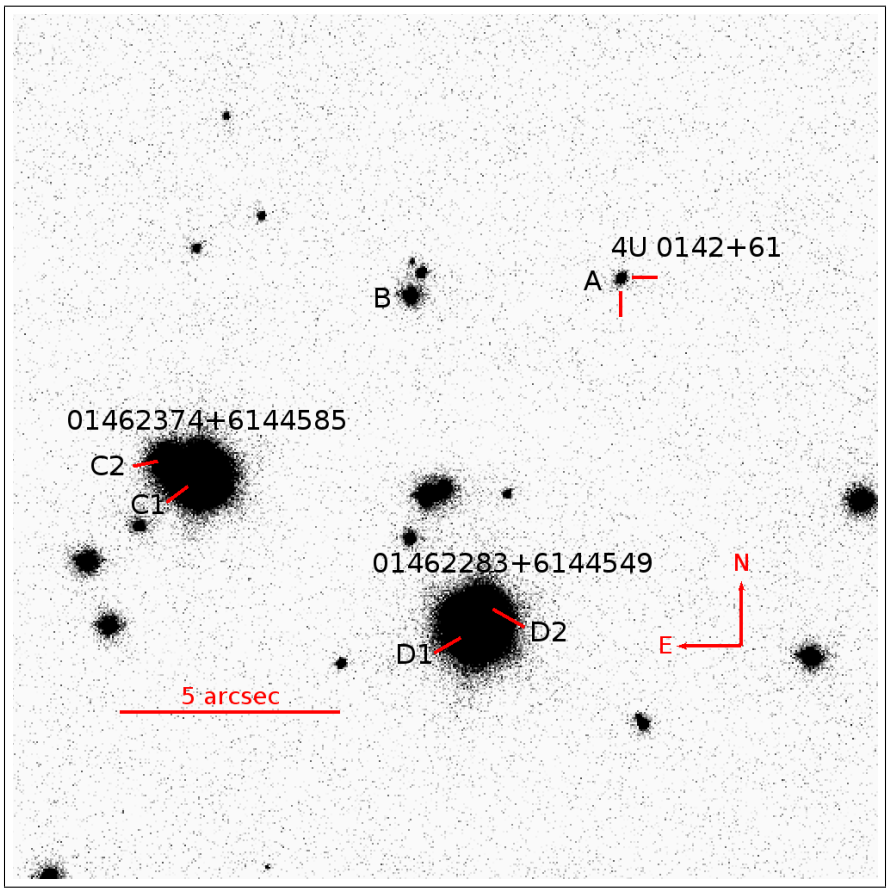

Figure 5.4. A 20″× 20″ K_p band image around AXP 4U 0142+61 acquired with the NIRC2 camera and the Keck LGS-AO system. Star A is the optical and IR counterpart of AXP 4U 0142+61 as proposed by Hulleman et al. (2000b) and confirmed by Kern & Martin (2002). The 2MASS stars 2MASS 01462374+6144585 and 2MASS 01462283+6144549 are resolved into two components C1, C2 and D1, D2 respectively. The blended magnitudes of the components are used to anchor the zeropoints of the image.

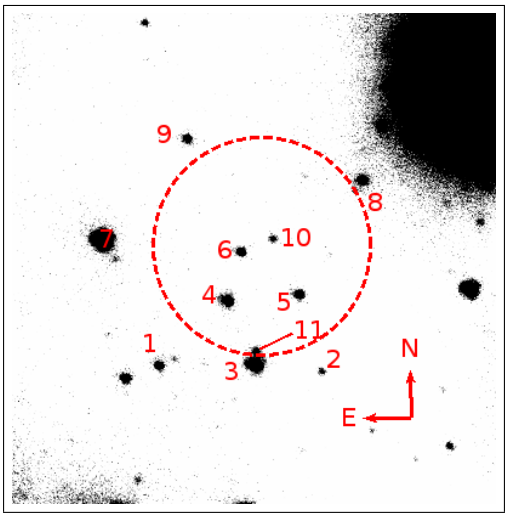

Figure 5.5. A $4 \times 4''$ K_s band image around the *Chandra* position of AXP 1E 1841−045 (Wachter et al. 2004). The red circle is the 3-σ position error ($0.9''$ radius). Sources are labelled as per Testa et al. (2008). None of the sources in the error circle are conclusively identified as the counterpart of the magnetar.

5.2.5 SGR 0501+4516

SGR 0501+4516 was discovered in 2008 as a burst detected by the Swift BAT telescope (Holland et al., 2008). The OIR counterpart was immediately reported by Tanvir & Varricatt (2008) as a $K \approx 18.6$ magnitude source. Gaensler & Chatterjee (2008) suggested that the proximity of SGR 0501+4516 to the edge of SNR HB9 and the absence of other SNRs in a radius of 15° pointed strongly to the association of SGR 0501+4516 and HB9. However, the separation of the SGR from the center of HB(was about $80'$ and would imply an angular velocity of $\sim 0.''7$ to $1.''2\,\mathrm{yr}^{-1}$ (Göğüş et al., 2010) which would be easily detectable. Using archival NIRC2 and HST data, we were able to show that this association is not possible given the proper motion of the magnetar.

5.2.6 AXP 1E 1841−045

AXP 1841−045 was discovered as a slowly rotating ($P_{\mathrm{rot}} = 11.8\,\mathrm{s}$) X-ray pulsar in the supernova remnant Kes 73 by Vasisht & Gotthelf (1997) from ASCA timing. Testa et al. (2008) proposed a NIR counterpart for AXP 1E 1841−045 but the identification was not conclusive. We observed AXP 1841−045 using the LGS-AO and the NIRC2 camera on 9 epochs between 2005 and 2009. The coadded exposure time between 15 to 45 minutes at each epoch depending on the observing circumstances. The limiting magnitude for each coadded observation was $K_s \approx 21$ mag.

Figure 5.5 shows a $4 \times 4''$ cutout from our K_s band image around the X-ray position of AXP 1E 1841−045 (red circle, Wachter et al. 2004). We registered our NIRC2 images to the 2MASS catalog with RMS residuals of 20 milli-arcseconds. The accuracy of the

Table 5.4. Summary of observations of SGR 1806−20.

Date & MJD (UTC MJD)	Filt	Cam	Exp (s)
2005-03-04 53433.641	K_p	N	1440 ✓
2005-04-30 53490.511	K_p	N	750
2005-08-10 53592.366	K_p	W	600
2005-08-11 53593.344	K_p	W	840
2005-09-26 53639.258	K_p	N	600 ✓
2006-07-03 53919.403	K_p	N	2820
2006-08-17 53964.304	K_p	N	1800 ✓
2007-05-22 54242.487	K_p	N	1020
2007-06-11 54262.403	K_p	N	2040
2007-07-16 54297.345	K_p	N	3000
2007-08-06 54318.329	K_p	N	2640 ✓
2008-05-21 54607.468	K_p	N	2460
2008-06-29 54646.407	K_p	N	3360
2008-07-26 54673.342	K_p	N	3180 ✓
2010-06-18 55365.442	K_p	W	80

Note. — A ✓ in Column 4 marks the images used for astrometric measurements.

2MASS coordinates for the brightness of our registration stars (K_s mag ≈ 11) is 70 − 80 milli-arcseconds. Testa et al. (2008) proposed star 9 as the counterpart for the AXP based on a 3-σ photometric variability. However, our astrometry shows that it lies outside the *Chandra* error circle. Given the NIR flux to X-ray flux ratios for other magnetars and the quiescent X-ray flux from AXP 1E 1841−045, it is highly probable that one of the objects in the field is the NIR counterpart of the magnetar.

5.3 Observations and Analysis

5.3.1 Observations

Starting in 2005 to the present time, we undertook a program for astrometric monitoring of magnetars with the 10-meter Keck 2 telescope using the Laser Guide Star Adaptive Optics (LGS-AO; Wizinowich et al., 2006; van Dam et al., 2006) and the Near-Infrared Camera 2 (NIRC2). The log of our observations can be found in Tables 5.4, 5.5, 5.6, 5.7 and 5.8.

5.3.1.1 NIRC2

The NIRC2 instrument has two modes: wide (W) and narrow (N) with a field-of-view (FoV) of ≈ 10 × 10 arcsecond and ≈ 40 × 40 arcsecond respectively. The corresponding pixel scales

Table 5.5. Summary of observations of SGR 1900+14.

Date & Time (UTC)	Filt	Cam	Exp (s)
2005-04-30 53490.558	K_p	N	1300 ✓
2005-08-09 53591.434	K_p	W	2400
2005-08-10 53592.400	K_p	W	300
2005-09-26 53639.349	K_p	W	720
2006-07-03 53919.472	K_p	N	1980
2006-07-04 53920.511	K_p	N	1920
2006-08-17 53964.439	K_p	N	1140 ✓
2006-10-13 54021.242	K_p	N	2220
2007-05-22 54242.550	K_p	N	1500 ✓
2007-06-11 54262.553	K_p	N	1260 ✓
2007-06-11 54262.582	H	N	660
2007-08-06 54318.455	K_p	N	1800 ✓
2007-11-03 54407.229	K_p	N	1260 ✓
2008-05-21 54607.564	K_p	N	1260
2008-06-29 54646.471	K_p	N	3660
2008-07-26 54673.405	K_p	N	2280 ✓
2008-10-22 54761.227	K_p	N	1680 ✓
2009-04-06 54927.599	K_p	N	1620
2009-07-17 55029.340	K_p	N	2100 ✓
2009-08-04 55047.346	K_p	N	2100
2009-09-29 55103.226	K_p	N	2340
2010-06-18 55365.470	K_p	N	2340 ✓

Note. — A ✓ in Column 4 marks the images used for astrometric measurements.

Table 5.6. Observations of AXP 1E 2259+586.

MJD UTC (DDDDD.D YY-MM-DD)	Filt	Airmass	Exp (s)	Notes[a]
53592.428 05-08-10	K_p	1.39	780	A
53592.437 05-08-10	H	1.36	840	F
53639.453 05-09-26	K_p	1.39	1320	A
53919.556 06-07-03	K_p	1.33	1140	A
53920.557 06-07-04	K_p	1.33	1080	F
53964.536 06-08-17	K_p	1.33	1800	AR
54021.299 06-10-13	K_p	1.30	900	A
54089.230 06-12-20	K_p	1.41	1980	A
54262.601 07-06-11	K_p	1.37	960	N
54318.553 07-08-06	K_p	1.31	2100	N
54407.362 07-11-03	K_p	1.42	1260	N
54646.563 08-06-29	K_p	1.34	3060	A
54673.534 08-07-26	K_p	1.29	3000	A
54761.330 08-10-22	K_p	1.30	3600	A
55029.524 09-07-17	K_p	1.32	1800	N
55047.471 09-08-04	K_p	1.33	3600	F
55103.368 09-09-29	K_p	1.29	3420	NG
56070.582 12-05-23	K_p	1.65	1680	NG
56160.463 12-08-21	K_p	1.29	4860	AG
56206.395 12-10-06	K_p	1.32	2340	AG

[a]Notes: A: Counterpart detected and used for astrometry
F: Counterpart detection was not sufficient for astrometry
G: Glare on the lower right corner of the detector
N: Counterpart not detected
R: Reference image for astrometry and photometry.

Table 5.7. Observations of AXP 4U 0142+61.

MJD UTC (DDDDD.D YY-MM-DD)	Filt	Airmass	Exp (s)	Notes[a]
53639.579 05-09-26	K_p	1.47412	1440.	A
53919.584 06-07-03	K_p	1.70994	2100.	F
53964.593 06-08-17	K_p	1.34345	2100.	AR
54021.550 06-10-13	K_p	1.53298	1500.	A
54089.299 06-12-20	K_p	1.3668	1860.	A
54318.621 07-08-06	K_p	1.34419	660.	A
54407.434 07-11-03	K_p	1.37516	1260.	F
54673.591 08-07-26	K_p	1.4195	1800.	A
54761.444 08-10-22	K_p	1.35228	2400.	A
55029.575 09-07-17	K_p	1.55636	1800.	F
55047.602 09-08-04	K_p	1.36098	2400.	A
55103.454 09-09-29	K_p	1.35571	1920.	FG
56206.446 12-10-06	K_p	1.34739	2700.	AG

[a]Notes: A: Counterpart detected and used for astrometry
F: Counterpart detection was not sufficient for astrometry
G: Glare on the lower right corner of the detector
N: Counterpart not detected
R: Reference image for astrometry and photometry.

Table 5.8. Observations of SGR 0501+4516.

MJD UTC (DDDDD.D YY-MM-DD)	Filt	Airmass	Exp (s)	Notes[a]
	NIRC2			
54704.600 08-08-26	K_p	–	–	A
56206.600 12-10-06	K_p	–	–	AG
56352.300 13-03-01	K_p	–	–	AG
	HST			
55488.100 10-10-19	F814W	–	–	AR

[a]Notes: A: Counterpart detected and used for astrometry
F: Counterpart detection was not sufficient for astrometry
G: Glare on the lower right corner of the detector
N: Counterpart not detected
R: Reference image for astrometry and photometry.

are 9.942 milli-arcsecond per pixel and 39.768 milli-arcsecond per pixel. The wide field images were obtained to aid transferring the photometry and astrometry from the low resolution 2MASS images to the small FoV narrow camera NIRC2 images. For SGR 1806−20 and SGR 1900+14, the narrow field images were used for the astrometric measurements. We are constrained to use the wide camera for the astrometry of AXP 1E 2259+586 and AXP 4U 0142+61. The choice of the wide camera was dictated by the low stellar density: there would have been insufficient reference stars in the narrow camera images to perform accurate relative astrometry. The rest of the data analysis procedure is same. Based on weather and faintness of each magnetar, multiple short (∼20 s) exposures were chosen to avoid saturating the detector. The typical full width at half maximum (FWHM) achieved in these observations was ≈ 70 milli-arcsecond ≈ 7 pix.

Each of the NIRC2 camera images was inspected for quality. Images in which the AO correction was poor were rejected. The shallow images with acceptable AO correction were rejected for astrometry due to the non-detection of the magnetar and/or lack of sufficient reference stars but were used to photometric calculate upper limits on the brightness. The images used in the final proper motion measurement are denoted by a ✓ in Column 4 of Tables 5.4 and 5.5 and an "A" in Column 5 of Tables 5.6 and 5.7.

In observations acquired after August 2009, a faint glare was observed on the lower right corner (south-west corner) of the detector. The shape and amplitude of the glare was variable with telescope orientation and was not correctable through surface fitting or modeling. The glare was masked in our reduction, thereby improving the astrometry of unmasked stars at the expense of losing a fraction of the stars available for astrometry. The images affected by the glare are flagged with a "G" in Column 5 of Tables 5.6 and 5.7.

5.3.2 Data Analysis

The images from the NIRC2 camera were reduced using the FITS analysis package `pyraf` in a standard manner by subtracting corresponding dark frames and flat-fielded using appropriate dome-flats. A sky fringe frame was made by combining dithered images of multiple targets with the bright stars masked. We used `SExtractor` (Bertin & Arnouts, 1996) for the preliminary detection and masking of stars. The fringe frame was subtracted after being scaled to the appropriate sky background level. Before coadding the frames, each frame was corrected for optical distortion using a distortion solution measured for NIRC2[2].

5.3.2.1 PSF Fitting

We used the `IDL` package `StarFinder` (Diolaiti et al., 2000) to perform PSF estimation, fitting and subtraction. This code iteratively estimates a normalized PSF shape from user selected stars, while subtracting faint neighboring stars to minimize the contamination of the PSF estimate. `StarFinder` fits a constant PSF shape over the entire field of view (FoV). This assumption appears to work well for the NIRC2 narrow camera FoV. The uniformity of the PSF over the FoV also mitigates the errors from centroiding variable PSFs.

[2]See http://www2.keck.hawaii.edu/inst/nirc2/forReDoc/post_observing/dewarp/

AO PSFs differ from PSFs obtained from atmospheric seeing limited observations in two aspects: Firstly, because the AO correction decorrelates as a function of distance from the AO reference source (i.e. sodium laser beacon), the PSF varies radially across the field of view. Secondly, since AO correction cannot correct all of the wavefront errors caused by atmospheric turbulence, even on-axis, AO PSFs have a distinctive shape with a sharp diffraction-limited (FWHM $\sim \lambda/D_{tel}$) core and a wide (FWHM $\sim$ atmospheric seeing) shallow halo around it. For the Keck AO system, these components are 44 milli-arcsecond and ~ 1 arcsecond respectively. The order of magnitude difference in size and brightness of the two components makes it challenging to accurately measure and subtract the PSF in the image. We describe how both these challenges are handled in the next paragraph.

To further reduce the effect of PSF variations, relative photometry and astrometry measurements were down-weighted farther away from the object under consideration. The details of the relative weighting are described in Section 5.3.2.2. The PSF model size was chosen to be 200 pixels (1.95 arcsecond) wide to encompass both the core and the halo of the PSF. The few brightest stars in each of the fields were used for estimating the halo contribution.

5.3.2.2 Relative Astrometry

Cameron et al. (2009) demonstrated a framework for high precision astrometry ($< 100\,\mu$arcsecond) through an optimal estimation technique that availed the correlations in stellar position jitter. We use the same methodology with modifications for including the proper motions of the stars over multiple epochs and an appropriate weighting scheme.

The dominant source of astrometric error in the single epoch, short exposure images of Cameron et al. (2009) was tip-tilt anisoplanatism. For our coadded long exposure images the tip-tilt anisoplanatism is averaged out. We constructed the covariance matrix theoretically using geometry of the field and a typical turbulence profile from Mauna Kea. The residual distortion of the NIRC2 distortion solution has a root-mean-square value of 1 milli-arcsecond. However the distortion residuals have higher values towards the edges[3]. To reduce the effect of residual distortion, especially in images with significant dithering, a separation-weighted measurement scheme (the θ term used below) was used to downweight stars far from the target.

To account for the proper motions of all the stars in the field, it was necessary to include the proper motion estimates in the framework and simultaneously estimate a least-squares fit for grid positions and proper motions. Given $N + 1$ stars detected in the field, the measurement of the offset between the target star and each of the remaining stars results in a set of vectors at each of the E epochs.

The differential offsets between star 0 and the grid of N reference stars at epoch k is written as a single column vector,

$$\mathbf{d}_{0k} = [x_{01}, \ldots, x_{0N}, y_{01}, \ldots, y_{0N}]_k^T.$$

Here $x_{ij} = x_j - x_i$ is the distance between the x-coordinate of the j^{th} reference star and the

[3] http://www2.keck.hawaii.edu/inst/nirc2/forReDoc/post_observing/dewarp/

x-coordinate of the i^{th} target star, and likewise for y. The goal of differential astrometry is to use $\mathbf{d}$ to determine the position of the target star with respect to the reference grid of stars at each epoch.

We use a linear combination of the elements of $\mathbf{d}$ with weights $\mathbf{W_i}$ to obtain the relative position of target star i at epoch k,

$$\mathbf{p}_{ik} = \mathbf{W}_i \mathbf{d}_{ik},$$

where, for example, the weight matrix for star 0, $\mathbf{W}_0$ is

$$\mathbf{W}_0 = \begin{bmatrix} w_{xx,01} & \dots & w_{xx,0N} & w_{xy,01} & \dots & w_{xy,0N} \\ w_{yx,01} & \dots & w_{yx,0N} & w_{yy,01} & \dots & w_{yy,0N} \end{bmatrix}.$$

We calculated weights as follows: $w^{-1}_{xx,ij} = w^{-1}_{yy,ij} = \sigma^2_{ij}$. Here $\sigma^2_{ij} = \sigma^2_m + \sigma^2_{TJ}\theta^2_{ij}$, where σ^2_{TJ} is the geometric mean of the parallel and perpendicular components of the tip-tilt jitter as defined in Equation 1 of Cameron et al. (2009); and θ_{ij} is the angular offset between the star i and the star j. We have used the notation $w_{xy,0j}$ to denote the weighting of the offset from the target star ($i = 0$) to star indexed j in the y direction which is used to determine the x component of the target's position, $\mathbf{p}$.

We assume a simple linear model for the stellar motion where $x = z_x + v_x t$. The differential offsets are thus a column vector,

$$\mathbf{d}_0 = \begin{bmatrix} z_{x,1} + v_{x,1}t - (z_{x,0} + v_{x,0}t) \\ \vdots \\ z_{x,N} + v_{x,N}t - (z_{x,0} + v_{x,0}t) \\ z_{y,1} + v_{y,1}t - (z_{y,0} + v_{y,0}t) \\ \vdots \\ z_{y,N} + v_{y,N}t - (z_{y,0} + v_{y,0}t) \end{bmatrix}$$

and the unknown quantities are,

$$\mathbf{b} = [z_{x,0}, \quad \dots \quad , z_{x,N}, v_{x,0}, \dots, v_{x,N}, \tag{5.1}$$

$$\dots, z_{y,0}, \quad \dots \quad , z_{y,N}, v_{y,0}, \dots, v_{y,N}]^T. \tag{5.2}$$

We solve for the variables $\mathbf{b}$ from the vector $\mathbf{d}$ given weights $\mathbf{W}$ in the least squares sense. For a given target, we use the same weights for all epochs. The overall x and y shifts of each image (i.e. the registration of the image) are fit as free parameters in this method.

NIRC2 is mounted at the Nasmyth focus of the Keck II telescope. A field-rotator allows the observer to set the position angle of the instrument. Our default position angle was zero degrees (North is up and East is to the left on the detector). However, there are small errors in the setting of the field rotator as well as tracking errors.

To measure this, we chose the images obtained on May 22, 2007 as the reference image for both the targets. The reference images were chosen on the basis of good AO correction

and image depth. We computed the rotation-angle and the plate-scale of the image at each epoch with respect to the reference image. We find that the rotation angle is within 0.5 degrees and the image scaling is within 0.1% relative to those of the reference image. The stellar position grids were corrected for the measured rotation and plate-scale changes before measuring their proper motions.

To understand the systematic effects caused by our choice of grid stars, we re-analyzed the centroiding data after randomly eliminating a selected number of stars from the reference grid. We compared the results to those obtained from our entire grid of stars. For example, by eliminating one randomly chosen star out of the 50 stars in the SGR 1900+14 field, the proper motions of all other stars change by $\Delta(\mu_\alpha, \mu_\delta) = (7.6 \pm 15.4, 17.1 \pm 13.7) \times 10^{-3}$ milli-arcseconds yr^{-1}. This is much smaller than our statistical errors of ~ 1 milli-arcsecond yr^{-1}. Hence we conclude that the choice of our reference grid is robust and does not add significant errors to our measurements.

5.3.2.3 Galactic Rotation

Since our relative astrometry framework calculates the proper motion of each object with respect to a grid of neighboring stars (i.e. with respect to the average motion of all other stars), it implicitly assumes that the net velocity of the field is zero. However, this is not true since the rotation of the Galaxy and the peculiar velocity of the Sun with respect to the local standard of rest (LSR) cause significant motions at the precision we seek. Our framework cannot measure the net velocity of the field without prior knowledge of the absolute motion of a few stars or equivalently, the absolute non-motion of an extra-galactic object in the field.

To correct for this effect, we need to calculate the mean galactic proper motion of all the stars in the field along the line of sight given by Galactic longitude and latitude (l, b). We modeled the differential rotation of the Galaxy and the local velocity of the Sun and calculated the effective proper motion of an object at a given position (r, l, b) in the Milky Way, where r is the distance away from the Sun. We made a model assuming the local velocity of the Sun to be $(U, V, W) = (10.0, 5.2, 7.2)\,\mathrm{km\,s^{-1}}$ (Dehnen & Binney, 1998) and that the Galaxy is rotating with a constant circular speed outside of $R_1 = 2\,\mathrm{kpc}$ of $220\,\mathrm{km\,s^{-1}}$, decreasing linearly inside of that R_1 (Binney & Tremaine, 2008). We set the distance from the Sun to the center of the Galaxy to $R_0 = 8.0\,\mathrm{kpc}$ (Eisenhauer et al., 2003). From the rotation curve, we calculate the Galactic proper motion $\vec{\mu}_{\mathrm{Gal}} = [\mu_\alpha, \mu_\delta]_{\mathrm{Gal}}$ of objects at various distances ($1\,\mathrm{kpc} \leq r \leq 20\,\mathrm{kpc}$) in the direction (l, b) of the magnetar that are moving with the Galactic flow.

We estimate the number density of stars in the Milky Way using the model calculated by Jurić et al. (2008) using SDSS data. They fit a thin disk, thick disk and a halo to the SDSS data set and calculate the number density function based on their fit. Along the line of sight, the number of stars in our field at a distance r from the Sun is proportional to $r^2\rho(R, Z)$, where $\rho(R, Z)$ is the number density of stars at the cylindrical coordinates $(R(r, l, b), Z(r, l, b))$ in the Milky Way.

For a given field, we calculate the velocity of the field $\vec{\mu}_{\mathrm{Field}} = [\mu_\alpha, \mu_\delta]_{\mathrm{Field}}$ as the integral of the proper motion weighted with the number density as described above. This gives,

Table 5.9. Proper motions calculated from the Galactic rotation model.

Object ID	Distance (kpc)	(l, b) (deg)	$\vec{\mu}_{\rm Field}$ $[\mu_\alpha, \mu_\delta]$ (milli-arcsecond yr^{-1})	$\vec{\mu}_{\rm Gal}$ $[\mu_\alpha, \mu_\delta]$ (milli-arcsecond yr^{-1})
SGR 1806−20	9 ± 2	$(10.0, -0.2)$	$[3.0, 4.8]$	$[4.2 \pm 0.9, 7.0 \pm 1.8]$
SGR 1900+14	12.5 ± 1.7	$(43.0, +0.8)$	$[2.7, 4.6]$	$[2.7 \pm 0.2, 4.8 \pm 0.4]$
AXP 1E 2259+586	3.2 ± 0.2	$(109.1, -0.996)$	$[2.1, 0.63]$	$[3.52 \pm 0.1, 0.69 \pm 0.03]$
AXP 4U 0142+61	3.6 ± 0.4	$(129.4, -0.431)$	$[0.97, -0.48]$	$[1.48 \pm 0.01, -0.98 \pm 0.06]$

$$\vec{\mu}_{\rm Field} = \frac{\int_{r_{min}}^{r_{max}} r^2 \rho(R(r,l,b), Z(r,l,b)) \times [\mu_{\alpha,\delta}(r,l,b)_{\rm Gal}] {\rm d}r}{\int_{r_{min}}^{r_{max}} r^2 \rho(R(r,l,b), Z(r,l,b)) {\rm d}r}.$$

Thus, the total proper motion of each object in the sky is $\vec{\mu}_{{\rm Sky},i} = \vec{\mu}_{{\rm R},i} + \vec{\mu}_{\rm Field}$. Table 5.9 lists the calculated proper motion for the field and the Galactic proper motion for an object at the distance of the magnetar for the targets.

5.3.2.4 Peculiar Motion

We are interested in back-tracing the proper motion of the magnetar to identify its birthsite and estimate the time since it left the birthsite. The relevant motion for this measurement is the relative proper motion between the magnetar and its progenitor. A reasonable assumption is that the progenitor, likely a young massive star, was moving with the Galactic rotation curve. We define the peculiar motion of the magnetar as the difference between its total proper motion $\vec{\mu}_{{\rm Sky},i}$ and its expected Galactic proper motion $\vec{\mu}_{\rm Gal}$, i.e. $\vec{\mu}_{{\rm Sky},i} = \vec{\mu}_{\rm Gal} + \vec{\mu}_{\rm Pec}$.

With this definition, the transverse velocity of the magnetar relative to its neighborhood becomes $r|\vec{\mu}_{\rm Pec}|$ in a direction θ, s.t. $\tan(\theta) = (\mu_\alpha/\mu_\delta)_{\rm Pec}$ East of North.

5.3.2.5 Photometry

`StarFinder` calculates flux estimates for stars in the field by scaling the normalized PSF model to best fit the image. We calculate the photometric zero-point (ZP) for each image by comparing the magnitudes of stars to the 2 Micron All Sky Survey (2MASS) Point Source Catalog (Skrutskie et al., 2006) and to published high-resolution studies of the fields which were anchored to the 2MASS catalog. The details of comparison stars for each field are given in Section 5.4.

For the wide field images photometry was performed using the `pyraf apphot` toolset as the uncrowded fields did not require the use of PSF fitting. Over the 40″FoV, the AO PSF varies in shape. To mitigate the effects of the changing PSF on the photometric measurements, we utilized comparison stars within 10″of the magnetar target over which the PSF is observed not to vary appreciably. The magnitudes of the stars in our images were tied to the measurements from the 2 Micron All Sky Survey (2MASS) Point Source Catalog (Skrutskie

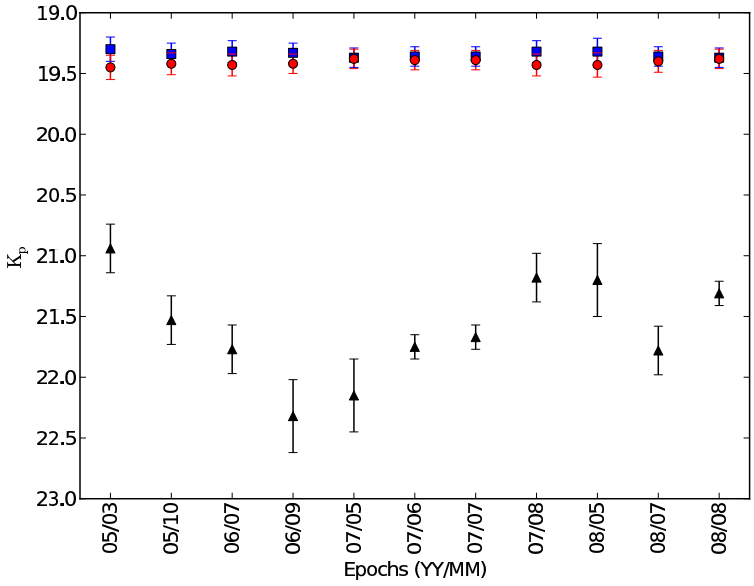

Figure 5.6. K_p magnitudes of stars around SGR 1806−20 measured over period of 3 years. The circles (red in the online version) correspond to star B and squares (blue in the online version) correspond to star C. The counterpart (star A) of SGR 1806−20 is marked by black triangles. We note a clear variation over a factor of 3 in the brightness of star A.

et al., 2006). In the fields of both AXP 1E 2259+586 and AXP 4U 0142+61, a number of 2MASS stars were found to have companions in our high-resolution images. We calculated a blending correction to the magnitudes measured from the NIRC2 images by combining the magnitudes of each star in a 3″radius (equal to the FWHM of the 2MASS star images of the magnetar fields). The combined magnitude is calculated as,

$$m_{blend} = -2.5 \log_{10}(\sum_i 10^{-m_i/2.5}),$$

where the m_i is the measured magnitude of the i^{th} star within the blending radius. We used the blended magnitudes to calculate the zeropoints of our images at each epoch and calculate the brightness of the magnetar.

5.4 Results

5.4.1 SGR 1806−20

We performed PSF fitting on the NIRC2 narrow camera images to identify 71 stars through 10 epochs. The positions of these 71 stars were used for relative astrometry.

We performed relative photometry on the stars A, B and C in Figure 5.1. The photometric zeropoints were measured by matching the magnitudes of stars B and C to the

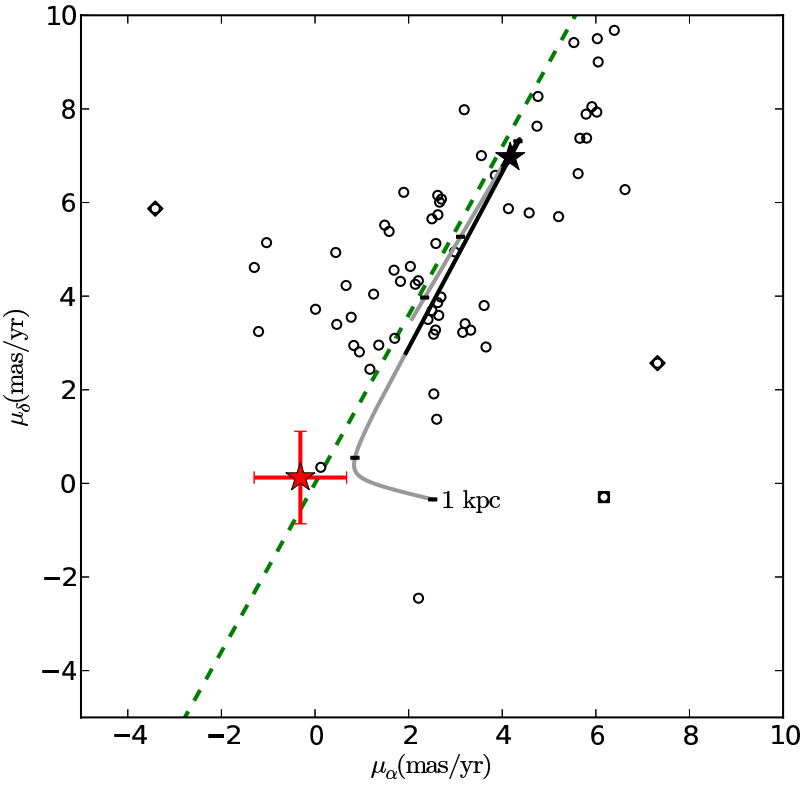

Figure 5.7. The proper motion of 71 stars in the field of SGR 1806−20 in the sky frame of reference. SGR 1806−20 is marked by the star with error bars (colored red in the online version). The remaining stars have only their best-fit values (hollow black circles) after adding the bulk motion of the field ($\vec{\mu}_{\rm Field} = (3.0, 4.8)$ milli-arcsecond yr^{-1}) (marked by a black '+'). The thick gray line represents the expected motion of stars from 1 to 22.8 kpc along this line of sight, as per the Galactic rotation model presented in Section 5.3.2.3. Black dashes along the line denote positions 1, 5, 10, 15 and 20 kpc away from the Sun. The section of the line representing objects at a distance of 9 ± 2 kpc from the Sun is marked with a black star and black line to denote the possible motion of the progenitor of SGR 1806−20. The dashed diagonal line (green in the online version) is the locus of objects with $\mu_b = 0$, i.e. with zero proper motion along galactic latitude. Other high proper-motion objects, probably halo stars are marked by diamonds. The square marks the nominally high proper-motion object near the edge of the detector. However, this measurement may be corrupted by distortion residuals and hence is not considered any further.

values measured by Kosugi et al. (2005). Figure 5.6 shows the measured magnitudes of the three stars. We observe a clear factor of 3 variation in the brightness of the IR counterpart of SGR 1806−20, star A, thus securing the identification of the IR counterpart of SGR 1806−20.

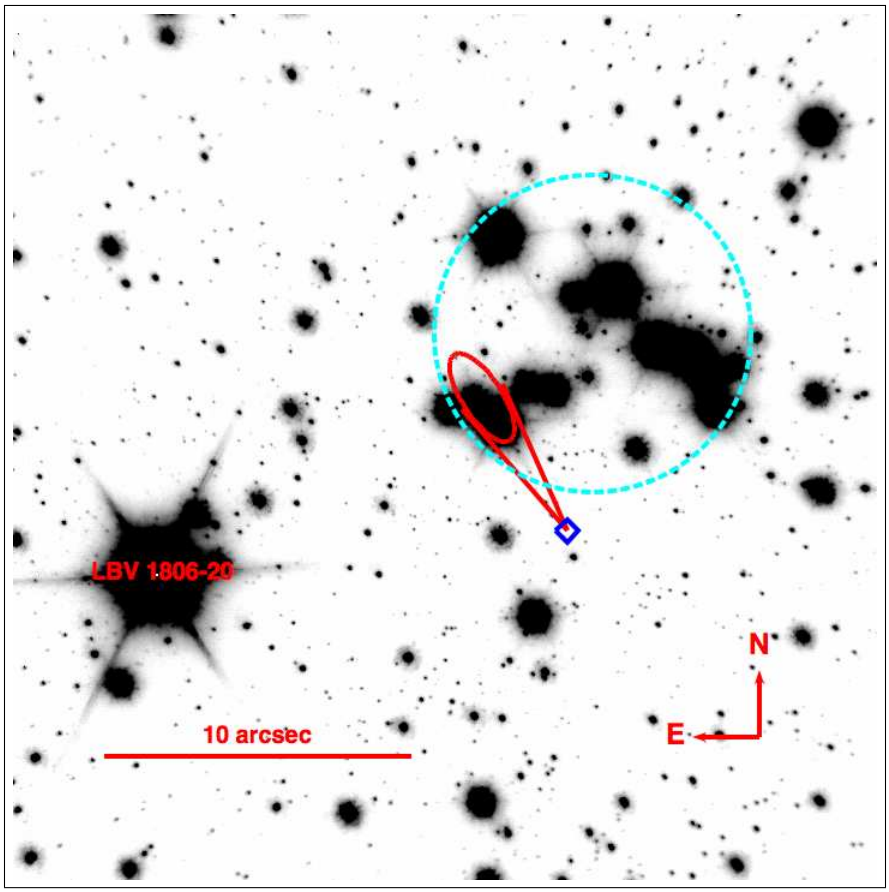

Figure 5.8. The position of SGR 1806−20 (diamond, blue in the online version) traced back by 0.65 kyr is marked by the ellipse (colored red in the online version). The size of the ellipse denotes the positional uncertainty corresponding to the uncertainty in the proper motion measurement. The solid lines (red in the online version) represent the 1-σ limits on the angle of motion. The dashed circle (cyan in the online version) denotes the cluster of massive stars corresponding to the mid-IR source of Fuchs et al. (1999). The position of the luminous blue variable LBV 1806−20 is marked.

5.4.1.1 Proper Motion

Figure 5.7 shows the measured proper motions of the stars in the SGR 1806−20 field. The field velocity correction was calculated to be $(\mu_\alpha, \mu_\delta)_{\rm Field} = (3.0, 4.8)$ milli-arcsecond yr^{-1}. The proper motion of SGR 1806−20 away from a putative progenitor in the galactic flow is $(\mu_\alpha, \mu_\delta) = (-4.5 \pm 1.4, -6.9 \pm 2.0)$ milli-arcsecond yr^{-1}. Assuming a distance of 9 ± 2 kpc, this corresponds to a linear velocity of 350 ± 100 km s^{-1} with an angle of $213^\circ \pm 10^\circ$ East of North.

Figure 5.8 shows the direction of motion of SGR 1806−20 with respect to its neighbors. Backtracing this space velocity would put the magnetar close to the cluster of massive stars about 650 years ago.

5.4.1.2 Other High Proper-Motion Stars

In Figure 5.7, we mark the high proper-motion objects with diamonds and squares. These stars deviate significantly from the dashed green line marking the locus of objects with $\mu_b = 0$, i.e. with zero proper motion along the galactic latitude. These are probably halo stars moving at a high speed through the Galactic disk.

5.4.2 SGR 1900+14

We observed SGR 1900+14 at 13 epochs with an exposure time of about 1 hour at each observation. Using K_p-band photometry and $H - K_p$ band color (at a single epoch), we present variability and color measurements of SGR 1900+14 and its surrounding stars. Our absolute astrometry is matched to positions as reported by Testa et al. (2008) with an accuracy of 6 milli-arcsecond. They reported a 3-σ astrometric uncertainty of $0.81''$ which we adopt for comparison with the radio position for Figure 5.2.

In three images of the SGR 1900+14 field that had excellent AO correction, we detected a faint source (labelled 10 in Figure 5.2) $0.2''$ away from star 3. Source 10 is not detected by Testa et al. (2008) as it was blended with star 3. However, we detected no variation in the combined brightness of star 3 and 10 in our data and the measurements from Testa et al. (2008) within 0.07 mag. Star 10 is a factor of ~ 40 fainter than star 3. With this ratio, assuming no variation in the light from star 3, we can constrain the maximum variation in the brightness of star 10 to be 0.4 mag as compared to the 0.48 mag variation measured for star 7 and no variation for star 3 reported by Testa et al. (2008). Thus, we continue to accept star 7 as the IR counterpart of SGR 1900+14.

5.4.2.1 Variability

Figure 5.9 shows the photometry of stars 2–7 (except 5)[4]. The median magnitude offsets of stars 2, 3 and 4 were used as relative ZP offsets and the absolute ZP offsets were calculated using K_p magnitudes as reported by Testa et al. (2008). The counterpart suggested by Testa et al. (2008), star 7, was not detected at the edge of star 3 on epochs when the images were not sufficiently deep or the AO performance was not satisfactory. The non-detections were marked with the upper limit on the flux (black triangles). Including the upper limits on flux, star 7 shows slight variability but it is not conclusive.

During our entire observation period from 2005 to 2010, the X-ray counterpart of SGR 1900+14 showed burst activity in only one period from March to June 2006 (Israel et al., 2008). Unfortunately, we have no IR observations between September 2005 and July 2006. Of these, the AO performance in July 2006 was not satisfactory leading to poor photometry and source confusion. As shown in Table 5.10, the persistent X-ray luminosity as measured by Israel et al. (2008) and Mereghetti et al. (2006) showed a slight increase in March 2006 and decreased to the pre-burst value by April 2006. Thus the lack of NIR variability is not surprising.

[4]Star 5 is excepted from all further discussion since it is far away from the X-ray position error circle and does not affect any of the conclusions. Its identification in the middle of the numbering range is an unfortunate quirk of the numbering scheme that was implemented in previous literature.

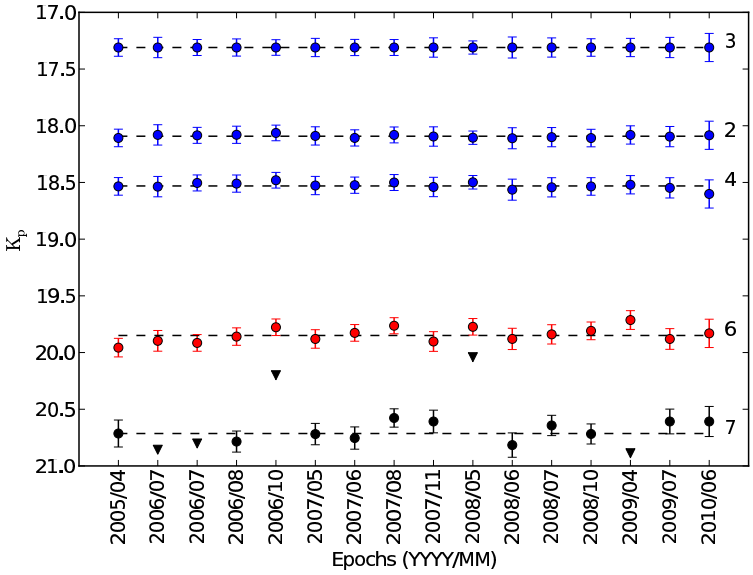

Figure 5.9. Relative photometry light-curves of stars 2–7 (except 5) around SGR 1900+14. To reduce the effect of PSF variations over the field, relative photometry was performed on nearby stars and the absolute calibration was performed by matching stars 2, 3 and 4 to their magnitudes as measured by Testa et al. (2008). The inverted triangles mark 3-σ upper limits for star 7 when it was not detected at the edge of star 3.

Table 5.10. Persistent X-ray luminosity of SGR 1900+14 in the 1-10 keV band.

Interval (UTC Date)	F_X (10^{-12} erg cm^{-2} s^{-1})
20 Sep 2005 - 22 Sep 2005	4.8 ± 0.2[a]
25 Mar 2006 - 27 Mar 2006	4.6 ± 0.8[b]
28 Mar 2006 - 28 Mar 2006	6.3 ± 1.7[b]
01 Apr 2006 - 01 Apr 2006	5.5 ± 0.4[a]
08 Apr 2006 - 10 Apr 2006	5.0 ± 1.4[b]
11 Apr 2006 - 15 Apr 2006	5.0 ± 0.7[b]

[a] Absorbed 0.8-12 keV flux from Mereghetti et al. (2006).

[b] Unabsorbed 1-10 keV flux from Israel et al. (2008).

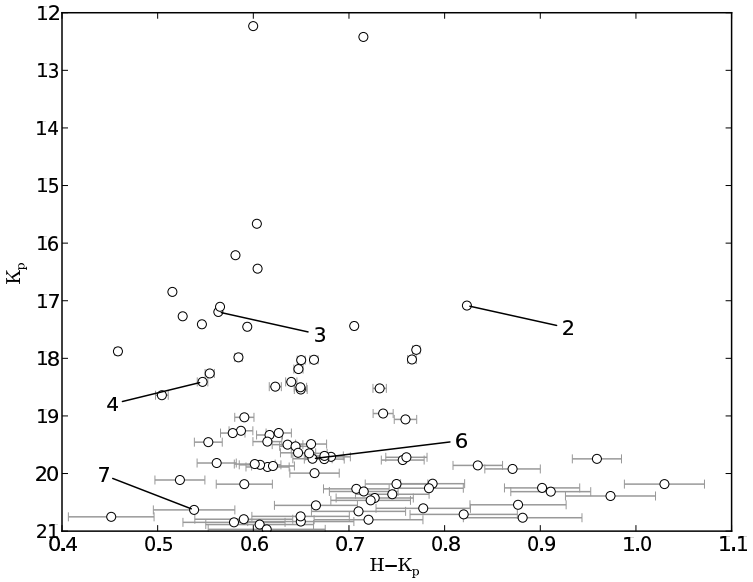

Figure 5.10. $H - K_p$ color vs K_p magnitude diagram for 50 stars in the SGR 1900+14 field. Stars 2–7 (except 5) are marked.The H band image zero-point has a systematic uncertainty of ~ 0.5 mag which would effectively only change the scale of the $x-$axis.

5.4.2.2 Color Measurement

During the June 11, 2007 observations, we obtained K_p and H band images of the field. These images were used to determine the colors of stars near SGR 1900+14. No high-resolution H band photometry of this field has been performed previously, so we chose to use 2MASS measurements of bright stars to calculate the ZP offsets for the H band image. The problem with this implementation was that stars bright enough to be included in the 2MASS catalog were were saturated in the NIRC2 images which were intended to image the faint magnetar. We rely on the reconstruction of the saturated cores of bright stars by `StarFinder`. This increases the error in photometric measurement and hence in the ZP estimate. We estimate this systematic error in H band ZP to be 0.5 mag. This systematic error changes the scaling on the x-axis of the color-magnitude diagram (Figure 5.10) and should not change the conclusion if the magnetar were to have a color distinctly different from other stars in the field.

Figure 5.10 shows an $H - K_p$ color vs. K_p magnitude diagram for the 50 stars in the field. Stars 2–7 are labeled. Neither star 6 nor star 7 have abnormal colors and neither is distinctive. There is no clear structure (for example, a main-sequence) in the color-magnitude diagram. This is probably due to the varied distances, ages and extinctions to the stars in this direction. Table 5.11 lists the H and K_p band magnitudes of stars 2–7 (except 5) as shown in Figure 5.10. Magnetars are not known to fall in a specific color band and our lack of understanding of the background physics prevents us from predicting the shape of the IR emission spectrum (Testa et al., 2008). We conclude that the lack of a

Table 5.11. H and K_p band photometry for stars near SGR 1900+14.

Object ID	RA (J2000) (deg)	Dec (J2000) (deg)	H band (mag)	K_p band (mag)
2	$19^h\,07^d\,14.28^s$	$9^\circ\,19'\,18.84''$	18.57 ± 0.003	17.98 ± 0.002
3	$19^h\,07^d\,14.30^s$	$9^\circ\,19'\,19.63''$	17.76 ± 0.002	17.19 ± 0.001
4	$19^h\,07^d\,14.28^s$	$9^\circ\,19'\,19.78''$	18.96 ± 0.005	18.41 ± 0.003
6	$19^h\,07^d\,14.34^s$	$9^\circ\,19'\,19.92''$	20.41 ± 0.02	19.74 ± 0.01
7	$19^h\,07^d\,14.31^s$	$9^\circ\,19'\,19.74''$	21.17 ± 0.04	20.63 ± 0.02

Note. — The zero-point error in the photometry is 0.5 mag for H band and 0.1 mag for K_p band.

distinctive color for any star near the location of SGR 1900+14 is not significant.

5.4.2.3 Proper Motion

Figure 5.11 shows the measured proper motions of 50 stars in the neighborhood of SGR 1900+14. The velocity offset, calculated from the galactic rotation, is $(\mu_\alpha, \mu_\delta)_{\rm Field} = (2.7, 4.6)$ milli-arcsecond $\rm yr^{-1}$. For star 7, we calculate a proper motion of $(\mu_\alpha, \mu_\delta) = (-2.1 \pm 0.4, 0.6 \pm 0.5)$ milli-arcsecond $\rm yr^{-1}$ away from a putative progenitor moving with the galactic flow. At a distance of 12.5 ± 1.7 kpc, this corresponds to a transverse space velocity of $130 \pm 30\,\rm km\,s^{-1}$.

Figure 5.12 shows the direction of motion of SGR 1900+14 with respect to its neighbors. Backtracing this space velocity would put the magnetar close to the cluster of massive stars about 6 kyr ago.

Star 6 and star 3 are the only two other sources detected inside the 3-σ error circle around the radio position of SGR 1900+14. Their velocities are marked by a black triangle (Star 6) and an inverted black triangle (Star 3) in Figure 5.11. Their velocities suggest that these are regular galactic stars moving in the plane of the galaxy (dashed green line).

Table 5.12 gives the proper motions measured for each of the stars 2–7 along with their corresponding transverse space velocity assuming a distance of 12.5 kpc.

5.4.3 AXP 1E 2259+586

5.4.4 Astrometry

We performed relative astrometry using a grid of 42 stars over 11 epochs. Of the original 45 stars, it was discovered that the centroiding of three stars located at the edges of the image was corrupted and these stars were velocity outliers. These three stars were removed from the proper motion framework. The robustness of our astrometric framework is demonstrated by the fact that the proper motion measurements changed by $\lesssim 0.1$ milli-arcsecond $\rm yr^{-1}$. Figure 5.13 shows the measured proper motions of the 42 stars in the field. The field velocity correction, as given in Table 5.9, was $(\mu_\alpha, \mu_\delta)_{\rm Field} = (2.1, 0.63)$ milli-arcsecond $\rm yr^{-1}$. The

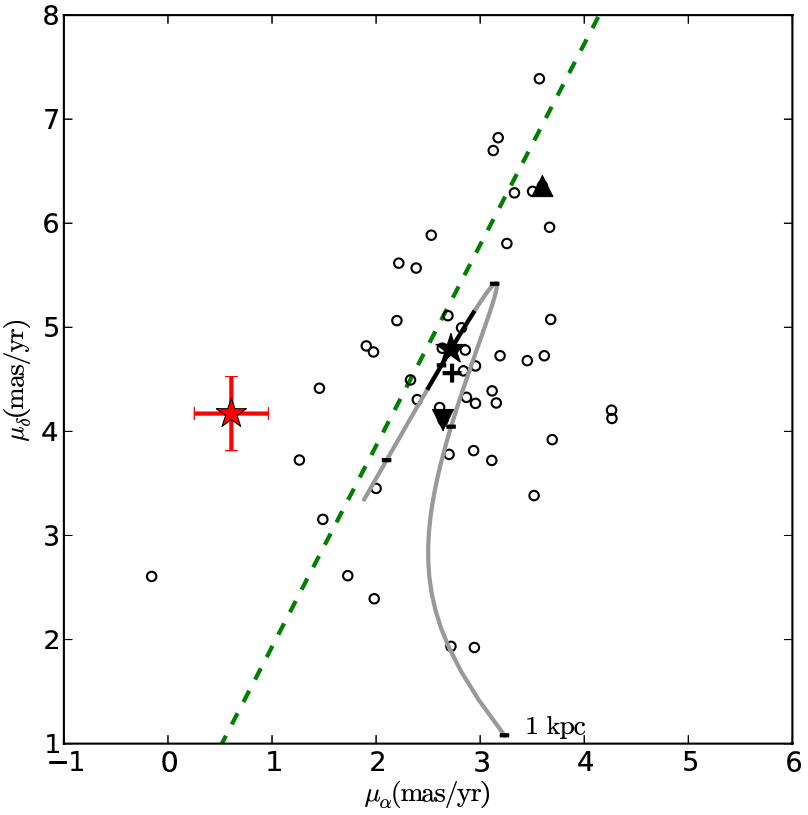

Figure 5.11. The proper motion of 50 stars in the field of SGR 1900+14 in the sky frame of reference. The putative counterpart of SGR 1900+14 is marked by the star with error bars (colored red in the online version). The proper motions of star 6 (solid black triangle) and star 3 (inverted black triangle) seem to lie along the Galactic rotation curve. The remaining stars have only their best-fit values (hollow black circles) after adding the bulk motion of the field ($\vec{\mu}_{\rm Field} = (2.7, 4.6)$ milli-arcsecond yr^{-1}) (marked by a black +). The thick gray line represents the expected motion of stars from 1 to 19.8 kpc along this line of sight, as per the Galactic rotation model presented in Section 5.3.2.3. Black dashes along the line denote positions 1, 5, 10, 15 and 20 kpc away from the Sun. The section of the line representing objects at a distance of 12.5 ± 1.7 kpc from the Sun is marked with a black star and a black line to denote the possible motion of the progenitor of SGR 1900+14. The dashed diagonal line (green in the online version) is the locus of objects with $\mu_b = 0$, i.e. with zero proper motion along galactic latitude.

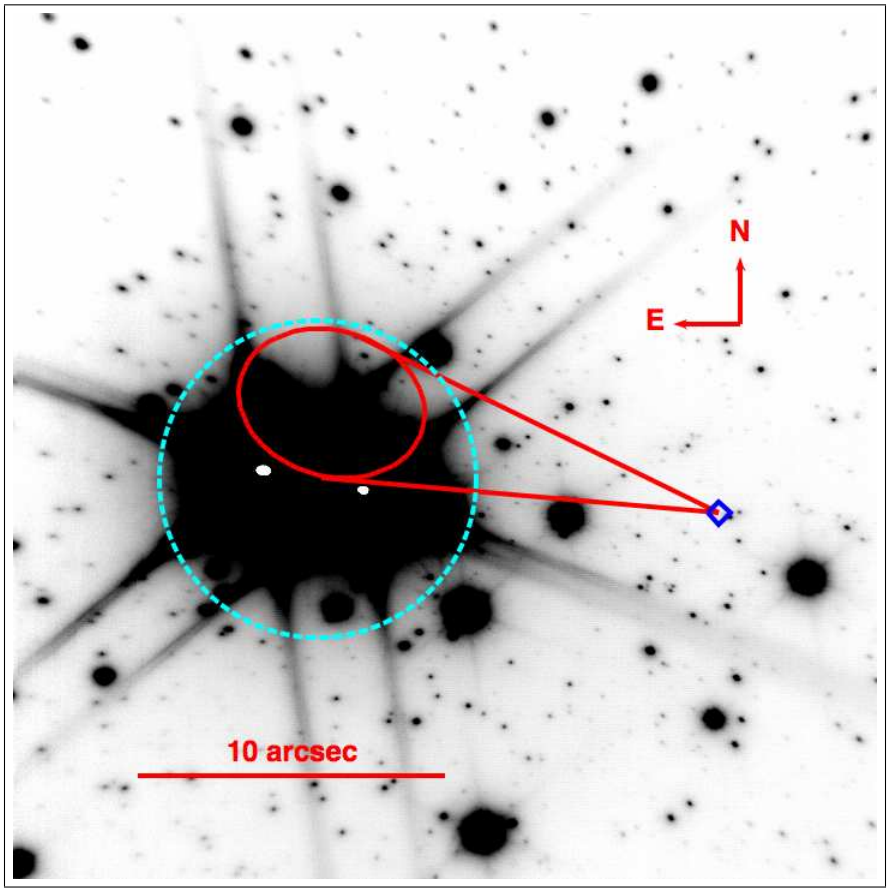

Figure 5.12. The position of the putative counterpart of SGR 1900+14 (blue diamond) traced back by 6 kyr is marked by the solid ellipse (red in the online version). The size of the ellipse denotes the positional uncertainty corresponding to the uncertainty in the proper motion measurement. The solid (red) lines represent the 1-σ limits on the angle of motion. The dashed circle (cyan in the online version) denotes the cluster of massive stars (Vrba et al., 2000).

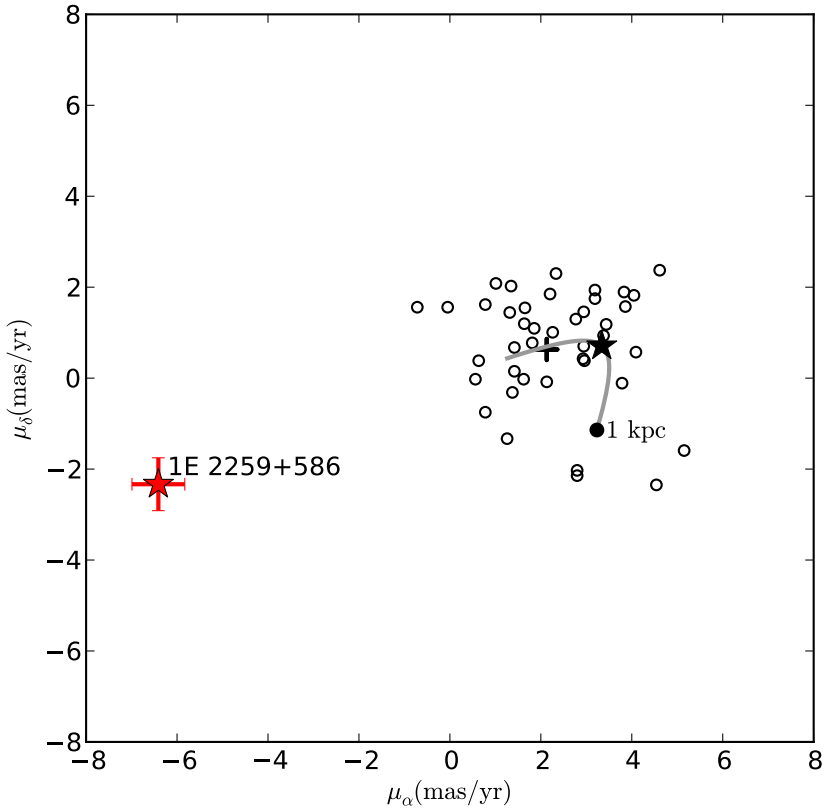

Figure 5.13. The proper motion of 42 stars in the field of AXP 1E 2259+586 in the sky frame of reference. The counterpart of AXP 1E 2259+586 is marked by the star with error bars (colored red in the online version). The remaining stars have only their best-fit values (hollow black circles) after adding the bulk motion of the field ($\vec{\mu}_{\rm Field} = (2.1, 0.63)$ milli-arcsecond yr^{-1}) (marked by a black +). The thick gray line represents the expected motion of stars from 1 to 20 kpc along this line of sight, as per the Galactic rotation model presented in Section 5.3.2.3. The filled black circle at the bottom end of the line denotes the Galactic rotation at 1 kpc away from the Sun. The section of the line representing objects at a distance of 3.2 ± 0.2 kpc from the Sun is marked with a black star and a black line to denote the possible motion of the progenitor of AXP 1E 2259+586.

Table 5.12. Proper motions measured for stars near SGR 1900+14.

Object	$\vec{\mu}_{\rm Pec}$ (milli-arcsecond yr^{-1})	Velocity (km s^{-1})	Direction E of N
2	$(-0.11, -0.55)$	33 ± 25	191 ± 143
3	$(-0.08, -0.67)$	40 ± 25	$\cdots$
4	$(-0.74, -2.39)$	148 ± 30	197 ± 10
6	$(+0.88, +1.58)$	107 ± 30	30 ± 12
7	$(-2.11, -0.61)$	130 ± 30	254 ± 10

Note. — The values have been corrected for the galactic rotation offsets. The transverse space velocities are calculated assuming a distance of 12.5 kpc. 1-σ error bars on $\vec{\mu}_{\rm Pec}$ are $(0.4, 0.5)$ milli-arcsecond yr^{-1}.

proper motion of the magnetar in the Galactic frame is $(\mu_\alpha, \mu_\delta) = (-6.4 \pm 0.6, -2.3 \pm 0.6)$ milli-arcsecond yr^{-1}. Assuming a distance of 3.2 ± 0.2 kpc, the Galactic proper motion of AXP 1E 2259+586 corresponds to a linear velocity of 103 ± 10 km s^{-1} with an angle of $250^\circ \pm 6^\circ$ East of North. Our measurement is in contrast to the proper motion measurement by Kaplan et al. (2009) from a 5 yr baseline *Chandra X-ray Observatory* images. However, we note that their statistical errors (40 milli-arcsecond yr^{-1}) are significantly larger than our precision (0.7 milli-arcsecond yr^{-1}).

The proper motion of AXP 1E 2259+586 away from its birth site is $(\mu_\alpha, \mu_\delta) = (-9.9 \pm 1.1, -3.0 \pm 1.1)$ milli-arcsecond yr^{-1} including the 15 km s^{-1} dispersion of the putative progenitor. The tangential component of the ejection velocity would be 157 ± 17 km s^{-1}. The proper motion vector is directed away from the center of CTB 109 providing conclusive evidence for the link between AXP 1E 2259+586 and CTB 109.

Figure 5.14 shows the movement of the magnetar overlaid on an *XMM Newton* mosaic of CTB 109. The current center of the SNR is located at RA (J2000)= $23^{\rm h}\,01^{\rm m}\,34^{\rm s}$, Dec (J2000)= $+58^\circ\,53'\,00''$) (Kothes et al., 2006, quoted without an error estimate). We estimated an error by manually estimating the best fit circle to the outside of the SNR shell. We conservatively estimate that the position of the center is accurate to a radius of $30''$. However, this position cannot be used to estimate a kinematic age for AXP 1E 2259+586 because the apparent centers of SNR are known to shift due to uneven expansion. We discuss this further in Section 5.5.

5.4.5 Photometry

Figure 5.15 shows the photometric measurements of AXP 1E 2259+586 from September 2005 to October 2012. AXP 1E 2259+586 has not shown much X-ray or soft γ-ray activity in this period. On April 28, 2012 (MJD 56045), Archibald et al. (2012) detected a factor of two increase in the 1-10 keV flux as compared to the long-term average from *SWIFT*

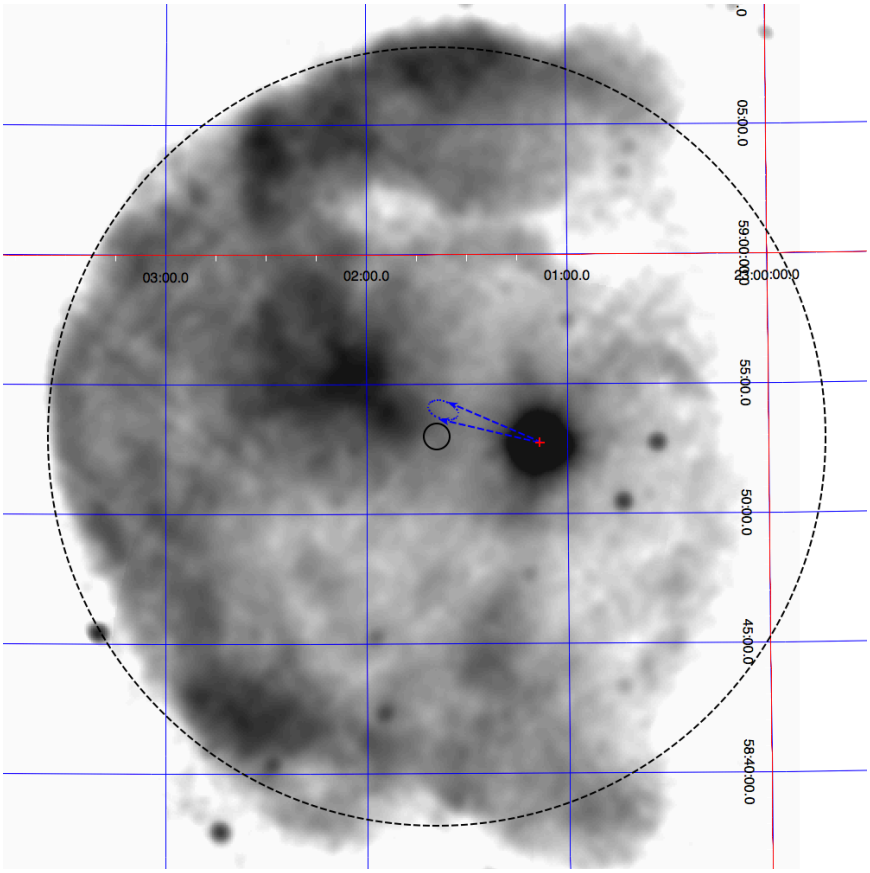

Figure 5.14. The proper motion of AXP 1E 2259+586 overlaid on an *XMM Newton* image of CTB 109. The dashed black circle denotes the outer extent of the SNR shell. The + symbol (colored red in the online version) marks the position of AXP 1E 2259+586. The solid black circle indicates the center of the SNR with an error radius of 30″. The position of AXP 1E 2259+586 traced backwards by 24±5 kyr is indicated by the dashed ellipse (colored blue in the online version).

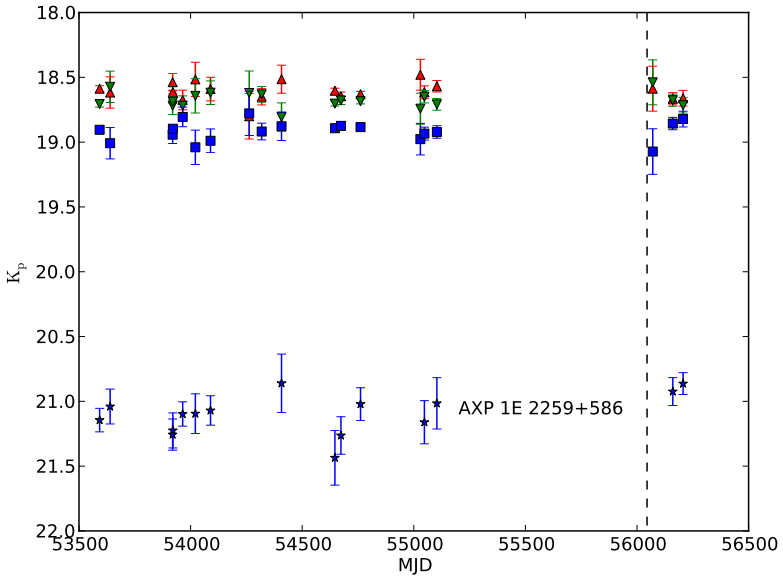

Figure 5.15. Photometric time series of AXP 1E 2259+586. The stars are identified as per Figure 5.3. Upright triangles (red in the online version) denote star N, inverted triangles (green in the online version) denote star I and squares (blue in the online version) denote star J. The median brightnesses of these three stars were used to anchor the photometric zeropoints over each epoch. The photometry of the magnetar itself is denoted by blue '*' symbols. The dashed vertical line marks the April 2012 epoch at which X-ray brightening ofAXP 1E 2259+586 was observed.

XRT monitoring and a possibly related event on April 21, 2012 (MJD 56038) the *Fermi GBM* (Foley et al., 2012). This event is marked in Figure 5.15 with a vertical line. Despite this activity, we do not see a significant change in the NIR flux of AXP 1E 2259+586. However, the sparse sampling of IR flux and the time separation between the X-ray activity and the IR flux measurement prevent us from drawing significant conclusions about the implications of the difference in IR and X-ray variability.

5.4.6 AXP 4U 0142+61

5.4.7 Astrometry

We performed relative astrometry using a grid of 30 stars over 9 epochs. Figure 5.16 shows the measured proper motions of the 30 stars in the field. The field velocity correction, as given in Table 5.9, was $(\mu_\alpha, \mu_\delta)_{\rm Field} = (0.97, -0.48)$ milli-arcsecond yr^{-1}. The proper motion of AXP 4U 0142+61 in the Galactic frame is $(\mu_\alpha, \mu_\delta) = (-4.1 \pm 1, 1.9 \pm 1)$ milli-arcsecond yr^{-1}.Assuming a distance of 3.4 ± 0.4 kpc, this corresponds to a tangential velocity of 72 ± 18 km s^{-1}

The proper motion of AXP 4U 0142+61 away from its putative birth site is $(\mu_\alpha, \mu_\delta) = (-5.6 \pm 1.3, 2.9 \pm 1.3)$ milli-arcsecond yr^{-1}. We calculate the tangential component of the ejection velocity of 102 ± 26 km s^{-1} with an angle of $300^\circ \pm 12^\circ$ East of North.

We attempted to identify a possible birthsite for AXP 4U 0142+61 in the direction opposite to its observed motion. By estimating the age of the magnetar, we can set a limit on the distance that AXP 4U 0142+61 may have moved since its genesis. It is clear that the characteristic age of magnetars calculated from the spin-down rate is not a good metric for the physical age of the pulsars because of the frequent flaring and glitching activity (Woods et al., 2002, 2003). Indeed, in TCK12, we showed that the kinematic age of SGR 1900+14 and SGR 1806−20 was a factor of three to four larger than their characteristic age. The characteristic age of AXP 4U 0142+61 is ∼70 kyr. Hence, it is hard to believe that a potential birth-site/progenitor can be more than about 3×70 kyr $\times\, 6''$ kyr$^{-1} \approx 20'$ away from the current location of AXP 4U 0142+61.

From catalogs of OB associations (Mel'Nik & Dambis, 2009; Tetzlaff et al., 2010), we identified Cas OB8 as the nearest OB association at a separation of ∼50 arcminutes away from AXP 4U 0142+61. The physical size of the cluster is estimated to be 43 pc at an estimated distance of 2 kpc (from catalog by Tetzlaff et al., 2010). The distance of AXP 4U 0142+61 is thus inconsistent with a hypothesis of its genesis in Cas OB8.

Using the `SIMBAD` database and `Aladin`, we created a map of all sources around AXP 4U 0142+61 (Figure 5.17). Table 5.13 lists all the non-stellar objects in the search cone that have been cataloged. There are two X-ray sources, two radio sources and a few IR sources from IRAS. However, each of these sources has only been identified in their respective catalogs and there have been no studies of their properties. With the lack of detailed information, we can only estimate the chances of a source being associated with AXP 4U 0142+61 based on its location, motion and an upper limit on the age.

The absence of a detectable SNR or a putative birth-site (possibly an OB association) associated with AXP 4U 0142+61 may result from from the old age of AXP 4U 0142+61.

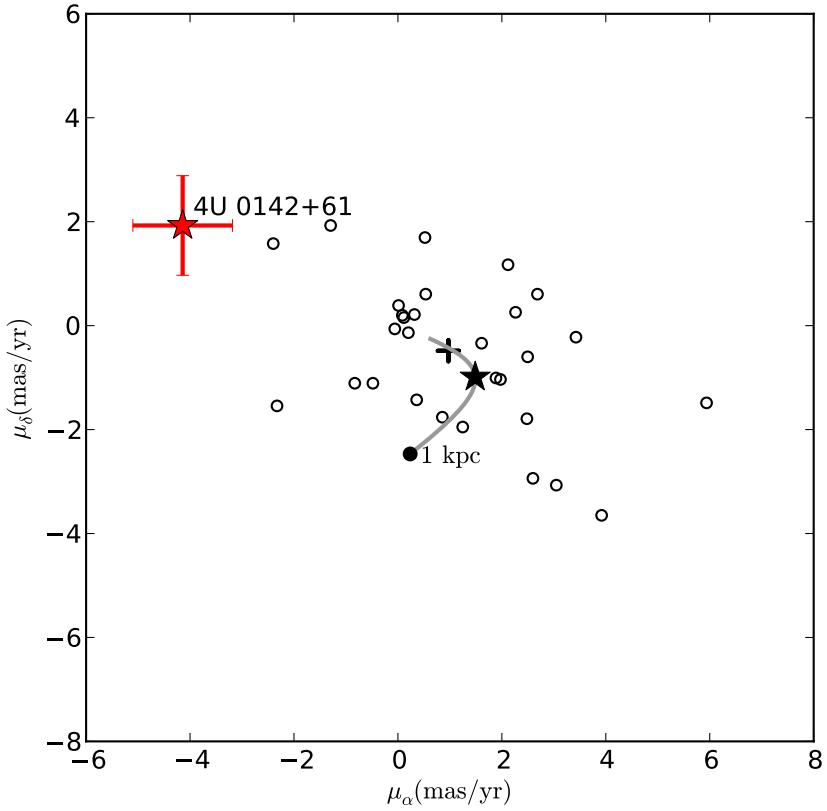

Figure 5.16. The proper motion of 30 stars in the field of AXP 4U 0142+61 in the sky frame of reference. The counterpart of AXP 4U 0142+61 is marked by the star with error bars (colored red in the online version). The remaining stars have only their best-fit values (hollow black circles) after adding the bulk motion of the field ($\vec{\mu}_{\rm Field} = (0.97, -0.48)$ milliarcsecond yr^{-1}) (marked by a black +). The thick gray line represents the expected motion of stars from 1 to 20 kpc along this line of sight, as per the Galactic rotation model presented in Section 5.3.2.3. The filled black circle at the bottom end of the line denotes the Galactic rotation at 1 kpc away from the Sun. The section of the line representing objects at a distance of 3.2 ± 0.2 kpc from the Sun is marked with a black star and a black line to denote the possible motion of the progenitor of AXP 4U 0142+61.

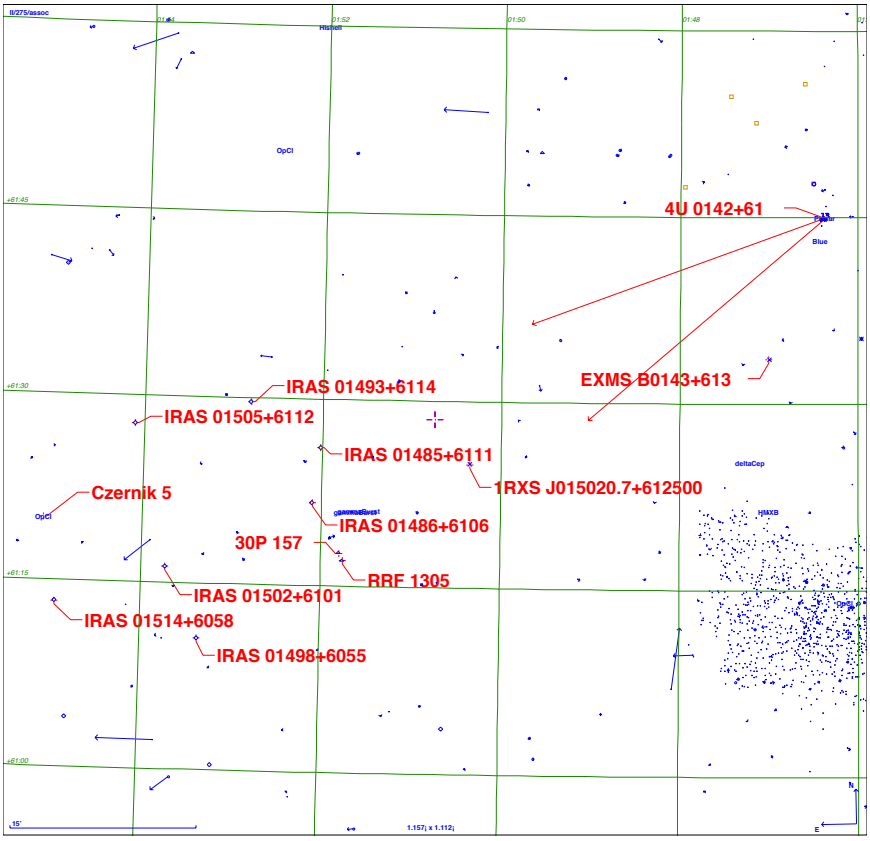

Figure 5.17. Sources in a $\sim 1^\circ \times 1^\circ$ field to the south-east of AXP 4U 0142+61. The arrows emanating from the position of AXP 4U 0142+61 are the search cone formed by tracing the proper motion of AXP 4U 0142+61 backwards in time. Objects identified as stars in the SIMBAD database have not been labelled. We selected all objects that were unidentified from the IRAS catalog, *ROSAT* catalog and other accessible databases. For velocity scale, if AXP 4U 0142+61 were to be associated with 1RXS J015020.7+612500, the kinematic age of AXP 4U 0142+61 would be 330 kyr.

Table 5.13. Unidentified and exotic objects in the backward trace of AXP 4U 0142+61.

Object ID	(α, δ) (J2000) (HH:MM:SS DD:MM:SS)	Separation (arcmin)	Kinematic Age (kyr)	Simbad Type
EXMS B0143+613	01:47:00 +61:33:36	12	110	X[a]
1RXS J015020.7+612500	01:50:20.8 +61:25:00	35	330	X
IRAS 01485+6111	01:52:01.4 +61:26:08	45	430	IR
IRAS 01486+6106	01:52:06.8 +61:21:39	47	450	IR
RRF 1305	01:51:45.9 +61:17:04	48	460	Radio
30P 157	01:51:48 +61:17:42	48	460	Radio
IRAS 01493+6114	01:52:49.1 +61:29:41	49	470	IR
IRAS 01505+6112	01:54:06.6 +61:27:43	58	550	IR
IRAS 01502+6101	01:53:44.2 +61:16:17	60	570	IR
IRAS 01498+6055	01:53:21.8 +61:10:35	61	580	IR
Cl Czernik 5	01:55:06 +61:20	67	640	OpCl[b]
IRAS 01514+6058	01:54:57.4 +61:13:19	69	660	IR

[a] Not in direct search cone. See Figure 5.17

[b] Czernik (1966), Diameter = $8'$, $\sim$50 stars

Table 5.14. High-energy events of AXP 4U 0142+61 between September 2005 and October 2012.

Date	MJD	Flux/Fluence	Activity	Ref
Apr 6, 2006	53831.3	100 counts	RXTE/PCA, Small Burst	Kaspi et al. (2006)
Jun 25, 2006	53911.05	100 − 200 counts	RXTE/PCA, 4 Small Bursts	Dib et al. (2006)
Feb 7, 2007	54138.42	3600 counts s^{-1}	RXTE/PCA, Burst	Gavriil et al. (2007)
Jul 29, 2011	55771	3500 counts s^{-1}	SWIFT/BAT, Burst	Oates et al. (2011)
Jan 12 2012	55938	2000 counts s^{-1}	SWIFT/BAT, Burst	Barthelmy et al. (2012)

From the catalog of Galactic SNRs (Ferrand & Safi-Harb, 2012, [5]), we note that only a handful of detectable SNRs, such as Kes 67, W41, G065.1+00.6, G192.8−01.1 and G359.1−00.5, are older than 10^5 years. It is not unlikely for the SNR shell to diffuse into the ISM at such a timescale.

5.4.8 Photometry

Figure 5.18 shows the NIR photometry of AXP 4U 0142+61 from September 2005 to October 2012. Over this period, there have been a series of high-energy activity events associated with AXP 4U 0142+61. Table 5.14 lists the epochs of the activity. The typical fluences

[5] See http://www.physics.umanitoba.ca/snr/SNRcat/

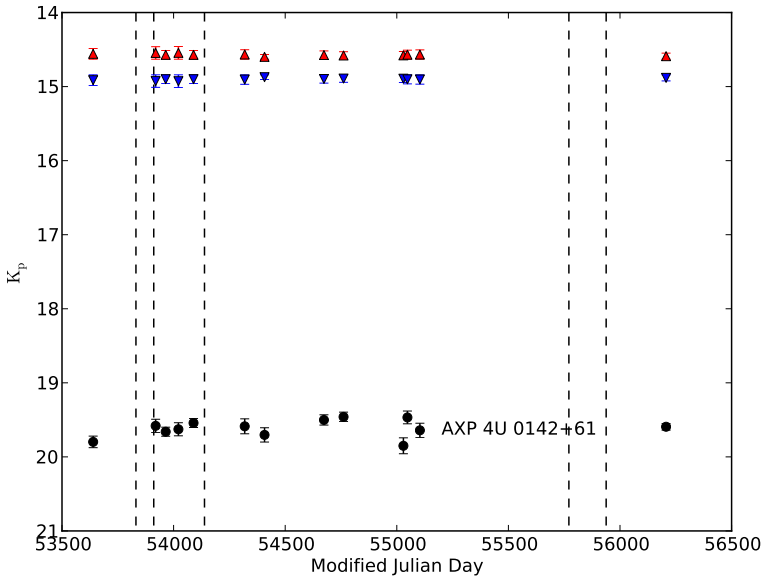

Figure 5.18. Photometric time series of AXP 4U 0142+61. The K_p magnitude of AXP 4U 0142+61 is denoted by black circles. The photometry was anchored to the brightness of stars C1, C2 and D1, D2 as marked in Figure 5.4. The photometry is corrected to account for the blending of the stars. The photometry of C1 is denoted by inverted triangles (colored blue in the online version of the paper) and the photometry of D1 is denoted by upright triangles (colored red in the online version). The dashed vertical lines indicate epochs of X-ray or soft γ-ray activity from AXP 4U 0142+61as detailed in Table 5.14.

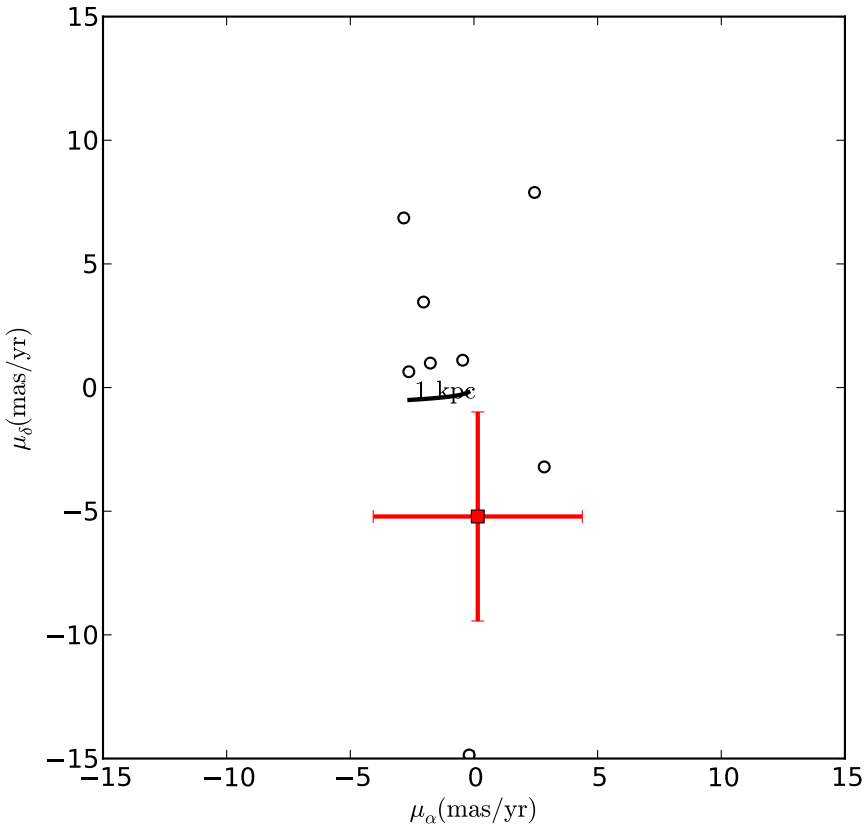

Figure 5.19. The proper motions of all the objects in the vicinity of SGR 0501+4516 are marked (black circles). The proper motion of the magnetar counterpart is marked by red error bars. The thick gray line denotes the proper motion caused by galactic rotation in the direction of the magnetar from 1 kpc to 8 kpc.

of the burst have been ∼100 counts, which represent very small activity similar to the smallest bursts from AXP 1E 1048−5937 (Kaspi et al., 2006). The quiescent flux of the magnetar did not change significantly through these epochs. The epochs are also plotted in Figure 5.18 with vertical lines. We measure small (0.5 mag) variations in IR flux through our observations. However, as with AXP 1E 2259+586, we cannot conclusively link them with the X-ray activity due to the sparse sampling and time delays.

5.4.9 SGR 0501+4516

Because of the low number density of stars along the line of sight of SGR 0501+4516, there are very few reference stars to perform astrometry. Consequently, our astrometric precision for this target is far worse than that for our previous measurements. We can limit the proper motion of SGR 0501+4516 to $\lesssim 10$ milli-arcsecond yr^{-1}. With such an angular velocity, if the magnetar were to originate in HB9, its age would be about 0.5 million years, far greater than the spin-down age of the magnetar, the known lifetimes of any other magnetar and

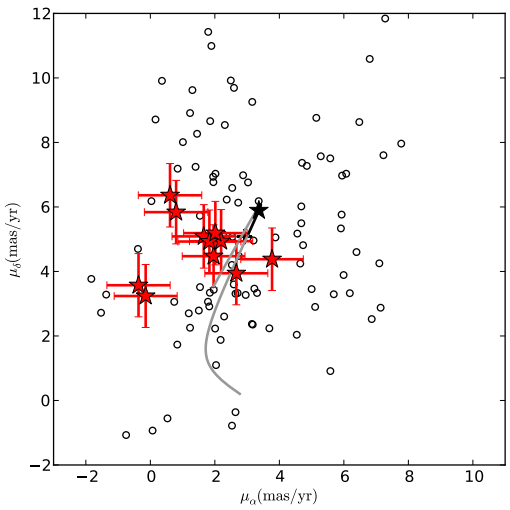

Figure 5.20. The proper motions of all the objects in the vicinity of AXP 1E 1841−045 are marked with red error bars. The other stars in the $10 \times 10''$ image are marked by black circles. The black star denotes the proper motion of a hypothetical progenitor at the distance of Kes 73 moving with the Galactic rotation (thick gray line).

the age of HB9. Hence we conclude that SGR 0501+4516 is very definitely not associated with HB9. A SIMBAD search of objects in a radius of $\approx 13'$ (based on the proper motion and the characteristic age of 16 kyr (Göğüş et al., 2010) multiplied by a factor of upto 5) does not reveal any possible birth site.

From the HEASARC nH column density calculator, I found that the objects along this line of sight with the same estimate of nH= $6^{+5}_{-0.3} \times 10^{21}$ cm as SGR 0501+4516 are scattered along a distance between 0.5 to 1.5 kpc. At a distance of 1.5 kpc, the proper motion corresponds to tangential space velocity of 70 km s^{-1}.

5.4.10 AXP 1E 1841−045

Without an identified counterpart, we can only set upper limits to the proper motion of AXP 1E 1841−045. Figure 5.20 shows the proper motions of all the objects in the vicinity of the AXP. The proper motions are corrected for the motion of the Milky Way as per Tendulkar et al. (2012). The upper limit for the proper motions of any of the objects is ~ 4 milli-arcseconds yr^{-1}. At the nominal distance of Kes 73 (8.5 kpc, Tian & Leahy 2008), this corresponds to a transverse space velocity of 160 km s^{-1}.

5.5 Discussion

Using LGS adaptive-optics supported near-IR observations, we have measured the proper motions of SGR 1806−20 and SGR 1900+14 to be $(\mu_\alpha, \mu_\delta) = (-4.5, -6.9) \pm (1.4, 2.0)$ milli-arcsecond yr^{-1} and $(\mu_\alpha, \mu_\delta) = (-2.1, -0.6) \pm (0.4, 0.5)$ milli-arcsecond yr^{-1} respectively.

These correspond to a linear transverse velocity of $350 \pm 100\,\mathrm{km\,s^{-1}}$ and $130 \pm 30\,\mathrm{km\,s^{-1}}$ respectively at the measured distances of their putative associations. Previously, using Very Long Baseline Interferometry (VLBI) at radio wavelengths, transverse linear velocities have been measured only for two magnetars: the AXP 1E 1810−197: 212 ± 35 $\mathrm{km\,s^{-1}}$ (Helfand et al., 2007) and the AXP PSR J1550−5418: $280 \pm 120\,\mathrm{km\,s^{-1}}$ (Deller et al., 2012). The radio counterpart for AXP PSR J1622−4950 has been recently identified by Levin et al. (2010) and would lead to an accurate proper motion measurement with VLBI. With the transverse velocity measurements for two AXPs and two SGRs in the $100 - 400\,\mathrm{km\,s^{-1}}$ range, it is highly unlikely that each of these objects has an extremely high radial velocity component. Hence we conclude that magnetars as a family do not possess the high space velocities ($\sim 1000\,\mathrm{km\,s^{-1}}$) that were expected earlier (cf. Rothschild & Lingenfelter 1996).

Consider the space velocities of other families of neutron stars in contrast with magnetars. Canonical radio pulsars ($B \sim 10^{11}\,\mathrm{G}$) have typical space velocities of $\sim 200 - 300\,\mathrm{km\,s^{-1}}$ (Hobbs et al., 2005). Tetzlaff et al. (2010) traced the motions of 4 young, hot X-ray bright isolated neutron stars to associate them with progenitors and constrain their ages. They calculated the space velocities of these objects to be $\sim 350 \pm 180\,\mathrm{km\,s^{-1}}$. There are a few fast moving pulsars such as PSR J1357−6429, which is a Vela-like radio pulsar has a transverse velocity of $1600 - 2000\,\mathrm{km\,s^{-1}}$ (Kirichenko et al., 2012), but these seem to be outliers from the family. From the these data, we observe that perhaps velocities are not a good discriminator of different groups of neutron stars and their origins.

5.5.1 Association

Our measured proper motions provide very good evidence linking SGR 1806−20 to the cluster of massive stars. The time required for SGR 1806−20 to move from the cluster to its current position is 650 ± 300 yr. It may not be a surprise that one of the younger supernovae in our galaxy resulted from the magnetar. However, SGR 1806−20 lies in the galactic plane behind dust clouds which create very high extinction in the visible wavelengths. Hence, the supernova associated with the magnetar may not have been visible to the naked eye. For SGR 1900+14, we rule out any association with the supernova remnant G 42.8+0.6 and confirm that this magnetar is associated with the star cluster. The time to trace the magnetar back to the cluster is 6 ± 1.8 kyr.

The turn-off masses for the clusters with which the magnetars are associated allow us to place lower limits on the progenitor masses of these magnetars. Currently, progenitor mass estimates exist for three of the magnetars:
SGR 1806−20: $48^{+20}_{-8}\,\mathrm{M_\odot}$ (Bibby et al., 2008),
CXO J1647−455: $> 40\,\mathrm{M_\odot}$ (Muno et al., 2006; Ritchie et al., 2010) and
SGR 1900+14: $17 \pm 2\,\mathrm{M_\odot}$ (Davies et al., 2009).

We note that only the two youngest SGRs have a star cluster in their vicinity. The lack of a star cluster in the vicinity of the older SGRs (despite ages of 4 to 10 kyr) suggests that it is not essential that SGRs should be associated with star clusters. Furthermore, the inferred progenitor masses of SGR 1900+14 does not compel us to believe that SGRs arise from massive stars. We conclude that binarity likely has a bigger role in forming SGRs.

Table 5.15. List of all known magnetar proper motions[a]

Object	$V_{tangent}$ ($km\,s^{-1}$)	Assoc.	Method	Ref.
AXP 1E 1810−197	212 ± 35	–	Radio; VLBI	Helfand et al. (2007)
AXP 1E 1547.0−5408[b]	280 ± 120	SNR G327.24−0.13	Radio; VLBI	Deller et al. (2012)
SGR 1900+14	130 ± 30	Cluster	NIR; LGSAO	Tendulkar et al. (2012)
SGR 1806−20	350 ± 100	Cluster	NIR; LGSAO	Tendulkar et al. (2012)
AXP 1E 2259+586	157 ± 17	SNR CTB 109	NIR; LGSAO	Tendulkar et al. (2013)
AXP 4U 0142+61	102 ± 26	–	NIR; LGSAO	Tendulkar et al. (2013)
SGR 0501++4516	≈ 70	HB9 (disproved by this result)	NIR; LGSAO	Tendulkar et al, unpublished
AXP 1E 1841-045	$\lesssim 160$		NIR; LGSAO	(Tendulkar, 2013)

[a]These are the tangential components of the ejection velocities.

[b]Also known as PSR J1550−5418

5.5.2 Braking Index

If the association of the SGRs with the star clusters is taken for granted, we can constrain the braking index of the magnetars. The braking index n is calculated from the following implicit equation:

$$n = 1 + \frac{P}{T\dot{P}}(1 - (P_0/P)^{(n-1)}).$$

Here, T is the kinematic age of the magnetar (time taken to move from cluster to present position) and P_0 is the spin period at birth.

The instantaneous $\dot{P}$ is known to vary by a factor of three to four corresponding to large variations of braking torque on the magnetar (Woods et al., 2002, 2007). We use the X-ray timing measurements from Kouveliotou et al. (1998); Mereghetti et al. (2005b); Woods et al. (2007); Marsden et al. (1999); Woods et al. (2002, 2003); Mereghetti et al. (2006); Nakagawa et al. (2009) to calculate an average $\dot{P}$ of $49 \times 10^{-11}\,s\,s^{-1}$ for SGR 1806−20 and $17 \times 10^{-11}\,s\,s^{-1}$ for SGR 1900+14 from 1996 to 2006.

Assuming $P_0/P \ll 1$, we estimate n to be $1.76^{+0.65}_{-0.24}$ for SGR 1806−20 and $1.16^{+0.04}_{-0.07}$ for SGR 1900+14. This is significantly smaller than the canonical value of $n = 3$ for the magnetic dipole spindown mechanism for pulsars. Low braking indices have been discussed in the context of twisted magnetospheres (eg. Thompson et al., 2002) and particle wind spindown (e.g. Tong et al., 2012). However, the large variations in $\dot{P}$ over tens of years implies that these measurements cannot be taken at face value.

5.5.3 Proper Motions of the Magnetar Family

Table 5.15 lists the six available measurements of the tangential space velocities of magnetars. Figure 5.21 combines the probability distributions (assumed to be gaussian) of all the six magnetar tangential velocities. The weighted average velocity is $200\,km\,s^{-1}$ with

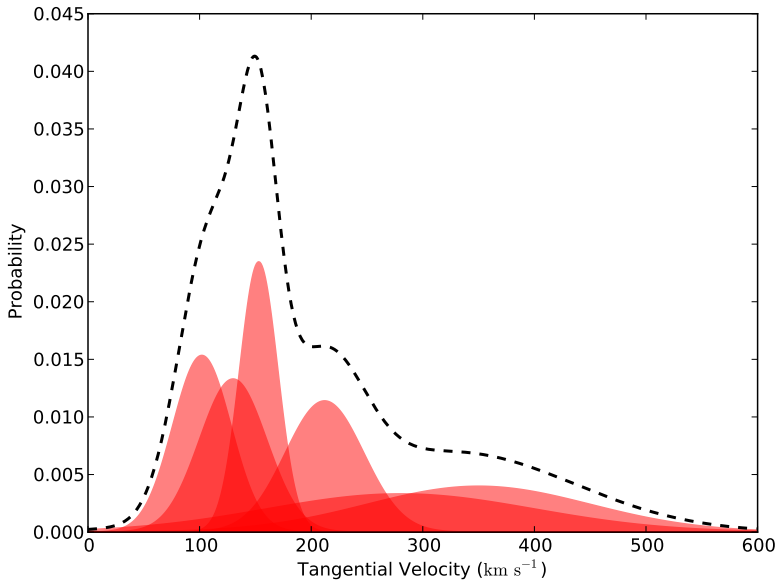

Figure 5.21. The probability distributions of the tangential velocities of six magnetars as detailed in Table 5.15 are plotted as filled curves (colored red in the online version). The dashed black line is the sum of the individual probability distributions. The mean and standard deviation of this distribution is 200 km s^{-1} and 100 km s^{-1}. This is very well consistent with the mean and standard deviation of the normal pulsar population (Hobbs et al., 2005).

a weighted standard deviation of $100\,\mathrm{km\,s^{-1}}$. This is in good agreement with the tangential velocities of the pulsar population which is measured to be $211\,\mathrm{km\,s^{-}}1$ (Hobbs et al., 2005) with an standard deviation of $\sim 100\,\mathrm{km\,s^{-1}}$. Thus, the kinematics of magnetars are completely consistent with those of pulsars.

Given this velocity distribution, it is improbable that SGR 0526−66 has a $\sim 10^3\,\mathrm{km\,s^{-1}}$ velocity. This adds to the growing body of evidence suggesting that SGR 0526−66 may not be associated with SNR N49 (Gaensler et al., 2001; Klose et al., 2004; Badenes et al., 2009; Park et al., 2012). The original expectation of a large natal kick came from the idea that SGR 0526−66 had rapidly moved to the edge of SNR N49 and the since discredited idea that short hard GRBs are from the galactic halo (Rothschild & Lingenfelter, 1996). With these measurements, the probability of finding a magnetar with a large ($\gtrsim 1000\,\mathrm{km\,s^{-1}}$) space velocity is very low and NS kick mechanisms, as enumerated in Lai (2004), may be applicable in a very small fraction of supernovae. Along with the conclusion from Vink & Kuiper (2006) that supernovae associated with magnetars show no evidence of milli-second proto-neutron stars or higher than typical energetics, the idea of what makes magnetar creating supernovae different from pulsar creating supernovae need to be revisited.

5.5.4 Age of CTB 109 and AXP 1E 2259+586

There has been much recent work to estimate the age of CTB 109. Sasaki et al. (2004) modeled the shell of CTB 109 as a Sedov-Taylor shock with data from deep *XMM Newton* observations. They estimate the age of CTB 109 to be $8.8 \pm 1\,\mathrm{kyr}$. More recent work by (Sasaki et al., 2013, ; in review, personal communication) reports the age to be $14 \pm 2\,\mathrm{kyr}$. These estimates are in contrast with previous estimates from Wang et al. (1992) (3 kyr; hydrodynamical simulations of X-ray temperature), Rho & Petre (1997) (6 - 21 kyr; ionization modeling) and Parmar et al. (1998) (3 kyr; ionization modeling and spectra). The consensus put forth by these studies is that the supernova exploded at the eastern edge of a dense giant molecular cloud complex detected in CO by Israel (1980). The western edge of the expanding supernova shell has been slowed and quenched due to its collision with the molecular cloud and its eastern edge, expanding into a less dense interstellar medium is significantly less quenched. The apparent center of the expanding shell would be expected to move eastward. We observe this in our measurements.

The separation between the current center of CTB 109 and AXP 1E 2259+586 would correspond to a kinematic age of $24 \pm 5\,\mathrm{kyr}$ which is significantly larger than the estimated age of CTB 109. This discrepancy implies that the current center of CTB 109 has moved to the east, opposite to the movement of AXP 1E 2259+586. It is more worthwhile to reverse the calculation to find the actual center of the explosion. Assuming the age of the remnant to be $14 \pm 2\,\mathrm{kyr}$, we can estimate that AXP 1E 2259+586 moved $2'.4 \pm 0.4'$ towards the west after the explosion and consequently the current center of CTB 109 would have moved by $1'.6 \pm 0.4'$ to the east after the explosion. Back calculating from the current position of AXP 1E 2259+586, we estimate that the explosion occurred at $(\alpha, \delta)_{J2000} = (23^{\mathrm{h}}\,00^{\mathrm{m}}\,50^{\mathrm{s}}, +58^{\circ}\,52'\,02'')$. The error ellipse at this position has a semi-major axis of $\sigma_{maj} = 26''$, a semi-minor axis of $\sigma_{min} = 15''$ oriented at an angle of 17° south of west.

5.6 Epilogue and Future Work

While the magnetar proper motion survey was in progress, new magnetars were discovered through X-ray bursts, including SGR 0418+5729, a low B-field magnetar (Rea et al., 2010) (and more recently SGR 1822−1606: Camero-Arranz et al. (2013)) challenging the belief that the strength of the B-field sets the magnetar population apart from the canonical pulsar population. Altogether, since 2005, nine magnetars (summarized in Table 5.16) have been discovered including the Galactic Center magnetar SGR 1745−2900 (Kennea et al., 2013b,a). Seven of the new objects can be observed from Mauna Kea.

In early 2013, we started an observing program to create a database of deep ($K_s \approx 22$ mag) high resolution NIR images of each new magnetar. The database would have two main purposes. To help identify the NIR counterpart and to serve as a baseline image for astrometric measurements at the later time when the magnetar counter part is identified. Since only 2 SGRs and 4 AXPs have well identified optical/NIR counterparts and only 3 AXPs have radio counterparts, each new counterpart would be a prized addition to our small collection.

The identification of magnetars in NIR is not straightforward. NIR colors of magnetars are not well understood and can be misleading when used as the basis for identification (see Testa et al., 2008). Regular monitoring of magnetar fields in order to detect small (~ 0.2 mag) photometric variations is observing-time intensive and difficult due to the problem of accurate AO photometry. However the NIR flux from magnetars has been observed to vary by factors between three to ten during and after X-ray flaring of magnetars (see Kaspi et al., 2003; Rea et al., 2004, etc.). We plan to leverage the NIR variability of magnetars during flares (identified from the GRB Coordinate Notification messages, typically 3 to $4\,\mathrm{yr}^{-1}$) to identify counterparts through Target of Opportunity (ToO) observations. In June 2013, we finished the imaging each of the magnetar fields to the required depth.

5.6.1 Do Magnetars Have Fallback Disks?

There is still an open question as to how the NIR emission of magnetars is emitted. SGRs and AXPs have been most widely studied in the $1-10$ keV band due to their high X-ray luminosity ($L_X \sim 10^{35-36}\,\mathrm{ergs\,s^{-1}}$). The magnetar model successfully explains the high X-ray luminosity of SGRs and AXPs as thermal blackbody emission ($k_BT \sim 0.5$ keV) emitted from the magnetar crust. The surface temperature is maintained by frictional losses of the twisted internal magnetic field untwisting through the crust (Thompson et al., 2002). A fraction of the thermal emission can undergo resonant compton scattering in the energetic plasma above the surface and is observed as a tail at 2−10 keV with a photon index $\Gamma = 2-4$.

The optical/IR (OIR) luminosity ($L \sim 10^{32}\,\mathrm{ergs\,s^{-1}}$) is higher than the extrapolation of the thermal X-ray spectrum (Israel et al., 2003) which indicates that the OIR emission is produced differently than the X-ray emission. There are two basic ideas about the source of the OIR emission; (a) interaction of the plasma with the magnetic field in the magnetar's atmosphere or (b) reprocessing of the X-ray emission on a fall-back disk around the magnetar.

Among the magnetospheric emission models, the proposed sources of optical/IR emis-

Table 5.16. New magnetars discovered since 2005.

Target	RA (hh:mm:ss)	Dec (dd:mm:ss)	NIR[a]	Access[b]
SGR 0501+4516	05:01:06	+45:16:34	Y	Y
SGR 0418+5729	04:18:33	+57:32:23	N	Y
SGR 1745−2900	17:45:40	−29:00:30	N	Y
SGR 1833−0832	18:33:44	−08:31:08	N	Y
SGR 1822−1601	18:22:18	−16:04:27	N	Y
SGR 1834−0846	18:34:52	−08:45:56	N	Y
AXP J 1714−3810	17:14:05	−38:10:31	N	N
AXP J 1622−4950	16:22:45	−49:50:54	N	N
AXP J 1845−0258	18:44:55	−02:56:53	N	Y

[a]Column 4 specifies the identification of a NIR counterpart.

[b]Column 5 specifies the accessibility of the target from Mauna Kea.

sion includes coherent emission from plasma instabilities (Eichler et al., 2002), synchrotron emission from relativistic electrons, cyclotron emission from ions and curvature radiation (Beloborodov & Thompson, 2007).

Disks around Magnetars van Paradijs et al. (1995) first suggested that a fall-back disk from the supernova could explain the X-ray luminosity of AXPs through accretion without invoking an extremely strong magnetic field. The disk would extract angular momentum to rapidly slowdown the pulsar. However, it was difficult to explain the extreme energetics of SGR flares with accretion. A series of authors (most recently Trümper et al., 2013) improved this model for AXPs to explain the OIR emission as thermal emission from disk heated by high-energy radiation from the magnetar.

Indeed, Wang et al. (2006); Wang & Kaspi (2008) showed that the optical to mid-IR spectral energy distribution (SED) of AXP 4U 0142+61 (see Figure 5.22) is well fit by a two component model; a power-law component, probably emanating from the magnetosphere of the magnetar and a thermal blackbody component consistent with a heated disk in the 2.2−24 μm range. Kaplan et al. (2009) detected a similar SED for AXP 1E 2259+586.

However, the fall-back disk interpretation was complicated by OIR variability that had no corresponding X-ray variability (Durant & van Kerkwijk, 2006). The fact that the 27% pulse fraction in optical emission (Kern & Martin, 2002) is higher than the pulse fraction in its X-ray emission is also difficult to reconcile with the passive fallback disk model except under special geometric conditions (Ertan & Cheng, 2004).

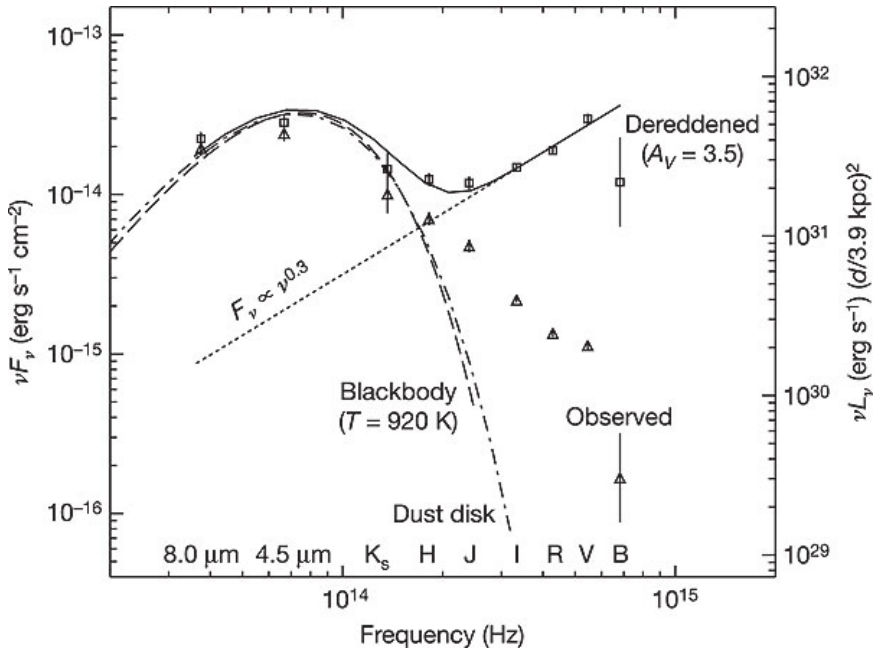

Figure 5.22. The SED of AXP 4U 0142+61 (adapted from Wang et al. (2006)). The observed spectrum (lower points) is a strongly reddened version of the actual spectrum (upper line, reconstructed by de-reddening). Due to the high reddening, it is important to observe AXP 4U 0142+61 in close to NIR as possible. Adapted by permission from Macmillan Publishers Ltd: Wang Z. et al. 2006, *Nature*, 440, 772 , copyright (2006).

Currently, there is no proof of the presence or absence of a fall-back disk around AXPs. The question of where the OIR emission of magnetars originates from is wide open. Table 5.17 summarizes the expected polarization signal from each model in the time averaged emission. All magnetospheric emission is expected to produce a polarization signature while disk emission would be unpolarized. A single polarization measurement will be able to distinguish between all emission models. We have been awarded time to perform deep (1%) linear polarimetry ofAXP 4U 0142+61 in October 2013 to shed light on the

We would like to thank M. van Kerkwijk and C. Thompson for their critical comments and extensive discussions and Dr. Manami Sasaki for generously providing the *XMM Newton* mosaic of CTB 109 for Figure 5.14. The data presented herein were obtained at the W.M. Keck Observatory, which is operated as a scientific partnership among the California Institute of Technology, the University of California and the National Aeronautics and Space Administration. The Observatory was made possible by the generous financial support of the W.M. Keck Foundation.

Table 5.17. Expected polarization signal for various emission mechanisms.

Mechanism	Linear Polarization	Circular Polarization
Coherent Emission from Plasma Instabilities[1]	–	Strong
Synchrotron Emission from Relativistic Electrons[2]	Strong	Weak
Cyclotron Emission from Ions[2]	Weak	Geometry Dependent
Curvature Radiation[2]	Strong	–
Disk Reprocessing[3]	–	–

[1]Eichler et al. (2002)

[2]Beloborodov & Thompson (2007)

[3]Ertan & Cheng (2004)

Appendix A

List of Publications

A.1 Journal Publications

Tendulkar, S. P., Cameron, P. B., & Kulkarni, S. R. 2013, ApJ, 772, 31

Terziev, E., Law, N. M., Arcavi, I., et al. 2013, ApJS, 206, 18

Muirhead, P. S., Vanderburg, A., Shporer, A., et al. 2013, ApJ, 767, 111

Baranec, C., Riddle, R., Law, N. M., et al. 2013, J. Vis. Exp. (72), e50021, doi:10.3791/50021, arXiv:1302.3224

Tendulkar, S. P., Cameron, P. B., & Kulkarni, S. R. 2012, ApJ, 761, 76

Law, N. M., Kraus, A. L., Street, R., et al. 2012, ApJ, 757, 133

Riddle, R. L., Burse, M. P., Law, N. M., et al. 2012, Proc. SPIE, 8447,

Baranec, C., Riddle, R., Ramaprakash, A. N., et al. 2012, Proc. SPIE, 8447,

Cenko, S. B., Bloom, J. S., Kulkarni, S. R., et al. 2012, MNRAS, 420, 2684

Kasliwal, M. M., Kulkarni, S. R., Arcavi, I., et al. 2011, ApJ, 730, 134

A.2 Conference Proceedings and Other

Tendulkar, S. P. 2013, IAU Symposium, 291, 514

Law, N. M., Morton, T., Baranec, C., et al. 2013, American Astronomical Society Meeting Abstracts, 221, #334.06

Tendulkar, S. P., Baranec, C., Riddle, R. L., et al. 2013, American Astronomical Society Meeting Abstracts, 221, #305.03

Riddle, R. L., Baranec, C., Law, N. M., et al. 2013, American Astronomical Society Meeting Abstracts, 221, #305.01

Tendulkar, S. P., Cameron, P. B., & Kulkarni, S. R. 2012, American Astronomical Society Meeting Abstracts #219, 219, #237.03

Baranec, C., Riddle, R., Ramaprakash, A. N., et al. 2011, Adaptive Optics: Methods, Analysis and Applications (AO), AWA2, 3 pages, 2

Riddle, R. L., Baranec, C., Ramaprakash, A. N., et al. 2011, Bulletin of the American Astronomical Society, 43, #157.11

Tendulkar, S. P., Kasliwal, M. M., Quimby, R., & Kulkarni, S. R. 2009, The Astronomer's Telegram, 2291, 1

Kasliwal, M. M., Quimby, R., Shara, M., et al. 2009, The Astronomer's Telegram, 2290, 1

Appendix B

ADC Calculations

In this section, we shall go through the derivation of the calculations for the positions of the ADC rotation angles. The symbols used in the calculations are described in Table B.1

Our telescope has an equatorial mounting. There is no field rotation on our camera. Hence, the image axes will be fixed with respect to the equatorial grid. The parallactic vector (the vector pointing to the zenith) rotates on the image. We need to know the angle between the image axis and parallactic vector so that we can rotate the ADC axes to align with the parallactic angle

Table B.1. Symbols used in the ADC calculations.

Symbol	Description
α	Right ascension of the target
δ	Declination of the target
H	Hour angle of the target
ϕ	Latitude of the observatory
a	Elevation of the target
A	Azimuth of the target (measured towards east from north)
ζ	Zenith angle of the target
p	Parallactic angle at the target location
Ω	Sidereal rotation rate
t	Time since (or till) meridian transit of the target

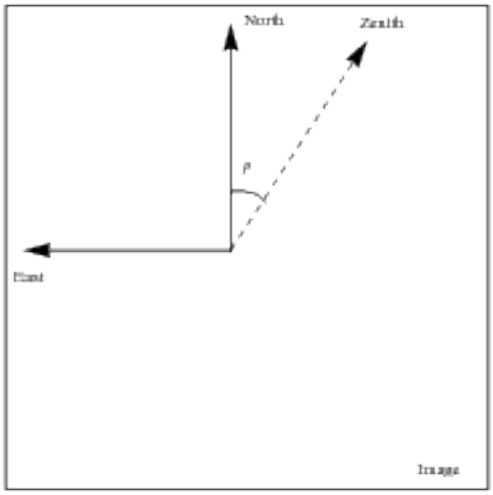

From the cosine rule, we get,

$$\cos\zeta = \sin\phi\sin\delta + \cos\phi\cos\delta\cos H, \tag{B.1}$$

$$\cos p = \frac{\sin\phi - \sin\delta\cos\zeta}{\cos\delta\sin\zeta}. \tag{B.2}$$

And from the sine rule,

$$\sin p = \frac{\sin H\cos\phi}{\sin\zeta}. \tag{B.3}$$

Substitute H as a function of time: $H = \Omega t$. ζ goes from 0 to $\pi/2$ so $\cos^{-1}$ is well defined.

$$\zeta = \cos^{-1}(\sin\phi\sin\delta + \cos\phi\cos\delta\cos\Omega t), \tag{B.4}$$

$$p = \sin^{-1}(\frac{\sin\Omega t\cos\phi}{\sqrt{1-\cos^2\zeta}}), \tag{B.5}$$

$$p = \sin^{-1}(\frac{\sin\Omega t\cos\phi}{\sqrt{1-(\sin\phi\sin\delta + \cos\phi\cos\delta\cos\Omega t)^2}}). \tag{B.6}$$

To ensure that the rotation stages can handle the required rotation rates, let us calculate the rate of change of the parallactic angle and the zenith angle.

Zenith angle:

$$\frac{\mathrm{d}\zeta}{\mathrm{d}t} = -\Omega\cos\delta\cos\phi\sin\Omega t. \tag{B.7}$$

Parallactic angle:

$$\frac{\mathrm{d}p}{\mathrm{d}t} = \frac{\Omega \cos\phi \left(\cos\Omega t \left(1 - (\cos\delta\cos\phi\cos\Omega t + \sin\delta\sin\phi)^2\right) - \cos\delta\cos\phi(\cos\delta\cos\phi\cos\Omega t + \sin\delta\sin\phi)\sin^2\Omega}{((1 - (\cos\delta\cos\phi\cos\Omega t + \sin\delta\sin\phi)^2)^{3/2}\sqrt{1 - \frac{\cos^2\phi\sin^2\Omega t}{1-(\cos\delta\cos\phi\cos\Omega t+\sin\delta\sin\phi)^2}}} \tag{B.8}$$

We plot the rate as a function of time for a star passing close to the zenith.
(We've determined that we can allow a zenith hole of 3 deg where we do not need an ADC. See below)

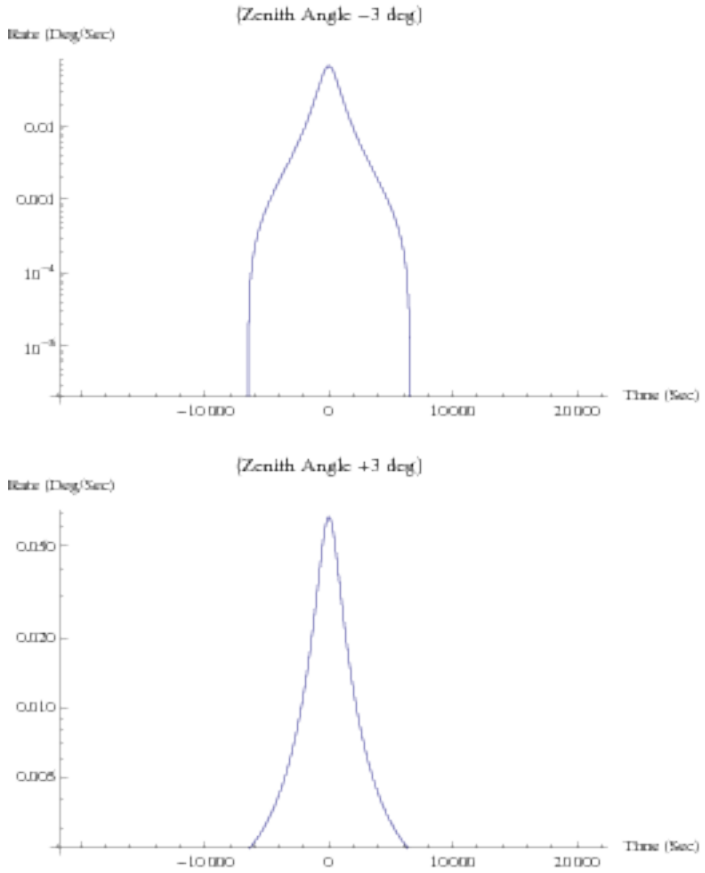

We also calculate the maximum rates of parallactic angle change: (in deg/sec)
Maximum rotation velocity for parallactic angle = 0.067 deg/sec

Angle between the prisms: Let the angle between the prisms be 2ψ.

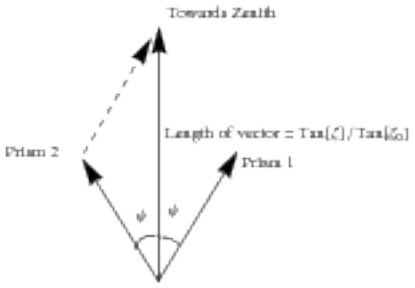

ζ_0 is the maximum zenith angle the ADC is designed for.
ζ is the actual zenith angle of observation.
Prism vectors are of unit length in this scaling.

Assuming an atmospheric dispersion model: $\theta = \frac{\theta_{\max}}{\tan \zeta_{\max}} \tan \zeta$.

$$\cos \psi = \frac{\tan \zeta}{\tan \zeta_{\max}}, \tag{B.9}$$

$$\cos \psi = \frac{1}{\tan \zeta_{\max}} \frac{\sqrt{1 - (sin\phi \sin \delta \cos \phi \cos \delta \cos \Omega t)^2}}{\sin \phi \sin \delta + \cos \phi \cos \delta \cos \Omega t}. \tag{B.10}$$

Since ψ takes values from 0 to $\pi/2$, the cosine is invertible.

$$\psi = \cos^{-1} \left(\frac{1}{\tan \zeta_{\max}} \frac{\sqrt{1 - (\sin \phi \sin \delta \cos \phi \cos \delta \cos \Omega t)^2}}{\sin \phi \sin \delta + \cos \phi \cos \delta \cos \Omega t} \right). \tag{B.11}$$

We plot the prism rotation as a function of zenith angle to check this.

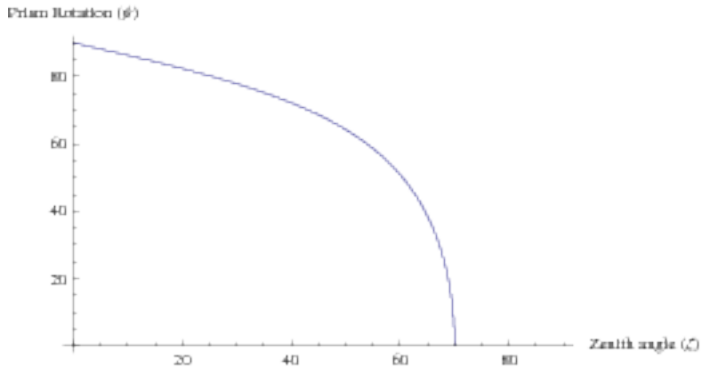

Rate of rotation:

$$\begin{aligned}\frac{\mathrm{d}\psi}{\mathrm{d}t} &= -\left(\Omega\cos\delta\cos\phi\cot\zeta_{\max}\sin\Omega t\right)/ \\ &\quad \left(\left(\cos\delta\cos\phi\cos\Omega t+\sin\delta\sin\phi\right)^2\sqrt{1-\left(\cos\delta\cos\phi\cos\Omega t+\sin\delta\sin\phi\right)^2}\right. \\ &\quad \left.\sqrt{1-\frac{\cot^2\zeta_{\max}\left(1-\left(\cos\delta\cos\phi\cos\Omega t+\sin\delta\sin\phi\right)^2\right)}{\left(\cos\delta\cos\phi\cos\Omega t+\sin\delta\sin\phi\right)^2}}\right). \qquad \text{(B.12)}\end{aligned}$$

We need to calculate the maximum rotation speed this will need.

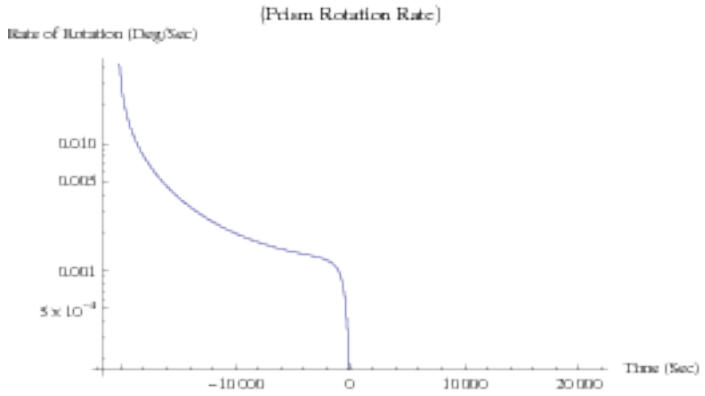

Lookup table for atmospheric dispersion strength The strength of the atmospheric dispersion is quite well approximated by $\tan\zeta$. However, if we need to go down to a zenith angle of 80 degrees, there are additional corrective terms which need to be added. That makes the equation a bit difficult to calculate. So it would be useful to interpolate the strength of dispersion from a lookup table.

Appendix C

AO Algorithm

The AO algorithm is the algorithm for reconstructing the wavefront from the wavefront sensor measurements and calculating the positions of the deformable mirror actuators and the TT mirror. Since the laser guide star (LGS) is insensitive to TT variations, we need a separate camera to measure the position of a TT guide star close to the target. Figure C.1 shows the algorithm for LGS mode operations.

C.0.1 TT Camera

According to the original design, the Robo-AO instrument would have a visible band camera (Andor EMCCD) and an IR camera which can interchangeably as the science camera and the TT camera. In this case, the camera which is being used as the TT camera would be specified a region of interest containing the TT star to be read out at a high frame rate. This would be a small section of the CCD, say 32 x 32 pixels. There are many methods to calculate the centroid of the images. One possibility is to fit a gaussian PSF to the image and try to centroid it. This is best done in Fourier space. The other option is to take a weighted centroid, which is faster but less accurate. Currently the centroiding method has been implemented.

Robo-AO is currently not equipped with an IR camera which can be read out fast enough and has sufficiently low noise to be used as a TT camera during visible band science operation. The Andor EMCCD is used as a Lucky Imaging camera and the TT correction will be applied in post processing. In the Lucky Imaging mode, full frame images are captured at a high frame rate (8 Hz on the Andor EMCCD) and stored. In post processing, the lowest SNR images are dropped and the remaining images are coadded after correcting for image jitter. For more information, the reader is directed to Nick Law's thesis.

C.0.2 Laser TT Mirror

The UV laser (355 nm) is launched into the sky as a 15 cm aperture beam from the side of the telescope. In order to compensate for the flexure of the telescope optics and the laser assembly as the orientation of the telescope changes, we need to include a TT mirror in the laser beam path before its launch. The flexure of the laser beam projector optics with respect to the telescope optics would cause the laser spot to shift in the field of view of the

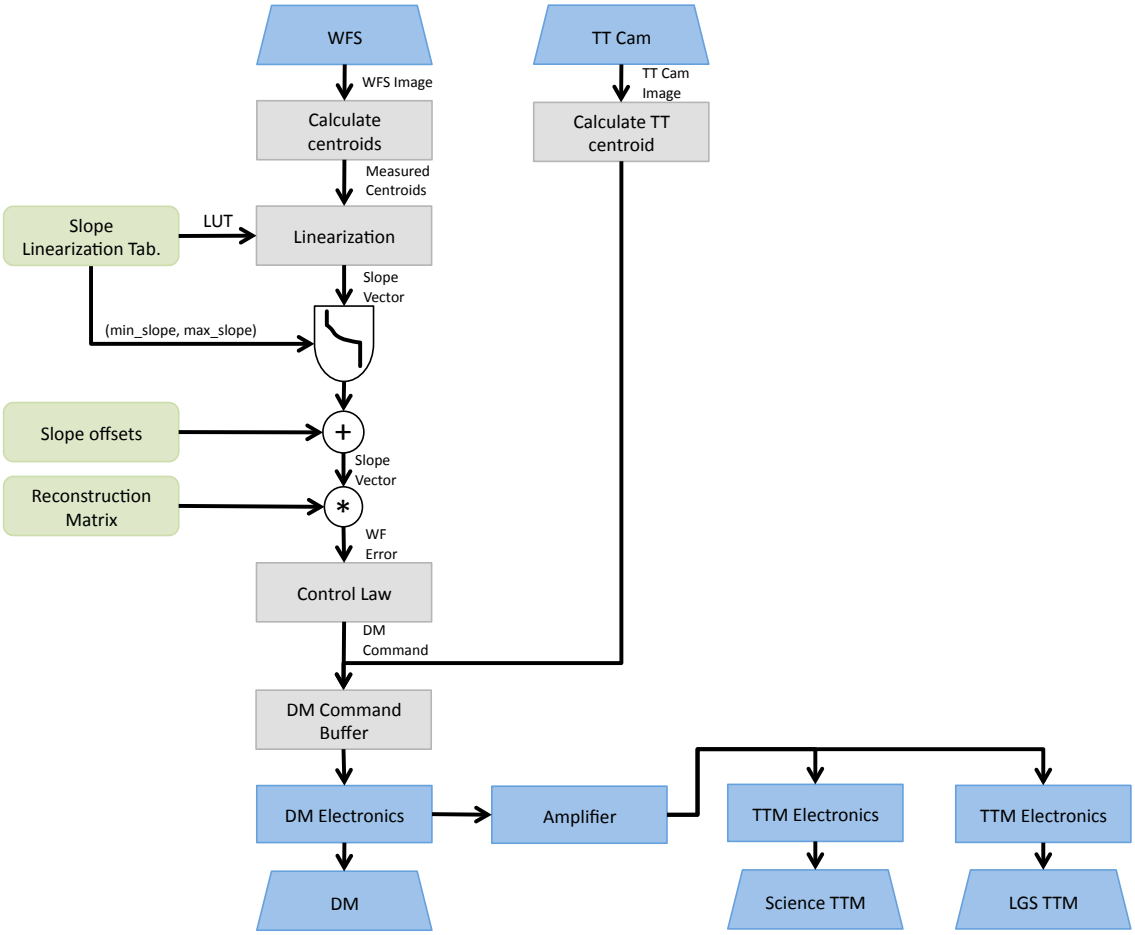

Figure C.1. The algorithm used for processing input from the WFS sensor in LGS mode operation. The algorithm used for centroiding and the control law is same as in the NGS mode.

telescope. This is detected as a TT measurement in the WFS sensor. The reconstructor matrix passes this TT measurement to the laser TT mirror.

C.0.3 LGS Reconstructor

The reconstructor matrix for the LGS mode calculates the corrections from different data sources as compared to the NGS mode reconstructor matrix. The following corrections are calculated from data measured from the WFS sensor and TT camera.

- **DM Actuator Commands**: Calculated from WFS sensor measurements
- **Science TTM**: Calculated from TT camera centroids
- **Laser TTM**: Calculated from WFS sensor measurements

C.0.4 Input

A new wavefront sensor (WFS) image is the beginning of the reconstruction loop. In our implementation, the image is passed as a linear array of values. The array is formed by raster scanning the WFS CCD. The WFS CCD is setup for 3 x 3 binning and produces an image of 26 x 26 pixels. The linear array has 676 values.

Not all the pixels correspond to a valid sub-aperture. A list of sub-apertures to be used and the pixels corresponding to them is loaded into the memory during initialization as `subaperture`. It is read from the configuration file `subaperture.cfg`.

In the NGS mode, the TT information is calculated from the WFS image itself. This is the primary difference between the NGS mode and the LGS mode where the TT information comes from the measured centroid of the TT camera.

C.0.5 Centroiding

The Shack-Hartmann WFS measures the average slope of the wavefront in each lenslet sub-aperture using the movement of the image of the guide star. We calculate the centroid of the guide star image in each sub-aperture to measure the local slopes. Figure C.2 shows the algorithm used for for calculating the centroids.

The hardware design ensures that each guide star spot is nominally centered in the middle of a 2 x 2 pixel area on the WFS CCD. We denote the intensity values of the 4 pixels as a_i, where $i = 0, 1, 2, 3$ is the pixel number. The pixels are numbered as,

$$\begin{pmatrix} 2 & 3 \\ 0 & 1 \end{pmatrix} \tag{C.1}$$

The x and y coordinates of the centroid are defined as,

$$x = \frac{a_3 + a_2 - a_1 - a_0}{a_3 + a_2 + a_1 + a_0}, \tag{C.2}$$

$$y = \frac{a_3 - a_2 + a_1 - a_0}{a_3 + a_2 + a_1 + a_0}. \tag{C.3}$$

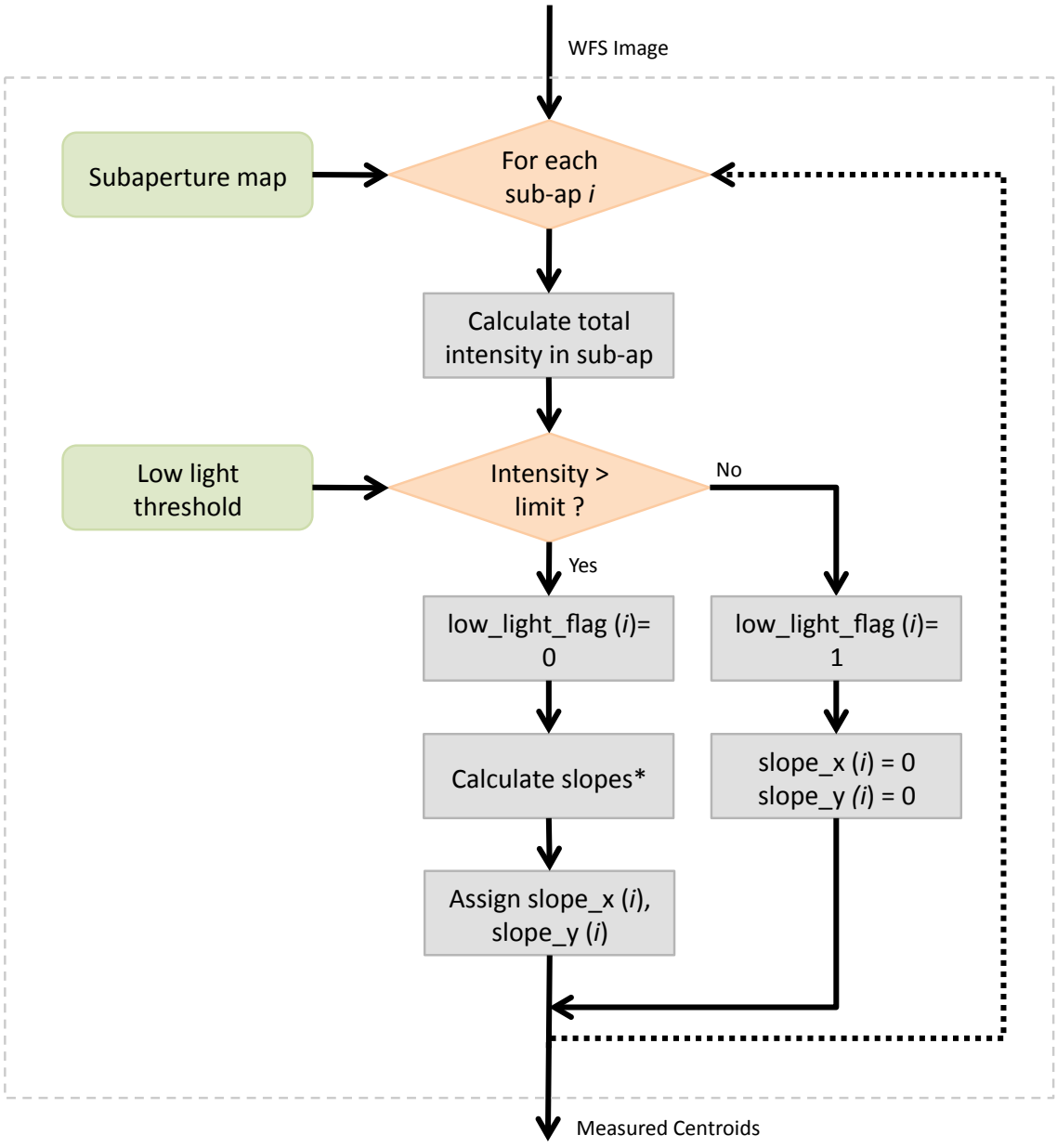

Figure C.2. The algorithm used for calculating the centroids of sub-apertures in the WFS image.

The denominator of the fraction is the total intensity ($I = a_3 + a_2 + a_1 + a_0$.) of the guide star as seen by the sub-aperture. The loop is intended to work in extremely low light conditions. It is possible that the intensity is very low in certain frames. If the intensity is very small in value, the division can create spurious results for centroid values. To avoid this situation, the intensity in each sub-aperture is compared to a preset value in the `low_light_limit` variable. If the intensity is low, the `low_light_flag` for that sub-aperture is set and the x and y coordinates of the centroid are set to zero.

If there is sufficient light, the calculation proceeds as described above. In the implementation, one step of calculation is saved by assigning $d = a_3 - a_0$. The x and y positions are then calculated as,

$$x = \frac{d + a_2 - a_1}{I}, \tag{C.4}$$

$$y = \frac{d - a_2 + a_1}{I}. \tag{C.5}$$

The values are stored in two linear arrays, one for x values and another for y values and passed on.

C.0.6 Linearization of the Slopes

The centroid coordinates calculated in the previous section are an highly non-linear function of the coordinates of the center of the guide star image. The calculated coordinates quickly saturates to a maximum value as the guide star image moves almost moves to one side of the bi-cell.

Since the local slope is proportional to the position of the guide star image, we need to correct this saturation effect. This is done with the help of a pre-calculated lookup table.

The same lookup table also clips the measured slope to be within limited values so that spurious values are rejected. If the value is larger than the maxima of the lookup table, it is replaced by the maxima.

To correct for non common path errors in the system, offsets are added to the corrected slopes. The offsets are stored in `slope_x_offsets` and `slope_y_offsets`, defined as linear arrays and loaded from the configuration file `slopes_offsets.dat`. Since the non common path errors will be different for the IR and Visible cameras, we will have two different sets of slope offsets to choose from.

C.0.7 Matrix Multiplication

To calculate the shape of the wavefront, the local slopes are numerically integrated. The numerical integration is represented as a matrix multiplication with the vector of slopes. The reconstructor matrix is predefined and is loaded into memory at initialization.

The reconstructor matrix (or just reconstructor) to be used depends on the atmospheric conditions and the amount of correction to be used. The reconstructors may be synthesized by choosing different weights for different Zernike modes. In very bad atmospheric

conditions, we may choose to correct only the lower order modes to prevent the loop from becoming unstable.

We are currently using reconstructors synthesized from our knowledge of the setup geometry. The WFS and DM are setup in a Fried configuration which is well studied and understood. The problem of waffle modes is tackled by adding a small fraction of a flat DM actuator positions. This creates a small tendency for the DM to regain the flat position and prevents the growth of waffle modes.

C.0.8 Control Law

Since the optics are setup in a closed loop configuration, the positions calculated by the reconstructor are the difference between the DM actuator positions and the wavefront shape. We need to choose how the calculated errors are applied to the DM without creating instability or oscillations in the feedback loop. A large volume of literature in control theory is available on the subject of stability of control loops. Since Robo-AO needs to work autonomously, we rank stability higher than extreme accuracy of correction. Two of the simplest control laws have been considered for implementation and are described below.

Proportional Control The basic idea of proportional control is that the signal given to the actuator is proportional to the measured error. The proportionality factor is the gain set by the user. We'll do some quick calculations of the control law and its behavior.

Let the local wavefront displacement about its mean as $\phi(t)$ and the position of the corresponding DM actuator as $c(t)$. We can assume a factor of proportionality P between them such that $\phi(t) = Pc(t)$ would be the condition which would remove all error.

We will characterize this control law by its response to a step change. Let $\phi(t) = 0$ initially. At $t = 0$, the wavefront changes to ϕ_o. Let the error between the corrected wavefront and the incoming wavefront be $e(t) = \phi_o - \phi(t)$.

The proportional control law states that,

$$c(t+T) = Ke(t) = K(\phi_o - \phi(t)), \tag{C.6}$$

where T is the latency (time period) between measurement of the wavefront and the actuation of the DM and K is the feedback gain of the system.

If we know P, from previous measurement or by theoretical calculations, we can write,

$$\phi(t+T) = PK(\phi_o - \phi(t)). \tag{C.7}$$

If we solve this recurrence relation, we get,

$$\phi(nT) = \frac{PK}{1+PK}\phi_o + (-PK)^{\frac{t}{T}}\phi_o \tag{C.8}$$

$$\Rightarrow c(nT) = \frac{K}{1+PK}\phi_o + \frac{1}{P}(-PK)^{\frac{t}{T}}\phi_o \tag{C.9}$$

For the control system to converge very close to the required value, we need PK to be as high as possible. However, if K is large, the second term of the equation can blow up to

large values as the system goes unstable.

Integral Control The basic idea of this control law is to have the control signal to be proportional to the integral of the error over time. Thus we write,

$$c(t+T) = c(t) + Ke(t) \tag{C.10}$$
$$\phi(t+T) = \phi(t) + PK(\phi_o - \phi(t)) \tag{C.11}$$
$$\tag{C.12}$$

We solve the recurrence relation to get,

$$\phi(nT) = \phi_o - \phi_o(1-PK)^{\frac{t}{T}}. \tag{C.13}$$

In this, we see that, if $|1-PK| < 1$, then the system converges to the right value. For rapid convergence, need $PK \to 1$.

This control law is also very insensitive to fluctuations or uncertainties in the value of P. If the actual value of the process gain (P in previous example) is Q, we get,

$$\phi(nT) = \phi_o - \phi_o(1-QK)^{\frac{t}{T}}, \tag{C.14}$$

which is still a good control law as long as $|1-QK| < 1$. This allows for a larger range of variation in P.

Modified Integral Control We chose to implement the integral control law with some modifications (Figure C.3). In vector notation, we use the following equation:

$$\mathbf{C}(t+T) = \mathbf{C}(t) + K\mathbf{E}(t) + L(\mathbf{F} - (\mathbf{C}(t) + K\mathbf{E}(t))). \tag{C.15}$$

The vector $\mathbf{C}(t+T)$ denotes the new positions of the DM actuators, $\mathbf{C}(t)$ denotes the old positions of the DM, $\mathbf{E}(t)$ denotes the error calculated from the matrix multiplication and $\mathbf{F}$ is a vector specifying a 'flat map' that describes flat position for the DM. K and L are the loop gain and the leak constant respectively. By introducing the leak constant ($L << 1$), the system has a very small tendency to return to the flat map in absence of any error measurement/input.

Before the commands are sent to the DM, the actuator positions are clipped between zero and a maximum value to prevent damage to the DM. The DM electronics also clips the signals to a safe limit. This only adds another level of safety.

At this point, the TT actuators are treated separately from the other DM actuators by using a different value of loop gain and a different value of maximum deviation.

The TT information for the laser launch telescope will also be processed at this stage in a manner similar to the TT. It will compensate for flexure in the laser launch telescope and the observation telescope. This is yet to be implemented since we are currently using the system in a natural guide star setup.

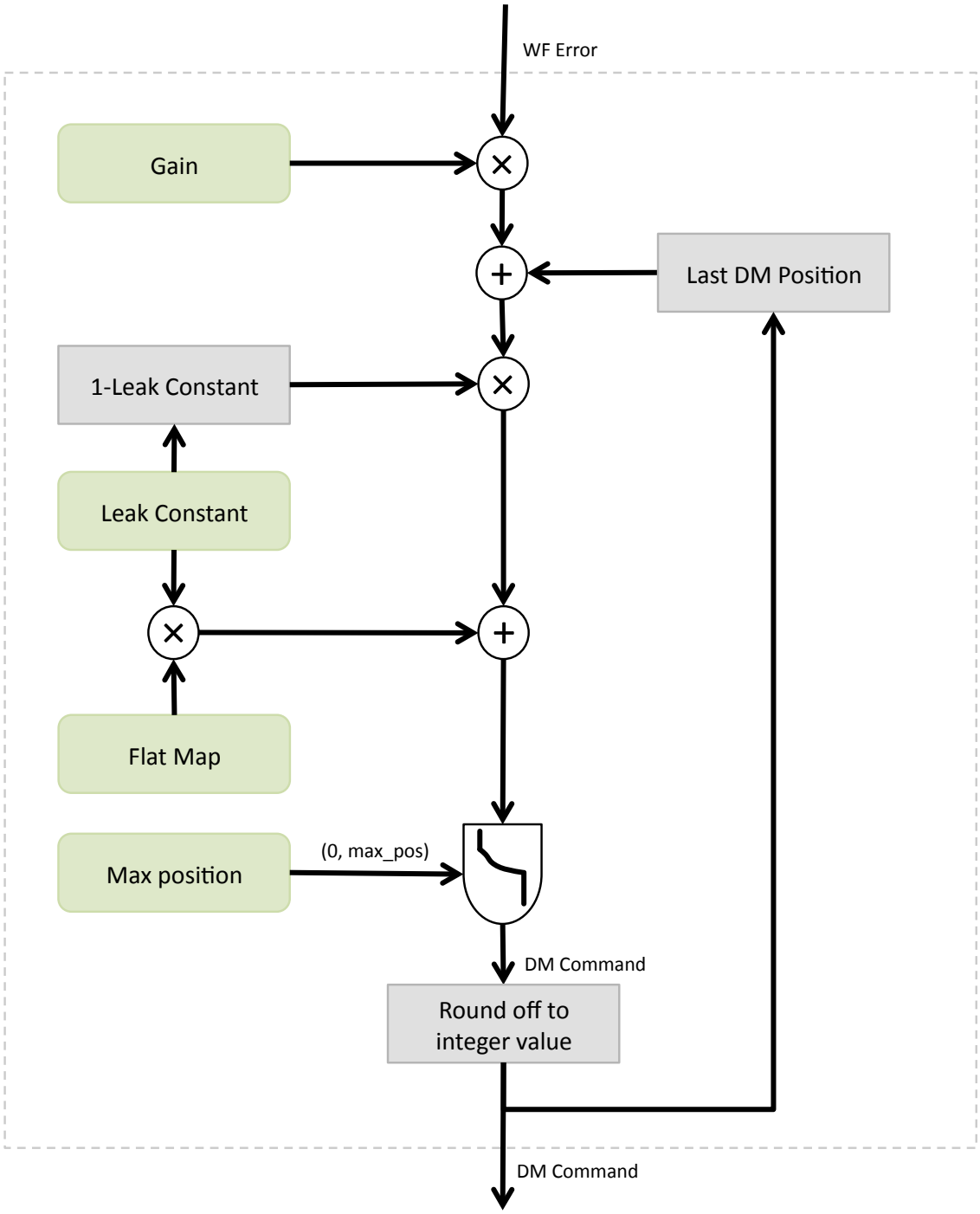

Figure C.3. The algorithm for the modified control law applied for the control of the DM actuators.

C.0.9 Output

At the end of the calculation, the vector of DM actuator positions is remapped to the vector sent to the DM controller. Only the actuators within the size of the telescope pupil as defined by the `ACTUATOR_MAP_FILE` are controlled.

Bibliography

Ahmic, M., Jayawardhana, R., Brandeker, A., Scholz, A., van Kerkwijk, M. H., Delgado-Donate, E., & Froebrich, D. 2007, ApJ, 671, 2074

Amara, A., & Quanz, S. P. 2012, MNRAS, 427, 948

Archibald, R. F., Kaspi, V. M., Beardmore, A. P., Gehrels, N., & Kennea, J. 2012, The Astronomer's Telegram, 4080, 1

Aspin, C., Puxley, P. J., Hawarden, T. G., Paterson, M. J., & Pickup, D. A. 1997, MNRAS, 284, 257

Babcock, H. W. 1953, PASP, 65, 229

Badenes, C., Harris, J., Zaritsky, D., & Prieto, J. L. 2009, ApJ, 700, 727

Baraffe, I., Chabrier, G., Allard, F., & Hauschildt, P. H. 1998, A&A, 337, 403

Baranec, C., et al. 2012, in Society of Photo-Optical Instrumentation Engineers (SPIE) Conference Series, Vol. 8447, Society of Photo-Optical Instrumentation Engineers (SPIE) Conference Series

Baranec, C., et al. 2013, J. Vis. Exp., 72, e50021

Baranec, C. J., Dekany, R., Kulkarni, S. R., Law, N. M., Ofek, E., Kasliwal, M. M., & Velur, V. 2010, Deployment of low-cost replicable laser adaptive optics on 1-3 meter class telescopes, White Paper for NAS Decadal Survey Astro2010

Barthelmy, S. D., et al. 2012, GRB Coordinates Network, 12829, 1

Basinger, S. A., Redding, D. C., Lowman, A. E., Burns, L. A., Liu, K. Y., & Cohen, D. 2000, in Society of Photo-Optical Instrumentation Engineers (SPIE) Conference Series, Vol. 4013, Society of Photo-Optical Instrumentation Engineers (SPIE) Conference Series, ed. J. B. Breckinridge & P. Jakobsen, 749–756

Beloborodov, A. M., & Thompson, C. 2007, ApJ, 657, 967

Bertin, E., & Arnouts, S. 1996, A&AS, 117, 393

Bibby, J. L., Crowther, P. A., Furness, J. P., & Clark, J. S. 2008, MNRAS, 386, L23

Binney, J., & Tremaine, S. 2008, Galactic Dynamics: Second Edition (Princeton University Press)

Boden, A. F., Torres, G., Duchêne, G., Konopacky, Q., Ghez, A. M., Torres, R. M., & Loinard, L. 2012, ApJ, 747, 17

Camero-Arranz, A., et al. 2013, in IAU Symposium, Vol. 291, IAU Symposium, 353–355

Cameron, P. B., Britton, M. C., & Kulkarni, S. R. 2009, AJ, 137, 83

Cameron, P. B., et al. 2005, Nature, 434, 1112

Cenko, S. B., et al. 2006, PASP, 118, 1396

Chassat, F. 1992, Propagation optique a travers la turbulence atmospherique etude modale de l'anisoplanetisme et application a l'optique adaptative

Ciddor, P. E. 1996, Appl. Opt., 35, 1566
Close, L. M., Siegler, N., Freed, M., & Biller, B. 2003, ApJ, 587, 407
Correia, S., Zinnecker, H., Ratzka, T., & Sterzik, M. F. 2006, A&A, 459, 909
Czernik, M. 1966, Acta Astron., 16, 93
D'Antona, F., & Mazzitelli, I. 1997, Mem. Soc. Astron. Italiana, 68, 807
Davies, B., Figer, D. F., Kudritzki, R.-P., Trombley, C., Kouveliotou, C., & Wachter, S. 2009, ApJ, 707, 844
Davies, R., & Kasper, M. 2012, Annual Review of Astronomy and Astrophysics, 50, 305
Davies, R. I., et al. 2006, ApJ, 646, 754
Davis, R. S. 1992, Metrologia, 29, 67
de Luca, A., Caraveo, P. A., Esposito, P., & Hurley, K. 2009, ApJ, 692, 158
de Pater, I., Wong, M. H., Marcus, P., Luszcz-Cook, S., Ádámkovics, M., Conrad, A., Asay-Davis, X., & Go, C. 2010, Icarus, 210, 742
Dehnen, W., & Binney, J. J. 1998, MNRAS, 298, 387
Deller, A. T., Camilo, F., Reynolds, J. E., & Halpern, J. P. 2012, ApJ, 748, L1
Descamps, P., et al. 2011, Icarus, 211, 1022
Dib, R., Kaspi, V., Gavriil, F., & Woods, P. 2006, The Astronomer's Telegram, 845, 1
Diolaiti, E., Bendinelli, O., Bonaccini, D., Close, L. M., Currie, D. G., & Parmeggiani, G. 2000, in SPIE Conference Series, Vol. 4007, SPIE Conference Series, ed. P. L. Wizinowich, 879–888
Duchêne, G., Bouvier, J., & Simon, T. 1999, A&A, 343, 831
Duchêne, G., McCabe, C., Ghez, A. M., & Macintosh, B. A. 2004, ApJ, 606, 969
Durant, M., & van Kerkwijk, M. H. 2006, ApJ, 650, 1070
Egner, S., et al. 2010, 77364V
Eichler, D., Gedalin, M., & Lyubarsky, Y. 2002, ApJ, 578, L121
Eikenberry, S. S., et al. 2004, ApJ, 616, 506
Eisenhauer, F., Schödel, R., Genzel, R., Ott, T., Tecza, M., Abuter, R., Eckart, A., & Alexander, T. 2003, ApJ, 597, L121
Ertan, Ü., & Cheng, K. S. 2004, ApJ, 605, 840
Fahlman, G. G., & Gregory, P. C. 1981, Nature, 293, 202
Ferrand, G., & Safi-Harb, S. 2012, Advances in Space Research, 49, 1313
Figer, D. F., Najarro, F., & Kudritzki, R. P. 2004, ApJ, 610, L109
Foley, S., Kouveliotou, C., Kaneko, Y., & Collazzi, A. 2012, GRB Coordinates Network, 13280, 1
Folha, D. F. M., & Emerson, J. P. 1999, A&A, 352, 517
Frail, D. A., Kulkarni, S. R., & Bloom, J. S. 1999, Nature, 398, 127
Fuchs, Y., Mirabel, F., Chaty, S., Claret, A., Cesarsky, C. J., & Cesarsky, D. A. 1999, A&A, 350, 891
Gaensler, B. M., & Chatterjee, S. 2008, GRB Coordinates Network, 8149, 1
Gaensler, B. M., Slane, P. O., Gotthelf, E. V., & Vasisht, G. 2001, ApJ, 559, 963
Gaensler, B. M., et al. 2005, Nature, 434, 1104
Gavriil, F. P., Dib, R., Kaspi, V. M., & Woods, P. M. 2007, The Astronomer's Telegram, 993, 1
Gerchberg, R. W., & Saxton, W. O. 1972, Optik, 35, 237

Ghez, A. M., Neugebauer, G., & Matthews, K. 1993, AJ, 106, 2005
Giacconi, R., Murray, S., Gursky, H., Kellogg, E., Schreier, E., & Tananbaum, H. 1972, ApJ, 178, 281
Golimowski, D. A., Durrance, S. T., & Clampin, M. 1993, ApJ, 411, L41
Goode, P. R., Yurchyshyn, V., Cao, W., Abramenko, V., Andic, A., Ahn, K., & Chae, J. 2010, ApJ, 714, L31
Göğüş, E., Woods, P. M., Kouveliotou, C., Kaneko, Y., Gaensler, B. M., & Chatterjee, S. 2010, ApJ, 722, 899
Gregory, P. C., & Fahlman, G. G. 1980, Nature, 287, 805
Hardy, J. W. 1998, Adaptive Optics for Astronomical Telescopes
Hart, M. 2010, Appl. Opt., 49, D17
Hartmann, D., et al. 1996, in American Institute of Physics Conference Series, Vol. 366, High Velocity Neutron Stars, ed. R. E. Rothschild & R. E. Lingenfelter, 84–88
Helfand, D. J., Chatterjee, S., Brisken, W. F., Camilo, F., Reynolds, J., van Kerkwijk, M. H., Halpern, J. P., & Ransom, S. M. 2007, ApJ, 662, 1198
Hillenbrand, L. A., & White, R. J. 2004, ApJ, 604, 741
Hobbs, G., Lorimer, D. R., Lyne, A. G., & Kramer, M. 2005, MNRAS, 360, 974
Holland, S. T., et al. 2008, GRB Coordinates Network, 8112, 1
Hulleman, F., Tennant, A. F., van Kerkwijk, M. H., Kulkarni, S. R., Kouveliotou, C., & Patel, S. K. 2001, ApJ, 563, L49
Hulleman, F., van Kerkwijk, M. H., & Kulkarni, S. R. 2000a, Nature, 408, 689
—. 2004, A&A, 416, 1037
Hulleman, F., van Kerkwijk, M. H., Verbunt, F. W. M., & Kulkarni, S. R. 2000b, A&A, 358, 605
Hurley, K. 2011, Physica E Low-Dimensional Systems and Nanostructures, 43, 681
Hurley, K., et al. 1999, Nature, 397, 41
—. 2005, Nature, 434, 1098
Ishimaru, A. 1978, Wave propagation and scattering in random media. Vol._1.
Israel, F. P. 1980, AJ, 85, 1612
Israel, G., et al. 2005, A&A, 438, L1
Israel, G. L., Mereghetti, S., & Stella, L. 1993, IAU Circ., 5889, 1
—. 1994, ApJ, 433, L25
Israel, G. L., et al. 2003, ApJ, 589, L93
—. 2008, ApJ, 685, 1114
Jester, S., et al. 2005, AJ, 130, 873
Johns-Krull, C. M., & Valenti, J. A. 2001, ApJ, 561, 1060
Jones, T. A., Swinbank, A. M., Ellis, R. S., Richard, J., & Stark, D. P. 2010, MNRAS, 404, 1247
Jurić, M., et al. 2008, ApJ, 673, 864
Kaplan, D. L., Chatterjee, S., Hales, C. A., Gaensler, B. M., & Slane, P. O. 2009, AJ, 137, 354
Kaplan, D. L., Fox, D. W., Kulkarni, S. R., Gotthelf, E. V., Vasisht, G., & Frail, D. A. 2002, ApJ, 564, 935
Kaspi, V., Dib, R., & Gavriil, F. 2006, The Astronomer's Telegram, 794, 1

Kaspi, V. M., Gavriil, F. P., & Woods, P. M. 2002a, GRB Coordinates Network, 1432, 1
Kaspi, V. M., Gavriil, F. P., Woods, P. M., Jensen, J. B., Roberts, M. S. E., & Chakrabarty, D. 2003, ApJ, 588, L93
Kaspi, V. M., Jensen, J., Rigaut, F., Hatakeyama, A., & Woods, P. M. 2002b, GRB Coordinates Network, 1438, 1
Kennea, J. A., et al. 2013a, ApJ, 770, L24
—. 2013b, The Astronomer's Telegram, 5009, 1
Kern, B., & Martin, C. 2002, Nature, 417, 527
Kirichenko, A., Danilenko, A., Mennickent, R. E., Pavlov, G., Shibanov, Y., Zharikov, S., & Zyuzin, D. 2012, ArXiv e-prints
Klose, S., et al. 2004, ApJ, 609, L13
Köhler, R., Kunkel, M., Leinert, C., & Zinnecker, H. 2000, A&A, 356, 541
Köhler, R., Petr-Gotzens, M. G., McCaughrean, M. J., Bouvier, J., Duchêne, G., Quirrenbach, A., & Zinnecker, H. 2006, A&A, 458, 461
Kolmogorov, A. 1941, Akademiia Nauk SSSR Doklady, 30, 301
Konopacky, Q. M., Ghez, A. M., Rice, E. L., & Duchêne, G. 2007, ApJ, 663, 394
Kopon, D., Close, L. M., & Gasho, V. 2008, 70156M
Kornilov, V., Tokovinin, A., Shatsky, N., Voziakova, O., Potanin, S., & Safonov, B. 2007, MNRAS, 382, 1268
Kosugi, G., Ogasawara, R., & Terada, H. 2005, ApJ, 623, L125
Kothes, R., Fedotov, K., Foster, T. J., & Uyanıker, B. 2006, A&A, 457, 1081
Kothes, R., & Foster, T. 2012, ApJ, 746, L4
Kothes, R., Uyaniker, B., & Yar, A. 2002, ApJ, 576, 169
Kouveliotou, C., et al. 1993, Nature, 362, 728
—. 1998, Nature, 393, 235
—. 1999, ApJ, 510, L115
Koyama, K., et al. 1989, PASJ, 41, 461
Kraus, A. L., & Hillenbrand, L. A. 2009, ApJ, 704, 531
—. 2012, ApJ, 757, 141
Kraus, A. L., & Ireland, M. J. 2012, ApJ, 745, 5
Kraus, A. L., Ireland, M. J., Martinache, F., & Hillenbrand, L. A. 2011, ApJ, 731, 8
Kraus, A. L., Ireland, M. J., Martinache, F., & Lloyd, J. P. 2008, ApJ, 679, 762
Kraus, A. L., White, R. J., & Hillenbrand, L. A. 2005, ApJ, 633, 452
—. 2006, ApJ, 649, 306
Kulkarni, S. R., Matthews, K., Neugebauer, G., Reid, I. N., van Kerkwijk, M. H., & Vasisht, G. 1995, ApJ, 440, L61
Lafrenière, D., Marois, C., Doyon, R., Nadeau, D., & Artigau, É. 2007, ApJ, 660, 770
Laher, R. R., Gorjian, V., Rebull, L. M., Masci, F. J., Fowler, J. W., Helou, G., Kulkarni, S. R., & Law, N. M. 2012, PASP, 124, 737
Lai, D. 2004, in Cosmic explosions in three dimensions, ed. P. Höflich, P. Kumar, & J. C. Wheeler, 276
Laros, J. G., Fenimore, E. E., Fikani, M. M., Klebesadel, R. W., & Barat, C. 1986, Nature, 322, 152
Law, N. M., Mackay, C. D., & Baldwin, J. E. 2006, A&A, 446, 739

Law, N. M., et al. 2009, ApJ, 692, 924
Leinert, C., Richichi, A., & Haas, M. 1997, A&A, 318, 472
Leinert, C., Zinnecker, H., Weitzel, N., Christou, J., Ridgway, S. T., Jameson, R., Haas, M., & Lenzen, R. 1993, A&A, 278, 129
Levin, L., et al. 2010, ApJ, 721, L33
Linfield, R. P., Colavita, M. M., & Lane, B. F. 2001, ApJ, 554, 505
Liu, M. C. 2006, in Society of Photo-Optical Instrumentation Engineers (SPIE) Conference Series, Vol. 6272, Society of Photo-Optical Instrumentation Engineers (SPIE) Conference Series
Luhman, K. L. 2004, ApJ, 614, 398
—. 2012, ARA&A, 50, 65
Mackay, C., Basden, A., & Bridgeland, M. 2004, in Society of Photo-Optical Instrumentation Engineers (SPIE) Conference Series, Vol. 5499, Society of Photo-Optical Instrumentation Engineers (SPIE) Conference Series, ed. J. D. Garnett & J. W. Beletic, 203–209
Mahajan, V. N. 1983, J. Opt. Soc. Am., 73, 860
Marchis, F., et al. 2006, Nature, 439, 565
Marois, C., Lafrenière, D., Doyon, R., Macintosh, B., & Nadeau, D. 2006, ApJ, 641, 556
Marsden, D., Rothschild, R. E., & Lingenfelter, R. E. 1999, ApJ, 520, L107
Mazets, E. P., Golenetskij, S. V., & Guryan, Y. A. 1979, Soviet Astronomy Letters, 5, 343
McClure-Griffiths, N. M., & Gaensler, B. M. 2005, ApJ, 630, L161
Mel'Nik, A. M., & Dambis, A. K. 2009, MNRAS, 400, 518
Mereghetti, S. 2008, A&A Rev., 15, 225
Mereghetti, S., Götz, D., von Kienlin, A., Rau, A., Lichti, G., Weidenspointner, G., & Jean, P. 2005a, ApJ, 624, L105
Mereghetti, S., et al. 2005b, ApJ, 628, 938
—. 2006, ApJ, 653, 1423
Morini, M., Robba, N. R., Smith, A., & van der Klis, M. 1988, ApJ, 333, 777
Muno, M. P., et al. 2006, ApJ, 636, L41
Nakagawa, Y. E., et al. 2009, PASJ, 61, 387
Noll, R. J. 1976, Journal of the Optical Society of America (1917-1983), 66, 207
Oates, S. R., et al. 2011, GRB Coordinates Network, 12209, 1
Oppenheimer, B. R., & Hinkley, S. 2009, ARA&A, 47, 253
Palla, F., & Stahler, S. W. 1999, ApJ, 525, 772
Palmer, D. M., et al. 2005, Nature, 434, 1107
Park, S., Hughes, J. P., Slane, P. O., Burrows, D. N., Lee, J.-J., & Mori, K. 2012, ApJ, 748, 117
Parmar, A. N., Oosterbroek, T., Favata, F., Pightling, S., Coe, M. J., Mereghetti, S., & Israel, G. L. 1998, A&A, 330, 175
Patience, J., Ghez, A. M., Reid, I. N., Weinberger, A. J., & Matthews, K. 1998, AJ, 115, 1972
Rea, N., et al. 2004, A&A, 425, L5
—. 2010, Science, 330, 944
Reipurth, B., Guimarães, M. M., Connelley, M. S., & Bally, J. 2007, AJ, 134, 2272
Rho, J., & Petre, R. 1997, ApJ, 484, 828

Richichi, A., Leinert, C., Jameson, R., & Zinnecker, H. 1994, A&A, 287, 145
Riddle, R. L., et al. 2012, in Society of Photo-Optical Instrumentation Engineers (SPIE) Conference Series, Vol. 8447, Society of Photo-Optical Instrumentation Engineers (SPIE) Conference Series
Ritchie, B. W., Clark, J. S., Negueruela, I., & Langer, N. 2010, A&A, 520, A48
Roddier, C., Roddier, F., Northcott, M. J., Graves, J. E., & Jim, K. 1996, ApJ, 463, 326
Roe, H. G. 2002, Publications of the Astronomical Society of the Pacific, 114, pp. 450
Ross, T. S. 2009, Appl. Opt., 48, 1812
Rothschild, R. E., & Lingenfelter, R. E., eds. 1996, American Institute of Physics Conference Series, Vol. 366, High Velocity Neutron Stars
Sarazin, M., & Roddier, F. 1990, A&A, 227, 294
Sasaki, M., Plucinsky, P. P., Gaetz, T. J., & Bocchino, F. 2013, A&A, 552, A45
Sasaki, M., Plucinsky, P. P., Gaetz, T. J., Smith, R. K., Edgar, R. J., & Slane, P. O. 2004, ApJ, 617, 322
Schaefer, G. H. 2011, ArXiv e-prints
Schaefer, G. H., Prato, L., Simon, M., & Zavala, R. T. 2012, ApJ, 756, 120
Siess, L., Dufour, E., & Forestini, M. 2000, A&A, 358, 593
Simon, M., Beck, T. L., Greene, T. P., Howell, R. R., Lumsden, S., & Prato, L. 1999a, AJ, 117, 1594
Simon, M., Close, L. M., & Beck, T. L. 1999b, AJ, 117, 1375
Simon, M., et al. 1995, ApJ, 443, 625
Skrutskie, M. F., et al. 2006, AJ, 131, 1163
Sparks, W. B., & Ford, H. C. 2002, ApJ, 578, 543
Spreeuw, H., Scheers, B., & Wijers, R. A. M. J. 2010, A&A, 509, A99
Stone, R. C. 1996, Publications of the Astronomical Society of the Pacific, 108, pp. 1051
—. 2002, Publications of the Astronomical Society of the Pacific, 114, pp. 1070
Svirski, G., Nakar, E., & Ofek, E. O. 2011, MNRAS, 415, 2485
Tanvir, N. R., & Varricatt, W. 2008, GRB Coordinates Network, 8126, 1
Tatarskii, V. I. 1961, Wave Propagation in Turbulent Medium (McGraw-Hill)
Tendulkar, S. P. 2013, in IAU Symposium, Vol. 291, IAU Symposium, 514–516
Tendulkar, S. P., Cameron, P. B., & Kulkarni, S. R. 2012, ApJ, 761, 76
—. 2013, ApJ, 772, 31
Testa, V., et al. 2008, A&A, 482, 607
Tetzlaff, N., Neuhäuser, R., Hohle, M. M., & Maciejewski, G. 2010, MNRAS, 402, 2369
Thatte, N., Abuter, R., Tecza, M., Nielsen, E. L., Clarke, F. J., & Close, L. M. 2007, Monthly Notices of the Royal Astronomical Society, 378, 1229
Thompson, C., & Duncan, R. C. 1993, ApJ, 408, 194
—. 1995, MNRAS, 275, 255
—. 1996, ApJ, 473, 322
Thompson, C., Lyutikov, M., & Kulkarni, S. R. 2002, ApJ, 574, 332
Thomsen, M., Britton, M., & Pickles, A. 2007, in Bulletin of the American Astronomical Society, Vol. 39, American Astronomical Society Meeting Abstracts #210, #117.01
Tian, W. W., Leahy, D. A., & Li, D. 2010, MNRAS, 404, L1
Tody, D. 1986, in Society of Photo-Optical Instrumentation Engineers (SPIE) Conference

Series, Vol. 627, Society of Photo-Optical Instrumentation Engineers (SPIE) Conference Series, ed. D. L. Crawford, 733

Tody, D. 1993, in Astronomical Society of the Pacific Conference Series, Vol. 52, Astronomical Data Analysis Software and Systems II, ed. R. J. Hanisch, R. J. V. Brissenden, & J. Barnes, 173

Tong, H., Xu, R. X., Song, L. M., & Qiao, G. J. 2012, ArXiv e-prints

Torres, R. M., Loinard, L., Mioduszewski, A. J., Boden, A. F., Franco-Hernández, R., Vlemmings, W. H. T., & Rodríguez, L. F. 2012, ApJ, 747, 18

Trümper, J. E., Dennerl, K., Kylafis, N. D., Ertan, Ü., & Zezas, A. 2013, ApJ, 764, 49

van Dam, M. A., et al. 2006, PASP, 118, 310

van Kerkwijk, M. H., Kulkarni, S. R., Matthews, K., & Neugebauer, G. 1995, ApJ, 444, L33

van Paradijs, J., Taam, R. E., & van den Heuvel, E. P. J. 1995, A&A, 299, L41

Vasisht, G., Kulkarni, S. R., Frail, D. A., & Greiner, J. 1994, ApJ, 431, L35

Vink, J., & Kuiper, L. 2006, MNRAS, 370, L14

Vrba, F. J., Henden, A. A., Luginbuhl, C. B., Guetter, H. H., Hartmann, D. H., & Klose, S. 2000, ApJ, 533, L17

Vrba, F. J., et al. 1996, ApJ, 468, 225

Wachter, S., Ramirez-Ruiz, E., Dwarkadas, V. V., Kouveliotou, C., Granot, J., Patel, S. K., & Figer, D. 2008, Nature, 453, 626

Wang, Z., Chakrabarty, D., & Kaplan, D. L. 2006, Nature, 440, 772

Wang, Z., & Kaspi, V. M. 2008, ApJ, 675, 695

Wang, Z., Qu, Q., Luo, D., McCray, R., & Mac Low, M.-M. 1992, ApJ, 388, 127

White, R. J., & Ghez, A. M. 2001, ApJ, 556, 265

White, R. J., Ghez, A. M., Reid, I. N., & Schultz, G. 1999, ApJ, 520, 811

Wizinowich, P. L., et al. 2006, PASP, 118, 297

Woods, P. M., Kouveliotou, C., Finger, M. H., Göğüş, E., Wilson, C. A., Patel, S. K., Hurley, K., & Swank, J. H. 2007, ApJ, 654, 470

Woods, P. M., Kouveliotou, C., Göğüş, E., Finger, M. H., Swank, J., Markwardt, C. B., Hurley, K., & van der Klis, M. 2002, ApJ, 576, 381

Woods, P. M., et al. 2003, ApJ, 596, 464

Wynne, C. G. 1996, MNRAS, 282, 863

—. 1997, MNRAS, 285, 130

Yi, S. K., Kim, Y.-C., & Demarque, P. 2003, ApJS, 144, 259

Ziad, A., Schöck, M., Chanan, G. A., Troy, M., Dekany, R., Lane, B. F., Borgnino, J., & Martin, F. 2004, Appl. Opt., 43, 2316